



THE HONG KONG
POLYTECHNIC UNIVERSITY

香港理工大學

Pao Yue-kong Library

包玉剛圖書館

Copyright Undertaking

This thesis is protected by copyright, with all rights reserved.

By reading and using the thesis, the reader understands and agrees to the following terms:

1. The reader will abide by the rules and legal ordinances governing copyright regarding the use of the thesis.
2. The reader will use the thesis for the purpose of research or private study only and not for distribution or further reproduction or any other purpose.
3. The reader agrees to indemnify and hold the University harmless from and against any loss, damage, cost, liability or expenses arising from copyright infringement or unauthorized usage.

IMPORTANT

If you have reasons to believe that any materials in this thesis are deemed not suitable to be distributed in this form, or a copyright owner having difficulty with the material being included in our database, please contact lbsys@polyu.edu.hk providing details. The Library will look into your claim and consider taking remedial action upon receipt of the written requests.

**NOVEL VIBRATION-ASSISTED
ULTRAPRECISION MACHINING SYSTEM FOR
GENERATING MICRO/NANOSTRUCTURED
SURFACES**

HANHENG DU

PhD

The Hong Kong Polytechnic University

2022

The Hong Kong Polytechnic University
Department of Industrial and Systems Engineering

**Novel vibration-assisted ultraprecision machining
system for generating micro/nanostructured surfaces**

Hanheng Du

A thesis submitted in partial fulfillment of the requirements
for the degree of Doctor of Philosophy

May 2022

CERTIFICATE OF ORIGINALITY

I hereby declare that this thesis is my own work and that, to the best of my knowledge and belief, it reproduces no material previously published or written, nor material that has been accepted for the award of any other degree or diploma, except where due acknowledgement has been made in the text.

_____ (Signed)

Hanheng Du _____ (Name of student)

Abstract

Micro/nanostructured surfaces with regular patterns are drawing ever-increasing attention and are widely used in a range of modern industries due to their tribological, optical, and antibacterial properties, etc. For instance, the micro/nanostructures on the lotus leaf exhibit higher superhydrophobicity and self-cleaning properties. The micro-dimple surfaces can decrease the friction force by 80%. How to machine these functional micro/nanostructured surfaces has become the current research focus. The lithography-based or laser-based machining process is the widely used machining method, but they are limited by the high cost or low surface finish. Vibration-assisted machining is a promising process to solve these problems. However, existing vibration-assisted machining systems still suffer from low bandwidth or high coupling ratio, which affects the machining efficiency and machining flexibility.

In this thesis, a novel two-degree-of-freedom vibration-assisted ultraprecision machining (2DOF-VAUM) system with high machining efficiency and high machining flexibility is designed to machine these micro/nanostructures. In addition to the design of the 2DOF-VAUM system, the modeling of the cutting force, the functional applications of the 2DOF-VAUM system are also studied. The thesis includes four main research parts as follows:

(1) The first part designs the novel 2DOF-VAUM system with a bandwidth of 3000Hz and a low coupling ratio of less than 5%. In the mechanical design, a quasi-ellipse amplification mechanism is proposed to amplify the displacement of the piezoelectric actuator. In comparison with the existing amplification mechanisms, the proposed quasi-ellipse amplification mechanism possesses a compact structure, which can efficiently enhance the bandwidth of the machining. Besides, the orthogonal layout

of the amplification mechanism can decrease the coupling ratio. A detailed multi-physics finite element method is proposed to precisely simulate the working performance of this designed 2DOF-VAUM system. Considering the three-dimensional shape of the cutting tool, machining parameters, and elastic recovery of the workpiece material, a numerical simulation algorithm of the micro/nanostructure generation is then developed to predict the surface topography and provide the guidance in the machining parameter selection.

(2) The second part focuses on the cutting force modeling during micro/nanostructure machining. A practical cutting force prediction model with high accuracy is established with consideration of the periodical vibration motion, tool geometry, and workpiece material, which fills the gap in the cutting force prediction in micro/nanostructure machining. In this model, the instantaneous shear angle is calculated based on the time-varying vibration trajectory. The shear strain and shear strain rate inside the primary shear zone is evaluated by the analysis of the non-equidistant shear zone. The influence of the cutting tool geometry on the cutting force is also investigated considering the relative size between the tool radius and the maximal depth-of-cutting. The shuttle-shaped and bamboo-shaped microstructures are machined on the surface of the difficult-to-machining material, pure titanium TA2, which validates the effectiveness of the proposed cutting force prediction model at different machining parameters.

(3) The third part investigates the application of the developed 2DOF-VAUM system on the magnesium alloy surfaces. Micro/nanostructure generation on the magnesium alloy surface remains a challenge due to its flammability and ignition. The developed 2DOF-VAUM system is applied to effectively solve this problem. Various shape microstructures and sawtooth-shaped nanostructures are successfully machined

on the magnesium alloy surface. In this micro/nanostructure machining, no burn marks are found, which demonstrates the safety of the developed 2DOF-VAUM system. Besides, the sawtooth-shaped nanostructures induce the optical effect to generate the colorful letters and colorful flower image.

(4) The fourth part investigates another application of the developed 2DOF-VAUM system. The developed 2DOF-VAUM system is used to generate and hide optical information on the workpiece surface. This study extends the function of the nanostructures to the field of information science. The quick response (QR) code containing the optical information “Let’s Beat COVID-19 Together” is machined on the workpiece surface. The content of the QR code can be easily read via the smartphone. By adjusting the facet spacing of the nanostructures, the optical information “LOVE” can be hidden. The hidden information is read when the view angle reaches the certain angle. For other view angles, only disturbance information “8888” is viewed.

Overall, this research develops a novel 2DOF-VAUM system to generate the various micro/nanostructures and carries out the systemic study on the machining system design, the cutting force modeling, and the machining system application. The main contributions and significance of this thesis can be concluded as follows: (1) a novel two-degree-of-freedom vibration-assisted ultraprecision machining system with superior working performances was developed, which can generate various micro/nanostructures on workpiece surfaces. (2) A practicable cutting force prediction model was established, which fills the gap in cutting force prediction in the field of micro/nanostructure and also helps to better understand the material removal mechanism during micro/nanostructure machining. (3) The micro/nanostructure generation on the magnesium alloy surfaces was systematically investigated, which

Abstract

expands the function of the magnesium alloy to the field of optics. (4) The generation and hiding method of optical information was proposed based on the periodic nanostructures, which makes the function of nanostructures extend to information storage, information communication, and information hiding.

Publication arising from the thesis

Journal Articles

1. Mengnan Jiang, Yang Wang, Fayu Liu, **Hanheng Du**, Yuchao Li, Huanhuan Zhang, Suet To, Steven Wang, Chin Pan, Jihong Yu, David Quéré, and Zuankai Wang. “Inhibiting the Leidenfrost effect above 1,000° C for sustained thermal cooling.” **Nature** 601, no. 7894 (2022): 568-572. (**Q1, Impact Factor: 69.504**)
2. **Hanheng Du**, Mengnan Jiang, Zuankai Wang, Zhiwei Zhu, and Suet To. “Generating micro/nanostructures on magnesium alloy surfaces using ultraprecision diamond surface texturing process.” **Journal of Magnesium and Alloys**. Accepted. (**Q1, IF=11.813**).
3. **Hanheng Du**, Mengnan Jiang, Zhiwei Zhu, Zuankai Wang, and Suet To. “Ultraprecision tool-servo cutting of pure nickel for fabricating micro/nanostructure arrays”. **Materials & Design**. (2022) 110913. (**Q1, IF=9.417**).
4. **Hanheng Du**, Suet To, Wai Sze Yip, Zhiwei Zhu. “Development and assessment of a novel two-degree-of-freedom vibration generator for generating and hiding optical information”. **Mechanical Systems and Signal Processing** 181 (2022): 109470. (**Q1, IF= 8.934**).
5. **Hanheng Du**, Waisze Yip, Zhiwei Zhu, and Sandy To. “Development of a two-degree-of-freedom vibration generator for fabricating optical microstructure arrays.” **Optics Express** 29, no. 16 (2021): 25903-25921. (**Q2, Impact Factor: 3.833**)
6. Minjie Liu, **Hanheng Du**, Yaqi Cheng, Huanxi Zheng, Yuankai Jin, Suet To, Steven Wang, and Zuankai Wang. “Explosive Pancake Bouncing on Hot

Superhydrophilic Surfaces.” **ACS Applied Materials & Interfaces** (2021). (**Q1, Impact Factor: 10.383**)

7. **Hanheng Du**, Suet To, Tengfei Yin, and Zhiwei Zhu. “Microstructured surface generation and cutting force prediction of pure titanium TA2.” **Precision Engineering** 75 (2022) 101–110. (**Q2, Impact Factor: 3.315**)

8. **Hanheng Du**, Tengfei Yin, Wai Sze Yip, Zhiwei Zhu, and Suet To. “Generation of structural colors on pure magnesium surface using the vibration-assisted diamond cutting.” **Materials Letters** 299 (2021): 130041. (**Q2, Impact Factor: 3.574**)

9. **Hanheng Du**, Tengfei Yin, Denghui Li, Zhiwei Zhu, Suet To. “Nanostructure machining and its application in surface information”. **Surfaces and interfaces**. Minor revision. (**Q1, Impact Factor: 6.137**)

10. **Hanheng Du**, Zhiwei Zhu, and Suet To. “Design, analysis, and test of a novel vibration-assisted ultraprecision cutting system for the fabrication of high aspect ratio nanostructures”. Preparation for the draft.

11. **Hanheng Du**, Zhiwei Zhu, and Suet To. “Experimental and numerical investigations on ultraprecision machining of microstructured surfaces of tungsten carbide in laser-assisted diamond cutting”. In preparation.

Conference Presentations

Hanheng Du, Zhiwei Zhu, Suet To. “Development of a novel vibration-assisted ultraprecision cutting system for fabricating high aspect ratio micro/nanostructures”, The 9th International Conference of Asian Society for Precision Engineering and Nanotechnology (ASPEN 2022), Oral presentation.

Chapters in Books

Hanheng Du, Waisze Yip, Zhiwei Zhu, and Suet To. “Ultra-Precision Diamond Machined Freeform Optical Parts and Structures.” In *Encyclopedia of Materials: Metals and Alloys*, pp. 462-477. Elsevier, 2021.

Acknowledgments

First and foremost, I would like to express my deep appreciation to my chief supervisor, Prof. Suet To, for her strong support and positive encouragement during my doctoral program. I am very happy to be her Ph.D. student to conduct academic research. Thanks are given to my co-supervisor, Prof. Zhiwei Zhu, for his valuable comments on my research work.

Besides my supervisors, I thank Prof. Zuankai Wang of the City University of Hong Kong. He gave me lots of encouragement, which make me full of confidence to carry out my research. I also thank my group members (Dr. Waisze Yip, Dr. Thomas Cheng, Dr. Zejia Zhao, Dr. Zanwen Sun, Dr. Denghui Li, Mr. Tengfei Yin, Mr. Yexiang Fu, Mr. Zhuoxuan Zhuang, Mr. Hongting Zhou, Mr. Oscar Kwok, Mr. Yuqi Dai, and so on) for their kind help on my research and daily life. I appreciate all staff in State Key Laboratory of Ultra-precision Machining Technology, especially Mr. Ka Chun Cheung, Mr. Tai Wa Chung, Mr. Jon Wong, Mr. Tsz Hin Fan, and Ms. Crytal Choy, for providing the experimental support for me. I also express thanks to the office colleagues, such as Dr. Chenliang Wu, Dr. Gao Yang, Dr. Songman Wu, Mr. Shansan Gao, Mr. Ruobin Wang, etc. We had a great time together.

Last, my greatest thanks are given to my mother, father, and sister for their love, care, and support during my whole study stage. Especially, I would like to express thanks to my lovely nieces, Jianing Zhang and Huining Zhang. They are very little and do not realize that their innocent laughter and chatting give me spiritual motivating force to overcome my current difficulties. After each video chatting with them, I always felt full of vitality, which helps me continue to conduct research and write papers.

Table of contents

Abstract	i
Publication arising from the thesis.....	v
Acknowledgments.....	viii
Table of contents.....	ix
List of figures.....	xiv
List of tables.....	xxii
List of acronyms	xxiii
Chapter 1 Introduction	1
1.1 Research background.....	1
1.2 Research objectives.....	4
1.3 Thesis organization	6
Chapter 2 Literature review	8
2.1 Introduction.....	8
2.2 Micro/nanostructured surface machining method	9
2.2.1 Additive material process	10
2.2.2 Deforming process	12
2.2.3 Beam-assisted process	13
2.2.4 Electric-field-assisted process.....	17
2.2.5 Chemical etching process	20

Table of contents

2.2.6 Lithography process.....	22
2.2.7 Ultraprecision diamond cutting.....	24
2.3 Vibration-assisted machining system	31
2.3.1 One-degree-of-freedom vibration-assisted machining system	32
2.3.2 Two-degree-of-freedom vibration-assisted machining system.....	36
2.4 Cutting force modeling	39
2.5 Machining of titanium, magnesium, and their alloys	40
2.6 Functional applications of the micro/nanostructured surface	43
2.7 Summary	47
Chapter 3 Design of the vibration-assisted ultraprecision machining system	49
3.1 Introduction.....	49
3.2 Mechanical design	50
3.3 Multi-physics simulation of the working performances	55
3.3.1 Piezoelectric material property calculation.....	55
3.3.2 Simulation process	58
3.4 Numerical simulation of the micro/nanostructure generation	59
3.4.1 Discretization of the cutting tool and workpiece	62
3.4.2 Modeling of the cutting motion trajectory	63
3.4.3 Evaluation of the material elastic recovery.....	65
3.5 Experimental details.....	67
3.5.1 Working performance test.....	67

Table of contents

3.5.2 Micro/nanostructured surface machining	68
3.6 Results and discussion	70
3.6.1 Working performance	70
3.6.2 Micro/nanostructured surfaces	73
3.7 Summary	77
Chapter 4 Practicable cutting force prediction model.....	79
4.1 Introduction.....	79
4.2 Characteristics of the vibration-assisted ultraprecision machining	80
4.2.1 Time-varying material removal behavior	80
4.2.2 Controllable vibration trajectory	82
4.3 The cutting force prediction modeling.....	86
4.3.1 Instantaneous shear angle	88
4.3.2 Non-equidistant shear zone model.....	88
4.3.3 Instantaneous cutting area.....	92
4.3.4 Instantaneous cutting force	94
4.4 Experimental details.....	95
4.5 Results and discussion	98
4.5.1 Surface topography characterization.....	98
4.5.2 Cutting forces verification	99
4.5.3 Tool wear	102
4.6. Summary	104

Table of contents

Chapter 5 Micro/nanostructure machining on the magnesium alloy surface	106
5.1 Introduction.....	106
5.2 Reliability evaluation of the 2DOF-VAUM system	107
5.3 Finite element model.....	108
5.4 Structural color generation principle	111
5.5 Experimental procedures	113
5.6 Results and discussion	116
5.6.1 Microstructure topography characterization	116
5.6.2 Cutting force analysis in microstructure generation	117
5.6.3 Chip morphology investigation.....	119
5.6.4 Structural color observation.....	120
5.6.5 Tool wear mechanism exploration.....	123
5.7 Summary.....	125
Chapter 6 Generation, hiding, and replication of nanostructure-induced optical information.....	127
6.1 Introduction.....	127
6.2 Optical information generation and hiding.....	128
6.3 Optical information replication.....	131
6.4 Experimental procedures	132
6.5 Results and discussion	133
6.5.1 Optical information readout.....	133

Table of contents

6.5.2 Nanostructure topography characterization	134
6.6 Summary	136
Chapter 7 Conclusions and suggestions for future work	138
7.1 Conclusions.....	138
7.2 Suggestions for future work.....	141
Appendices	145
Appendix I Multifunction I/O device (USB-6341, National Instruments Corp.)	145
Appendix II High-performance piezo amplifier (E-617, Physik Instrumente)	146
Appendix III 4-axis ultra-precision machine (350FG, Moore Nanotechnology)	147
Appendix IV Multicomponent dynamometer (9256C1, Kistler Instrument Corp.)	148
Appendix V Capacitive displacement sensor (Elite, Lion Precision).....	149
Reference	150

List of figures

Figure 1.1 Research framework.....	7
Figure 2.1 Micro/nanostructured surface machining method.....	9
Figure 2.2 Schematic diagram of the two-photon polymerization process (Lin and Xu, 2018).....	11
Figure 2.3 Micro/nanostructures fabricated by the two-photon polymerization. (a) Microneedle (Faraji Rad et al., 2021), (b) woodpile microstructure (Geng et al., 2019), (c) triangular truss microstructure (Geng et al., 2019), and (d) 8 μ m-long micro bull (Ushiba et al., 2013).	12
Figure 2.4 Schematic diagram of the laser beam machining system (Ta et al., 2015).	14
Figure 2.5 Micro/nanostructures machined by the laser beam machining. (a) Ripple-shaped microstructure (Wu et al., 2009), (b) microdot arrays (Mao et al., 2017), (c) microchannel (Chun et al., 2016), and (d) micropillar (Tanvir Ahmmed et al., 2014).	15
Figure 2.6 Schematic diagram of the FIB direct milling (Yao and Epstein, 2010).	16
Figure 2.7 Nanostructures machined by the FIB milling. (a)Nanohole (Hahn et al., 2020), (b) elliptical nanostructures (Gao et al., 2012), (c) Fresnel lens (Wilhelmi et al., 2010), and (d) Beijing Olympic logo (Xu et al., 2009).	16
Figure 2.8 Schematic diagram of the micro-EDM (Jahan et al., 2009).	17
Figure 2.9 Microstructures machined by the micro-EDM. (a) Micro-hole on the tungsten carbide surface (Jahan et al., 2009), (b) needlelike microstructures (Dahmardeh et al., 2011), (c) microchannel (Hösel et al., 2011), and (d) star-shaped deep hole (Ferraris et al., 2011).....	18
Figure 2.10 Schematic diagram of the micro-ECM (Saxena et al., 2018).....	19

List of figures

Figure 2.11 Microstructures machined by the micro-ECM. (a) Micro hole array (Kim et al., 2005), (b) micro hemisphere (Kim et al., 2005), (c) microcavity (Liu et al., 2012), and (d) microgroove (Chen et al., 2016).	20
Figure 2.12 Schematic diagram of the chemical etching process.	21
Figure 2.13 Nanostructures machined by the chemical etching process (Lin et al., 2013). (a) Nanopillar arrays, (b) nanorod arrays, (c) nanopencil arrays, and (d) nanocone arrays.	21
Figure 2.14 Schematic diagram of the lithography process (Lawson and Robinson, 2016).	23
Figure 2.15 Micro/nanostructures machined by the lithography process. (a) Micro-grating (Hsieh and Lee, 2013), (b) inclined arc pitted groove (H. Chen et al., 2017), (c) square micro-hole (Enlund et al., 2005), and (d) mushroom-like pillar (Su et al., 2003).	23
Figure 2.16 Schematic diagram of the single-point diamond turning (Zhang et al., 2019).	25
Figure 2.17 Micro/nanostructures machined by the single-point diamond turning. (a) Micro-lens (Zhang et al., 2019), (b) micro-pillar (Liu et al., 2021), (c) radiant nanostructure array (To et al., 2016), and (d) hexagonal cavity array on the freedom surface (To et al., 2016).	25
Figure 2.18 Schematic diagram of the ultraprecision fly cutting (S. J. Zhang et al., 2016).	26
Figure 2.19 Micro/nanostructures machined by the ultraprecision fly cutting. (a) Micro-lens array (Zhu et al., 2015b), (b) micro-pyramid array (Ge et al., 2018), (c) hybrid micro-pyramid array (Zhu et al., 2015c), and (d) sinusoidal grid	

List of figures

microstructure with the imposition of secondary unidirectional phase gratings (Zhu et al., 2015c).....	27
Figure 2.20 Hardware configuration of the slow-tool-servo machining.....	28
Figure 2.21 (a) Three-dimensional topography of the micro-lens array and (b) cross-sectional profile.	28
Figure 2.22 Schematic diagram of the vibration-assisted machining.....	29
Figure 2.23 Typical mechanical structures of the resonant vibration-assisted machining system. (a) Beam structure (Suzuki et al., 2007) and (b) V-shaped structure (Guo and Ehmann, 2013a).....	30
Figure 2.24 Micro/nanostructures machined by resonant vibration-assisted machining system. (a) Sinusoidal and zigzag grooves on hardened steel (Suzuki et al., 2011), (b) trapezoidal structures (Zhang et al., 2013), (c) hexagonal dimple patterns (Suzuki et al., 2011), and (d) dimple patterns (Guo and Ehmann, 2013b).....	31
Figure 2.25 The classification of the vibration-assisted machining system.	32
Figure 2.26 The development timeline of the typical one-degree-of-freedom vibration-assisted machining system.....	33
Figure 2.27 Microstructures machined by the one-degree-of-freedom vibration-assisted machining system (W. Le Zhu et al., 2019). (a)Single-sinusoidal surface, (b) bi-sinusoidal surface, (c) radial surface, and (d) water-drop surface.	36
Figure 2.28 The development timeline of typical two-degree-of-freedom vibration-assisted machining system.....	37
Figure 2.29 Microstructures machined by the two-degree-of-freedom vibration-assisted machining system. (a) Elongated micro-dimple surface (W. Le Zhu et al., 2017), (b) hierarchical micro-channels surface (W. Le Zhu et al., 2017), (c)	

List of figures

micro-dimple surface (Jieqiong et al., 2017), and (d) sinusoidal wavy surface (Y. Liu et al., 2019).....	38
Figure 2.30 Frontal and inclined views of the <i>Morpho didius</i> wing. (a) and (c) wing in the air, (b) and (d) wing in liquid ethanol, (e) and (f) wing in different viewing angles (Kinoshita et al., 2008).	43
Figure 2.31 SEM images of <i>Morpho didius</i> (Kinoshita et al., 2008).....	44
Figure 2.32 (a) Generation of Monet’s Impression, (b) higher magnification image of the dotted box in (a), and (c) SEM image of nanostructures (Tan et al., 2014).....	44
Figure 2.33 (a) Schematic setup of resonant laser printing and (b) paintings of the resonant laser printing (X. Zhu et al., 2017).....	45
Figure 2.34 (a) Different patterns machined by the laser interference lithography, (b) SEM image of the microstructures, and (c) AFM image of microstructures (Wu et al., 2019).	46
Figure 2.35 (a) Machining principle of the ultrasonic elliptical vibration machining (Guo and Yang, 2019) and (b) Mona Lisa portrait pattern machined by ultrasonic elliptical vibration machining (Yang et al., 2017).	46
Figure 2.36 (a) Machining principle of the vibration-assisted fly cutting and (b) iridescent color machined by vibration-assisted fly cutting (He et al., 2020).	47
Figure 3.1 The topology of two amplification mechanisms. (a) Lever amplification and (b) triangular amplification.....	51
Figure 3.2 The mechanical structure of the 2DOF-VAUM system. (a) The 3D model and (b) the photograph.....	53

List of figures

Figure 3.3 Hardware configuration of the two-degree-of-freedom vibration-assisted ultraprecision machining system during micro/nanostructure machining.	54
Figure 3.4 (a) The axis nomenclature in the piezoelectric material and (b) the schematic of the working principle of the PEA.....	57
Figure 3.5. Meshed multi-physics FEM model of the 2DOF-VAUM system.....	59
Figure 3.6. Principle of micro/nanostructured surface generation.....	60
Figure 3.7. Flowchart of the numerical simulation algorithm.	61
Figure 3.8. SEM images of the cutting tool. (a) Top view and (b) side view.....	63
Figure 3.9. Discretization results of (a) the cutting tool and (b) the workpiece.	63
Figure 3.10. (a)The illustration of material elastic recovery and (b) the elastic recovery function with respect to cutting thickness.	66
Figure 3.11. The working performance test platform of the 2DOF-VAUM system. (a) The schematic diagram and (b) the hardware platform.....	67
Figure 3.12. The experimental setup for machining micro/nanostructured surfaces...	68
Figure 3.13 Measurement and simulation results of the bandwidth.	71
Figure 3.14 Measurement and simulation results of the coupling ratio. (a) Simulated displacement trajectories; displacements (b) along the cutting direction and (c) along the DoC direction.	72
Figure 3.15. Surface topography and geometrical error of (a) Case 1 and (b) Case 2.	74
Figure 3.16 Surface roughness of Case 1 and (b) Case 2.	76
Figure 4.1 Simulation results of the finite element method about instantaneous $\phi_0 t$. (a) Conventional machining and (b) vibration-assisted ultraprecision machining. The $\phi_0 t$ is an angle between the horizontal and the shear plane.	81

List of figures

Figure 4.2 Schematic diagrams of the working principle. (a) Ultrasonic vibration-assisted machining and (b) vibration-assisted ultraprecision machining.	82
Figure 4.3 The three-dimensional mechanical structure and kinematic diagram of the designed two-degree-of-freedom vibration-assisted ultraprecision machining system. Labels QEAU and FGU denote quasi-ellipse amplification unit and flexure guidance unit.	85
Figure 4.4 The cutting edge of the cutting tool. (a) AFM three-dimensional image and (b) A-A cross-section profile plot.	86
Figure 4.5 Flowchart of the cutting force prediction modeling in vibration-assisted ultraprecision machining.	87
Figure 4.6 Schematic diagram of the non-equidistant shear zone model.	89
Figure 4.7 Schematic diagram of the instantaneous cutting area. (a) The radius of the cutting tool is larger than the maximum of the instantaneous depth-of-cutting and (b) the radius of the cutting tool is smaller than the maximum of the instantaneous depth-of-cutting.	94
Figure 4.8 Cutting force diagram of orthogonal vibration-assisted ultraprecision machining.	95
Figure 4.9 Experimental setup of the vibration-assisted ultraprecision machining.	97
Figure 4.10 Optical images and surface topographies. (a) Optical image of Case 1, (b) optical image of Case 2, (c) surface topography of Case 1, and (d) surface topography of Case 2.	99
Figure 4.11 Comparison graphs of predicted and measured cutting forces of (a) F_x in Case 1 and (b) F_z in Case 1; modeling biases of (c) F_x in Case 1 and (d) F_z in Case 1.	101

List of figures

Figure 4.12 Comparison graphs of predicted and measured cutting forces of (a) F_x in Case 2 and (b) F_z in Case 2; modeling biases of (c) F_x in Case 2 and (d) F_z in Case 2.	102
Figure 4.13 SEM images of the single-crystal diamond cutting tool before machining.	103
Figure 4.14 (a) SEM image of the single-crystal diamond cutting tool after machining and (b) the EDX spectrum of Point I.	104
Figure 5.1 The maximum stress of the mechanical structure of the two-degree-of-freedom vibration-assisted ultraprecision machining.	108
Figure 5.2 Finite element model of the vibration-assisted ultraprecision machining process.	109
Figure 5.3 Simulation setting of the finite element model in software Abaqus.	111
Figure 5.4 Generation principle of the structural color.	113
Figure 5.5 The experiment setup of the micro/nanostructure machining. (a) Full-view and (b) close-up view.	115
Figure 5.6 Optical micrographs of microstructures of (a) Case 1, (b) Case 2, and (c) Case 3.	116
Figure 5.7 The measured and simulated cutting forces. (a) Case1, (b) Case 2, (c) Case 3, and (d) snapshot of the simulated machining process in Case1.	118
Figure 5.8 SEM images of the chip morphology. (a) The ultraprecision turning process and (b) the vibration-assisted ultraprecision machining process.	120
Figure 5.9 Photographs of (a) mirror surface, (b) colorful letters “SKL”, “HKPU”, and “Mg alloy”, and (c) colorful flower.	121
Figure 5.10 AFM images of nanostructures of (a) letter “S” in Figure 5.9 and (b) letter “M” in Figure 5.9.	122

List of figures

Figure 5.11 SEM images of the single-crystal diamond cutting tool. (a) Rake face of the new cutting tool, (b) flank face of the new cutting tool, (c) rake face of the worn cutting tool, and (d) flank face of the worn cutting tool.....	123
Figure 5.12 Raman spectrum of (a) the new single-crystal diamond cutting tool and (b) the worn single-crystal diamond cutting tool.	124
Figure 6.1 Schematic illustration of the optical information generation and hiding.	129
Figure 6.2 Toolpaths of (a) QR code and (b) hidden information “LOVE”.....	130
Figure 6.3 Schematic illustration of the replication steps of optical information.....	131
Figure 6.4 The experiment setup of the optical information generation, hiding, and replication.	132
Figure 6.5 Generation and hiding results of optical information.....	133
Figure 6.6 Replication results of optical information “Let’s Beat COVID-19 Together”.	134
Figure 6.7 Three-dimensional topographies and profiles of the nanostructures. (a) AFM image of point A in Figure 6.5(b), (b) A1-A2 cross-sectional profile, (c) AFM image of point B in Figure 6.5(f), (d) B1-B2 cross-sectional profile, (e) AFM image of point C in Figure 6.5(f), and (f) C1-C2 cross-sectional profile.....	135
Figure 6.8 Three-dimensional topography of the replicated nanostructures. (a) AFM image of point D in Figure 6.6 and (b) D1-D2 cross-sectional profile...	136
Figure 7.1 (a) The mechanical structure of the novel vibration-assisted ultraprecision machining system and (b) SEM images of the new type of single-crystal diamond cutting tool.	143
Figure 7.2 The schematic of the experimental setup of water droplet self-transport.	144

List of tables

Table 2.1 Main differences between the micro-ECM and micro-EDM.	19
Table 3.1 Key dimensions of the mechanical structure.	54
Table 3.2 Material properties of the mechanical structure.	54
Table 3.3 Piezoelectric material property provided by the supplier.	57
Table 3.4 The properties of the copper alloy H62.	69
Table 3.5 The process parameters.	69
Table 4.1 The properties of the commercially pure titanium TA2.	97
Table 4.2 The experimental process parameters.	97
Table 5.1 The properties of the AZ31B magnesium alloy.	111
Table 5.2 Johnson-Cook constants of the AZ31B magnesium alloy(Chen et al., 2019).	111
Table 5.3 The machining parameters.	115
Table 6.1 Comparison results of the theoretical value and experimental value of the facet spacing.	136

List of acronyms

AFM=Atomic force microscopy

AOM=Acousto-optic modulator

CNC=Computer numerical control

CTH=Cutting tool holder

DoC=Depth-of-cutting

DOF=Degree-of-freedom

ECM=Electrochemical machining

EDM=Electrical discharge machining

EDX=Energy-dispersive X-ray spectroscopy

FEM=Finite element method

FGU=Flexure guidance unit

FTS=Fast tool servo

MEMS=Micro-electromechanical systems

MTTF=Mean time to failure

1D=One-dimensional

PEA=Piezoelectric actuator

PZT=Piezoelectric

QEAU=Quasi-ellipse amplification unit

QR=Quick response

SEM=Scanning electron microscope

SPDT= Single-point diamond turning

STS=Slow tool servo

3D=Three-dimensional

List of acronyms

2D=Two-dimensional

2DOF-VAUM=two-degree-of-freedom vibration-assisted ultraprecision

machining

UV=Ultraviolet

UVAM=Ultrasonic vibration-assisted machining

VAUM=Vibration-assisted ultraprecision machining

Chapter 1 Introduction

1.1 Research background

The development of modern industrialization is a learning process from nature (Yan et al., 2020). A large number of important achievements in human history are directly inspired by nature, which has become a training center for scientists and engineers from multidisciplinary fields (Malshe et al., 2013). Over millions of years, nature has evolved numerous and nearly perfect materials, systems, and surfaces from nano/microscale to macroscale for humans to assimilate and emulate. For instance, the *Morpho* butterfly, an insect that lives in central and south America, has multiscale structures from nanometer to millimeter on their wing scales. These multiscale structures not only generate brilliant iridescent colors but also enable the butterfly wing scales to have self-cleaning and superhydrophobicity functions (Sato et al., 2009; Zheng et al., 2006). Mimicking the *Morpho* butterfly wings, a high-quality and functional opal film has been fabricated, which possesses both structural color and superhydrophobic properties (Sato et al., 2009). Shark is the fast swimmer in the ocean due to its special skin that is covered by the microgroove. These microgrooves are aligned along the longitudinal body axis, which decreases the resistance of water flowing (Bechert et al., 2000; Jung and Bhushan, 2009). Inspired by the drag reduction property of this microstructure, the microgroove has been applied in lots of fields, such as a full-body swimsuit called “LZR Racer” invented by the Speedo. At the 2008 Beijing Olympics, twenty-three world records had been broken by swimmers wearing an LZR Racer due to its excellent property on drag reduction. Lotus leaf exhibits the

self-cleaning property for minimizing particle adhesion (Bhushan et al., 2009). Self-cleaning implies that water droplets with some dirty dirt can easily roll off the surface and then effectively prevent dirt from being suspended from it. This function can be employed in vehicle windshields, exterior paint for buildings, and solar panels (Yao et al., 2011).

How to machine these nature-inspired micro/nanostructured surfaces with high efficiency and low cost has become the research hotspot in both academic and engineering areas. According to the machining principle, the micro/nanostructure machining process can be classified into additive material process (Hnilova et al., 2012), beam-assisted process (Rotella et al., 2017; Xu et al., 2012), chemical etching process (Yuan et al., 2014), lithography process (Raut et al., 2015; Yang and Aizenberg, 2005), ultraprecision diamond cutting (Guo et al., 2014; Zhang et al., 2015), and so on. Although beam-assisted processes, such as laser beam machining, has the advantage of their flexibility, it has the difficulties to machine micro/nanostructure on the low absorptivity or high reflectivity materials (Dubey and Yadava, 2008). Lithography process suffers from low efficiency and high cost due to its laborious multi-step processes. Chemical etching process can improve the material removal rate for decreasing the machining time, but the surface quality of micro/nanostructures is not high due to the influence from the etching. Additive material process, such as the two-photon polymerization, obsesses with specified materials (Cademartiri and Bishop, 2015) and is limited by the expensive facilitates (Torgersen et al., 2013; Xiong et al., 2012). Ultraprecision diamond cutting is well suited at this micro/nanostructure machining (Dornfeld et al., 2006). Although no post-processing is required for the nanometric surface generation in machining, its processing time is not acceptable for

mass production. Therefore, to efficiently machine these functional micro/nanostructured surfaces, extensive efforts have been devoted to resolving the aforementioned problems in the machining field. Vibration-assisted machining process that utilizes the additional motion of the cutting tool is fast developing. It is widely considered to be a promising technology for machining the micro/nanostructured surfaces. In this process, the machining system still faces the problems of the low degree-of-freedom, low output stiffness, and low bandwidth. The development of a novel vibration-assisted ultraprecision machining system with superior performances is urgently required.

Cutting force is a significant physical indicator for understanding the material removal mechanism in machining. It contains rich information on the machining parameters, material properties of the workpiece, geometric shape of the cutting tool (Z. Zhu et al., 2019a). Although the study of cutting forces in turning and milling has been enough developed (Li et al., 2011; Srinivasa and Shunmugam, 2013), the investigation of cutting forces in the micro/nanostructure machining is not sufficient. This blocks the in-depth understanding of the material removal mechanism in micro/nanostructure machining. Hence, a practical cutting force prediction model needs to be established to help the understanding of the material removal mechanism in the micro/nanostructure machining.

With the ever-increasing demand for lightweight in automotive, electronics, aerospace, biomedical, and other fields, magnesium alloys have received wide attention due to the characteristics of low density, high specific strength, high thermal conductivity, and so on (Trang et al., 2018; Xu et al., 2015). But micro/nanostructure machining on the magnesium alloy surface still faces challenges due to the flammability

and ignition of the magnesium alloy. The vibration-assisted ultraprecision machining system can be applied to explore the machinability of micro/nanostructure on magnesium alloy surface and investigate the corresponding chip morphology, cutting force, and tool wear.

Optical information is an indispensable part of human society, which serves as a means of displaying information, transmitting data, and monitoring healthcare (Isapour and Lattuada, 2018). The current main methods for generating the optical information are to use dyes or pigments. However, these ways result in serious pollution and health problems (Li et al., 2021). Optical information generated by the light interaction with the micro/nanostructures is an environment-friendly alternative (Fu et al., 2018). The vibration-assisted ultraprecision machining system can be also employed to generate and hide optical information.

Overall, the micro/nanostructure machining with high efficiency and high surface quality still faces several challenges. A novel vibration-assisted ultraprecision machining system needs to be developed to solve these problems, including the mechanical design of the machining system, the prediction of cutting forces, and functional applications of the micro/nanostructures.

1.2 Research objectives

The overall objective of this thesis is to develop a novel vibration-assisted ultraprecision machining system for generating micro/nanostructured surfaces. A practical cutting force model is proposed to predict the cutting forces during machining micro/nanostructures. Two applications of micro/nanostructures are systematically investigated. Specifically, the objectives of this research are:

- (1) To design a novel two-degree-of-freedom vibration-assisted ultraprecision machining system with high bandwidth and low coupling ratio for machining micro/nanostructured surfaces.
- (2) To establish a multi-physics finite element model for precisely simulating and foretelling the working performances of the developed machining system in terms of the working frequency range and coupling ratio.
- (3) To propose a numerical simulation algorithm of micro/nanostructure generation with the comprehensive consideration of the three-dimensional geometric shape of the cutting tool, the cutting trajectory, and the elastic recovery of workpiece material.
- (4) To establish a practical cutting force model to predict the cutting forces in micro/nanostructure generation and enhance the understanding of the material removal mechanism of micro/nanostructure machining.
- (5) To investigate the machinability of the micro/nanostructure on the difficult-to-machine material (pure titanium TA2) and easy-to-flame material (AZ31B magnesium alloy), including micro/nanostructure topography, cutting forces, tool wear mechanism.
- (6) To explore the applications of micro/nanostructures on information science, such as optical information generation, hiding, and replication, and extend the application range of the two-degree-of-freedom vibration-assisted ultraprecision machining system.

1.3 Thesis organization

The thesis takes machining micro/nanostructures as a center and performs three layers of research, i.e., design layer, model layer, and application layer, as shown in Figure 1.1. The thesis includes seven chapters.

Chapter 1 is an introduction. It describes the research background, research objective, and thesis organization.

Chapter 2 reviews the previous research studies on the micro/nanostructure machining methods, the development history of the vibration-assisted machining system, cutting force modeling, machining of titanium, magnesium, and their alloys, and functional applications of the micro/nanostructured surfaces.

Chapter 3 reports the research work of the design layer, in which a novel two-degree-of-freedom vibration-assisted ultraprecision machining system is designed. The multi-physics simulation model of the working performances of this machining system and a numerical simulation algorithm of micro/nanostructure generation on the metal surface are also introduced.

Chapter 4 reports the research work of the model layer, in which a practical cutting force model is established to predict the cutting forces in micro/nanostructure machining. Investigation of machining micro/nanostructures on the difficult-to-machine material (pure titanium TA2) is also introduced.

Chapter 5 reports the research work of the application layer, in which the micro/nanostructure on the easy-to-flame material (AZ31B magnesium alloy) is generated. The related micro/nanostructure topography, cutting forces, and tool wear mechanism are also introduced.

Chapter 1 Introduction

Chapter 6 reports another field of the application layer. The optical information can be generated and hidden by the developed two-degree-of-freedom vibration-assisted ultraprecision machining system.

Chapter 7 concludes this research and presents suggestions for future work.

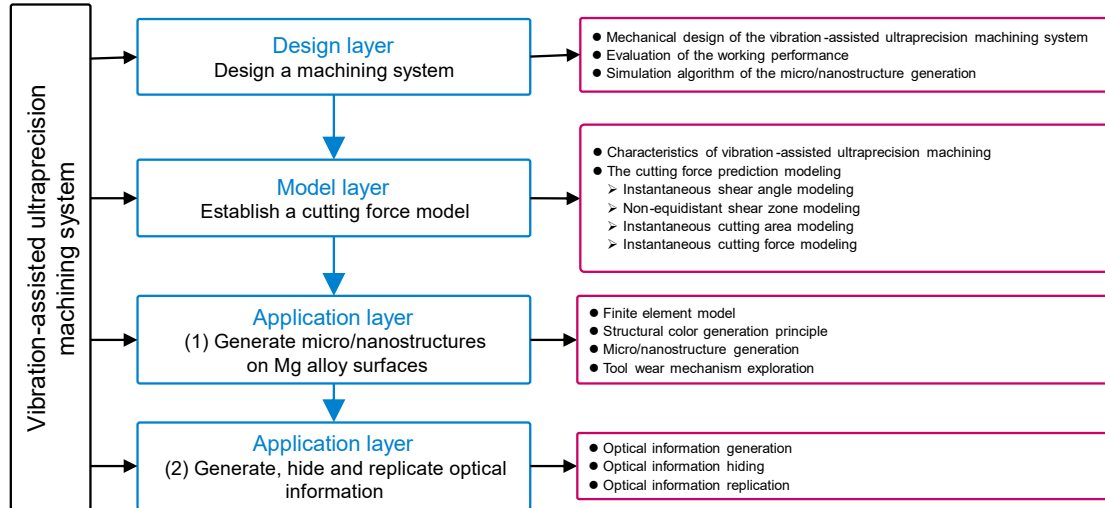


Figure 1.1 Research framework.

Chapter 2 Literature review

2.1 Introduction

Micro/nanostructured surfaces have a decisive impact on the functional performance of products. The micro/nanostructured surfaces have the capability of improving the optical, thermal, mechanical, and biological properties (Bruzzone et al., 2008; Malshe et al., 2013; Whitesides, 2006). For instance, the micro-lens plate can help the LED to uniformly deliver light only into the street (Lee et al., 2013). The micro/nanostructures greatly enhance the spray cooling heat transfer of the sample surface (Chen et al., 2018). The sinusoidal grid surface can be employed as a surface encoder for multi-axis position measurement (Gao et al., 2003). Micro/nanostructures on NiTi alloy surface kill 100% colonized *Pseudomonas aeruginosa* and 95.6% colonized *Staphylococcus aureus* after twenty-four-hour incubation, effectively preventing the bacterial infection (Ma et al., 2020). These functional micro/nanostructured surfaces have periodic patterns. A variety of machining methods have been proposed to effectively generate these functional surfaces.

This chapter will firstly investigate the machining method of micro/nanostructured surfaces in Section 2.2. And then the vibration-assisted machining system with one degree-of-freedom and two-degree-of-freedom are systematically reviewed in Section 2.3. The models of cutting force in machining are briefly demonstrated in Section 2.4. Section 2.5 gives the introduction to the applications of micro/nanostructures. Finally, a summary is drawn about this literature review.

2.2 Micro/nanostructured surface machining method

Micro/nanostructured surfaces can be achieved by different machining methods. According to the micro/nanostructure formation modality, it can be divided into the additive material process, deforming process, and the subtractive material process, as shown in Figure 2.1. In this section, an overview of the typical machining methods, such as additive material process, beam-assisted process, electric-field-assisted, and so on, are given along with the machining principle and fabricated micro/nanostructures.

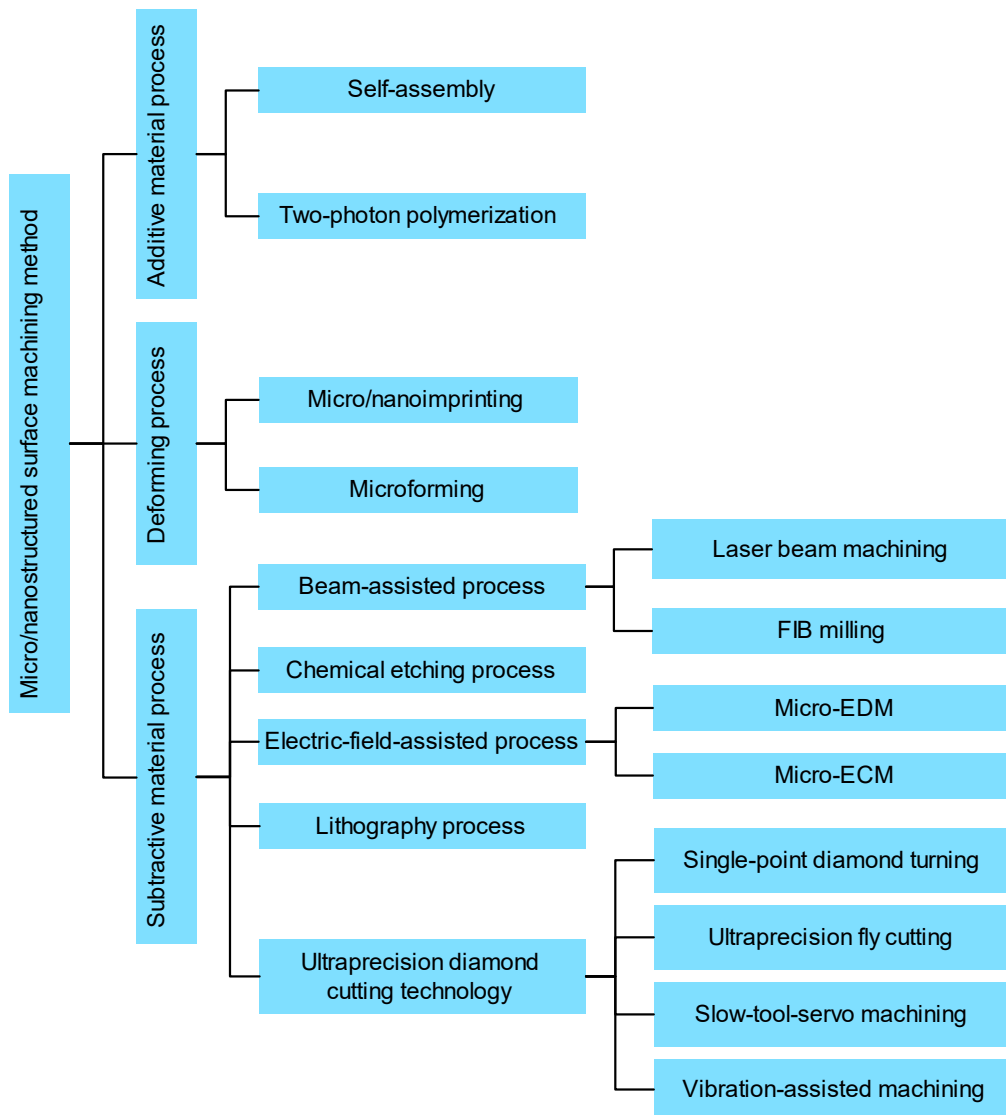


Figure 2.1 Micro/nanostructured surface machining method.

2.2.1 Additive material process

The additive material process is a typical bottom-up machining method that machines the micro/nanostructures from the atomic or molecular scale to nano or microscale (Zuo et al., 2019). It includes self-assembly and two-photon polymerization.

(1) Self-assembly

Self-assembly is the spontaneous organization of making individual components into complex organized structures (Grzelczak et al., 2010; Mayer et al., 2018). This process is manipulated by the physical and chemical properties of substrate surfaces, nanoparticles, and their interactions (Karg et al., 2015). The driving forces that organize these individual components into organized micro/nano include capillary forces, Van der Waals forces, electrostatic forces, hydrogen bonding forces, hydrophobic forces, etc (Biswas et al., 2012). Micro/nanostructures are achieved when the equilibrium of these forces is reached. Sometimes, external magnetic, electric, fluidic, or temperate fields can also be used to induce the generation of micro/nanostructures with a specific shape. Hierarchical micro/nanostructure fabricated by the self-assembly process is applied in different fields. For example, the colloid-crystal membrane can be used in nucleic acid amplification tests, which guarantee highly precise and sensitive detection (D. Zhang et al., 2018). The wettability of the polyimide films can be changed from hydrophobic to superhydrophobic, which can be potentially employed in the self-cleaning field (Xu and Wang, 2018). Self-assembly is a low fabrication cost and mild fabrication process, and it is easy to realize in laboratories. But it also has distinct disadvantages in limited lattice structures and uncontrollable defeats (Ding et al., 2020)

(2) Two-photon polymerization

In the two-photon polymerization process, a femtosecond or picosecond laser is used to provide a focused laser pulse. When the pulse focuses on the volume of a photosensitive material (or photoresist), the photoinitiator molecules start the polymerization by two-photon absorption. When the absorption energy exceeds the threshold of the photosensitive resin, the polymerized material forms the micro/nanostructure, and the non-polymerized material is washed out to uncover the micro/nanostructure (Faraji Rad et al., 2021). The process of two-photon polymerization is illustrated in Figure 2.2. A Ti: sapphire laser with the wavelength 780 nm is used to provide consistent light. Then, the light passes through an acoustic-optic modulator (AOM), a neutral density filter, a beam expander, and a series of a mirror. It finally focuses on the photosensitive material through an objective lens. At the same time, a positioning stage and two galvanometric mirrors are employed to control the movements in the direction of the x , y , and z axes, respectively (Lin and Xu, 2018).

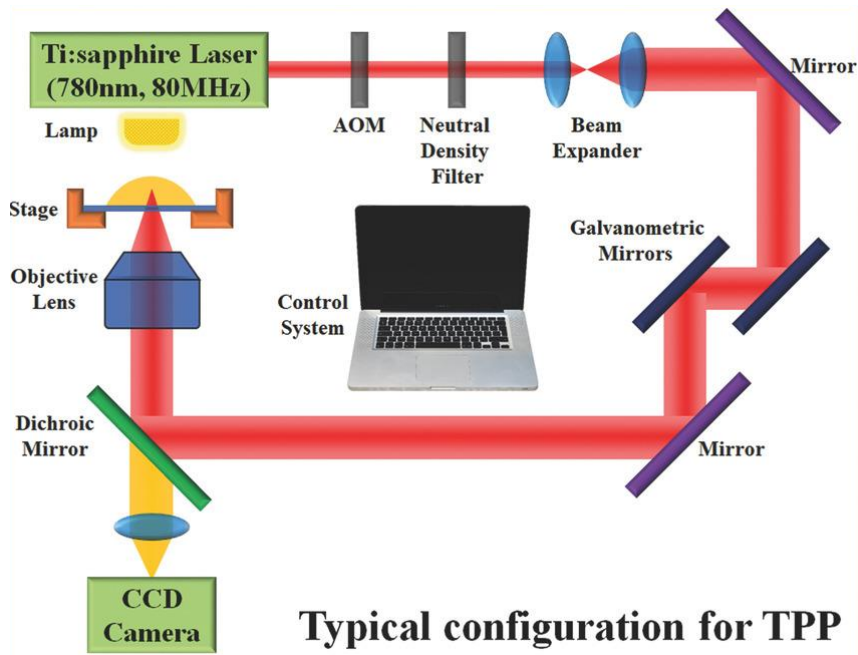


Figure 2.2 Schematic diagram of the two-photon polymerization process (Lin and Xu, 2018).

The material of the micro/nanostructures is not limited to just polymers but includes modified ceramics (Doraiswamy et al., 2006), water-soluble biocompatible materials (Balmert et al., 2021), and polyethylene glycol (Gittard et al., 2010). Through programming the laser focal point to move in three-dimensional space, different shaped micro/nanostructures, such as microneedle and micro bull, can be formed by the two-photon polymerization process, as shown in Figure 2.3.

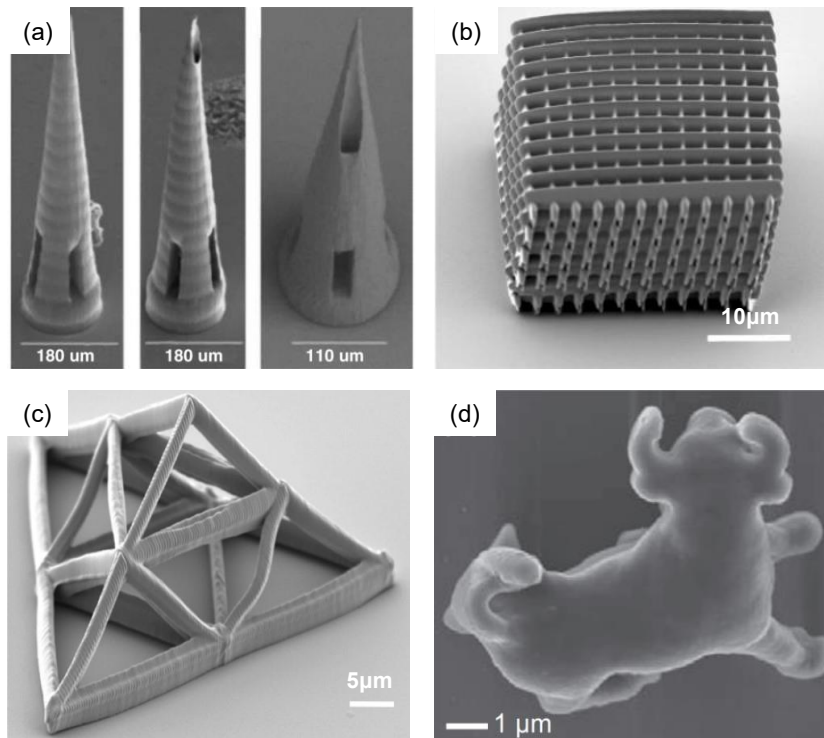


Figure 2.3 Micro/nanostructures fabricated by the two-photon polymerization. (a) Microneedle (Faraji Rad et al., 2021), (b) woodpile microstructure (Geng et al., 2019), (c) triangular truss microstructure (Geng et al., 2019), and (d) 8μm-long micro bull (Ushiba et al., 2013).

2.2.2 Deforming process

In the deforming process, an irreversible deformation was applied to obtain the desired micro/nanostructures by permanently changing the shape of the workpiece. This process can be divided into the micro/nanoimprinting and the micro-forming.

(1) Micro/nanoimprinting

Micro-/nanoimprinting was proposed in 1995 to replicate micro/nanostructure arrays (Muanchan and Ito, 2018). This process has the advantages, such as low-cost, lower residual deformation, and high replication accuracy. The feature dimensions of replicated structures can be from the micrometer to the nanometer. Besides, it can generate high aspect-ratio micro/nanostructures on a thin substrate. The micro/nanoimprinting can be divided into ultraviolet micro/nanoimprinting and thermal micro/nanoimprinting. The ultraviolet micro/nanoimprinting is suitable for ultraviolet-curable materials with the help of ultraviolet light. Thermal micro/nanoimprinting is suitable for softened thermoplastic materials.

(2) Microforming

Microforming is a promising method to fabricate metallic microparts, which are widely applied in micro-electromechanical systems and micro-system technologies (Geiger et al., 2001). This process has the merits of low cost, good productivity, and controlled quality. The feature dimensions of microparts can range from the millimeter to the submillimeter (Fu and Chan, 2013). In the microforming process, the size effects affect the deformation behaviors of metals, such as flow stress, flow behavior, elastic recovery, and ductility (Engel and Eckstein, 2002). Therefore, the size effects have to be considered when fabricating metallic microparts using this process. Micro-hole, micro-groove, micro-screws, and micro-frames are always fabricated by this process.

2.2.3 Beam-assisted process

Beam-assisted process is a physical machining process that uses the laser beam or focused ion beam to fabricate micro/nanostructures. Therefore, it can be divided into laser beam machining and focused ion beam (FIB) milling.

(1) Laser beam machining

Laser is one of the most flexible tools to machine multiscale micro/nanostructures. Laser beam machining is the most common method to generate these micro/nanostructures, which utilizes the high-intensity laser to gradually ablate the workpiece material for machining the designed patterns with a size of 100nm-10 μ m (Brinksmeier et al., 2020). A schematic illustration of the laser beam machining is shown in Figure 2.4.

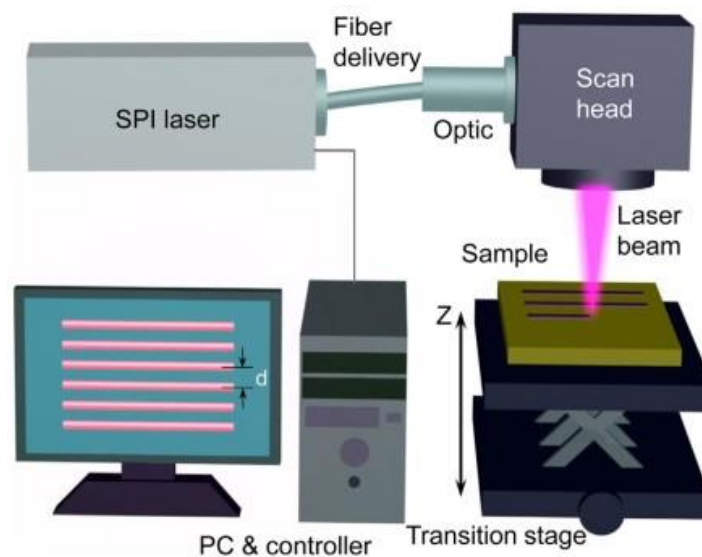


Figure 2.4 Schematic diagram of the laser beam machining system (Ta et al., 2015).

Different shaped micro/nanostructures are machined by this laser beam machining process. For instance, periodic ripples and cone-shaped spikes were machined on stainless steel surface. The structures possess superhydrophobic properties (Wu et al., 2009). Wave-like and coral-like micro/nanostructures were fabricated on the crystalline silicon surface (Cao et al., 2020). Other typical micro/nanostructures fabricated by laser beam machining are shown in Figure 2.5.

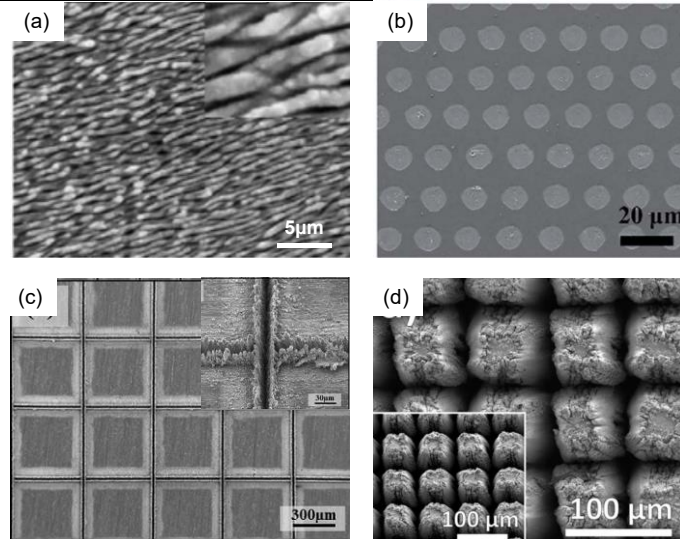


Figure 2.5 Micro/nanostructures machined by the laser beam machining. (a) Ripple-shaped microstructure (Wu et al., 2009), (b) microdot arrays (Mao et al., 2017), (c) microchannel (Chun et al., 2016), and (d) micropillar (Tanvir Ahmmed et al., 2014).

(2) FIB milling

FIB milling is a powerful and direct machining tool, which provides the machining resolution down to several nanometers (Li and Liu, 2018). It also has the merit of one-step fabrication. That means that there are no pattern transfer steps. Besides, the FIB milling process is preferred for most materials (e.g., metals, glass, ceramics, silicon, etc.) (Fu and Bryan, 2004). Its machining principle is shown in Figure 2.6. The FIB milling is a continuous collision process that the beam of gallium ions from a liquid metal ion source beats the targeted area to remove workpiece materials. The Ga^+ ion is the most common ion, which is extracted from the gallium liquid metal ion source. Ga^+ ions are accelerated down to the ion column and then focused onto the sample surface through the electrostatic lenses. The optimum ion probe can be obtained by adjusting apertures and all lenses (Sezen, 2016). The material removal rate mainly relies on the beam voltage and current applied in the process. In this FIB milling system, scanning electron microscopy (SEM) is used for imaging in real-time during the FIB milling.

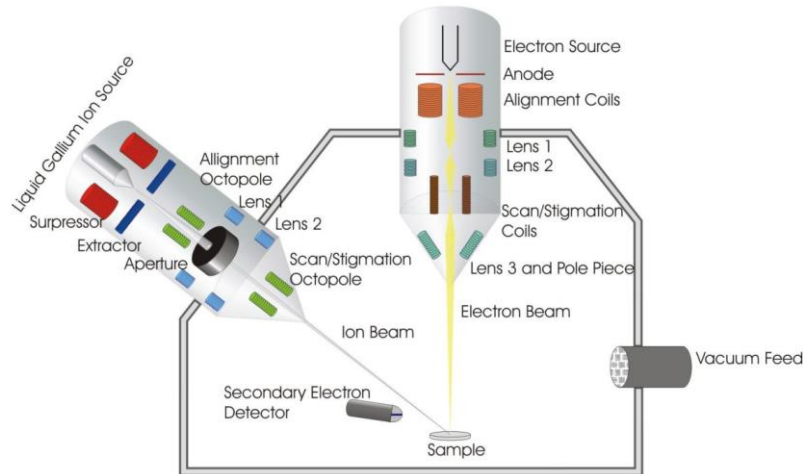


Figure 2.6 Schematic diagram of the FIB direct milling (Yao and Epstein, 2010).

FIB milling can be used to create both simple structures, such as nanohole and elliptical nanostructures, and complex patterns, such as Fresnel lens and Beijing Olympic logo, as shown in Figure 2.7.

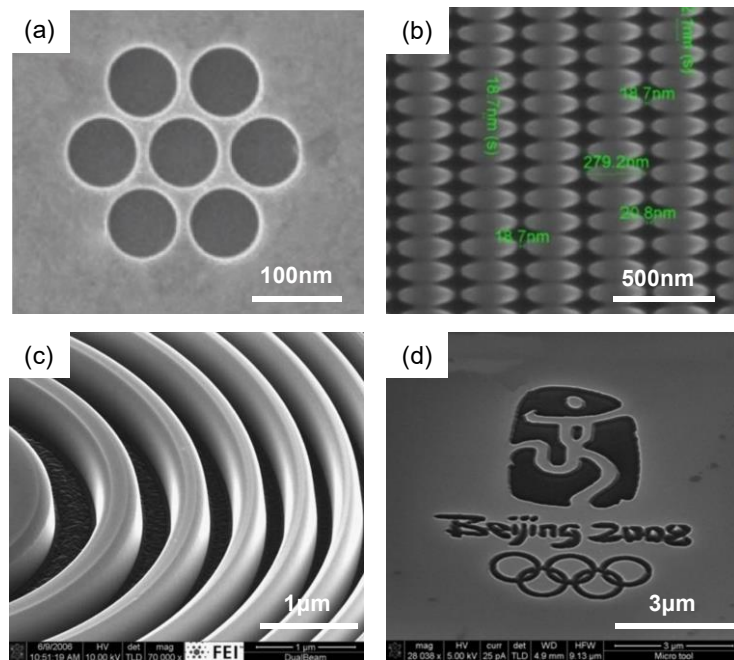


Figure 2.7 Nanostructures machined by the FIB milling. (a) Nanohole (Hahn et al., 2020), (b) elliptical nanostructures (Gao et al., 2012), (c) Fresnel lens (Wilhelmi et al., 2010), and (d) Beijing Olympic logo (Xu et al., 2009).

2.2.4 Electric-field-assisted process

Electric-field-assisted process includes micro-electrical discharge machining(micro-EDM) and micro-electrochemical machining(micro-ECM).

(1) Micro-EDM

Micro-EDM is a non-contact and electrothermal machining process, and there is no cutting force existence between the workpiece and tool. Figure 2.8 illustrates the machining principle of the Micro-EDM. It is based on a simple theory. When two electrodes come closer to each other in a dielectric fluid, the dielectric medium breaks down and the electrical sparks are generated between the electrodes (the tool and the workpiece). The thermal energy will be released to remove the workpiece material by melting and evaporation (Jerald et al., 2013). By precise manipulation of the amount of thermal energy released, desired micro/nanostructures are achieved on any electrically conductive material, such as metals, metallic alloys, graphite, or even some ceramic materials with high surface accuracy (Jahan et al., 2009).

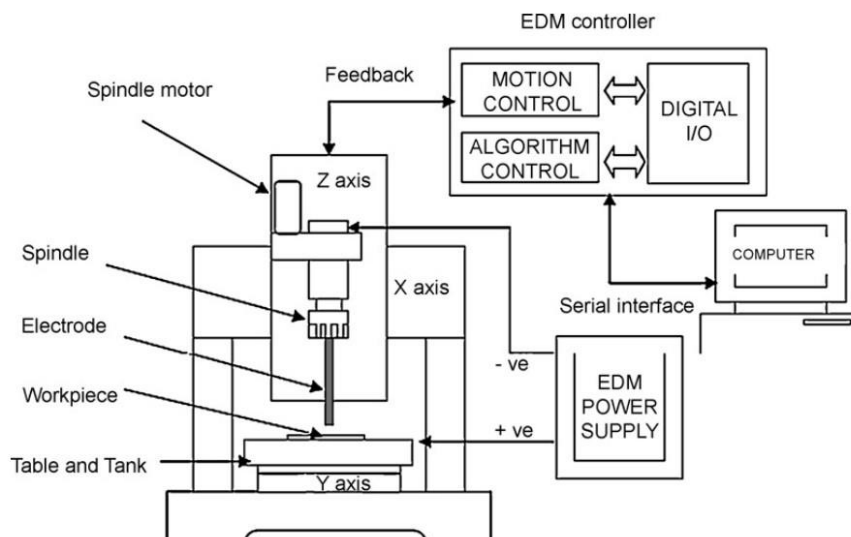


Figure 2.8 Schematic diagram of the micro-EDM (Jahan et al., 2009).

Micro-EDM can be employed to machine different microstructures, especially on difficult-to-machine materials. Figure 2.9 shows some typical microstructures.

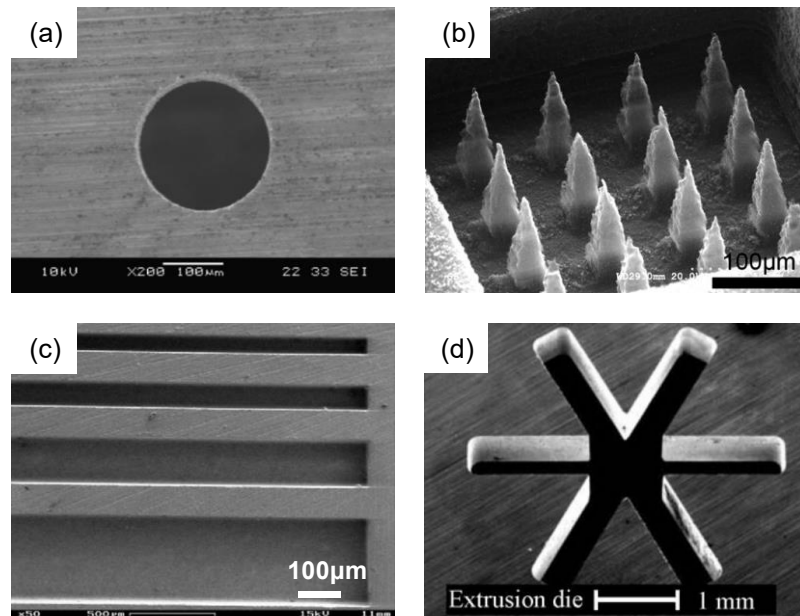


Figure 2.9 Microstructures machined by the micro-EDM. (a) Micro-hole on the tungsten carbide surface (Jahan et al., 2009), (b) needlelike microstructures (Dahmardeh et al., 2011), (c) microchannel (Hösel et al., 2011), and (d) star-shaped deep hole (Ferraris et al., 2011).

(2) Micro-ECM

The micro-ECM process is applied in a wide range of fields such as automotive, aerospace, microelectronics, and biomedical, etc (Saxena et al., 2018). Because it has many merits, such as no electrode wear and good surface quality. In micro-ECM, the principle of material removal is based on anode dissolution. Compared with the micro-EDM process, the material removal rate of the micro-ECM process is relatively lower since the low voltage, small current, and the short pulses must be employed in micro-ECM to assure required shape accuracy. But the micro-ECM process has several valuable advantages, such as no tool wear, fine surface roughness, and no heat-affected layer on the surface (Yong and Ruiqin, 2013). Although the micro-EDM and micro-ECM have the same features, such as non-contact between the workpiece and tool and

machinability for difficult-to-machining materials, their machining principles are different. The main differences between the micro-ECM and micro-EDM are listed in Table 2.1.

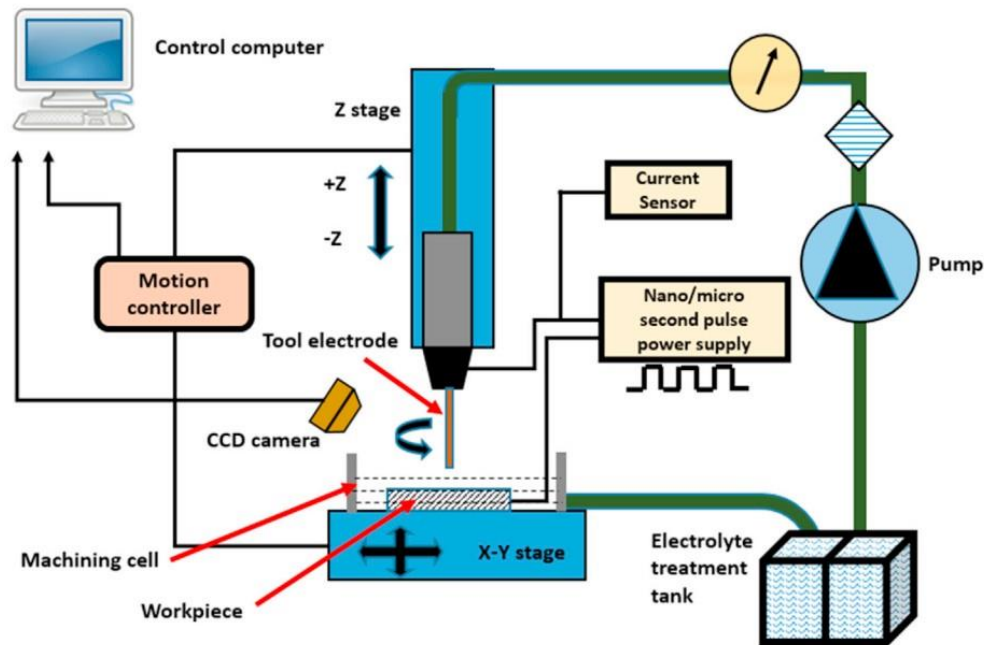


Figure 2.10 Schematic diagram of the micro-ECM (Saxena et al., 2018).

Table 2.1 Main differences between the micro-ECM and micro-EDM.

	Micro-ECM	Micro-EDM
Material removal mechanism	Electrochemical machining (material removal due to electrochemical reaction)	Thermal machining (material melt and evaporation due to heat)
Working fluid	Conductive electrolyte	Non-conductive fluid
Surface quality	Superfine	Fine
Machining accuracy	Low	High
Tool wear	No wear	Wear
Workpiece material	Metal material	Conductive materials and some non-conductive materials
Machining stability	Unstable	Stable

With the assistance of a computer-aided design & computer-aided manufacturing technology together with multi-axis motion platforms, micro-ECM can be applied for machining the micro-hole array, micro hemisphere, microcavity, and microgroove, as shown in Figure 2.11.

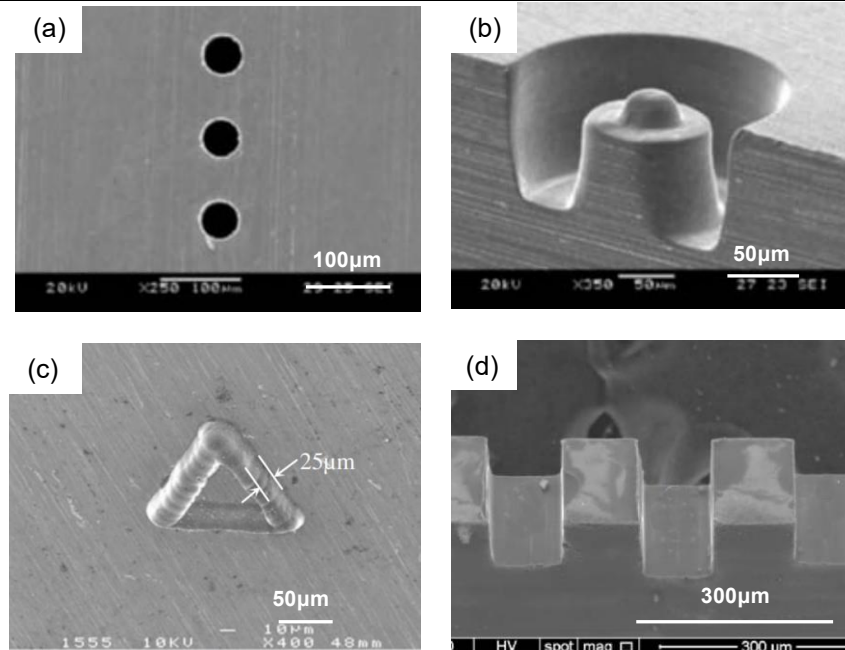


Figure 2.11 Microstructures machined by the micro-ECM. (a) Micro hole array (Kim et al., 2005), (b) micro hemisphere (Kim et al., 2005), (c) microcavity (Liu et al., 2012), and (d) microgroove (Chen et al., 2016).

2.2.5 Chemical etching process

Chemical etching process, also known as chemical milling, which uses liquid chemical agents to remove the workpiece material and create micro/nanostructures by means of a chemical reaction. The area that does not need to be machined will be protected by a mask. After the process is finished, the workpiece will be thoroughly cleaned to stop further reaction and material removal. The machining mechanism of the chemical etching process is shown in Figure 2.12.

This process not only can be applied to metal materials, such as copper, titanium, steel, nickel, and aluminum but also machine micro/nanostructures on the diamond or silicon wafer.

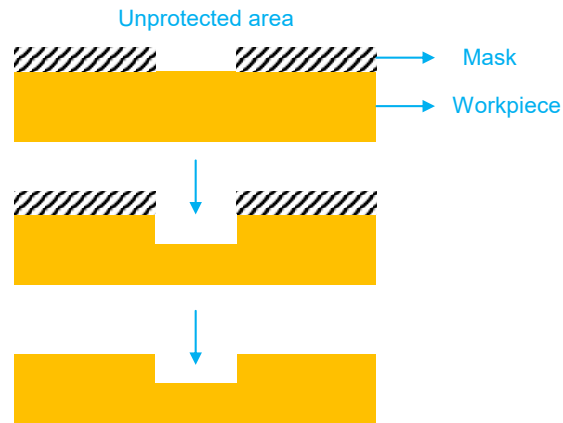


Figure 2.12 Schematic diagram of the chemical etching process.

Figure 2.13 shows SEM images of the nanopillar arrays, nanorod arrays, nanopencil arrays, and nanocone arrays, which are machined by the chemical etching process.

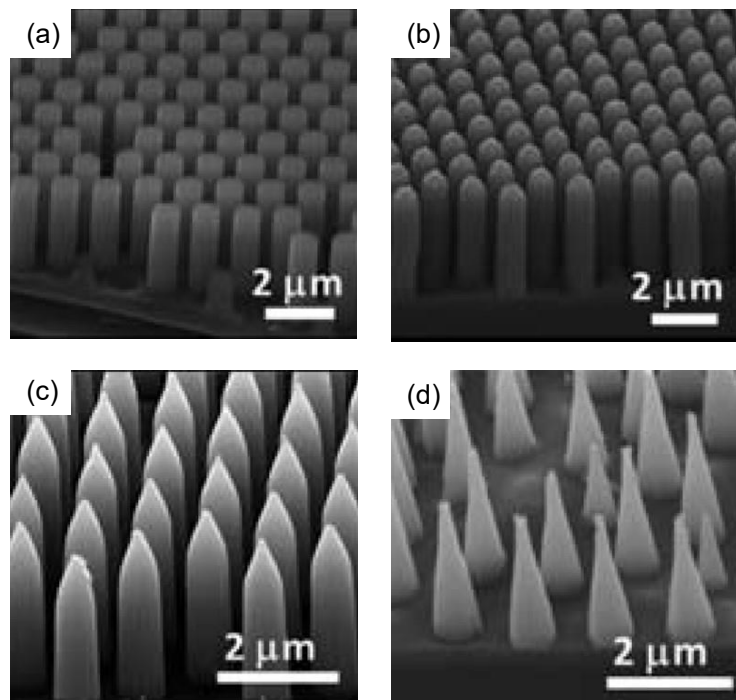


Figure 2.13 Nanostructures machined by the chemical etching process (Lin et al., 2013). (a) Nanopillar arrays, (b) nanorod arrays, (c) nanopencil arrays, and (d) nanocone arrays.

2.2.6 Lithography process

Lithography process is often applied in the field of semiconductors. It can be divided into photolithography (UV light is used to generate the micro/nanostructures.), imprint lithography (A mold is used to generate the micro/nanostructures.), and e-beam lithography (Electron beams are used to generate the micro/nanostructures.). For massive production, photolithography is the most applied form of lithography. Figure 2.14 shows the schematic diagram of this process.

The photolithography process begins in the upper left and then goes to the right side. A silicon wafer is coated with a thin film that serves as the etch-resistant hard mask. The photoresist is coated onto the thin film. The UV light is then shone down through a mask made of quartz with a pattern, which allows the UV light through certain regions to generate the pattern on the resist. This pattern causes a chemical change in the resist, which allows some of the photoresists to be removed by a special solution, called “developer”.

The next step is development. The developer is poured on the resist. For the positive-tone photoresist, the exposed areas become soluble in the developer while other areas remain on the wafer. For the negative-tone photoresist, unexposed areas are soluble in the developer. In the etching process, the areas that are not protected by photoresists in the uppermost layer of the silicon wafer are removed by a liquid or plasma chemical agent. The remaining photoresist is removed through a chemical stripping process. Sometimes, the lithographic process will be repeated many times for generating multilayer micro/nanostructure patterns (Lawson and Robinson, 2016).

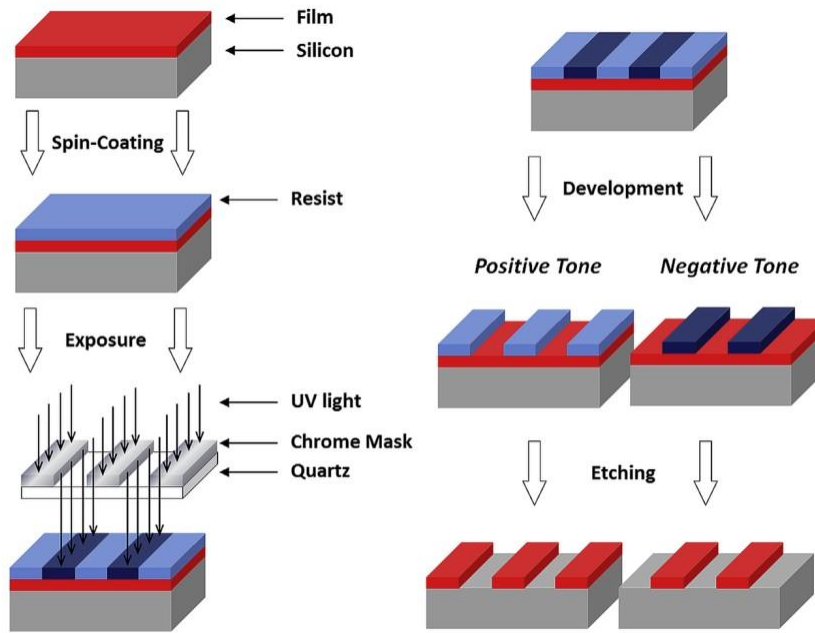


Figure 2.14 Schematic diagram of the lithography process (Lawson and Robinson, 2016).

Figure 2.15 shows SEM images of the micro-grating, micro-groove, square micro-hole, and mushroom-like pillar, which are machined by the lithography process.

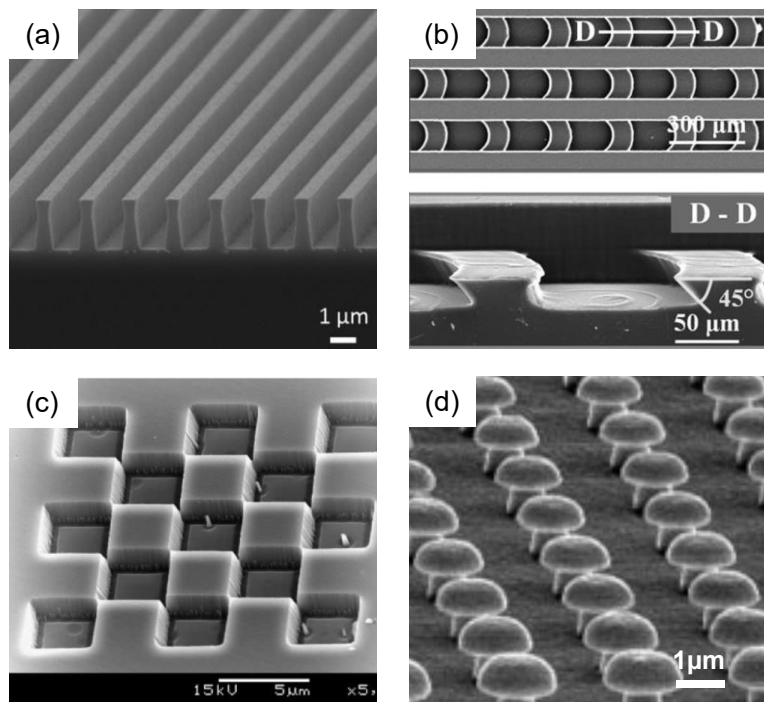


Figure 2.15 Micro/nanostructures machined by the lithography process. (a) Micro-grating (Hsieh and Lee, 2013), (b) inclined arc pitted groove (H. Chen et al., 2017), (c) square micro-hole (Enlund et al., 2005), and (d) mushroom-like pillar (Su et al., 2003).

2.2.7 Ultraprecision diamond cutting

Ultraprecision diamond cutting uses the single-crystal diamond tool to generate micro/nanostructures on the workpiece material surface based on the designed toolpath. The micro/nanostructure generation of ultraprecision diamond cutting highly depends on the duplication of the cutting tool profiles and relative tool/work motions on the machined surface (Du et al., 2022). It can be divided into single-point diamond turning, ultraprecision fly cutting, and vibration-assisted machining.

(1) Single-point diamond turning

Single-point diamond turning (SPDT) is an advanced micro/nano-machining process that employs a natural single-crystal diamond tool with nanometric edge sharpness to conduct a machining process. With the support of ultraprecision machines, accurate tool holders, and vibration isolation systems, the machining accuracy of this process can reach up to 1nm (Hatefi and Abou-El-Hosseini, 2020). Figure 2.16 shows the typical experimental setup of the ultraprecision diamond turning. Generally, the machine possesses an axial stiffness larger than 200 N/ μm , axial motion accuracy less than 15 nanometers, and feedback resolutions less than 1 nanometer (Zhou et al., 2010). In SPDT, a single-point diamond cutting tool is installed on a micro height-adjustable tool holder, and the workpiece is fixed on the spindle via the vacuum chuck.

Depth-of-cutting set in SPDT is usually in the order of a micrometer or less. A wide range of metals and metallic alloys can be machined by SPDT to generate the required micro/nanostructures. It includes aluminum alloy, copper alloys, and magnesium alloy. Some difficult-to-machining materials, such as silicon, chalcogenide glass, and germanium, also can be machined by SPDT (Hatefi and Abou-El-Hosseini, 2020).

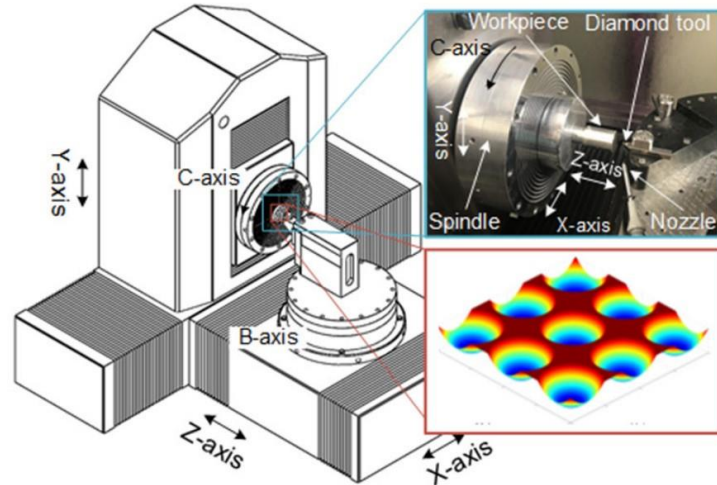


Figure 2.16 Schematic diagram of the single-point diamond turning (Zhang et al., 2019).

Figure 2.17 shows the topography of the micro/nanostructure, such as a micro-lens array, micro-pillar array, radiant nanostructure array, and hexagonal cavity array on the freedom surface, which are machined by single-point diamond turning process via designing the specific toolpath.

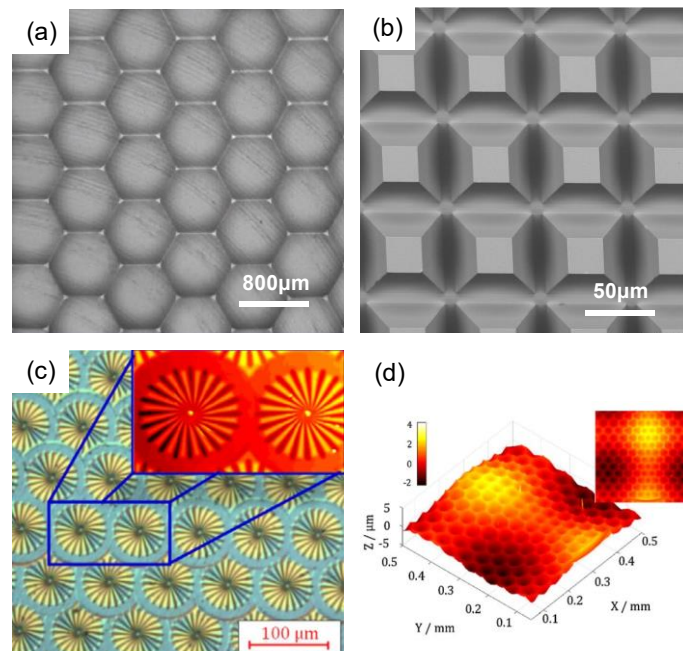


Figure 2.17 Micro/nanostructures machined by the single-point diamond turning. (a) Micro-lens (Zhang et al., 2019), (b) micro-pillar (Liu et al., 2021), (c) radiant nanostructure array (To et al., 2016), and (d) hexagonal cavity array on the freedom surface (To et al., 2016).

(2) Ultraprecision fly cutting

Ultraprecision fly cutting is to employ a rotational diamond tool to remove the workpiece materials and generate micro/nanostructures. Different from SPDT, in which cutting speed is highly dependent on the cutting radius, the cutting speed of the ultraprecision fly cutting is constant. The constant cutting speed is determined by the swing radius of the diamond tool. This unique machining characteristic of the ultraprecision fly cutting ensures the surface uniformity of the micro/nanostructures. However, the machining efficiency of the ultraprecision fly cutting is lower than that of SPDT (S. J. Zhang et al., 2016). Generally, UPFC includes two machining types according to the direction of the diamond tool in machining. If the tool direction is parallel to the spindle axis, it is named end- ultraprecision fly cutting (Zhu et al., 2015a), as shown in Figure 2.18(a). If the tool direction is perpendicular to the spindle axis, i.e. along the radial direction, it is named radial-ultraprecision fly cutting, as shown in Figure 2.18(b) (Cheung et al., 2006), which is also called ultra-precision raster milling. Figure 2.19 shows the micro/nanostructures machined by the ultraprecision fly cutting.

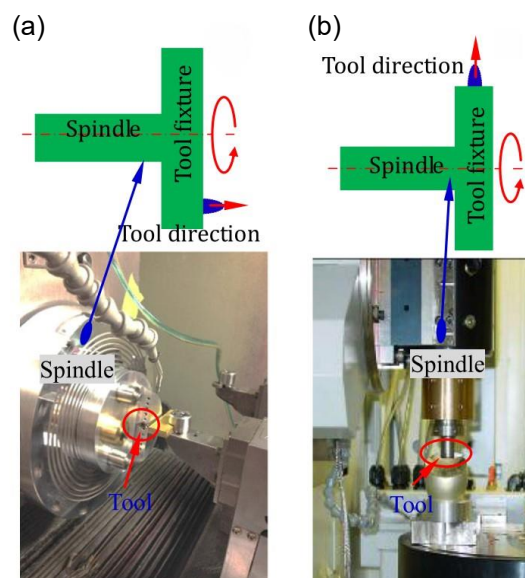


Figure 2.18 Schematic diagram of the ultraprecision fly cutting (S. J. Zhang et al., 2016).

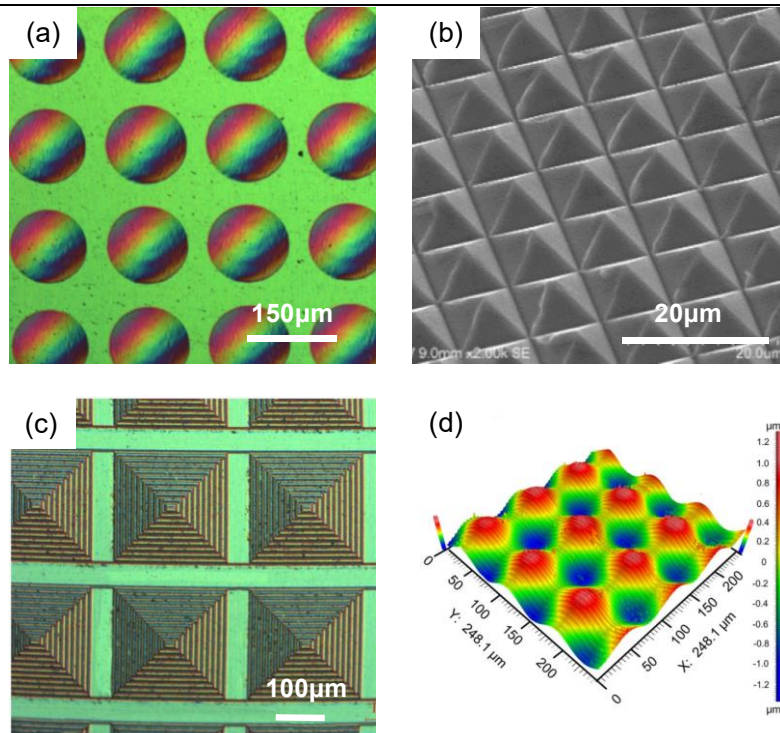


Figure 2.19 Micro/nanostructures machined by the ultraprecision fly cutting. (a) Micro-lens array (Zhu et al., 2015b), (b) micro-pyramid array (Ge et al., 2018), (c) hybrid micro-pyramid array (Zhu et al., 2015c), and (d) sinusoidal grid microstructure with the imposition of secondary unidirectional phase gratings (Zhu et al., 2015c).

(3) Slow-tool-servo machining

In the slow-tool-servo machining, the cutting tool is stationed on the Z-axis of the ultraprecision lathe and oscillates together with this axis at a low working frequency, typically less than 200 Hz. The workpiece is installed on the spindle (also called C-axis), which is controlled in position mode. The hardware configuration of the slow-tool-servo cutting is shown in Figure 2.20. In the slow-tool-servo machining, motions of all axes are fully synchronized and controlled to machine the microstructure arrays. The cutting tool oscillates forward and backward on the workpiece surface along the Z-axis. It also synchronizes with the angular position of the C-axis and the translational position of the X-axis (Yan and Fang, 2019). In other words, the Z-axis coordinate of the cutting tool is a function of the C-axis coordinate and X-axis coordinate. When

machining a microstructure array, all microstructures are continuously fabricated in one turning cycle (Mukaida and Yan, 2017). The slow-tool-servo machining has the merits of longer stroke, easy control, and simpler setup, which enables it to machine microstructure arrays on the workpiece surface.

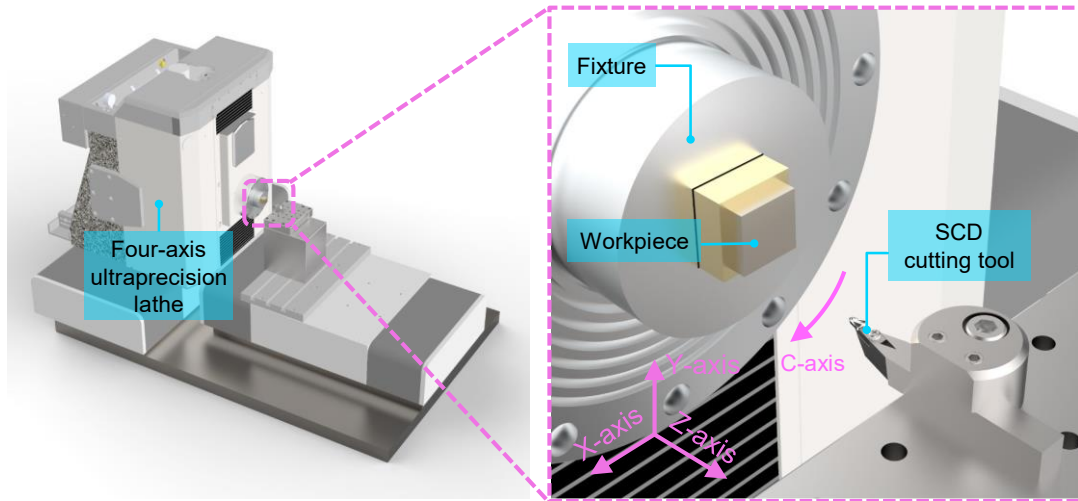


Figure 2.20 Hardware configuration of the slow-tool-servo machining.

Figure 2.21 shows the microstructure arrays machined by the Slow-tool-servo machining.

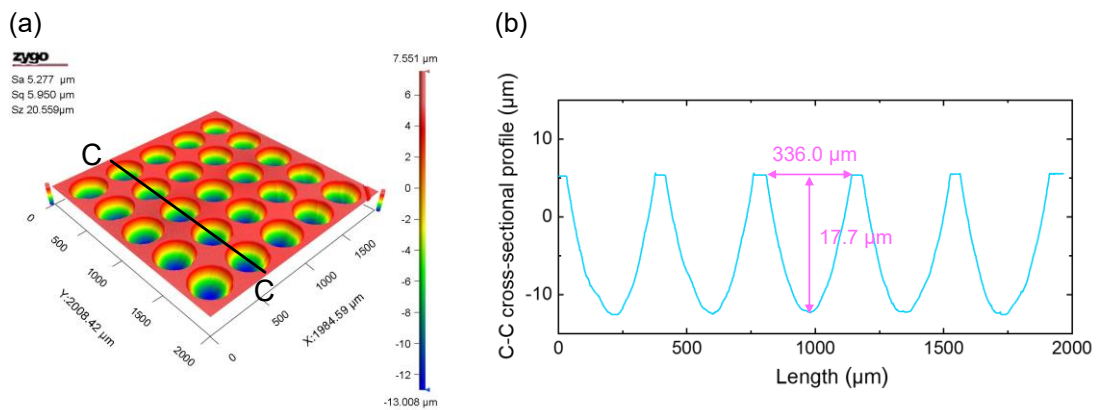


Figure 2.21 (a) Three-dimensional topography of the micro-lens array and (b) cross-sectional profile.

(4) Vibration-assisted machining

In the vibration-assisted machining process, a vibration motion with a small amplitude and high frequency is added to the cutting tool. Through the appropriate combination of the vibration motion and cutting velocity, the cutting tool will periodically move along the cutting trajectory to generate the micro/nanostructures on the workpiece surface, as shown in Figure 2.22.

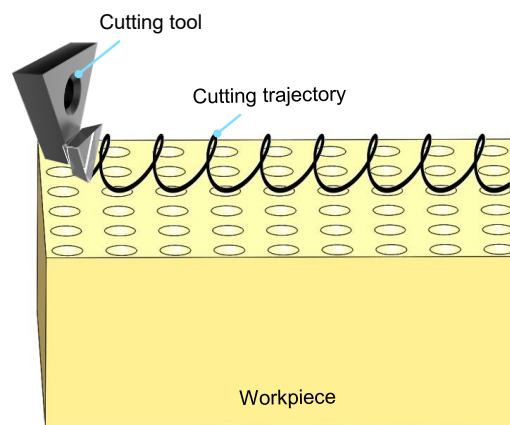


Figure 2.22 Schematic diagram of the vibration-assisted machining.

Vibration-assisted machining can be divided into resonant vibration-assisted machining and non-resonant vibration-assisted machining according to their working principles (J. Zhang et al., 2016). The resonant vibration-assisted machining works on a fixed resonant frequency of the mechanical structure, more than 20kHz, while the non-resonant vibration-assisted machining works at a flexible frequency. The vibration trajectory of the non-resonant vibration-assisted machining is provided by the actuators, such as the piezoelectric actuator and magnetostrictive actuator. This section focuses on the review of the resonant vibration-assisted machining.

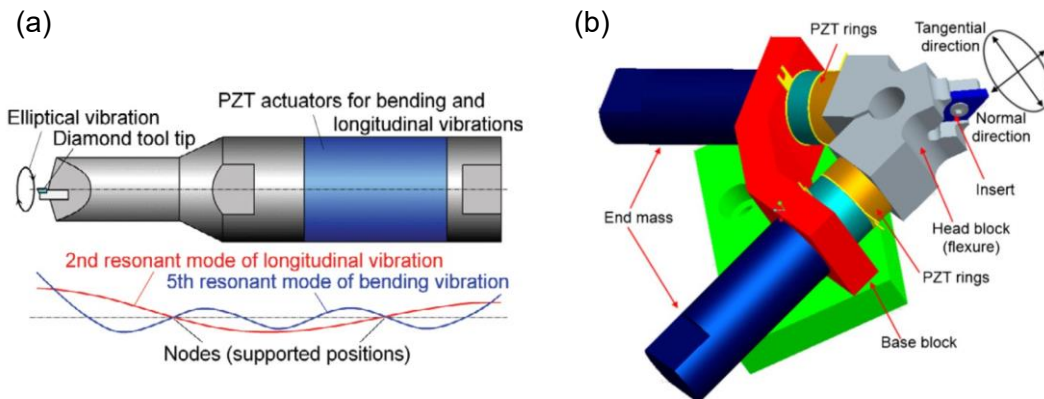


Figure 2.23 Typical mechanical structures of the resonant vibration-assisted machining system. (a) Beam structure (Suzuki et al., 2007) and (b) V-shaped structure (Guo and Ehmann, 2013a).

Figure 2.23 shows the typical mechanical structures of the resonant vibration-assisted machining system. For the beam structure, the piezoelectric (PZT) rings are stacked into a beam using a preload screw. When the exciting voltage signals with the phase shifts are input into PZT rings, the beam is forced to resonate in the second and fifth resonant modes. The machining system generates the elliptical trajectory at this resonant frequency. For the V-shaped structure, the PZT rings are placed between the end mass and head block through the preload screw. When the harmonic signals are input into the PZT rings, the longitudinal vibrations of the two PZT rings are coupled in the head block, generating the elliptical trajectory along the tangential direction and normal direction.

Figure 2.24 shows the micro/nanostructures machined by the resonant vibration-assisted machining system, such as sinusoidal and zigzag grooves on hardened steel, trapezoidal structures, hexagonal dimple patterns, and dimple patterns.

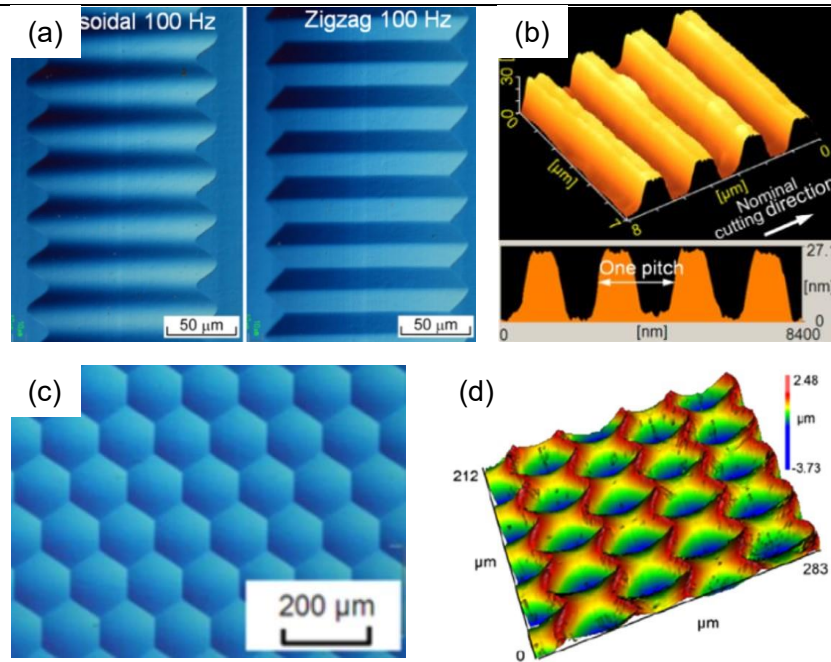


Figure 2.24 Micro/nanostructures machined by resonant vibration-assisted machining system.

(a) Sinusoidal and zigzag grooves on hardened steel (Suzuki et al., 2011), (b) trapezoidal structures (Zhang et al., 2013), (c) hexagonal dimple patterns (Suzuki et al., 2011), and (d) dimple patterns (Guo and Ehmann, 2013b).

2.3 Vibration-assisted machining system

Section 2.2.7 mainly reviews the resonant vibration-assisted machining system, but they only work at a fixed frequency and a fixed vibration trajectory, which limits the shape diversity of the micro/nanostructures. Non-resonant vibration-assisted machining system can effectively solve this problem since it has the capability of offering a flexible vibration trajectory in a continuous working frequency. The non-resonant vibration-assisted machining system is the research object of this thesis. Therefore, the term “vibration-assisted machining system” in other chapters of this thesis represents the non-resonant vibration-assisted machining system for avoiding misunderstanding. According to the degree-of-freedom (DOF) that the vibration-assisted machining system (VAMS), it can be divided into 1DOF-VAMS and multi-DOF-VAMS, as

shown in Figure 2.25. Because the 1DOF-VAMS and 2DOF-VAMS have the capability of generating the most micro/nanostructures, the 3DOF-VAMS is not investigated in this chapter.

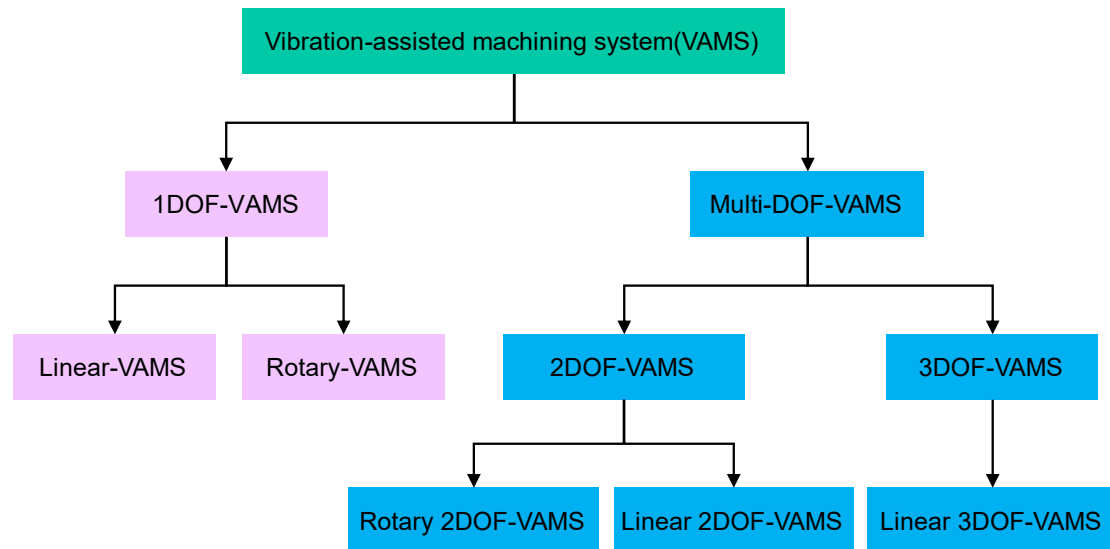
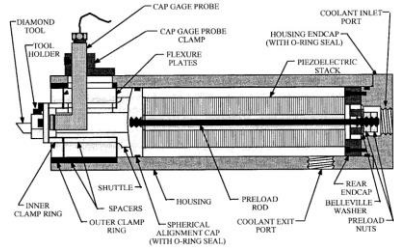


Figure 2.25 The classification of the vibration-assisted machining system.

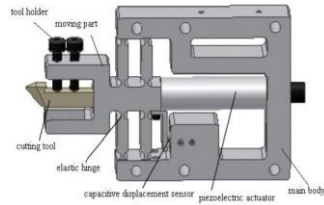
2.3.1 One-degree-of-freedom vibration-assisted machining system

One degree-of-freedom vibration-assisted machining system (1DOF-VAMS) was first developed with only one direction motion, and it can be used to fabricate sinusoidal surfaces, micro-lens arrays, and other microstructures. The development timeline of 1DOF-VG is shown in Figure 2.26. If the motions of the cutting tool are synchronized with the spindle and linear axes (X-axis, Y-axis, and Z-axis) of the machine, the vibration-assisted machining is also called fast tool servo (FTS) machining.

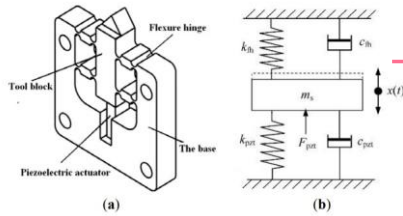
Chapter 2 Literature review



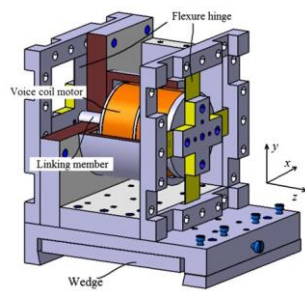
Cuttino et al., 1999



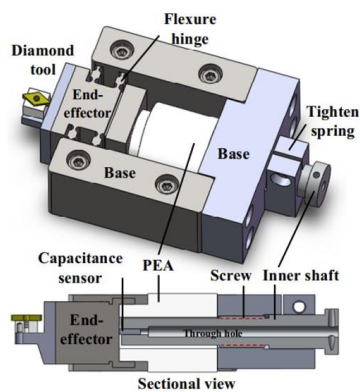
Wang and Sun, 2009



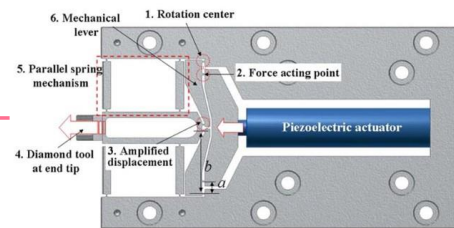
Zhu and Zhou, 2012



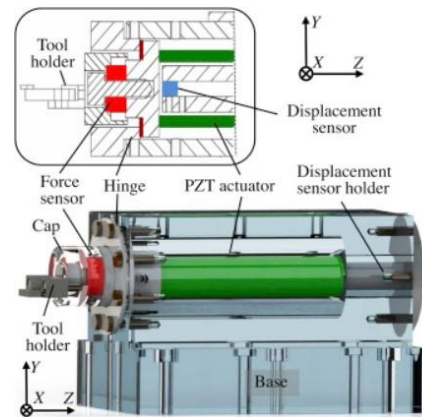
Lu et al., 2014



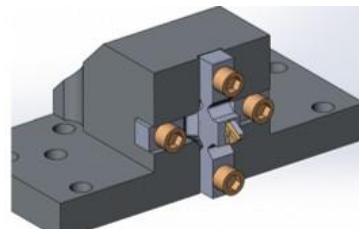
W. Le Zhu et al., 2019



Kim et al., 2009



Liu et al., 2014



Zhu et al., 2020

Figure 2.26 The development timeline of the typical one-degree-of-freedom vibration-assisted machining system.

The earlier design of the 1DOF-VAMS is employed to correct various machine-related errors, such as parasitic vibrations or spindle error (Fawcett, 1990; Patterson.S.R., 1985). In 1999, Cuttino et al. designed a 1DOF-VAMS for machining non-rotationally symmetric mirrors. In machining, a standard integral controller was applied to reduce the motion error caused by the hysteresis of the piezoelectrical actuator (Cuttino et al., 1999). Kim et al. designed a long-stroke 1DOF-VAMS that was installed on the Z-axis of a turning machine to machine free-form surfaces. Besides, an on-machine measurement device was employed to compensate for the residual form of errors during the machining. The experimental results show that the developed 1DOF-VAMS can produce the copper free-form mirrors of 50 mm diameter with a form accuracy of $0.15\mu\text{m}$ in peak-to-valley value error (Kim et al., 2009). To obtain a fine surface finish and high accuracy in a large area workpiece, Wang and Sun designed a 1DOF-VAMS with a capacitive displacement sensor to compensate for the straightness error of the X-axis translational slide (Wang and Sun, 2009).

For illustrating the dynamic hysteresis behaviors of the vibration-assisted machining system, Zhu and Zhou established a linearized hysteresis force model by combining the dynamic modeling of the 1DOF-VAMS. This model well depicts the rate-dependent hysteresis and easier control of the piezoelectrically actuated vibration-assisted machining system. The experimental results show the error of this model in the steady-state is less than $\pm 2.5\%$ within the full span range (Zhu and Zhou, 2012). Lu et al. proposed a method for analyzing the microstructure profile amplitude and wavelength in generating sinusoidal microstructures when the clearance angle of the cutting tool is smaller than the critical angle in vibration-assisted machining using the 1DOF-VAMS (Lu et al., 2014).

For increasing the stroke of the 1DOF-VAMS, Liu et al. employed the voice coil motor as an actuator and designed a flexure-hinge structure to guide the motion displacement of the voice coil motor (Liu et al., 2014). Without prior knowledge of the surface forms, it is hard for traditional ultraprecision machining to generate microstructures on non-planar brittle material. Motivated by this, Chen et al. developed a force-controlled FTS to conduct precision machining of the brittle material. A highly rigid piezoelectric-type force sensor was integrated into the tool holder for providing robustness and sufficient stiffness during the machining of the brittle material. Some micro-grooves were successfully machined on convex BK7 glass lens (Y. L. Chen et al., 2017).

The accurate tracking and control of the tool path play the significant role in the diamond machining of microstructured surfaces, Zhu et al. introduced an adaptive terminal sliding mode control strategy to realize the accurate and fast-tracking of the tool path and compensate the system nonlinearity. The stiffness of 1DOF-VAMS can be up to $550.8 \text{ N}/\mu\text{m}$ with the first-order natural frequency of 5.35 kHz. In comparison to other related control methods, the experimental results show that this control strategy significantly the performance, especially in tracking tool trajectories with high amplitudes and frequencies. The tracking error was only 0.1% for the changing trajectories during generating water-drop surfaces (W. Le Zhu et al., 2019). Taking advantage of the proposed controller, the single-sinusoidal surface, bi-sinusoidal surface, and radial surface were produced with high quality, as shown in Figure 2.27.

For realizing the nanomachining, Zhu et al. designed an ultra-FTS driven by the piezoelectric actuator. For guiding the motion of the FTS, novel flexure hinges with the notch profiles were proposed, which can be universally described by a rational Bézier

curve. The kinematics and dynamics properties of the mechanical structure were comprehensively modeled based on the Euler-Bernoulli beam theory. The dynamics testing shows the natural frequency can be up to 20 kHz. For a single frequency harmonic and a more complicated one with hybrid harmonics, the maximum error of the trajectory tracking was about 25 nm and 50 nm, respectively (Zhu et al., 2020).

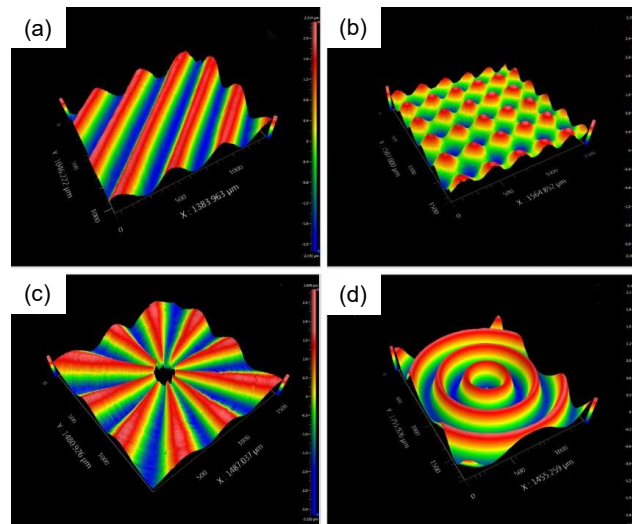


Figure 2.27 Microstructures machined by the one-degree-of-freedom vibration-assisted machining system (W. Le Zhu et al., 2019). (a) Single-sinusoidal surface, (b) bi-sinusoidal surface, (c) radial surface, and (d) water-drop surface.

2.3.2 Two-degree-of-freedom vibration-assisted machining system

When the vibration trajectory of the tool tip is in the two-dimensional plane, this kind of vibration-assisted machining system is called a two-degree-of-freedom vibration-assisted machining system (2DOF-VAMS). The development timeline of 2DOF-VAMS is shown in Figure 2.28. In 1999, Ahn et al. designed a two-dimensional vibration mechanism driven by two PZT actuators and found that two-dimensional vibration cutting process has many advantages in comparison with non-vibration cutting, such as decreasing the cutting force and improving the surface roughness (Ahn

Chapter 2 Literature review

et al., 1999). Zhu et al. designed the decoupled two-DOF flexural mechanism with a sort of Z-shaped flexure hinge and proposed the concept of the fast-tool-servo-assisted turning in the fabrication of micro-structured surfaces with scattering homogenization, and the maximal working frequency of this device is about 200Hz (Zhu et al., 2014).

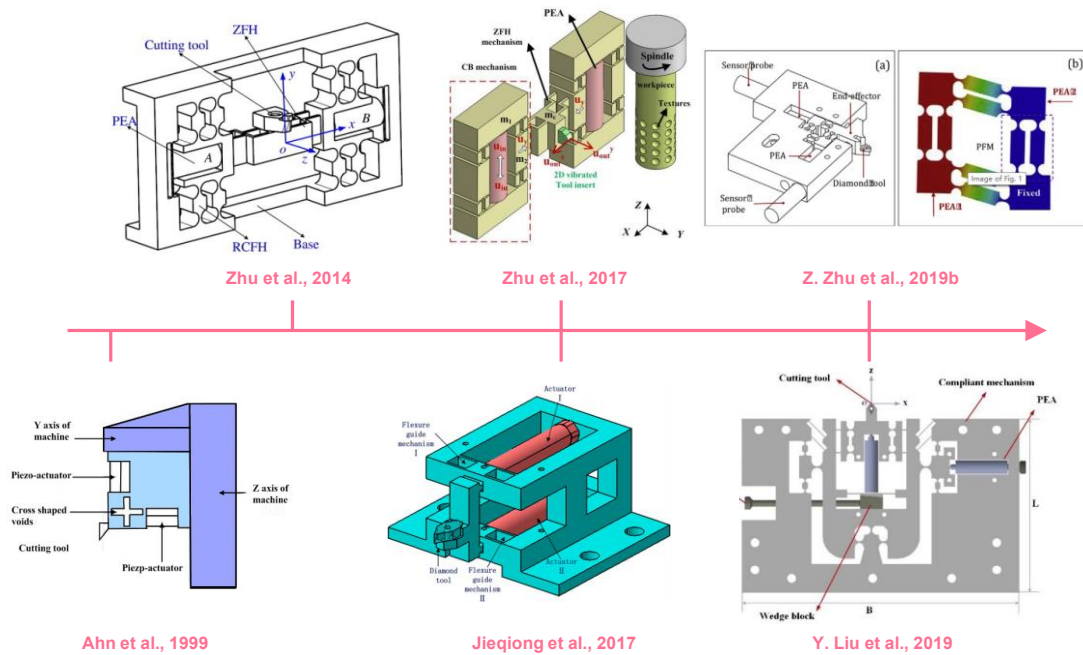


Figure 2.28 The development timeline of typical two-degree-of-freedom vibration-assisted machining system.

The vibration amplitude of 2DOF-VAMS determines the height of multifunctional micro/nanostructures during machining. Zhu et al. developed a 2DOF-VAMS with high vibration amplitude and high stiffness. The vibration displacement in machining directions is more than $70\mu\text{m}$ with stiffness of more than $9\text{N}/\mu\text{m}$. Adopting the matrix-based compliance modeling method is to theoretically analyze the vibration amplitudes, input stiffness, output stiffness, and working frequency of the vibration-assisted machining system. The various microstructures are machined by the designed 2DOF-VAMS. Based on the surface texture generation model and in-process monitored parameters, the machined microstructures can also be predicted (W. Le Zhu et al., 2017).

Lin et al. developed a piezoelectric parallel-driven 2DOF-VAMS. The experiment results show that the maximum strokes along the X- and Z-axes can reach $16.78\mu\text{m}$ and $15.35\mu\text{m}$, respectively, and the motion resolutions of both directions reach around 50 nm (Jieqiong et al., 2017).

To enhance the machining efficiency of the microstructures on brittle material surfaces, Zhu et al. developed a novel piezo-actuated 2DOF-VAMS with two degrees of freedom. And a typical microstructure without the cracks was successfully machined on a single crystal silicon wafer surface. The machining efficiency was increased by 16.35%, and the profile error is less than ± 90 nm (Z. Zhu et al., 2019b). For obtaining the translational motions along the X- and Z-axis directions of the ultra-precision lathe, Liu et al. developed a 2DOF-VAMS based on a high-rigidity four-bar mechanism. Its static and dynamic performance was conducted through finite element analysis (Y. Liu et al., 2019).

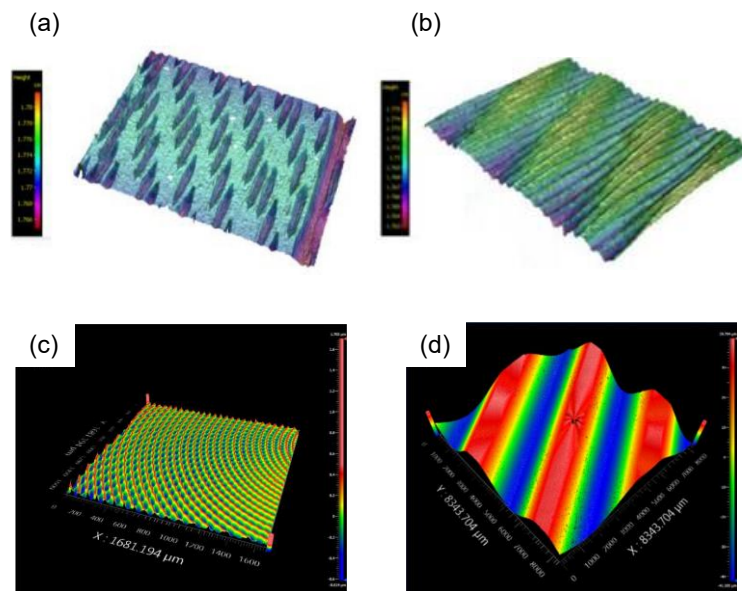


Figure 2.29 Microstructures machined by the two-degree-of-freedom vibration-assisted machining system. (a) Elongated micro-dimple surface (W. Le Zhu et al., 2017), (b) hierarchical micro-channels surface (W. Le Zhu et al., 2017), (c) micro-dimple surface (Jieqiong et al., 2017), and (d) sinusoidal wavy surface (Y. Liu et al., 2019).

Figure 2.29 demonstrates three-dimensional topographies of microstructured surfaces machined by the 2DOF-VAMS.

2.4 Cutting force modeling

Cutting force is an important physical indicator for ultraprecision diamond machining since it directly reflects the reaction between the cutting tool and workpiece (Chen et al., 2021), and it helps to understand the material removal mechanism. Taking advantage of the rich information of the material properties, tool geometry, and machining parameters in the cutting force, the cutting force analysis fast develops (Srinivasa and Shunmugam, 2013). However, very few studies are reported on cutting force prediction during texturing the surface, especially when generating the comprehensive microstructures in vibration-assisted ultraprecision machining. Because of the addition of vibration motion into the cutting tool, the relationship between the designed microstructures and corresponding cutting force becomes more complicated, which blocks the in-depth understanding of the material removal mechanism in vibration-assisted ultraprecision machining.

Although the research of cutting forces is very limited for vibration-assisted ultraprecision machining, the prediction of cutting forces in the turning and milling has been enough developed. As a pioneering researcher, Merchant proposed the orthogonal cutting force model and analyzed the relationships between components (Merchant, 1945). This model is called Merchant's model by the later researchers and engineers. Wu and Liu proposed a single shear plane model for orthogonal cutting to analyze the cutting force (Wu and Liu, 1985). However, the shear zone is not a plane, and it has thickness. So this model may not accurately predict the orthogonal cutting force

(Astakhov and Osman, 1996). In order to solve these shortcomings, Tounsi et al. proposed the non-equidistant shear zone model to derive the stress, strain, strain rate, and temperature in the plastic deformation zone (Tounsi et al., 2002). Li et al. further developed a non-equidistant shear zone model to build the deformation model (Li et al., 2011). After that, many scholars applied this model to predict cutting force and they demonstrated that numerical simulation results were consistent with the experimental results (Gao et al., 2016; Li et al., 2011). In terms of the cutting force in vibration-assisted ultraprecision machining, Shamoto et al. studied a simple cutting force model of the elliptical vibration machining to understand the cutting mechanics (Shamoto et al., 2008). Bai et al. employed the non-equidistant shear zone model to predict the orthogonal cutting forces and revealed the material removal mechanisms of the elliptical vibration machining (Bai et al., 2016). Zhu et al. developed a comprehensive cutting force model for vibration-assisted ultraprecision machining by considering the depth-of-cutting dependent shearing and ploughing (Z. Zhu et al., 2019a). However, this model makes the cutting force prediction relatively complicated, which significantly limits the practical applications in engineering.

2.5 Machining of titanium, magnesium, and their alloys

Titanium, magnesium, and their alloys belong to the light metal category because of their low density. Nowadays, machining is one important index for the metal part for new applications. This section reviews their machining process.

Titanium and titanium alloy have been broadly used in aerospace, nuclear, and biomedical industries (Yang et al., 2021) due to their outstanding properties, including a high strength-to-weight ratio (Devaraj et al., 2016), excellent corrosion resistance

(Zhongze Yang et al., 2020), and favorable biocompatibility (Ren et al., 2021). However, titanium and titanium alloy, as typical difficult-to-machine materials (Gao et al., 2018; Heidari and Yan, 2018), have poor machinability ascribing to the inherent properties of the material, such as the high strength and low modulus of elasticity, which significantly improve the difficulties of the machining and reduce the tool life (An et al., 2011). A large number of researchers and engineers performed research on the machining of titanium alloys. Sharif and Rahim investigated the influence of the coating in the tool when drilling titanium alloy, Ti6Al4V. An experiment found that the TiAlN-coated-drill considerably outperformed the uncoated-drill not matter in tool life or surface finish (Sharif and Rahim, 2007). Sun et al. examined the chip formation and cutting forces during dry turning of Ti6Al4V alloy. The continuous and segmented chips were formed under machining conditions of low cutting speed and large feed rate. The cutting force increased with increasing cutting speed from 10m/min to 21m/min and 57m/min to 75m/min due to the strain rate hardening at two different phases (low strain rate and high strain rate). Beyond these speed ranges, the cutting force decreased with the increase of the cutting speed (Sun et al., 2009).

Driven by the sustainability concept in the machining field, Deiab et al. applied minimum quantity lubrication and minimum quantity cooled lubrication techniques into the influence of the different strategies on energy consumption, surface roughness, and tool wear during turning of the titanium alloy Ti6Al4V (Deiab et al., 2014). Sui et al. used an ultrasonic vibration-assisted machining process to investigate the machining of the titanium alloy Ti6Al4V and found that the cutting forces decreased by 20-50% in comparison with the conventional machining and the tool life was lengthened by 1.5-3 times (Sui et al., 2017). Yip and To proposed the magnetic-field-assisted machining

process to systematically explore the machining of the titanium alloy Ti6Al4V. The experimental results showed that the magnetic field reduced the tool wear and the influence of the material recovery because the thermal conductivity of titanium alloys at the tool/workpiece interface was increased. The machining vibration was also suppressed because of the eddy current damping effect (W. S. Yip and To, 2019; Wai Sze Yip and To, 2019; Yip and To, 2017).

With the ever-increasing demand for lightweight in automotive, electronics, aerospace, biomedical, and other fields, magnesium alloys have received wide attention due to the characteristics of low density, high specific strength, high thermal conductivity, and so on (Cagan et al., 2020; Trang et al., 2018; Wang et al., 2021; Xu et al., 2015). Besides, magnesium alloy also possesses many attractive machining properties (Tekumalla et al., 2020), such as lower machining force and lower machining power required. Lu et al. investigated the effect of cutting parameters on microstructure, machining hardness, and surface roughness, and established a geometrical prediction model of the roughness in the high-speed cutting of the magnesium alloy (Lu et al., 2016). Viswanathan et al. employed the Taguchi method to optimize the turning parameters of the magnesium alloy for minimizing the tool flank wear, surface roughness, and cutting temperature. Turning experiments verified the effectiveness of the Taguchi method on the decrease of these three objectives (Viswanathan et al., 2018). Zhang et al. analyzed the effect of milling parameters on the magnesium alloy chip morphology and the influence of alloy composition on combustion state during the high-speed milling (H. Zhang et al., 2018). Varatharajulu et al. applied the multiple criteria decision-making methods to select the suitable drilling parameters to simultaneously minimize all the responses, such as drilling time and surface roughness

(Varatharajulu et al., 2021). However, micro/nanostructure generation on the magnesium alloy surface remains a challenge due to the flammability and ignition of the magnesium alloy.

2.6 Functional applications of the micro/nanostructured surface

Micro/nanostructures can enhance the performance and functionality of the metal surfaces and have been applied in various fields, such as optics (Zhu et al., 2014), bioengineering (Lutey et al., 2018), tribology (Ramesh et al., 2013), self-cleaning (S. Liu et al., 2019), to mention a few. One of the applications in optics is structural color, which is the consequence of complicated interactions between light and the micro/nanostructures. Many kinds of structural color have been found in nature. Figure 2.30 displays the structural color in the wings of *Morpho didius*. Figure 2.31 shows the corresponding micro/nanostructures in more detail. It can be found that the regular microstructures are distributed on the surface of the wing.

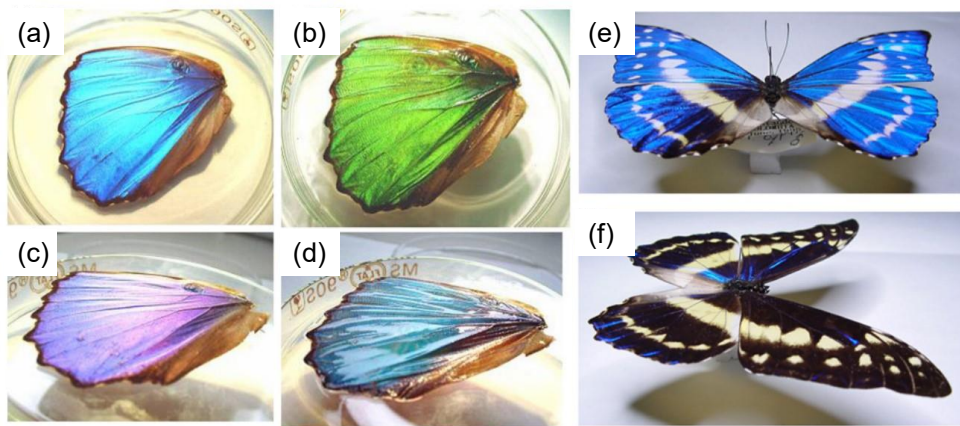


Figure 2.30 Frontal and inclined views of the *Morpho didius* wing. (a) and (c) wing in the air, (b) and (d) wing in liquid ethanol, (e) and (f) wing in different viewing angles (Kinoshita et al., 2008).

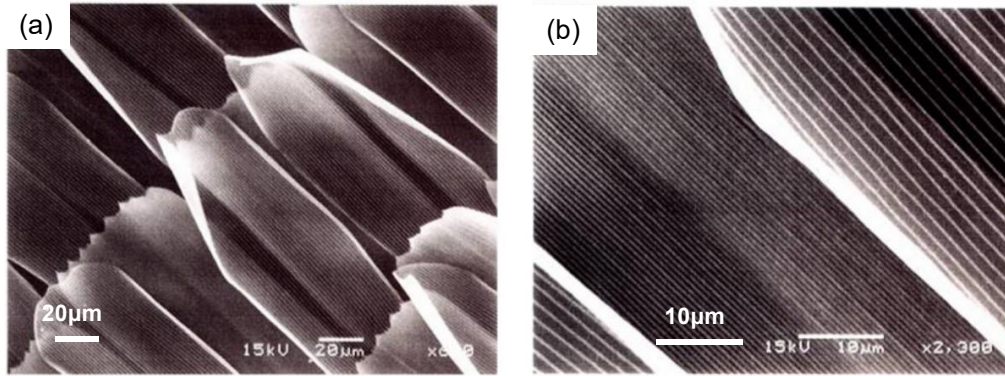


Figure 2.31 SEM images of *Morpho didius* (Kinoshita et al., 2008).

Inspired by the structural coloration mechanism in nature, many researchers employed different machining technology to generate the structural color. Tan et al. proposed the plasmonic color printing process to generate nanostructures to induce the structural color, as shown in Figure 2.32. These colors could also be fine adjusted by controlling the spacing between nanostructures. The color palette was also expanded from about 15 basic colors to more than 300 unique colors, which offers a new way to produce high-resolution and low-cost color printing with many applications in decorative beautification, identification code, and anti-counterfeiting (Tan et al., 2014).

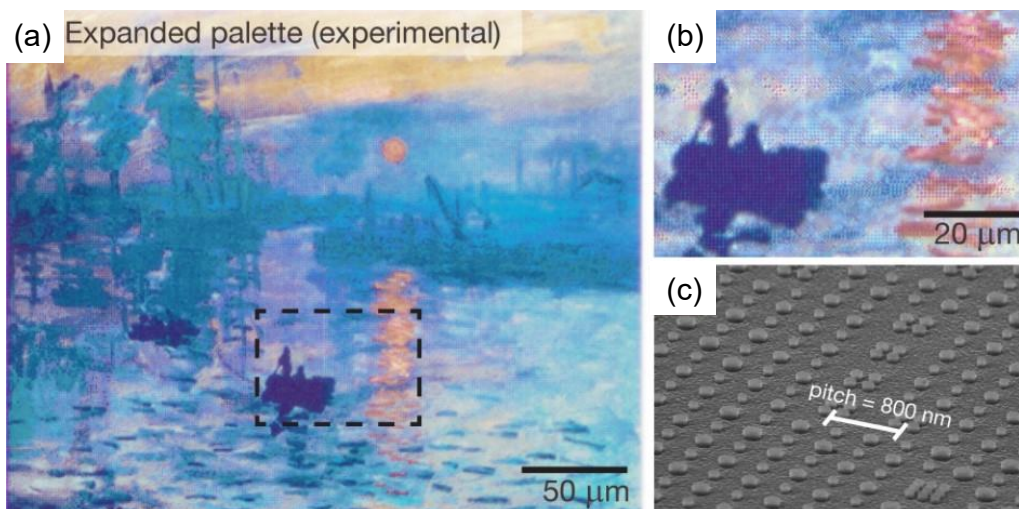


Figure 2.32 (a) Generation of Monet's *Impression*, (b) higher magnification image of the dotted box in (a), and (c) SEM image of nanostructures (Tan et al., 2014).

Zhu et al. developed a resonant laser printing technique for producing non-iridescent structural colors with high color contrast, which are ultrathin, environment-inert, and fully flexible. This technique used high-index dielectric materials to form the nanostructures and enabled color printing with a resolution of more than 100,000 DPI (X. Zhu et al., 2017). In comparison with another method of structural color generation, the technique is suitable for massive production and can be applied in printing and decoration. Figure 2.33 shows the schematic setup of resonant laser printing and corresponding structural colors.

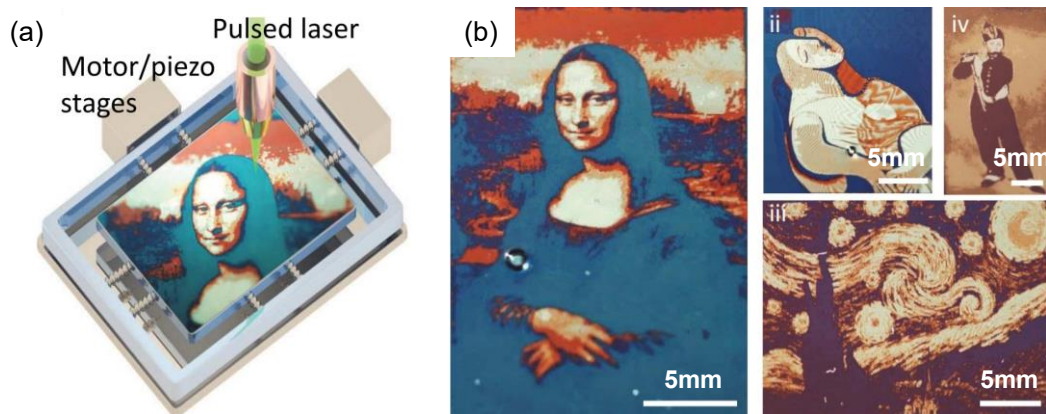


Figure 2.33 (a) Schematic setup of resonant laser printing and (b) paintings of the resonant laser printing (X. Zhu et al., 2017).

Wu et al. used the focused laser interference lithography process to directly machine the regular groove structures on the metal surface, which can induce the generation of the different patterns (such as a leaf, crab, and windmill) on various metals (such as stainless steel, titanium, copper, and so on), as shown in Figure 2.34, which demonstrates the excellent flexibility of this process (Wu et al., 2019).

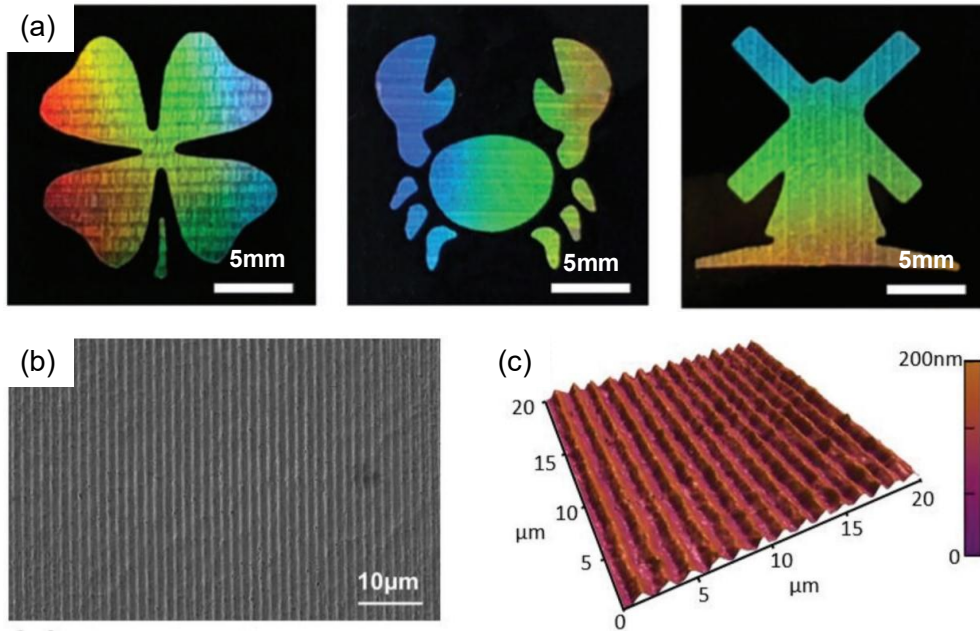


Figure 2.34 (a) Different patterns machined by the laser interference lithography, (b) SEM image of the microstructures, and (c) AFM image of microstructures (Wu et al., 2019).

Yang and Guo employed ultrasonic elliptical vibration machining to create the micro/nano-gratings, which induced the iridescent color generation.

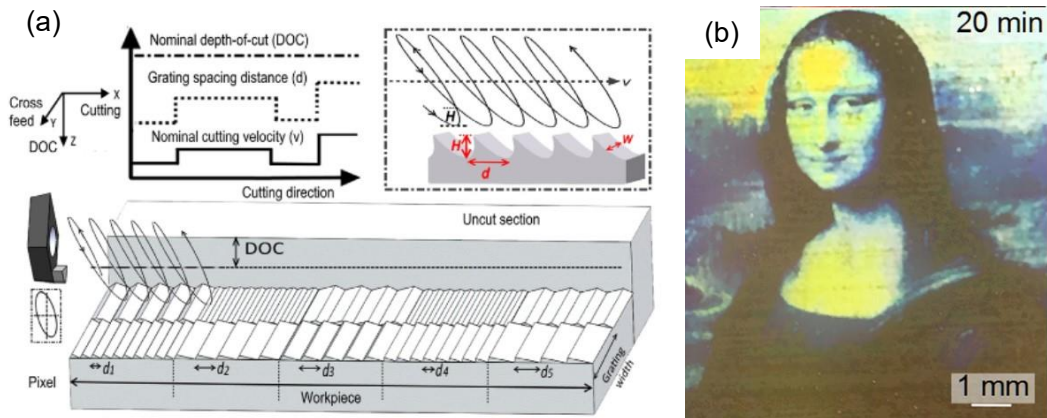


Figure 2.35 (a) Machining principle of the ultrasonic elliptical vibration machining (Guo and Yang, 2019) and (b) *Mona Lisa* portrait pattern machined by ultrasonic elliptical vibration machining (Yang et al., 2017).

Figure 2.35 illustrates the machining principle of this process and a *Mona Lisa* pattern is machined. By adjusting the cutting velocity, the spacing between the micro/nano-gratings can be controlled for inducing different colors (Guo and Yang,

2019; Yang et al., 2017; Yang and Guo, 2019). The proposed offers a direct mechanical machining method for structural coloration of metals, but the fixed working frequency limits the flexibility of this process.

He et al. proposed a vibration-assisted fly cutting to machine the two-level iridescent structures with high accuracy. The first-order microstructures correspond to the shape of the pattern. The second-order nanostructures act as the diffraction grating, which induces various iridescent patterns (He et al., 2020). The spacing of the second-order nanostructures can be flexibly adjusted by the feed rate. Figure 2.36 illustrates its machining principle and machined vivid colors. However, the low vibration frequency limits this massive application of this process.

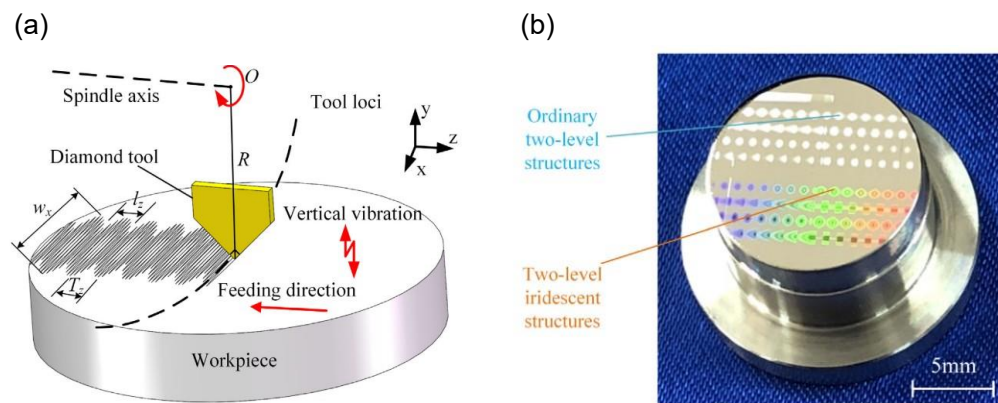


Figure 2.36 (a) Machining principle of the vibration-assisted fly cutting and (b) iridescent color machined by vibration-assisted fly cutting (He et al., 2020).

2.7 Summary

This chapter reviews the research work on micro/nanostructured surface machining methods, the development of the vibration-assisted machining system, cutting force modeling, machining of titanium, magnesium, and their alloys, and functional applications of the micro/nanostructures. However, there are still several challenges that need to be solved:

(1) A vast number of machining processes have been carried out to produce the micro/nanostructures, such as additive process, beam-assisted process, electric-field-assisted process, a chemical etching process, and so on, but they face the problems of the low machining efficiency, expensive equipment, and low surface quality.

(2) Vibration-assisted machining process, as a promising machining method, attracts the attention in micro/nanostructure machining. But current vibration-assisted machining systems suffer from a low degree of freedom or low working frequency, which limits the flexibility and machining efficiency of the micro/nanostructure generation.

(3) Cutting force model includes rich information of the workpiece material, tool geometry, and process parameters. However, very few studies focus on cutting force prediction during generating micro/nanostructure.

(4) Titanium, magnesium, and their alloys have been widely applied in automotive, electronics, aerospace, biomedical, and other fields. There is very limited knowledge on producing micro/nanostructures on their surfaces due to the poor machinability and easy flammability.

(5) Some machining processes can generate structural colors, but the application is still not extended into the information science, such as optical information generation and hiding.

Chapter 3 Design of the vibration-assisted ultraprecision machining system

3.1 Introduction

Micro/nanostructures with regular patterns on the metal surfaces are increasingly used in a range of modern industries, including biological, mechanical, tribological, optical, antibacterial components, data storage, etc (Yuan et al., 2020). For instance, the heat transfer can be significantly enhanced by decreasing the hydraulic diameter of the microchannel in the heat exchangers (Brandner et al., 2006). The micro-dimple surface can exhibit friction as much as 80% lower than the smooth surfaces (Ramesh et al., 2013). But how to manufacture these micro/nanostructures with high efficiency and low cost has acted as the research focus in both academic and engineering circles. Lithography-based process and laser ablation suffer from low efficiency or low surface quality (Dubey and Yadava, 2008; Radha et al., 2013). The vibration-assisted ultraprecision machining technique is widely considered to be a promising method for enhancing machining efficiency and surface quality (X. Liu et al., 2019). Establishing the two-degree-of-freedom vibration-assisted ultraprecision machining system with high degree-of-freedom and low coupling ratio is a key of this technique. Besides, to the best of our knowledge, there are very few attempts to simulate the working performance of the vibration-assisted ultraprecision machining system by directly inputting the voltage signals into the piezoelectric actuator (PEA) and treating the mechanical structure and PEAs as an entire part. Most of the studies input the displacement or force signals into the mechanical structure of the vibration-assisted

ultraprecision machining system and ignore the roles of PEAs in the simulation. In addition, the numerical simulation of the micro/nanostructure generation can predict the surface topography and provide the theoretical guidance in the selection of the process parameters before machining, but most research only consider the cutting edge and ignore the roles of rake face and clearance face in machining. Several studies neglect the elastic recovery of the workpiece material in the numerical simulation, in which the elastic recovery plays a significant part in the micro/nanostructure machining, especially for soft metal.

In this chapter, a novel two-degree-of-freedom vibration-assisted ultraprecision machining (2DOF-VAUM) system is designed, which solves the low degree-of-freedom and low bandwidth of the existing machining systems. To precisely simulate the working performance of this designed 2DOF-VAUM system, the detailed multi-physics finite element method is proposed. Considering the three-dimensional geometric shape of the cutting tool, the cutting motion trajectory, and the elastic recovery of the workpiece material, the numerical simulation algorithm of the micro/nanostructure generation is then established and used to precisely predict the surface topography. Finally, two types of unique microstructures are machined on the copper alloy surfaces to verify the feasibility and flexibility of the proposed 2DOF-VAUM system.

3.2 Mechanical design

The piezoelectric actuator is usually chosen to offer the input displacements of the 2DOF-VAUM system, but it has the inherent disadvantage of only providing the small stroke. Therefore, its displacement is required to amplify by a mechanical structure for complying with the requirements of the micro/nanostructure machining. The

Chapter 3 Design of the vibration-assisted ultraprecision machining system
displacement amplification mechanism is generally categorized into a lever amplification and a triangular amplification (Ling et al., 2016), as shown in Figure 3.1.

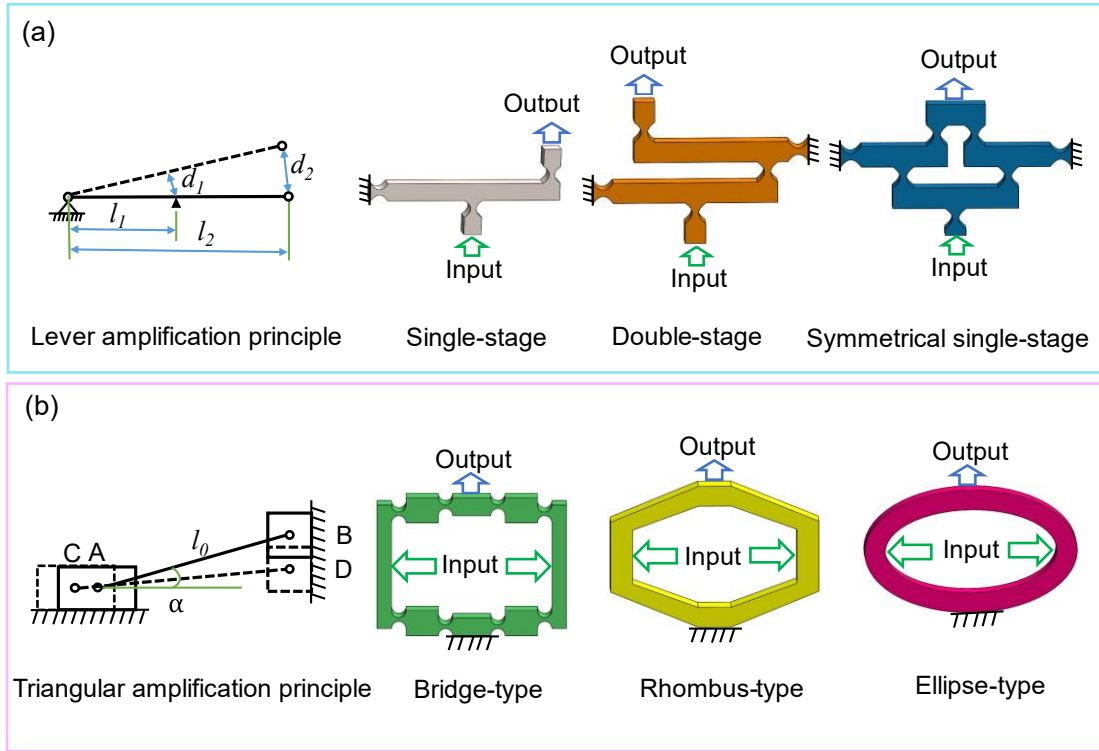


Figure 3.1 The topology of two amplification mechanisms. (a) Lever amplification and (b) triangular amplification.

For the lever amplification, the amplification ratio λ_l can be computed by analyzing the geometrical transform relationship of different links.

$$\lambda_l = \frac{d_2}{d_1} = \frac{l_2}{l_1} \quad (3.1)$$

where d_1 and d_2 are the input and output displacements, respectively; and l_1 and l_2 are the lengths of different parts of the link in Figure 3.1(a).

For the triangular amplification, the amplification ratio λ_t can be expressed:

$$\lambda_t = \frac{d_{BD}}{d_{AC}} = \lim_{\Delta\alpha \rightarrow 0} \frac{\sin \alpha - \sin(\alpha - \Delta\alpha)}{\cos(\alpha - \Delta\alpha) - \cos \alpha} = \cot \alpha \quad (3.2)$$

where d_{AC} and d_{BD} are the input and output displacements, respectively; and α is the angle between the link and the horizontal line before the small geometric deformation, as shown in Figure 3.1(b).

The lever amplification and triangular amplification have their own merits and drawbacks. For instance, lever amplification usually has a larger amplification ratio but needs larger structural sizes. In general, the larger structural sizes lead to a lower working frequency. In comparison with lever amplification, the triangular amplification has smaller structural sizes and a compact structure. In addition, its bilateral symmetric structure enables to minimize the undesired disturbance.

Based on the triangular amplification principle, in this study, the quasi-ellipse amplification unit (QEAU) is proposed to use by combining the ellipse-type with the rhombus-type. The QEAU has the advantages of efficient machining via the electrical discharge machining and fast assembly via the preload bolt. For realizing the two-dimensional motions in the machining plane, two QEAUs are arranged in an orthogonal layout to offer two independent motions since the orthogonal layout can decrease the coupling ratio by reducing the mutual influence of the two kinematic units. A flexure guidance unit (FGU) composed of two parallel leaf-spring flexure hinges is utilized to connect these two QEAUs.

The mechanical structure of the 2DOF-VAUM system is designed and presented in Figure 3.2(a). The periodic displacement motions offered by the PEA are firstly amplified by the QEAU, and consequently transferred to the cutting tool holder (CTH) by the FGU. The two preload bolts act as the preload spring to provide the constant force loads since the spring-load enhances the PEAs' dynamic push/pull performance. A natural single-crystal diamond cutting tool is fixed on the CTH, which is a

Chapter 3 Design of the vibration-assisted ultraprecision machining system

commercially available triangular indexable insert. By independently actuating and amplifying the left and right PEAs, the two-dimensional periodic motions of the tool tip can be generated in the machining plane. The stainless steel 304 is selected as the main material and the monolithic mechanical structure was machined by the low-speed wire electrical discharge machining. The overall dimensions of this device are 51mm×32mm×5.9mm, as shown in Figure 3.2(b).

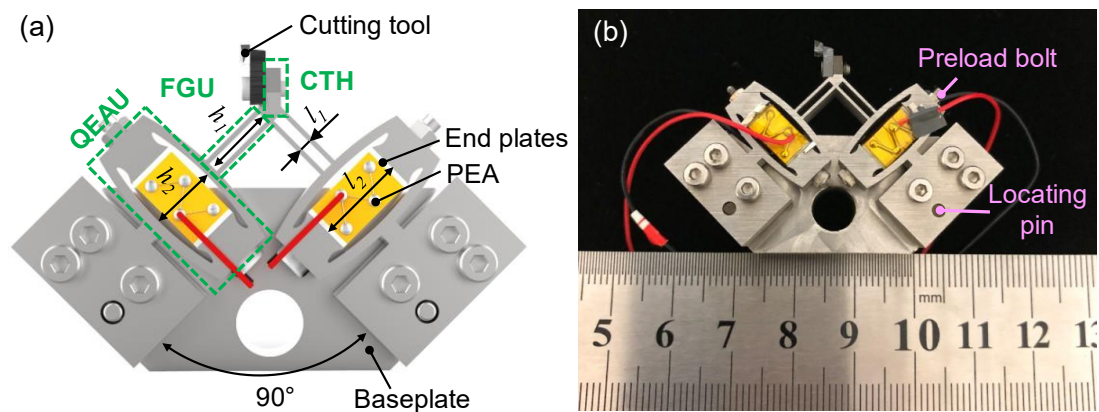


Figure 3.2 The mechanical structure of the 2DOF-VAUM system. (a) The 3D model and (b) the photograph.

The main size l_2 and thickness w are decided by the length and width of the piezoelectric actuator. The length and width of the chosen piezoelectric actuator are 8 ± 0.1 mm and 5.2 ± 0.1 mm, respectively. The values of l_2 and w are designed to be 8 mm and 5.9mm respectively for covering the whole piezoelectric actuator and avoiding the contact between other devices and the piezoelectric actuator during machining experiments. Then, other sizes, such as h_1 and l_1 , are decided based on l_2 and w . The smaller sizes, the higher bandwidth. Therefore, other sizes are designed as small as possible. To compensate for manufacturing and assembly tolerance, the end plates are employed to fill the gap between the PEA and the QEAU. The main sizes and

Chapter 3 Design of the vibration-assisted ultraprecision machining system
 material properties of the mechanical structure are listed in Table 3.1 and Table 3.2 for providing the input parameters for the following simulation.

Table 3.1 Key dimensions of the mechanical structure.

h_1	h_2	l_1	l_2	w
7.05mm	6.60mm	2mm	8mm	5.9mm

Table 3.2 Material properties of the mechanical structure.

Density	Young's modulus	Poisson's ratio	Shear modulus	Bulk modulus
7750 kg/m ³	1.93×10 ¹¹ pa	0.31	7.37×10 ¹⁰ pa	1.70×10 ¹¹ pa

In the micro/nanostructure machining, the hardware configuration of the 2DOF-VAUM system during micro/nanostructure machining is shown in Figure 3.3. In addition to the mechanical structure, it also has other accessories, such as computer, multifunction I/O device, the piezo amplifier.

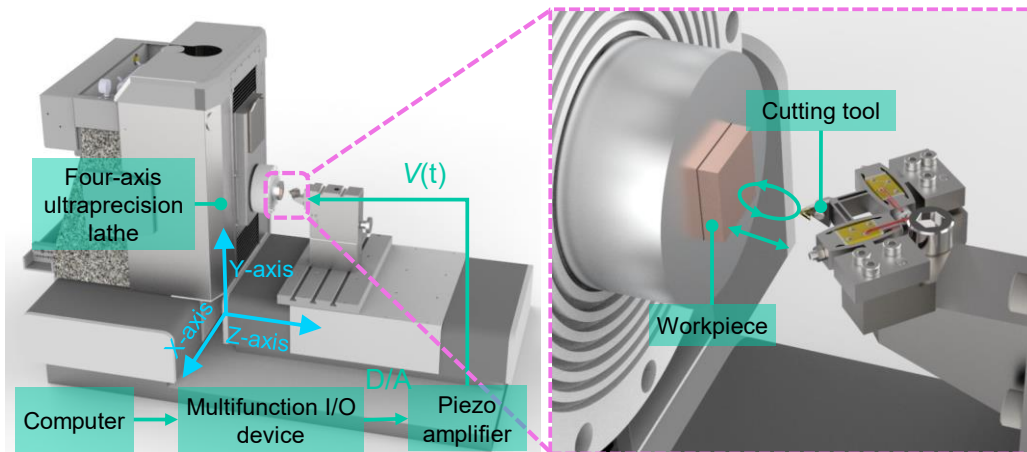


Figure 3.3 Hardware configuration of the two-degree-of-freedom vibration-assisted ultraprecision machining system during micro/nanostructure machining.

The computer provides the command signals through the programming software “LabVIEW”. The multifunction I/O device converts these digital signals into analogue signals. In order to satisfy the voltage requirement of the piezoelectric actuator, the analogue signals need to be amplified by the piezo amplifier to drive the two piezoelectric actuators. When the two piezoelectric actuators receive the amplified

voltage signals, they output the periodic vibration displacement with the same waveform as the command signals. The mechanical structure of the 2DOF-VAUM system will provide the vibration trajectory to generate the micro/nanostructured surfaces when it obtains the output displacements of the two piezoelectric actuators.

3.3 Multi-physics simulation of the working performances

The accurate simulation of working performances can offer feedback guidance to optimize the mechanical structure and reduce the design time. The multi-physics finite element method (FEM) is utilized to precisely simulate and foretell the bandwidth and coupling ratio, which are the two significant quantitative indices of working performances. The bandwidth of the designed 2DOF-VAUM system determines the range of usable working frequency, in which a higher working frequency means higher machining efficiency (J. Wang et al., 2019). On the other hand, the coupling ratio influences the control of vibration trajectories, in which a lower coupling ratio means higher effectiveness on control during machining (F. Wang et al., 2019).

3.3.1 Piezoelectric material property calculation

Determination of material properties is the first step in the multi-physics FEM process using the software ANSYS with Piezoelectric and MEMS extension. The piezoelectrical material properties include the compliance matrix, stress piezoelectric coefficient matrix, and the permittivity matrix at constant strain. According to electromechanical coupled constitutive relations of linear piezoelectricity, their relations are expressed as (Elka et al., 2004):

$$S_i = S_{ij}^E T_j + d_{im} E_m \quad (3.3)$$

$$\mathbf{D}_k = \mathbf{d}_{mi} \mathbf{T}_i + \boldsymbol{\varepsilon}_{mk}^T \mathbf{E}_k \quad (3.4)$$

$$\mathbf{T}_i = \mathbf{C}_{ij}^E \mathbf{S}_j - \mathbf{e}_{im} \mathbf{E}_m \quad (3.5)$$

$$\mathbf{D}_k = \mathbf{e}_{mi} \mathbf{S}_i + \boldsymbol{\varepsilon}_{mk}^S \mathbf{E}_k \quad (3.6)$$

where the vector \mathbf{S}_i , \mathbf{T}_i , $\mathbf{E}_{m/k}$ and \mathbf{D}_k are the strain, stress, electric field, and electric displacement, respectively. The matrices \mathbf{S}_{ij}^E , \mathbf{C}_{ij}^E , $\mathbf{d}_{im/mi}$, $\mathbf{e}_{im/mi}$, $\boldsymbol{\varepsilon}_{mk}^{T/S}$ are the mechanical compliance, the mechanical stiffness, the strain piezoelectric coefficient, the stress piezoelectric coefficient, and the permittivity, respectively. The subscript $i, j=1, 2, \dots, 6$ and $m, k=1,2,3$ refer to different directions within the material coordinate system illustrated in Figure 3.4. Axes 1, 2, and 3 correspond to the x -axis, y -axis, and z -axis, respectively while axes 4, 5, and 6 refer to rotational motion around the x -axis, y -axis, and z -axis, respectively. The superscripts E , S , and T denote the measurements taken at the constant electric field, constant strain, and constant stress.

For the PEAs along the poling axis 3, the piezoelectric material is the transversely isotropic material. So, several elements in the above matrices are either zero or expressed in terms of other parameters. Therefore, the fully constitutive Eqs. (3.3) and (3.4) can be reduced as follow:

$$\begin{bmatrix} S_1 \\ S_2 \\ S_3 \\ S_4 \\ S_5 \\ S_6 \end{bmatrix} = \begin{bmatrix} S_{11}^E & S_{12}^E & S_{13}^E & 0 & 0 & 0 \\ S_{12}^E & S_{11}^E & S_{13}^E & 0 & 0 & 0 \\ S_{13}^E & S_{13}^E & S_{33}^E & 0 & 0 & 0 \\ 0 & 0 & 0 & S_{44}^E & 0 & 0 \\ 0 & 0 & 0 & 0 & S_{55}^E & 0 \\ 0 & 0 & 0 & 0 & 0 & S_{66}^E \end{bmatrix} \begin{bmatrix} T_1 \\ T_2 \\ T_3 \\ T_4 \\ T_5 \\ T_6 \end{bmatrix} + \begin{bmatrix} 0 & 0 & d_{31} \\ 0 & 0 & d_{31} \\ 0 & 0 & d_{33} \\ 0 & d_{15} & 0 \\ d_{15} & 0 & 0 \\ 0 & 0 & 0 \end{bmatrix} \begin{bmatrix} E_1 \\ E_2 \\ E_3 \end{bmatrix} \quad (3.7)$$

$$\begin{bmatrix} D_1 \\ D_2 \\ D_3 \end{bmatrix} = \begin{bmatrix} 0 & 0 & 0 & 0 & d_{15} & 0 \\ 0 & 0 & 0 & d_{15} & 0 & 0 \\ d_{31} & d_{31} & d_{33} & 0 & 0 & 0 \end{bmatrix} \begin{bmatrix} T_1 \\ T_2 \\ T_3 \\ T_4 \\ T_5 \\ T_6 \end{bmatrix} + \begin{bmatrix} \varepsilon_{11}^T & 0 & 0 \\ 0 & \varepsilon_{22}^T & 0 \\ 0 & 0 & \varepsilon_{33}^T \end{bmatrix} \begin{bmatrix} E_1 \\ E_2 \\ E_3 \end{bmatrix} \quad (3.8)$$

For the mechanical compliance matrix (S_{ij}^E), the elements S_{11}^E and S_{33}^E are usually obtained by the supplier of PEAs (Thorlabs, PK4FA2H3P2), as listed in Table 3.3. The other elements ($S_{12}^E, S_{13}^E, S_{44}^E$, and S_{66}^E) in Eq. (3.7) can be obtained according to the computation method from the literature (Clement et al., 2013). Note that, in IEEE standard, the rows are defined as x, y, z, yz, xz , and xy , while multi-physics FEM input is expected to be ordered as x, y, z, xy, yz , and xz , so the conversion from IEEE format to ANSYS format is necessary accordingly.

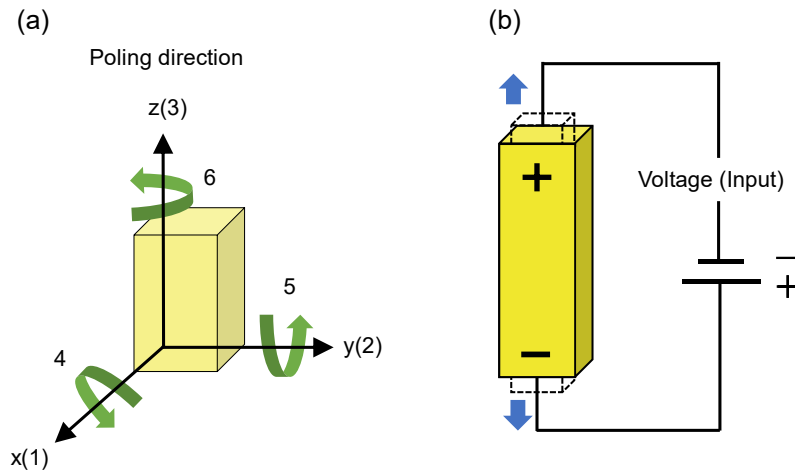


Figure 3.4 (a) The axis nomenclature in the piezoelectric material and (b) the schematic of the working principle of the PEA.

Table 3.3 Piezoelectric material property provided by the supplier.

Mechanical compliance coefficient(m ² /N)	Strain piezoelectric coefficient(C/N)	Permittivity coefficient at constant stress
$S_{11}^E=17 \times 10^{-12}$	$d_{31}=-320 \times 10^{-12}$	$\epsilon_{11}^T=3370$
$S_{33}^E=23 \times 10^{-12}$	$d_{33}=4.67 \times 10^{-8}$	$\epsilon_{22}^T=3370$
	$d_{15}=950 \times 10^{-12}$	$\epsilon_{33}^T=3300$

Then, the stress piezoelectric coefficient matrix e_{mi} and the permittivity matrix ϵ_{mk}^S at constant strain can be derived from Eqs. (3.3)-(3.6):

$$e_{mi} = d_{mi} [S_{ij}^E]^{-1} \quad (3.9)$$

$$\epsilon_{mk}^S = \epsilon_{mk}^T - d_{mi} [e_{mi}]^T \quad (3.10)$$

where $[s_{ij}^E]^{-1}$ is the inverse of the compliance matrix s_{ij}^E and $[e_{mi}]^T$ is the transpose of the stress piezoelectric coefficient matrix e_{mi} . Note that the element d_{33} in the Eqs. (3.9) and (3.10) present all stacks' the strain piezoelectric coefficient along the poling direction.

3.3.2 Simulation process

Apart from the material properties of PEA, the material properties of mechanical structure such as density, Young's modulus, and Poisson's ratio, are required to set into the same as the actual situation. For the input of the boundary conditions in the multi-physics FEM, the baseplate is fixed to constrain all degrees of freedom, as shown in Figure 3.5.

The swept method was performed to examine the bandwidth of the designed 2DOF-VAUM system. The amplitude of sinusoidal voltage signals inputted into the left and right PEAs was 5 V with the 0° phase difference between the two signals. And the frequency linearly increased from 0 to 4000 Hz with a step size of 10Hz. The corresponding amplitudes of the output displacement were extracted for analyses of the bandwidth.

Most of the symmetric mechanisms have a strong coupling effect that causes undesirable parasitic motions, which add difficulty to the positioning of the cutting tool and then influence the shape accuracy of the machined micro/nanostructures. The coupling ratio is widely regarded as the most essential index to demonstrate motion accuracy and control stability for the vibration-assisted machining system (Tang and Li, 2014). In terms of the coupling ratio simulation, the two sinusoidal voltage signals with the identical amplitude of 30V and the identical frequency of 10 Hz were inputted into the left and right PEAs. The phase difference between the two PEAs was set to 0°

Chapter 3 Design of the vibration-assisted ultraprecision machining system for pure depth-of-cutting motion and 180° for pure cutting motion. The vibration displacements of the cutting tool holder can be captured and recorded to analyze the coupling ratio of the 2DOF-VAUM system in this multi-physics FEM.

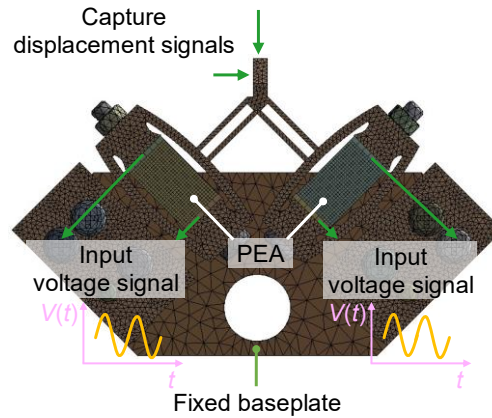


Figure 3.5. Meshed multi-physics FEM model of the 2DOF-VAUM system.

3.4 Numerical simulation of the micro/nanostructure generation

Figure 3.6 demonstrates the principle of micro/nanostructure generation on the metal surface. When the ultrafast vibration motions of the 2DOF-VAUM system are applied to machine the micro/nanostructure, the complex interactions between the cutting tool and the workpiece will occur (Guo and Ehmann, 2013b). During machining, the three-dimensional geometric shape of the cutting tool, cutting trajectory, and the effects of material elastic recovery determine the shapes and sizes of micro/nanostructures. For instance, the clearance angle of the cutting tool plays a key role in shaping the final surface topography of micro/nanostructures because of the interference between the flank face and the machined surface. The spacing (d) of the adjacent micro/nanostructures can be determined by the working frequency of the vibration-assisted ultraprecision machining system and the cutting speed.

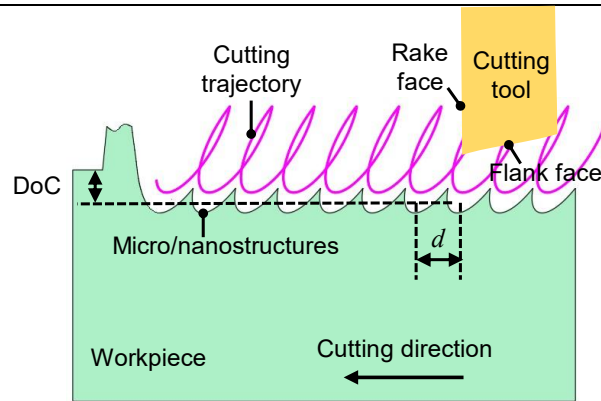


Figure 3.6. Principle of micro/nanostructured surface generation.

A numerical simulation algorithm of micro/nanostructure generation on the metal surface is proposed in this section based on comprehensive consideration of the three-dimensional geometric shape of the cutting tool, the cutting motion trajectory, and the elastic recovery of workpiece material. The numerical simulation algorithm not only predicts the surface topography but also provides guidance in the selection of the process parameters before machining the desired micro/nanostructures.

Its overall flowchart is illustrated in Figure 3.7. The cutting tool geometry, including the rake face, flank face, and cutting edge, is firstly discretized by the parametric functions. The workpiece geometry (a rectangle) is also discretized and stored in the form of mesh grids in the Cartesian coordinate system. The cutting tool coordinates with motion trajectories are the time-varying ($t = N_i \Delta t$) functions, which are then transformed to the workpiece coordinate system through the coordinate transformation.

Next, as the cutting tool intersects with the workpiece, the interference condition will be checked according to the Z value difference between the motion trajectory coordinate and the corresponding workpiece discretization point (grid point). The

Boolean operation will be conducted to update the Z value of the workpiece grid point, as shown in the green parts of Figure 3.7.

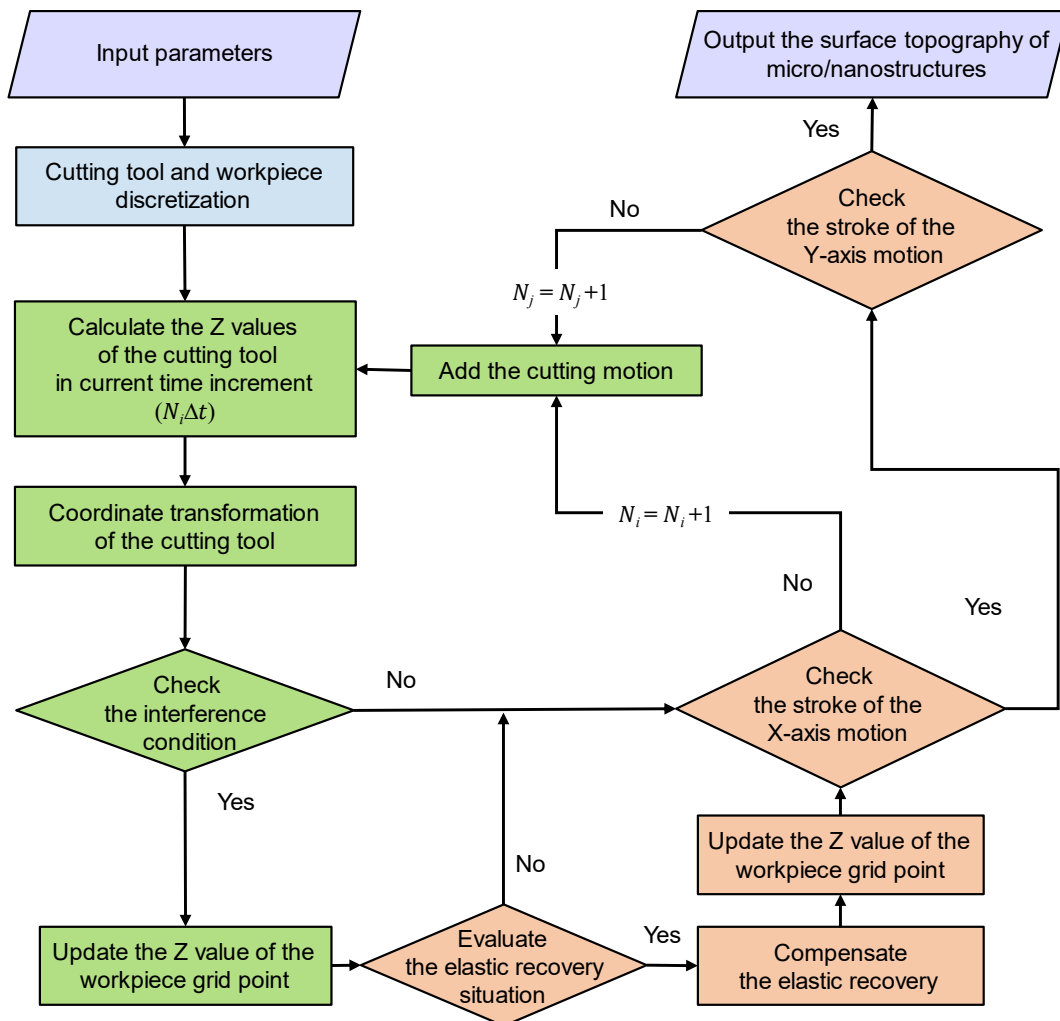


Figure 3.7. Flowchart of the numerical simulation algorithm.

Then, the material elastic recovery of the workpiece will be evaluated to predict the three-dimensional micro/nanostructures accurately. The Z value of the workpiece grid point will be further updated considering the material recovery. When completing cutting motion in the X-axis, the cutting tool returns to the origin point in the X-axis and feeds along Y-axis, as shown in the coffee color parts of Figure 3.7. Finally, the micro/nanostructures on the workpiece surface can be plotted through the programming

Chapter 3 Design of the vibration-assisted ultraprecision machining system of Matlab. The detailed descriptions of this numerical simulation algorithm are presented in the following sections.

3.4.1 Discretization of the cutting tool and workpiece

A standard equilateral triangular insert with an internal angle of 60° is employed as the cutting tool, which scanning electron microscope (SEM) images are shown in Figure 3.8. The cutting edge can be defined as an intersection between the rake face and the flank face. In micro-machining, the cutting depth is far smaller than the nose radius of the cutting tool, so only small parts of the cutting tool need to be discretized. According to literature (Guo and Ehmann, 2013b), the three-dimensional geometric shape of the cutting tool can be mathematically described in the local coordinate system by a set of parametric functions:

$$\begin{aligned} x_{insert}(m, n) &= \begin{cases} -(R + m) \cdot \sin n & m \leq 0 \\ -(R - m \cdot \sin \alpha) \cdot \sin n & m > 0 \end{cases} \\ y_{insert}(m, n) &= \begin{cases} 0 & m \leq 0 \\ m \cdot \cos \alpha & m > 0 \end{cases} \\ z_{insert}(m, n) &= \begin{cases} (R + m) \cdot \cos n & m \leq 0 \\ (R - m \cdot \sin \alpha) \cdot \sin n & m > 0 \end{cases} \end{aligned} \quad (3.11)$$

where the parameter m is an indicator of the different parts of the cutting tool. When $m > 0$, the segment function describes the flank face, while it describes the rake face when $m < 0$. The cutting edge is described when $m = 0$. n is the angle between the discretization point D and the tip E of the cutting tool, as shown in Figure 3.9(a). R is the radius of the tool nose.

For the workpiece, its geometric shape is a rectangle in the micro/nanostructure machining, which can be discretized in the orthogonal coordinate system. The discretized result is plotted in Figure 3.9(b).

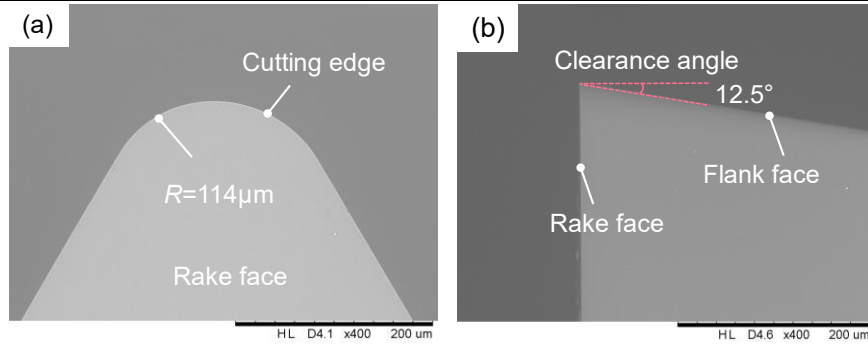


Figure 3.8. SEM images of the cutting tool. (a) Top view and (b) side view.

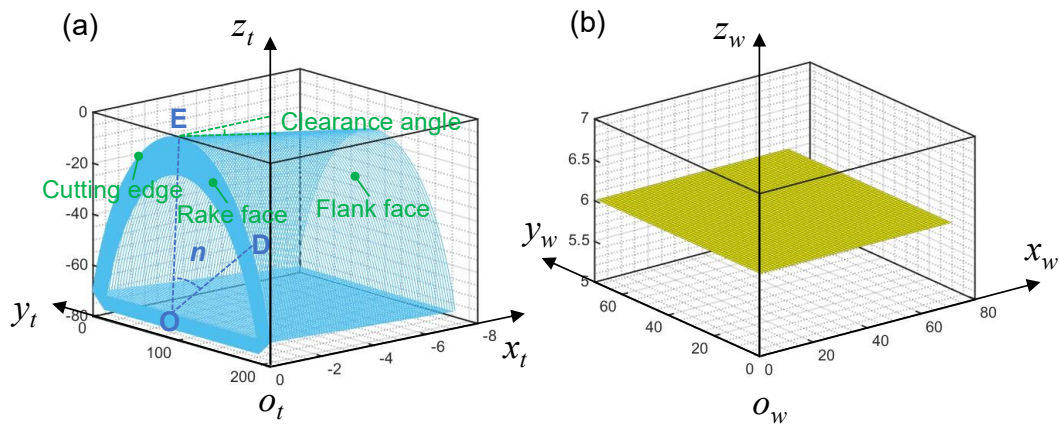


Figure 3.9. Discretization results of (a) the cutting tool and (b) the workpiece.

3.4.2 Modeling of the cutting motion trajectory

Before expressing the cutting motion trajectory, two three-dimensional Cartesian coordinate systems need to be defined, as depicted in Figure 3.9(a) and (b). The cutting tool coordinate system ($O_t-x_t y_t z_t$) is attached on the rake face of the cutting tool. And the three-dimensional shape of the cutting tool was described mathematically in this coordinate system. The workpiece coordinate system ($O_w-x_w y_w z_w$) is established on the workpiece surface. Considering the vibration trajectory (D_t) of the cutting tool, the discretization coordinates (C_d) of the cutting tool, and the cutting speed (V_c) in the O_t -

$x_t y_t z_t$ coordinate system, the motion trajectory coordinate (M_w) of the cutting tool in the $o_w-x_w y_w z_w$ coordinate system can be mathematically expressed as:

$$M_w = \mathbf{R}(\theta) \cdot \mathbf{T}(W_l - V_c N_i \Delta t, V_f N_j, \text{DoC}) \cdot (C_d + D_t) \quad (3.12)$$

where \mathbf{R} and \mathbf{T} are the rotation and translation matrices (Guo and Ehmann, 2013b), which let the tool tip motion in the local coordinate system transform into the workpiece coordinate system; θ is the rotation angle between the $o_t-x_t y_t z_t$ coordinate system and the $o_w-x_w y_w z_w$ coordinate system, and it equals zero as there is no rotation angle in these two coordinate systems; W_l is the length of the workpiece, i.e. the stroke of the X-axis motion; N_i is an increment and it will increase by 1 on each iteration; Δt is the time step of the simulation, and Δt can be given by $\min\{1/V_c, 1/60f\}$, in which f is the working frequency of the vibration-assisted ultraprecision machining system; V_f is the cross-feed along the Y-axis direction of the ultraprecision lathe; N_j is also an increment that represents the current cycle number of the cross-feed motion, and its value is determined by the ratio of the stroke of the Y-axis motion over the cross-feed. DoC represents the nominal depth-of-cutting.

The discretization coordinates C_d and vibration trajectory D_t of the cutting tool can be described by:

$$C_d = \begin{bmatrix} x_{insert}(m, n) \\ y_{insert}(m, n) \\ z_{insert}(m, n) \end{bmatrix} \quad (3.13)$$

$$D_t = \begin{bmatrix} D_t(x, N_i \Delta t) \\ D_t(y, N_i \Delta t) \\ D_t(z, N_i \Delta t) \end{bmatrix} \quad (3.14)$$

where $D_t(x, N_i \Delta t)$, $D_t(y, N_i \Delta t)$, and $D_t(z, N_i \Delta t)$ are the vibration trajectory components in the $o_t-x_t y_t z_t$ coordinate system.

Therefore, the motion trajectory coordinate of the cutting tool in the $o_w-x_wy_wz_w$

coordinate system can be written as:

$$\begin{aligned}
 \begin{bmatrix} W_x \\ W_y \\ W_z \\ 1 \end{bmatrix} &= \begin{bmatrix} \cos \theta & \sin \theta & 0 & 0 \\ -\sin \theta & \cos \theta & 0 & 0 \\ 0 & 0 & 1 & 0 \\ 0 & 0 & 0 & 1 \end{bmatrix} \begin{bmatrix} 1 & 0 & 0 & W_l - V_c N_i \Delta t \\ 0 & 1 & 0 & V_f N_j \\ 0 & 0 & 1 & \text{DoC} \\ 0 & 0 & 0 & 1 \end{bmatrix} \\
 &\cdot \left\{ \begin{bmatrix} x_{insert}(m, n) \\ y_{insert}(m, n) \\ z_{insert}(m, n) \\ 1 \end{bmatrix} + \begin{bmatrix} D_t(x, N_i \Delta t) \\ D_t(y, N_i \Delta t) \\ D_t(z, N_i \Delta t) \\ 0 \end{bmatrix} \right\} \\
 &= \begin{bmatrix} 1 & 0 & 0 & W_l - V_c N_i \Delta t \\ 0 & 1 & 0 & V_f N_j \\ 0 & 0 & 1 & \text{DoC} \\ 0 & 0 & 0 & 1 \end{bmatrix} \cdot \left\{ \begin{bmatrix} x_{insert}(m, n) \\ y_{insert}(m, n) \\ z_{insert}(m, n) \\ 1 \end{bmatrix} + \begin{bmatrix} D_t(x, N_i \Delta t) \\ D_t(y, N_i \Delta t) \\ D_t(z, N_i \Delta t) \\ 0 \end{bmatrix} \right\} \quad (3.15)
 \end{aligned}$$

For each iteration, if the Z value of the motion trajectory coordinate is less than the Z value of the workpiece grid point, which means that the cutting tool intersects with the workpiece, the Z value of the corresponding workpiece grid point will be replaced by the Z value of the motion trajectory coordinate. The Z value of the workpiece grid point will be updated for the first time.

3.4.3 Evaluation of the material elastic recovery

As the chosen workpiece material is generally soft metal such as copper alloy or aluminum alloy, the elastic recovery related to cutting thickness must be considered in the numerical simulation algorithm. Zhu et al. (Zhu et al., 2018) illustrated the material elastic recovery between the cutting tool and the workpiece during the diamond micromachining processing, as shown in Figure 3.10(a). In this study, a piecewise function is used to express the elastic recovery concerning cutting thickness (t_c), as shown in Figure 3.10(b). When t_c is smaller than the elastic deformation limit (t_e), which is taken as $0.01\mu\text{m}$ (Guo and Ehmann, 2013b), the material is considered to experience

a full recovery with no plastic deformation. The micro/nanostructure machining process turns into a pure sliding process. When t_c is between the t_e and the minimum chip thickness (h_{min}), part of the material elastically recovers. The machining process turns into a ploughing process. When t_c increases over the h_{min} , only the elastic recovery occurs. The elastic recovery remains a constant value, and the shear process plays the main role in this process. The piecewise function of the material elastic recovery can be mathematically given as:

$$\delta t_c = \begin{cases} t_c & t_c < t_e \\ \frac{(1-\varepsilon_p) \cdot h_{min} - t_e}{h_{min} - t_e} (t_c - t_e) & t_c \in [t_e, h_{min}] \\ t_e & t_c > h_{min} \end{cases} \quad (3.16)$$

where ε_p is the plastic strain (Zhu et al., 2018).

The Z value of the workpiece grid point is updated again according to the value of the material elastic recovery. Finally, the results of the numerical simulation algorithm of the micro/nanostructure generation on the workpiece surface can be shown through the programming of Matlab.

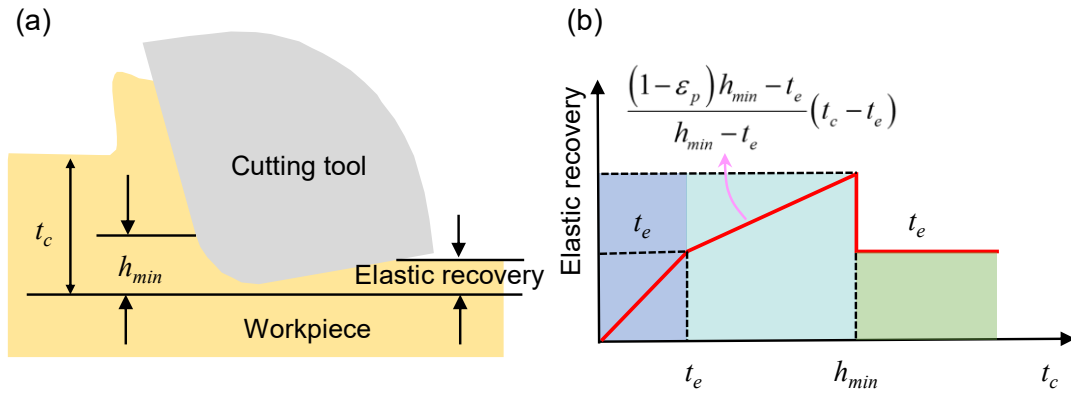


Figure 3.10. (a)The illustration of material elastic recovery and (b) the elastic recovery function with respect to cutting thickness.

3.5 Experimental details

3.5.1 Working performance test

For verifying the effectiveness of the established multi-physics FEM, a test platform for working performances was established and shown in Figure 3.11(a). In this platform, the computer offers the digital signals using a graphical programming software “LabVIEW”. The digital signals would be converted and amplified by the multifunction I/O device (NI DAQ USB-6341) and the high-performance piezo amplifier (PI, E-617.001) to drive the PEAs. The displacement signals of the cutting tool holder along the cutting direction and depth-of-cutting (DoC) direction, as shown in Figure 3.11(b), can be precisely measured by a pair of capacitive displacement sensors (Elite, Lion Precision).

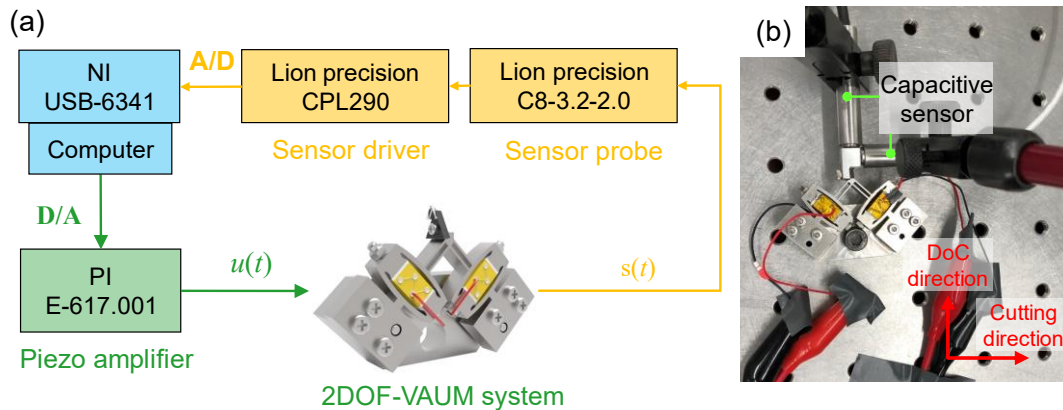


Figure 3.11. The working performance test platform of the 2DOF-VAUM system. (a) The schematic diagram and (b) the hardware platform.

Besides, LabVIEW’s user-interface has the capability of observing and monitoring the frequency response in real-time, which can help to adjust the time to stop the measure. To efficiently reduce the external disturbance, the testing experiments were carried out on a commercial platform with air-bearing supports. The bandwidth and

Chapter 3 Design of the vibration-assisted ultraprecision machining system
coupling ratio of the designed 2DOF-VAUM system were tested and the voltage signals
inputted into PEAs kept the same as the multi-physics FEM.

3.5.2 Micro/nanostructured surface machining

The machining of micro/nanostructures does not only demonstrate the capability of the proposed machining system in generating different micro/nanostructures but also verifies the effectiveness and accuracy of the proposed numerical simulation algorithm of the micro/nanostructure generation simultaneously. They were performed on a four-axis ultraprecision lathe (Moore Nanotech 350FG) with three linear axes and an air-bearing spindle. The 2DOF-VAUM system was fixed on the micro height adjust tool holder and the workpiece (the copper alloy H62, Keple Technology Co., Ltd, China) was fixed on a fixture that mounted on the spindle through the vacuum chuck. The detailed hardware setup is shown in Figure 3.12.

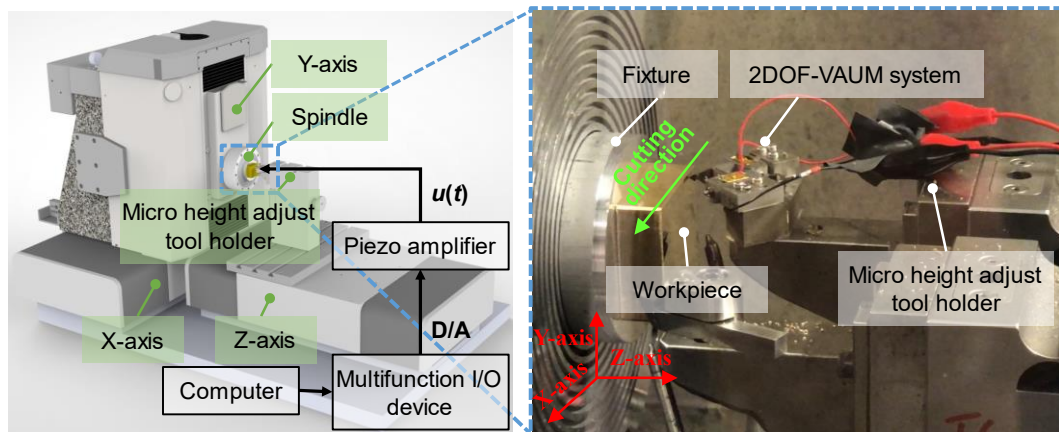


Figure 3.12. The experimental setup for machining micro/nanostructured surfaces.

The properties of H62 are listed in Table 3.4. The single-crystal diamond cutting tool (Contour Fine Tooling Inc., UK) with a round edge was selected for machining the micro/nanostructured surfaces. Its nose radius, clearance angle, and rake face angle are 0.114 mm, 12.5°, and 0°, respectively. The workpieces were firstly flatted with a

Chapter 3 Design of the vibration-assisted ultraprecision machining system
 spindle speed of 2000rpm, and the DoC and feedrate were set as 2 μ m and 2mm/min, respectively.

To compare the experimental results with the numerical simulation results, two samples were machined with unique microstructures. They are named as two cases in this study and the detailed process parameters for the two cases are tabulated in Table 3.5. The sinusoidal voltage signals were applied in all experiments. The input parameters for the numerical simulation algorithm were kept the same as the machining experiments. After experiments, the workpieces were cleaned in the ultrasonic cleaner using the alcohol for 10 minutes to wash off any residual chips and then dried in an air environment for 20 minutes. A white light interferometer with sub-nanometre resolution (Zygo Nexview) was employed to characterize the three-dimensional surface topography.

Table 3.4 The properties of the copper alloy H62.

Chemical composition (Weight, %)				Mechanical properties	
Cu	60.5-63.5	Sb	≤ 0.005	Density (Kg/m ³)	8430
Fe	≤ 0.15	Bi	≤ 0.002	Elongation (%)	32.6
Pb	≤ 0.08	Zn	Balance	Tensile strength (Mpa)	392
P	≤ 0.01	Impurity	≤ 0.5	Hardness (Hv)	121

Table 3.5 The process parameters.

Parameters		Case 1	Case 2
Cutting parameters	Depth-of-cutting	2 μ m	4 μ m
	Cutting velocity	1000mm/min	600mm/min
	Cross-feed	60 μ m	30 μ m
Voltage signal parameters	Amplitude	40V	40V
	Frequency	500Hz	1000Hz
	Phase difference	30°	30°

3.6 Results and discussion

3.6.1 Working performance

In terms of the bandwidth, the results of the simulation and the measurement of the amplitudes of vibration displacements along the depth-of-cutting direction are shown in Figure 3.13. It can be clearly seen that the values of the first-order resonant frequency for the traditional simulation, the multi-physics FEM simulation, and measurement are 3330Hz, 3280Hz, and 3230Hz, respectively. The deviation (1.5%) of the multi-physics FEM simulation method is smaller than that (3.1%) of the traditional simulation method that simply inputs the displacement signals into the vibration-assisted machining system. The amplitudes are stable and keep at 0.12 μ m before 3000Hz, so the bandwidth of the whole 2DOF-VAUM system can be determined as to 3kHz. This means the usable working frequency of the designed two-degree-of-freedom vibration-assisted ultraprecision machining system ranges from 0Hz to 3kHz. Besides, although the first-order resonant frequency from the multi-physics FEM simulation result is a little larger than that of the measurement result as no damping controls are set in the simulation, the overall trend of this simulation method and the measurement is well in accordance with each other.

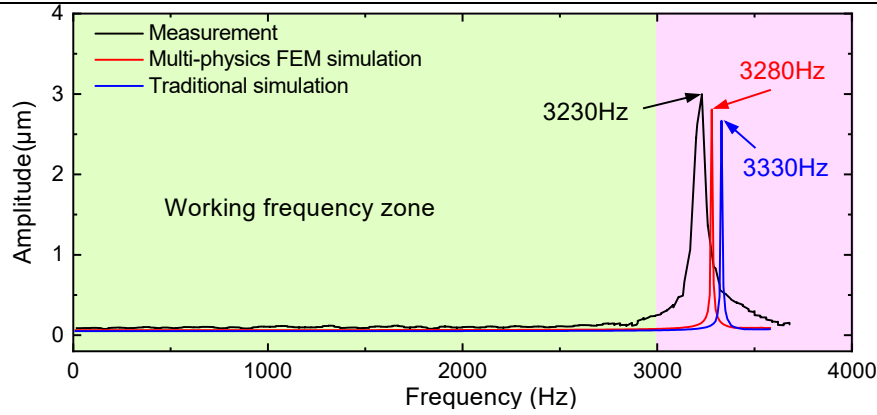


Figure 3.13 Measurement and simulation results of the bandwidth.

As for the coupling ratio of the designed 2DOF-VAUM system, the simulated displacement trajectories along DoC direction and cutting direction were captured in multi-physics FEM simulation, as shown in Figure 3.14(a).

The measurement and simulation results about the coupling ratio are plotted in Figure 3.14(b) and (c) respectively. The amplitudes of the traditional simulation, the multi-physics FEM simulation, and the measurement are $1.90\mu\text{m}$, $2.38\mu\text{m}$, and $2.59\mu\text{m}$ in the cutting direction. The smaller discrepancy shows that multi-physics FEM can be a very effective tool for analyzing the coupling ratio. According to the amplitude diversity between the desired motion and parasitic motion in the measurement results, the coupling ratios in the cutting direction and the DoC direction can be calculated as 2.32% and 4.86%, respectively.

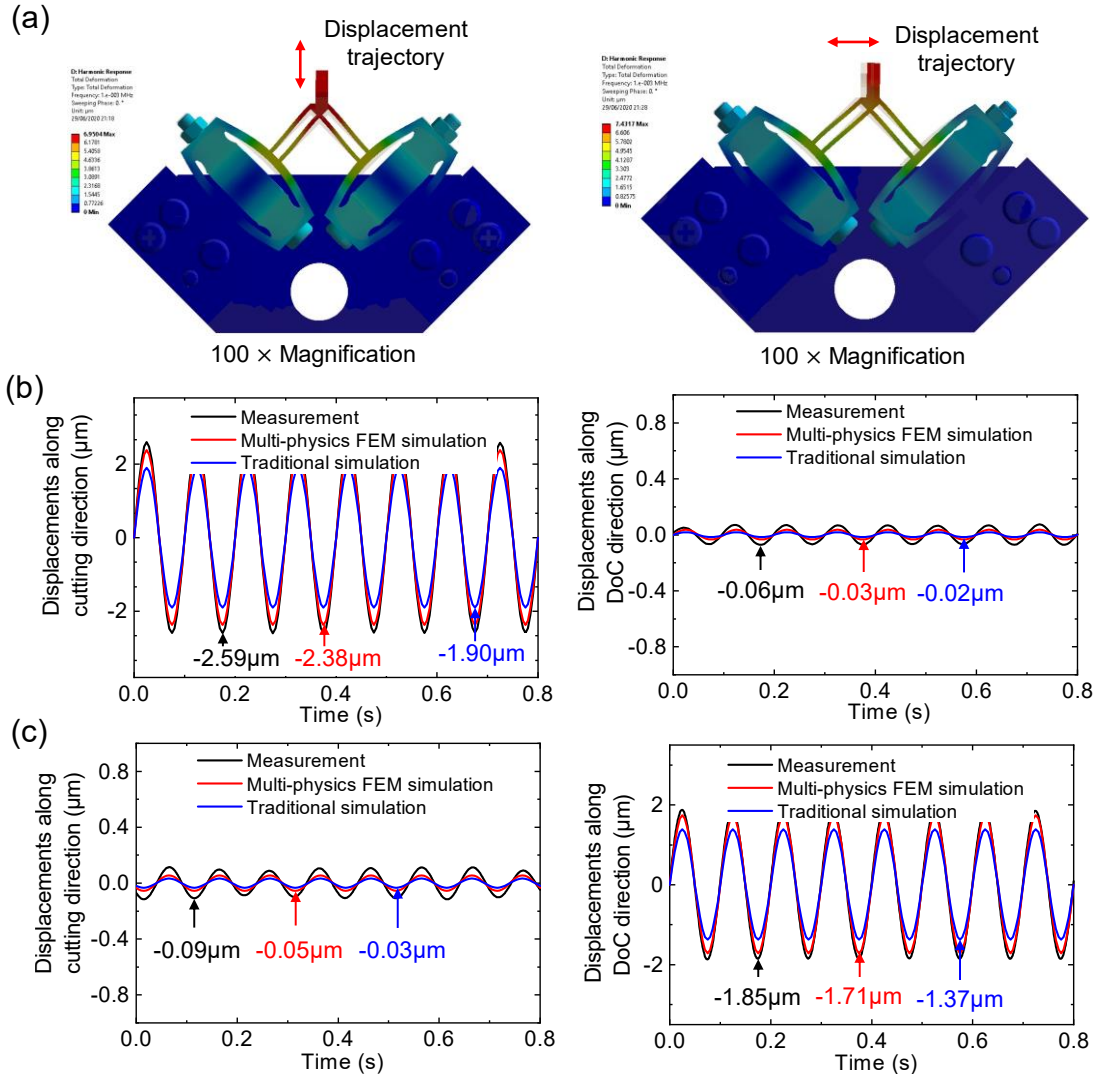


Figure 3.14 Measurement and simulation results of the coupling ratio. (a) Simulated displacement trajectories; displacements (b) along the cutting direction and (c) along the DoC direction.

In addition, the relationship between the input voltage signal and the output vibration trajectory can be expressed as:

$$\begin{bmatrix} D_d \\ D_c \end{bmatrix} = \begin{bmatrix} A_d & A_d \\ A_c & -A_c \end{bmatrix} \begin{bmatrix} V_{left}(t) + V_{left}^0 \\ V_{right}(t) + V_{right}^0 \end{bmatrix} \quad (3.17)$$

where D_d and D_c are the vibration trajectory along DoC direction and cutting direction, respectively. $V_{left}(t)$ and $V_{right}(t)$ are the input voltage signal for the left PEA and right PEA, respectively. A_d and A_c are the transformation coefficients. V_{left}^0 and V_{right}^0

are the voltage offset for guaranteeing that resultant input voltages are always positive according to the working requirements of the PEAs.

According to the amplitudes of the input voltage signal and the output displacement in the experiments, the coefficients A_d ($0.043\mu\text{m}/\text{V}$) and A_c ($0.031\mu\text{m}/\text{V}$) can be calculated, which supports to determine the input voltage signals of the PEAs according to the desired output displacement before machining micro/nanostructures.

3.6.2 Micro/nanostructured surfaces

The surface topographies of the Case 1 and Case 2 were obtained after experiments and are shown in Figure 3.15(a) and (b). Since the workpiece material is the soft metal copper alloy, the effect of material elastic recovery on the cutting process should be considered in the numerical simulation algorithm. In Case 1 and Case 2, the cutting thickness t_c is larger than the minimum chip thickness h_{min} , so the shear motion plays the predominant role in the machining of micro/nanostructures on the copper alloy surface and the elastic recovery remains a constant value ($0.01\mu\text{m}$) in the material elastic recovery modeling according to Eq. (3.16). In order to quantitatively analyze the geometrical error between the experiment and simulation, the cross-sectional profiles were extracted, as shown in Figure 3.15.

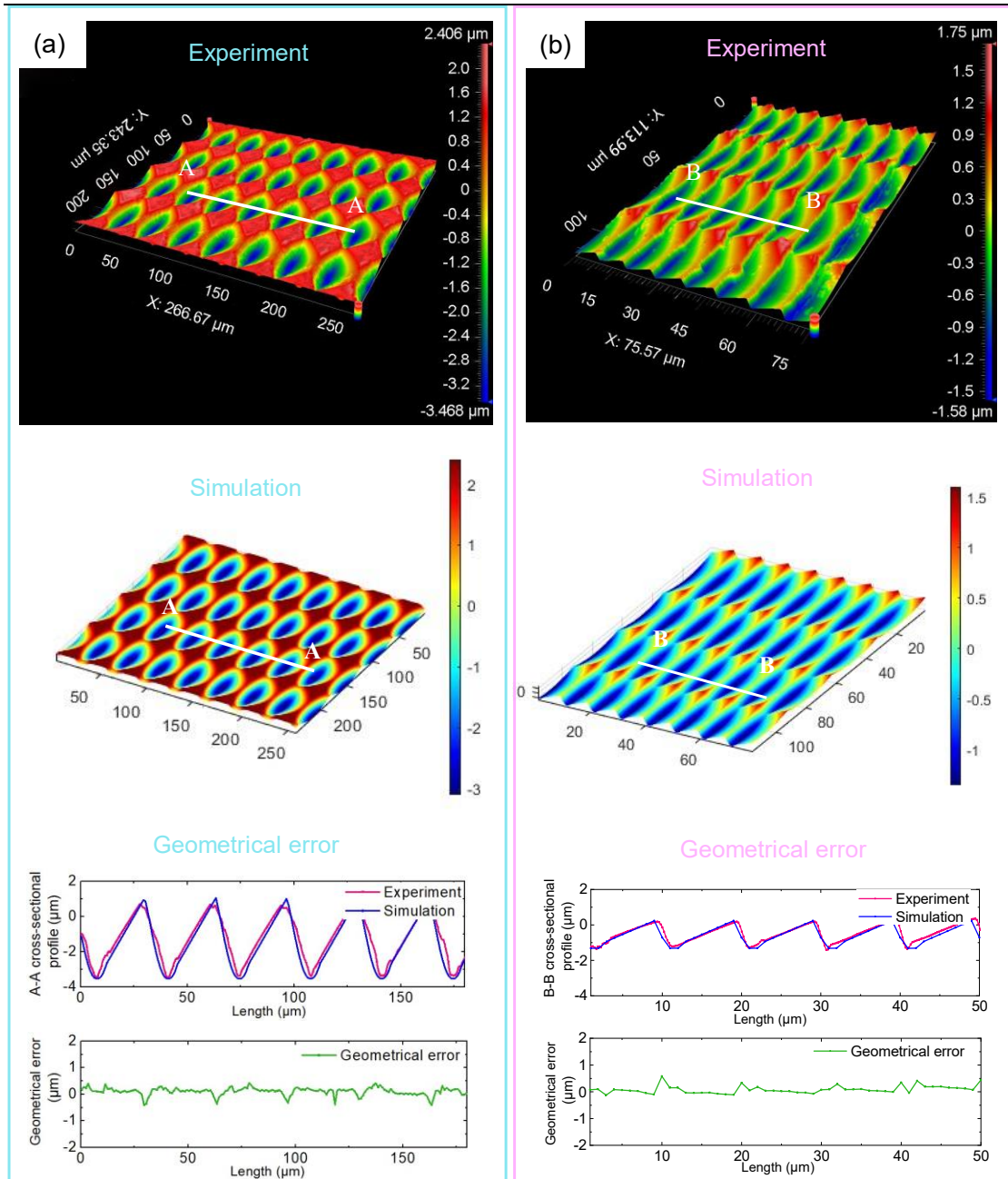


Figure 3.15. Surface topography and geometrical error of (a) Case 1 and (b) Case 2.

For Case 1, the average value of the geometrical errors along the A-A cross-sectional profile is $0.1\mu\text{m}$. For Case 2, the average value along the B-B cross-sectional profile is $0.02\mu\text{m}$. The simulation results match well with the measurement results in terms of the shapes and sizes of the microstructures on the metallic surface, which validates the effectiveness and accuracy of this algorithm. Therefore, this algorithm is

reliable to accurately predict the surface topography and supports the process parameter selection under comprehensive consideration of the influences of the cutting conditions and tool geometry before producing the desired micro/nanostructures on the workpiece surface.

In Case 1, the cutting velocity along the X-axis of the ultraprecision lathe was 1000mm/min and the DoC was 2 μ m. For the sinusoidal voltage signals that drive 2DOF-VAUM system to generate the vibration trajectory, the amplitude, frequency, and phase difference between the two PEAs were set as 40V, 500Hz, and 30 $^\circ$, respectively. When completing one cutting motion along X-axis, the cutting tool returned to the initial point in the X-axis and then feeds 60 μ m along Y-axis. Finally, the micro-dimple arrays were machined on the copper alloy surface, as shown in Figure 3.15(a). Similarly, the surface with micro-ratchet arrays was generated for Case 2, as shown in Figure 3.15(b).

During machining the micro/nanostructures on the workpiece surfaces, the cutting parameters and tool geometry simultaneously determine the surface topography of the desired microstructures. The spacing d of the adjacent microstructures along the cutting direction can be determined by the ratio of the cutting speed V_c of the ultraprecision lathe over the working frequency f of the machining system. In the two experiments, the spacing d decreased from 32.3 μ m in Case 1 to 9.9 μ m in Case 2, which agrees well with the theoretical results according to $d = V_c/f$ (from 33.33 μ m to 10 μ m). The tool geometry, especially the clearance angle of the cutting tool, plays a crucial role in shaping the final surface topography of microstructures because of the interference between the flank face and the machined surface. The flank face of Case 2 interferes with the machined surface due to the small clearance angle of the cutting tool and the

Chapter 3 Design of the vibration-assisted ultraprecision machining system
 decrement of the spacing, as shown in Figure 3.15(b). Therefore, the effect of cutting conditions and tool geometry on the process should be carefully considered before machining the micro/nanostructures.

Furthermore, no burr was observed at the boundaries of microstructures, showing evidence of better surface quality. To quantitatively evaluate the surface quality of machined microstructures, three square areas ($8\mu\text{m} \times 8\mu\text{m}$) inside the microstructures were chosen from different regions for measuring the surface roughness (R_a) by using the atomic force microscopy technique, as shown in Figure 3.16.

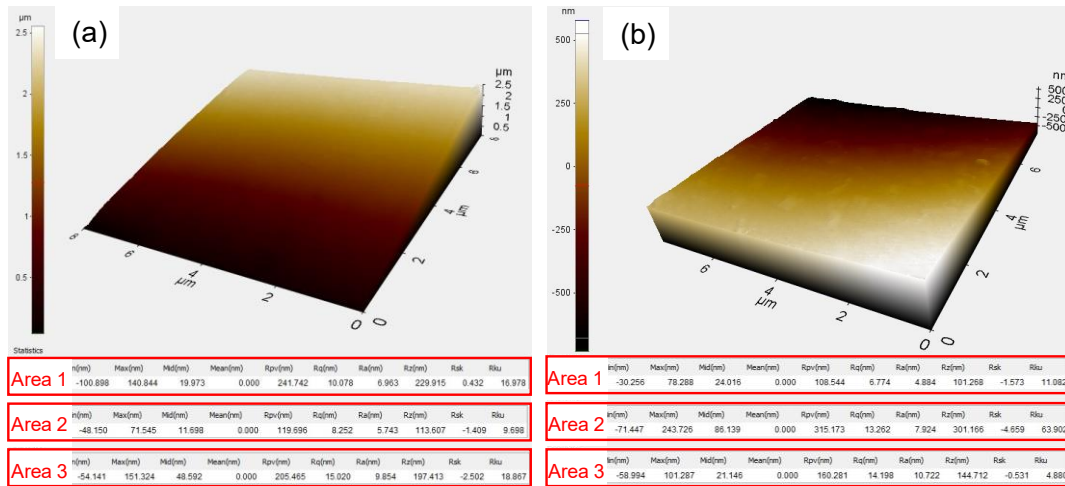


Figure 3.16 Surface roughness of Case 1 and (b) Case 2.

The measured average values of R_a were 7.52nm and 7.84nm for the Case 1 and the Case 2 respectively. The results indicate that a better surface finish can be achieved with the designed 2DOF-VAUM system. After experiments, there was no tool wear occurrence, which was observed by the SEM images of the tool tip. Therefore, this designed two-degree-of-freedom vibration-assisted ultraprecision machining system can contribute to the successful industrial application of micro/nanostructure generation.

3.7 Summary

In this chapter, a novel two-degree-of-freedom vibration-assisted ultraprecision machining (2DOF-VAUM) system is designed, and its hardware configuration is introduced. The systematic simulation, analysis, and verification work are conducted. The main conclusions are drawn as follows:

(1) Based on the proposed quasi-ellipse amplification unit, a 2DOF-VAUM system is designed for efficient and flexible machining of micro/nanostructures. This machining system can work at a frequency up to 3 kHz with a much lower coupling ratio (2.32% in the cutting direction and 4.86% in the DoC direction).

(2) The multi-physics FEM is proposed in detail to simulate the working performances of the 2DOF-VAUM system. The simulation results of the bandwidth and the coupling ratio (two quantitative indices of the working performances) are in good accordance with the measurement results, proving the effectiveness of this multi-physics FEM. It is a useful simulation approach not only useful in the area of ultraprecision machining but also in the area of micro/nano-positioning platform when simulating the working performances of the systems that use the PEAs as actuators.

(3) The proposed numerical simulation algorithm of micro/nanostructure generation on the metal surface not only considers the influence of the three-dimensional geometric shape of the cutting tool on the micro/nanostructure machining but also includes the effect of the elastic recovery of workpiece material. The experimental results validate the flexibility and accuracy of the proposed algorithm as the average geometrical error of this algorithm is less than $0.1\mu\text{m}$, which also shows that it captures the detailed surface topography and enables to provide the guidance in

Chapter 3 Design of the vibration-assisted ultraprecision machining system

the selection of the process parameters before machining the desired micro/nanostructures.

(4) The efficacy of the developed 2DOF-VAUM system is demonstrated by the generation of two kinds of microstructures (micro-dimple arrays and micro-ratchet arrays). Besides, the average value of surface roughness (R_a) inside the microstructures is smaller than 8nm, showing a better surface quality of the microstructures generated by the developed machining system.

Chapter 4 Practicable cutting force prediction model

4.1 Introduction

Cutting force is an important physical indicator for micro/nanostructure machining when using the developed 2DOF-VAUM system since it directly reflects the reaction between the cutting tool and workpiece (Chen et al., 2021), and it helps to understand the material removal mechanism, optimize the machining parameters, and improve machining conditions. Taking advantage of the rich information of the material properties, tool geometry, and machining parameters in the cutting force, the cutting force analysis fast develops (Srinivasa and Shunmugam, 2013). However, very few studies are reported on cutting force prediction during machining the micro/nanostructures on the metal surface.

In this chapter, a practicable cutting force prediction model with high accuracy is proposed based on the consideration of the periodical vibration motion, tool geometry, and material properties. Two unusual characteristics of the vibration-assisted ultraprecision machining process, i.e., the time-varying material removal behavior and controllable vibration trajectory, are illustrated. In the cutting force model, the instantaneous shear angle and cutting area are theoretically analyzed and the non-equidistant shear zone model is applied to evaluate the shear strain and shear strain rate inside the shear zone. Pure titanium TA2, as a typical difficult-to-material, is selected as the workpiece material. And it is widely applied in aerospace and medical fields. And two kinds of microstructures are machined to validate the effectiveness of the proposed cutting force model.

4.2 Characteristics of the vibration-assisted ultraprecision machining

In the vibration-assisted ultraprecision machining, the periodic vibration trajectory is added to the cutting tool. Combining with a cutting motion that the ultraprecision lathe provides, a specific cutting trajectory can be formed. The cutting tool removes the material along this cutting trajectory to generate the micro/nanostructures on the workpiece surface. In this section, the time-varying material removal behavior and controllable vibration trajectory, as two unique characteristics of the vibration-assisted ultraprecision machining process, are systematically investigated and explained.

4.2.1 Time-varying material removal behavior

In conventional machining, the cutting motion keeps unchanged since there is no additional motion to be imposed into the cutting tool. For the vibration-assisted ultraprecision machining process, the cutting motion continuously varies, including the time-varying depth-of-cutting and the time-varying cutting direction, since the cutting tool vibrates continuously on the workpiece surface. The time-varying characteristics of the vibration-assisted ultraprecision machining process result in the more complicated material removal behavior and time-varying cutting force. In order to have a deeper understanding of the differences between the conventional machining and vibration-assisted ultraprecision machining process, the multi-physics finite element method is utilized by using the explicit module of the commercial analysis software Abaqus 6.14. The diamond cutting tool is considered a rigid body. The resulting von Mises stress distribution in the cutting zone is demonstrated in Figure 4.1 with evenly

captured frames (0.06ms). An angle $\phi_0(t)$ between the horizontal and the shear plane is a core parameter governing the shearing based material removal behavior (Z. Zhu et al., 2019a). The results about the angle $\phi_0(t)$ by manually measuring via the software ImageJ are also shown in Figure 4.1. The $\phi_0(t)$ keeps constant in the conventional machining, around 33° , while this angle varies with time in vibration-assisted ultraprecision machining process. It firstly decreases from 38.39° at 3.36ms to 31.54° at 3.66ms and then increases to 35.11° at 3.78ms. In essence, the vibration of the cutting tool leads to the shear plane variation and induces the time-varying material removal behavior, which is totally different from conventional machining.

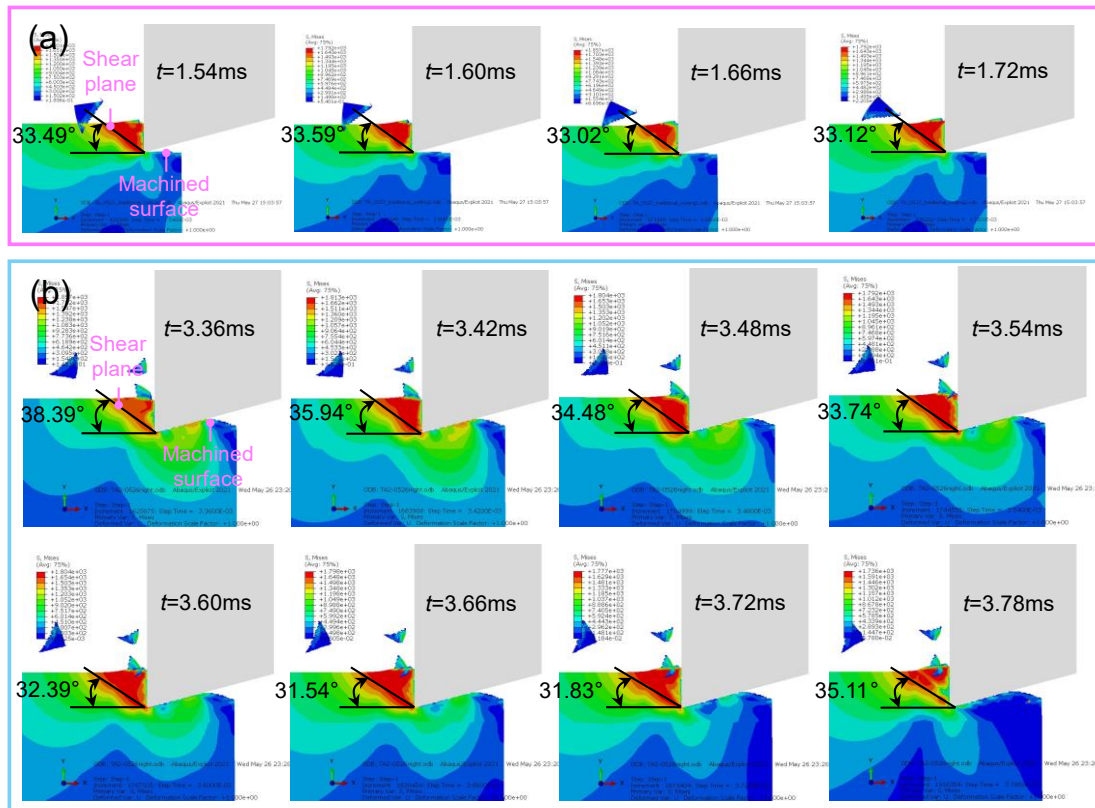


Figure 4.1 Simulation results of the finite element method about instantaneous $\phi_0(t)$. (a) Conventional machining and (b) vibration-assisted ultraprecision machining. The $\phi_0(t)$ is an angle between the horizontal and the shear plane.

4.2.2 Controllable vibration trajectory

Ultrasonic vibration-assisted machining is also to impose the vibration motion into the cutting tool to machine the difficult-to-machine material. Although the ultrasonic vibration-assisted machining has many benefits, such as lower machining forces (Shamoto and Moriwaki, 1999), less tool wear (Zhou et al., 2006), burr suppression (Ma et al., 2005), and better surface finish (Sui et al., 2017), it only works at a fixed ultrasonic frequency with the small amplitudes. It is because the ultrasonic vibration-assisted machining works in the resonant frequency of the mechanical structure, i.e., the resonant frequency of the transducer. In addition, its vibration trajectory, which is elliptical, cannot be adjusted. These inherent drawbacks lead to the fact that it loses the flexibility of generating the micro/nanostructures on the metallic surface. In contrast, the vibration-assisted ultraprecision machining process has the flexible working frequency and amplitude, which endues it with the excellent capability of machining the micro/nanostructures on the metallic surface with higher machining efficiency (Zhichao Yang et al., 2020) and lower surface roughness (Du et al., 2021b). The schematic diagrams of their working principle are shown in Figure 4.2.

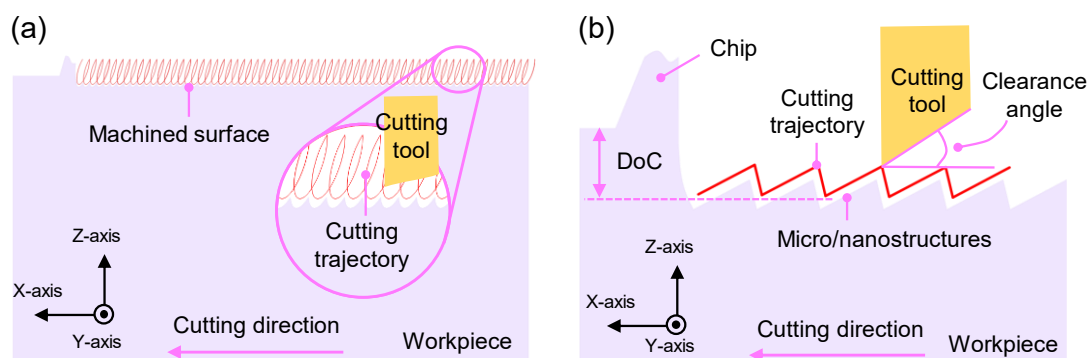


Figure 4.2 Schematic diagrams of the working principle. (a) Ultrasonic vibration-assisted machining and (b) vibration-assisted ultraprecision machining.

In the ultrasonic vibration-assisted machining process, the time-varying trajectory $(x_{UVAM}(t), z_{UVAM}(t))$ of the cutting tool with respect to the workpiece in Cartesian coordinate system can be given as:

$$x_{UVAM}(t) = a_{UVAM} \cos(2\pi f_{UVAM}t + \varphi_{UVAM}) + V_{UVAM}t \quad (4.1)$$

$$z_{UVAM}(t) = b_{UVAM} \sin(2\pi f_{UVAM}t) \quad (4.2)$$

where a_{UVAM} and b_{UVAM} are the vibration amplitudes along the cutting direction and depth-of-cutting direction, respectively. f_{UVAM} is the ultrasonic vibration frequency. φ_{UVAM} is the phase difference between the vibration trajectories. V_{UVAM} is the nominal cutting velocity of the ultrasonic vibration-assisted machining.

Another limitation in ultrasonic vibration-assisted machining is that the cutting velocity of the cutting tool must be far larger than the maximum vibration velocity along the cutting direction.

$$V_{UVAM} \gg 2\pi f_{UVAM}a_{UVAM} \quad (4.3)$$

Without loss of generality, the flexible vibration trajectory $(x_{VAUM}(t), z_{VAUM}(t))$ of the cutting tool in VAUM process can be given as:

$$x_{VAUM}(t) = f_{VAUM}^x(t) + V_{VAUM}t \quad (4.4)$$

$$z_{VAUM}(t) = f_{VAUM}^z(t) \quad (4.5)$$

where $f_{VAUM}^x(t)$ and $f_{VAUM}^z(t)$ are the displacement-time functions of the vibration trajectory along the cutting direction and depth-of-cutting direction, respectively. V_{VAUM} is the nominal cutting velocity.

In VAUM, the arbitrary $f_{VAUM}^x(t)$ and $f_{VAUM}^z(t)$ can be expressed by the superposition of several sinusoidal functions according to Fourier expansion, such as triangle vibration trajectory and quadrature vibration trajectory, not limited to the elliptical vibration trajectory. Combined with the nominal cutting velocity V_{VAUM} that

the 2DOF-VAUM system provides, the cutting trajectory $(x_{VAUM}(t), z_{VAUM}(t))$ described in Figure 4.2(b) can be flexibly designed for machining the desired micro/nanostructures on workpiece surfaces. The cutting velocities relative to the workpiece along the cutting direction and depth-of-cutting direction is also derived as:

$$v_{VAUM}^x(t) = \frac{d(x_{VAUM}(t))}{dt} = (f_{VAUM}^x(t))' + V_{VAUM} \quad (4.6)$$

$$v_{VAUM}^z(t) = \frac{d(z_{VAUM}(t))}{dt} = (f_{VAUM}^z(t))' \quad (4.7)$$

The angle $\omega(t)$ between the resultant cutting velocity and the horizontal direction is an indicator of the cutting state. When $\omega(t) < 0$, it means the cutting tool moves downhill, while the cutting tool moves uphill when $\omega(t) > 0$. When $\omega(t) = 0$, the cutting tool reaches the bottom or top of the cutting trajectory.

$$\omega(t) = \arctan\left(\frac{v_{VAUM}^z(t)}{v_{VAUM}^x(t)}\right) \quad (4.8)$$

In order to have a flexible vibration trajectory with the adjustable working frequency and vibration amplitudes, a two-degree-of-freedom vibration-assisted ultraprecision machining (2DOF-VAUM) system is developed, as shown in Figure 4.3. The detailed working principle is introduced in Chapter 3. The elliptical shape of the QEAU can efficiently avoid the fatigue failure of the mechanical structures when it vibrates several hundred times per second or even thousands of times per second. Besides, compared with compound bridge-type, the thickness of flexure hinge is more than sub-millimeter scale, which brings two benefits: (a) making the mechanical structure of the 2DOF-VAUM system more easily to be machined via the wire electrical discharge machining technology; (b) improving the output stiffness of the 2DOF-VAUM system.

The amplification ratio of this designed 2DOF-VAUM system is calculated by the triangular amplification principle. Assuming the angle ϑ shown in Figure 4.3(b) decreases to $(\vartheta - \Delta\vartheta)$ when the piezoelectric actuators provide push forces, the amplification ratio λ can be expressed according to the geometrical relationship between the input displacement and output displacement:

$$\lambda = \lim_{\Delta\vartheta \rightarrow 0} \frac{\sin \vartheta - \sin(\vartheta - \Delta\vartheta)}{\cos(\vartheta - \Delta\vartheta) - \cos \vartheta} = \cot \vartheta \quad (4.9)$$

The analytical result of the amplification ratio λ is computed to be 2.34. The relative error for the analysis value with respect to the FEM result (2.38) can be derived as 1.68%, which shows the theoretical analysis for the amplification ratio λ of the 2DOF-VAUM system has a much higher accuracy.

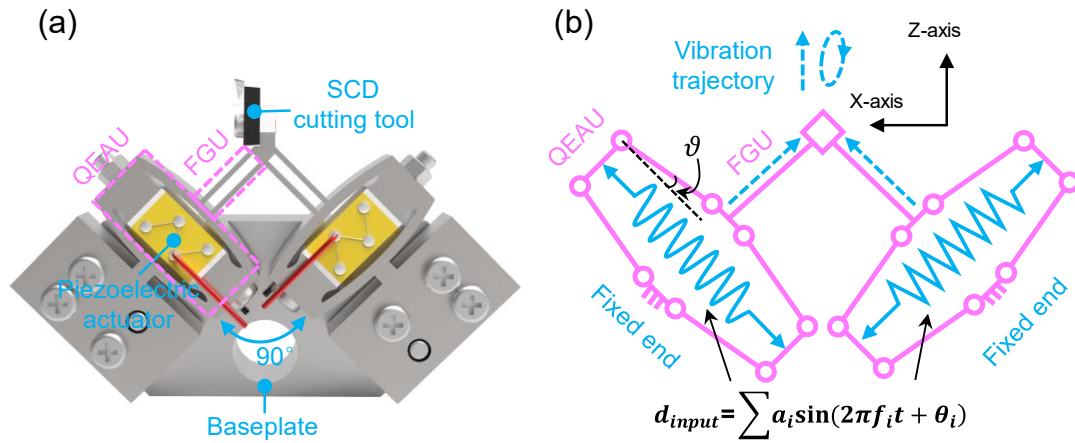


Figure 4.3 The three-dimensional mechanical structure and kinematic diagram of the designed two-degree-of-freedom vibration-assisted ultraprecision machining system. Labels QEAU and FGU denote quasi-ellipse amplification unit and flexure guidance unit.

In Chapter 3, the relationship between the input voltage signal and the output vibration trajectory is established but it ignores the influence of the coupling ratio. Considering the influence of the coupling ratio, this relationship can be expressed as:

$$\begin{bmatrix} f_{UDST}^x(t) \\ f_{UDST}^z(t) \end{bmatrix} = \begin{bmatrix} C_x^1 & C_x^2 \\ C_z^1 & C_z^2 \end{bmatrix} \begin{bmatrix} V_l(t) \\ V_r(t) \end{bmatrix} \quad (4.10)$$

where C_x^1 , C_x^2 , C_z^1 , and C_z^2 are the transformation coefficients. $V_l(t)$ and $V_r(t)$ are the input voltage signals for the left piezoelectric actuator and right piezoelectric actuator, respectively.

According to the test results from Figure 3.14, transformation coefficients can be computed as $0.0447\mu\text{m}/\text{V}$, $0.0416\mu\text{m}/\text{V}$, $0.0318\mu\text{m}/\text{V}$, and $-0.0298\mu\text{m}/\text{V}$, respectively. The input voltage signals in the vibration-assisted ultraprecision machining can be determined according to the desired time-varying displacements $f_{VAUM}^x(t)$ and $f_{VAUM}^z(t)$.

4.3 The cutting force prediction modeling

Some assumptions before establishing the practicable cutting force model are made:

(a) The cutting edge of the single-crystal diamond cutting tool is perfectly sharp (Molnar et al., 2019), which is validated by the atomic force microscopy (AFM) of the cutting edge, as shown in Figure 4.4. The radius of the cutting edge utilized in this study is $\sim 80\text{nm}$. The radius is two orders of magnitude smaller than the depth-of-cutting, so the influence of the cutting edge can be ignored.

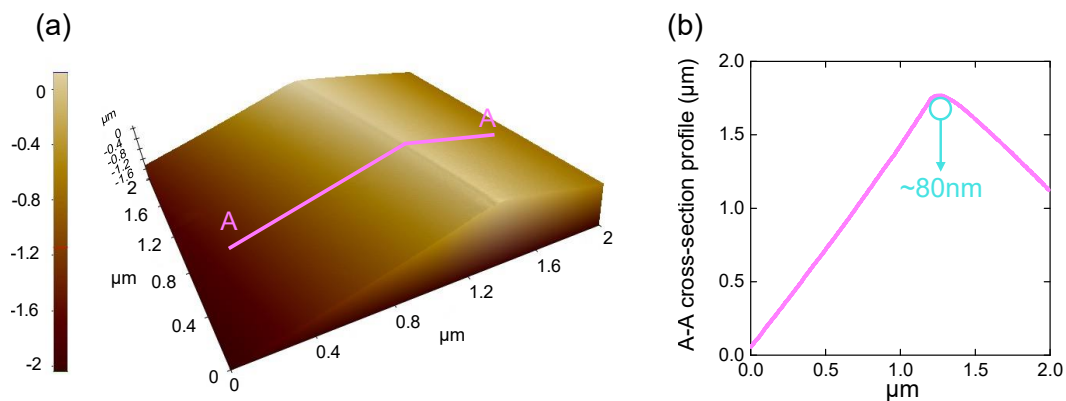


Figure 4.4 The cutting edge of the cutting tool. (a) AFM three-dimensional image and (b) A-A cross-section profile plot.

(b) The cutting tool is considered as a rigid body and the workpiece material is assumed to be homogeneous and isotropic (Moufki et al., 2006).

(c) The material removal satisfies the plasticity theory (Z. Zhu et al., 2019a).

The overall flowchart of this cutting force prediction model is illustrated in Figure 4.5. Firstly, the instantaneous shear angle is quantitatively analyzed. Next, the non-equidistant shear zone model is chosen to evaluate the shear strain rate and the shear strain in the shear zone. Then, the instantaneous cutting area is theoretically analyzed according to the cutting trajectory. The instantaneous shear forces in the main shear plane will be calculated based on the shear stress and cutting area through the Matlab program. Finally, the cutting forces along the cutting direction (F_x) and depth-of-cutting (F_z) are obtained according to the vector relationship of these forces with the shear force.

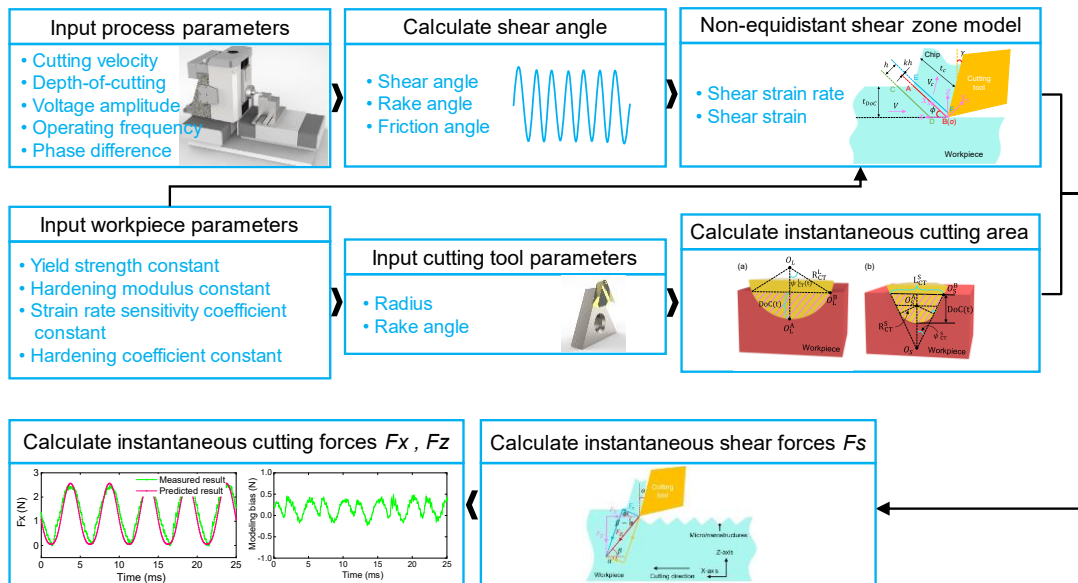


Figure 4.5 Flowchart of the cutting force prediction modeling in vibration-assisted ultraprecision machining.

4.3.1 Instantaneous shear angle

In vibration-assisted ultraprecision machining, the shear angle is the relative angle between the main shear plain and the cutting velocity direction. As the cutting direction periodically changes with time caused by the vibration of the cutting tool, the shear angle varies. The instantaneous shear angle can be expressed by (Z. Zhu et al., 2019a):

$$\phi(t) = \phi_0(t) + \phi_{VAUM}(t) \quad (4.11)$$

where $\phi_{VAUM}(t)$ is the angle that relates to the cutting velocity direction.

The $\phi_0(t)$ can be expressed by:

$$\phi_0(t) = \arctan\left(\frac{\xi_1 \cos \alpha_0}{1 - \xi_1 \cos \alpha_0}\right) + \arctan\left(\frac{\xi_2 \cos \alpha_{VAUM}(t)}{1 - \xi_2 \cos \alpha_{VAUM}(t)}\right) \quad (4.12)$$

where ξ_1 and ξ_2 are the equivalent ratios. In this study, ξ_1 and ξ_2 are set as 0.15. α_0 is the nominal rake angle of the cutting tool. And the α_{VAUM} is the variation of the rake angle induced by the vibration motion of the cutting tool, which can be obtained as:

$$\alpha_{VAUM}(t) = \omega(t) = \arctan\left(\frac{v_{VAUM}^z(t)}{v_{VAUM}^x(t)}\right) \quad (4.13)$$

In terms of $\phi_{VAUM}(t)$, it equals $\alpha_{VAUM}(t)$ (Z. Zhu et al., 2019a).

In addition, the practical rake angle is the angle between the rake face and the reference plane perpendicular to the cutting velocity, so it can be expressed as:

$$\alpha(t) = \alpha_0 + \alpha_{VAUM}(t) \quad (4.14)$$

4.3.2 Non-equidistant shear zone model

In vibration-assisted ultraprecision machining, the shear zone modeling of a workpiece is challenging and plays a crucial role in the cutting force prediction. The non-equidistant shear zone model with a thickness of h has been widely proved and

employed (Tounsi et al., 2002)(Astakhov et al., 2001). In this model, the entry shear plane CD and the exit shear plane EF are parallel but no-equidistant to the main shear plane AB, as shown in Figure 4.6. The shear band can be divided into two thicknesses: kh and $(1 - k)h$, while $k \in [0,1]$.

Two coordinate systems $\{o, x, z\}$ and $\{o, x_s, z_s\}$ are established. The x -axis and z -axis are the same in the cutting direction and depth-of-cutting direction. As shown in Figure 4.6, the directions of the x_s -axis and z_s -axis are parallel and perpendicular to the main shear plane AB, respectively. The values of shear strain rate, shear strain, and shear velocity inside the shear zone are calculated according to the coordinate of the z_s axis.

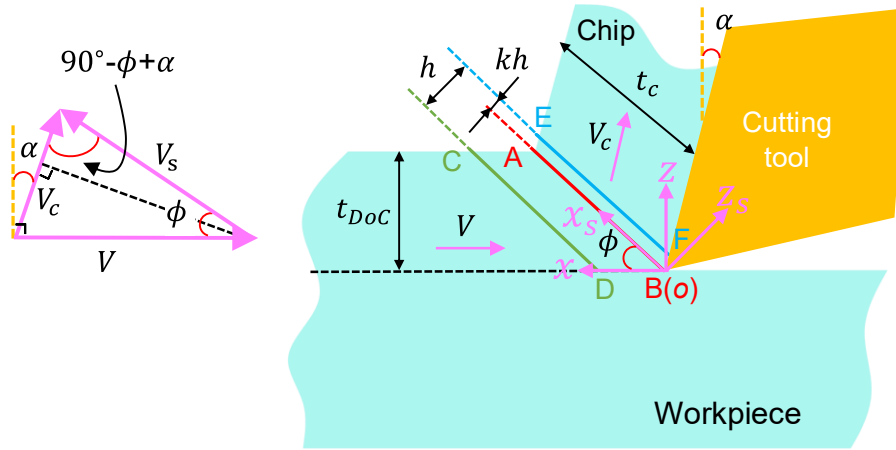


Figure 4.6 Schematic diagram of the non-equidistant shear zone model.

A piecewise power-law-distribution function is adopted to express the shear strain rate as follow (Bai et al., 2017):

$$\dot{\gamma} = \begin{cases} \frac{\dot{\gamma}_m}{[(1-\kappa)h]^q} [z_s + (1 - \kappa)h]^q & z_s \in [-(1 - \kappa)h, 0] \\ \frac{\dot{\gamma}_m}{(\kappa h)^q} (\kappa h - z_s)^q & z_s \in [0, \kappa h] \end{cases} \quad (4.15)$$

where $\dot{\gamma}_m$ represents the maximum shear strain rate in AB. q represents the non-uniform power law distribution of the tangential velocity in the primary shear zone. q equals 3

in this study as the cutting velocity is low (Bai et al., 2016). h represents the thickness of shear, which is evaluated from (Bai et al., 2017).

$$h = \frac{t_{DoC}}{10 \sin \phi} \quad (4.16)$$

where t_{DoC} and ϕ represent the depth-of-cutting and shear angle. The average value of $z_{VAUM}(t)$ and $\phi(t)$ in a vibration period $(0, T)$ are employed for improving the calculation efficiency.

$$t_{DoC} = \frac{1}{T} \int_0^T z_{VAUM}(t) dt \quad (4.17)$$

$$\phi = \frac{1}{T} \int_0^T \phi(t) dt \quad (4.18)$$

According to the relationship between the shear strain and the cutting velocity, the shear strain also can be expressed as follow:

$$\gamma = \begin{cases} \frac{\dot{\gamma}_m [z_s + (1-\kappa)h]^{q+1}}{V(q+1)[(1-\kappa)h]^q \sin \phi} & z_s \in [-(1-\kappa)h, 0] \\ -\frac{\dot{\gamma}_m (\kappa h - z_s)^{q+1}}{V(q+1)(\kappa h)^q \sin \phi} + \frac{\cos \alpha}{\sin \phi \cos(\phi - \alpha)} & z_s \in [0, \kappa h] \end{cases} \quad (4.19)$$

where V represents the cutting velocity. α represents the average rake angle of the cutting tool during machining.

$$V = \frac{1}{T} \int_0^T \sqrt{[v_{VAUM}^x(t)]^2 + [v_{VAUM}^z(t)]^2} dt \quad (4.20)$$

$$\alpha = \frac{1}{T} \int_0^T \alpha(t) dt \quad (4.21)$$

The shear velocity in the x_s -axis direction (v_{x_s}) and z_s -axis direction (v_{z_s}) can be obtained from the reference (Fu et al., 2014):

$$v_{x_s} = \begin{cases} \frac{\dot{\gamma}_m [z_s + (1-\kappa)h]^{q+1}}{(q+1)[(1-\kappa)h]^q} - V \cos \phi & z_s \in [-(1-\kappa)h, 0] \\ -\frac{\dot{\gamma}_m (\kappa h - z_s)^{q+1}}{(q+1)(\kappa h)^q} + V \sin \phi \tan(\phi - \alpha) & z_s \in [0, \kappa h] \end{cases} \quad (4.22)$$

$$v_{z_s} = V \sin \phi \quad z_s \in [-(1-\kappa)h, \kappa h] \quad (4.23)$$

Since the direction of shear velocity v_{x_s} in the entry shear plane CD and the exit shear plane EF is opposite, the shear velocity v_{x_s} in the main shear plane is assumed to be zero (Moufki et al., 2006). Therefore, the maximum shear strain rate $\dot{\gamma}_m$ and the proportion coefficient k can be solved:

$$\dot{\gamma}_m = \frac{(q+1)V\cos\alpha}{h\cos(\phi-\alpha)} \quad (4.24)$$

$$\kappa = \frac{\sin\phi\sin(\phi-\alpha)}{\cos\alpha} \quad (4.25)$$

In the hodograph, V , V_c , and V_s are the resultant cutting velocity, the chip velocity, and the shear velocity, respectively. And they constitute a vector triangle. Their vector relationship is illustrated in Figure 4.6.

In the non-equidistant shear zone, the constitutive model that describes the physical properties of the workpiece material should be established. Some material models have been proposed, such as the Johnson-cook model (JOHNSON and R., 1983), Oxley model (Oxley and Shaw, 1990), Maekawa et al. model (Maekawa et al., 1983), and Zerilli-Armstrong model (Zerilli and Armstrong, 1987). Nowadays, the Johnson-cook model is commonly implemented in cutting force modeling due to its simplicity and accuracy (Fernandez-Zelaia and Melkote, 2019). The shear stress τ can be expressed herein using Johnson-cook constitutive model as follows (Moufki et al., 2006):

$$\tau = \frac{1}{\sqrt{3}} [A + B(\frac{\gamma}{\sqrt{3}})^n] \left[1 + C \ln \left(\frac{\dot{\gamma}}{\dot{\gamma}_0} \right) \right] \left[1 - \left(\frac{T_s - T_0}{T_m - T_0} \right)^m \right] \quad (4.26)$$

where A , B , C , n , and m are the yield strength constant, hardening modulus constant, strain rate sensitivity coefficient constant, hardening coefficient constant, and thermal softening coefficient, respectively. $\dot{\gamma}_0$ is the reference shear strain rate and it is set as 1.0 s^{-1} in this study. T_s , T_0 , and T_m are the absolute temperature, room temperature, and melting temperature of the workpiece, respectively. In the Johnson-cook constitutive

model, the first bracketed term represents the effect of the strain hardening. The second bracketed term represents the effect of the strain rate. The third bracketed term represents the effect of thermal softening. Since the vibration-assisted ultraprecision machining is an intermittent and low-speed cutting process and a high-pressure oil mist is applied at the tool-workpiece interface to remove cutting heat, the effect of temperature is ignored in this study. For the pure titanium TA2, the other material constants are given in the reference (Tan and Xie, 2015): $A=830\text{Mpa}$, $B=1100\text{Mpa}$, $C=0.015$, and $n=0.15$. The shear strain rate $\dot{\gamma}$ and the shear strain γ can be calculated based on Eqs. (4.15)-(4.25).

4.3.3 Instantaneous cutting area

The instantaneous cutting area between the rake face and the workpiece is another important factor for the cutting force prediction model in the vibration-assisted ultraprecision machining on the TA2 surface. Different radius sizes of the cutting tool have different influences on the instantaneous cutting area, which can be categorized as two kinds according to the relative relationship between the radius of the cutting tool and the maximal depth-of-cutting.

If the radius of the cutting tool is much larger than the maximum value of the instantaneous depth-of-cutting, as shown in Figure 4.7(a), the instantaneous cutting area can be expressed using Eq. (4.27). In this case, the part arc of the cutting edge enters the workpiece.

$$A_{CA}^L(t) = (R_{CT}^L)^2 \psi_{CT}^L(t) - [R_{CT}^L - \text{DoC}(t)] \sqrt{2R_{CT}^L \text{DoC}(t) - [\text{DoC}(t)]^2} \quad (4.27)$$

where $\text{DoC}(t)$ is instantaneous depth-of-cutting that equals the difference between the nominal depth-of-cutting DoC_N and the $f_{V\text{AUM}}^z(t)$. R_{CT}^L is the radius of the cutting tool

in this condition. $\psi_{CT}^L(t)$ is the included angle between $O_L O_L^A$ and $O_L O_L^B$, as shown in Figure 4.7(a). The $\psi_{CT}^L(t)$ can be expressed as Eq. (4.29) according to the geometrical relationship between the cutting tool and the workpiece.

$$\text{DoC}(t) = \text{DoC}_N - f_{V_{AUM}}^z(t) \quad (4.28)$$

$$\psi_{CT}^L(t) = \cos^{-1} \left[\frac{R_{CT}^L - \text{DoC}(t)}{R_{CT}^L} \right] \quad (4.29)$$

If the radius of the cutting tool is much smaller than the maximum value of the instantaneous depth-of-cutting $\text{DoC}(t)$, as shown in Figure 4.7(b), the instantaneous cutting area can be expressed using Eqs. (30)-(33). In this case, the nose of the cutting tool is very small, the whole arc of the cutting edge enters the workpiece.

$$A_{CA}^S(t) = A_{CA}^1(t) + A_{CA}^2(t) + A_{CA}^3(t) \quad (4.30)$$

$$A_{CA}^1(t) = \frac{1}{2} [\text{DoC}(t) - R_{CT}^S] \left[L_{CT}^S + \frac{2R_{CT}^S}{\cos(\psi_{CT}^S)} \right] \quad (4.31)$$

$$A_{CA}^2(t) = 2 \times \frac{1}{2} \times R_{CT}^S \times [R_{CT}^S \times \tan(\psi_{CT}^S)] = (R_{CT}^S)^2 \tan(\psi_{CT}^S) \quad (4.32)$$

$$A_{CA}^3(t) = \frac{1}{2} \times 2 \times \left(\frac{\pi}{2} - \psi_{CT}^S \right) \times (R_{CT}^S)^2 = \left(\frac{\pi}{2} - \psi_{CT}^S \right) (R_{CT}^S)^2 \quad (4.33)$$

where $A_{CA}^1(t)$, $A_{CA}^2(t)$, and $A_{CA}^3(t)$ are the areas of three regions. R_{CT}^S is the radius of the cutting tool. $L_{CT}^S(t)$ is the maximal contact width between the cutting tool and the workpiece. ψ_{CT}^S is the included angle between $O_S O_S^A$ and $O_S O_S^B$, which can be calculated according to Eq. (4.34).

$$L_{CT}^S(t) = 2 \left\{ \frac{R_{CT}^S}{\cos(\psi_{CT}^S)} + [\text{DoC}(t) - R_{CT}^S] \tan(\psi_{CT}^S) \right\} \quad (4.34)$$

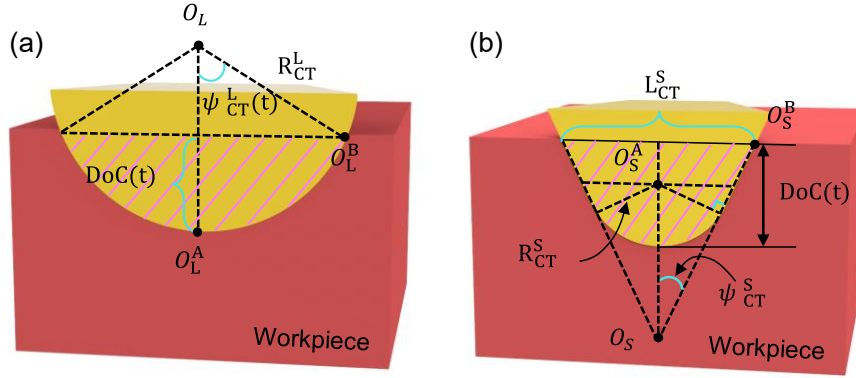


Figure 4.7 Schematic diagram of the instantaneous cutting area. (a) The radius of the cutting tool is larger than the maximum of the instantaneous depth-of-cutting and (b) the radius of the cutting tool is smaller than the maximum of the instantaneous depth-of-cutting.

4.3.4 Instantaneous cutting force

The cutting force highly depends on the volume of the material removal. The more the material removal, the larger the cutting force. The volume of the material removal depends on the instantaneous cutting area on the rake face. When the cutting tool gradually inserts into the workpiece, the instantaneous cutting force increase. The maximum cutting force occurs when the cutting tool reaches the valley of the cutting trajectory. When the cutting tool leaves the workpiece along the cutting trajectory, the instantaneous cutting force reduces.

As the vibration-assisted ultraprecision machining is an orthogonal cutting, the shear force F_s is proportional to the shear stress τ and instantaneous cutting area $A_{CA}^{L/S}(t)$ on the main shear plane. Therefore, the shear force F_s can be determined according to the Merchant's circle force diagram (Jieqiong et al., 2016; Zhao et al., 2020).

$$F_s = \frac{\bar{\tau} A_{CA}^{L/S}(t)}{\sin\phi} \quad (4.35)$$

where $\bar{\tau}$ is the average shear stress and can be expressed as:

$$\bar{\tau} = \frac{1}{h} \int_0^h \tau dz_s \quad (4.36)$$

The cutting forces in the cutting direction F_x and in the depth-of-cutting direction F_z are derived based on the vector relationship in Figure 4.8.

$$F_x = \frac{F_s \cos(\beta - \alpha)}{\cos(\phi + \beta - \alpha)} \quad (4.37)$$

$$F_z = \frac{F_s \sin(\beta - \alpha)}{\cos(\phi + \beta - \alpha)} \quad (4.38)$$

where β is the average friction angle and can be calculated by using the Merchant's formula (Zhang et al., 2020).

$$\beta = \frac{\pi}{2} + \alpha - 2\phi \quad (4.39)$$

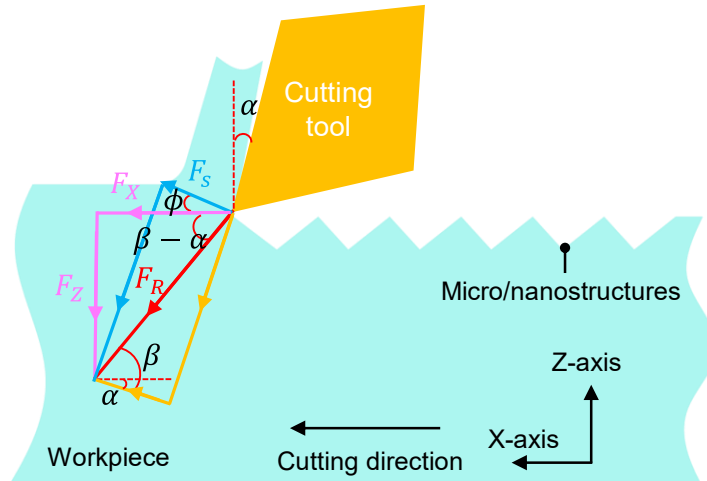


Figure 4.8 Cutting force diagram of orthogonal vibration-assisted ultraprecision machining.

4.4 Experimental details

The machining experiments were performed on a four-axis ultraprecision lathe (350FG, Moore Nanotechnology, America). The alpha-type commercial pure titanium TA2 rod with a purity of 99.2% (Keple Technology Co., Ltd., China) was fixed into a fixture mounted on the spindle through the vacuum chuck, as shown in Figure 4.9. The

properties of TA2 are listed in Table 4.1. The workpiece was firstly flatted with a spindle speed of 1500rpm, the DoC_N of $2\mu\text{m}$, and the feedrate of 4 mm/min, respectively. In this pre-machining, the nose radius, clearance angle, and rake angle of the diamond cutting tool (0.5mm RAD ROUGHER, Apex Diamond Products Ltd.) are 0.515mm, 10° , and 0° , respectively. In micro/nanostructure machining, the developed 2DOF-VAUM system was stationed on the dynamometer (9256C1, Kistler Instrument Corp.) via a screw. A natural single-crystal diamond cutting tool (N0.50mLEi, Contour Fine Tooling Inc.) with a round edge was selected for machining the microstructures on the TA2 surface. Its nose radius, clearance angle, and rake angle are 0.492mm, 15° , and 0° , respectively. The computer generated digital signals, which were then converted into analog signals by the multifunction I/O device (USB-6341, National Instruments Corp.) and they were magnified by the piezo amplifiers (E617.001, Physik Instrumente GmbH & Co.KG) to drive the 2DOF-VAUM system, as shown in Figure 4.9. The cutting forces along the X-axis and Z-axis in VAUM would be measured through the dynamometer (Kistler 9256C1), the charge amplifier (Kistler multichannel charge amplifier 5080), and PC software (Dyno ware). And the sampling ratio for the cutting force measurement was set as 20kHz. A high-pressure oil mist was employed at the tool-workpiece interface via a fine nozzle for dissipating the cutting heat and removing the chips. Two samples were machined with unique microstructures. They are named Case 1 and Case 2 and the detailed process parameters for the two cases are tabulated in Table 4.2.

After machining, the workpiece was cleaned in an ultrasonic cleaner with alcohol at room temperature for 5min. A white light interferometer with sub-nanometre resolution (NexviewTM, Zygo Corp.) was employed to characterize the three-

Chapter 4 Practicable cutting force prediction model

dimensional surface topography of the machined microstructures. The scanning electron microscope (SEM) (Tescan VEGA3) equipped with energy-dispersive X-ray spectroscopy (EDX) detector was utilized for identifying the chemical elements on the single-crystal diamond cutting tool surface after experiments.

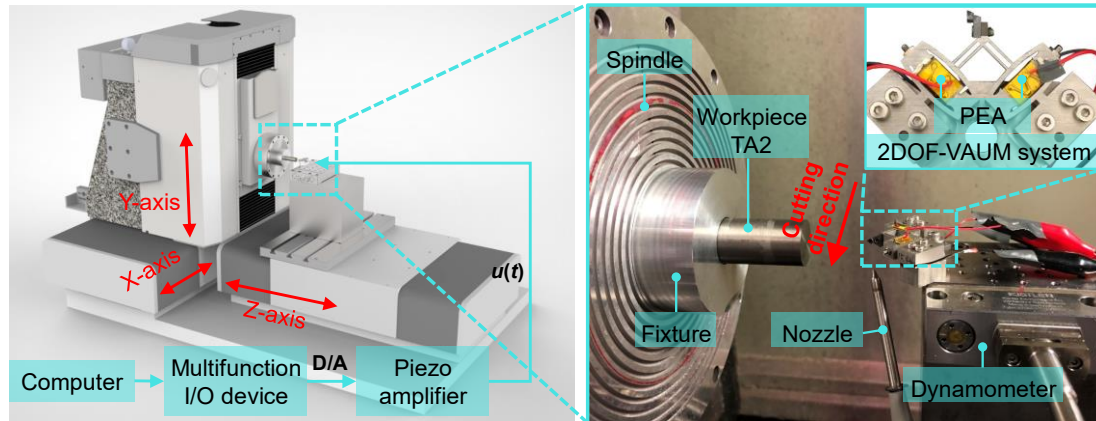


Figure 4.9 Experimental setup of the vibration-assisted ultraprecision machining.

Table 4.1 The properties of the commercially pure titanium TA2.

Chemical composition (Weight, %)				Mechanical properties	
Ti	>99.20	H	0.0015	Density (Kg/m ³)	4500
Fe	<0.075	O	0.1	Elastic modulus (Mpa)	107.8×10 ³
C	<0.08	others	0.5	Poisson' ratio	0.33
N	0.03				

Table 4.2 The experimental process parameters.

Cutting parameters	Case 1	Case 2
DoC _N	4 μm	4 μm
Nominal cutting velocity	600 mm/min	600 mm/min
Cross-feed	170 μm	170 μm
Voltage amplitude	40V	40V
Working frequency	200Hz	200Hz
Phase difference	0°	180°

4.5 Results and discussion

4.5.1 Surface topography characterization

After experiments, the surface topography of the microstructures of Case 1 and Case 2 are successfully obtained on the TA2 surface, as shown in Figure 4.10. In Case 1, the cutting velocity along the X-axis of the ultraprecision lathe is 600mm/min and the nominal depth-of-cutting is 4 μ m. The sinusoidal voltage signals are selected to drive the in-house developed 2DOF-VAUM system for providing the vibration trajectory in the machining plane. Their amplitude, frequency, and phase difference between the two piezoelectric actuators are set to be 40V, 200Hz, and 0 $^\circ$, respectively. The periodic straight-line vibration motion along the depth-of-cutting direction is generated and offered to the cutting tool. When completing one cutting motion along the X-axis direction, the cutting tool returns to the initial point in the X-axis of the ultraprecision lathe and then feeds 170 μ m along the cross-feed direction (Y-axis direction). Finally, the shuttle-shaped microstructures were machined on the difficult-to-machining material TA2 surface, as shown in Figure 4.10(a) and (c). The spacing d_1 along the cutting direction is 50.21 μ m, which has a close agreement with the theoretical value (50 μ m) according to $d_1 = V_{VAUM}/f$. f represent the working frequency of the vibration-assisted ultraprecision machining system.

Similarly, the phase difference of 180 $^\circ$ was used to offer the vibration motion along the cutting direction for machining the bamboo-shaped microstructures. The spacing d_2 along the cutting direction is 49.73 μ m, which also coincides with the theoretical value (50 μ m). The two unique microstructures are successfully machined on the TA2

surface, which demonstrates that the developed two-degree-of-freedom vibration-assisted ultraprecision machining has the capability of machining microstructures on the difficult-to-machining material.

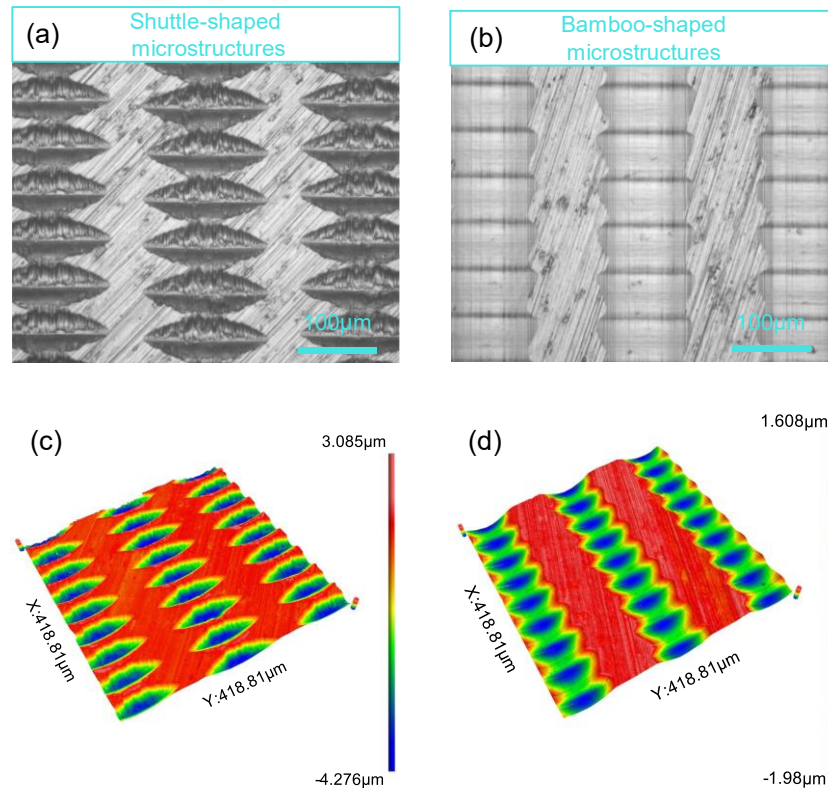


Figure 4.10 Optical images and surface topographies. (a) Optical image of Case 1, (b) optical image of Case 2, (c) surface topography of Case 1, and (d) surface topography of Case 2.

4.5.2 Cutting forces verification

To verify the developed cutting force prediction model, the cutting forces along the cutting direction (F_x) and the depth-of-cutting direction (F_z) for Case 1 and Case 2 are captured and shown in Figure 4.11 and Figure 4.12. The predicted cutting forces are obtained by inputting the identical process parameters into the prediction model using Matlab code.

As for Case 1 that generates shuttle-shaped microstructures, the measured results and predicted results of F_x and F_z are plotted in Figure 4.11(a) and (b). It can be clearly

observed that the predicted cutting forces and the measured results show good accordance with each other. The cutting forces periodically change following the cutting trajectory. The cutting forces gradually go up with the increase of the instantaneous depth-of-cutting and then reach the maximum value at the bottom of the microstructures. After that, the cutting forces decrease steadily with the decrease of the instantaneous depth-of-cutting. This unique phenomenon from the vibration-assisted ultraprecision machining is completely different from the conventional machining process in which the cutting forces keep unchanged. The measured peak-to-valley values of F_x and F_z in Case 1 are 2.39N and 2.68N and the predicted peak-to-valley values of that are 2.51N and 2.81N, so the modeling errors of F_x and F_z in Case 1 are 5.02% and 4.85%, respectively, which shows that the prediction results by the model coincide well with the measured ones. The modeling bias is another indicator that can describe the deviation of the prediction model from the measured results. The modeling biases of F_x and F_z in Case 1 are plotted in Figure 4.11(c) and (d). The average modeling bias $\bar{\sigma}$ is calculated according to Eq.(4.40). The modeling biases $\bar{\sigma}_1$ of F_x and F_z in Case 1 are 0.199N and 0.164N, respectively.

$$\bar{\sigma} = \frac{1}{N} \sum_{i=1}^{i=N} |\sigma_i| \quad (4.40)$$

where σ_i is i -th modeling bias; N is the total number of modeling biases.

In terms of Case 2 which generates the bamboo-shaped microstructures, the measured results and predicted results of Case 2 are presented in Figure 4.12. The measured peak-to-valley values of F_x and F_z are 0.53N and 0.21N, and the predicted peak-to-valley values of F_x and F_z in Case 2 are 0.58N and 0.22N, respectively. Likewise, the modeling errors of F_x and F_z can be calculated to be 9.43% and 4.76%, respectively. The modeling biases $\bar{\sigma}_2$ of F_x and F_z in Case 2 are 0.056N and 0.036N,

respectively. The main tendency and numerical values of the cutting force prediction model remain very consistent with measured cutting forces, again demonstrating the effectiveness of the developed cutting force prediction model.

In addition, it also can be found that the average cutting forces in Case 1 are approximately twice more than those in Case 2. It is mainly because the actual depth-of-cutting induced by the vibration motion of the 2DOF-VAUM system is much larger than that of Case 2 although other cutting parameters keep the same. The increase in cutting forces also influences the surface quality of the microstructures, and more scratches can be observed in Case 1 by the optical image, as shown in Figure 4.10(a). Moreover, the minimum values of F_x and F_z in Case 1 are zero while those of F_x and F_z in Case 2 are always larger than zero. The reason is that the cutting tool will leave the workpiece at some machining stage in Case 1 while it always stays in the workpiece at the whole machining stage in Case 2, whose phenomena can be validated by the surface topographies of microstructures, as shown in Figure 4.10(c) and (d).

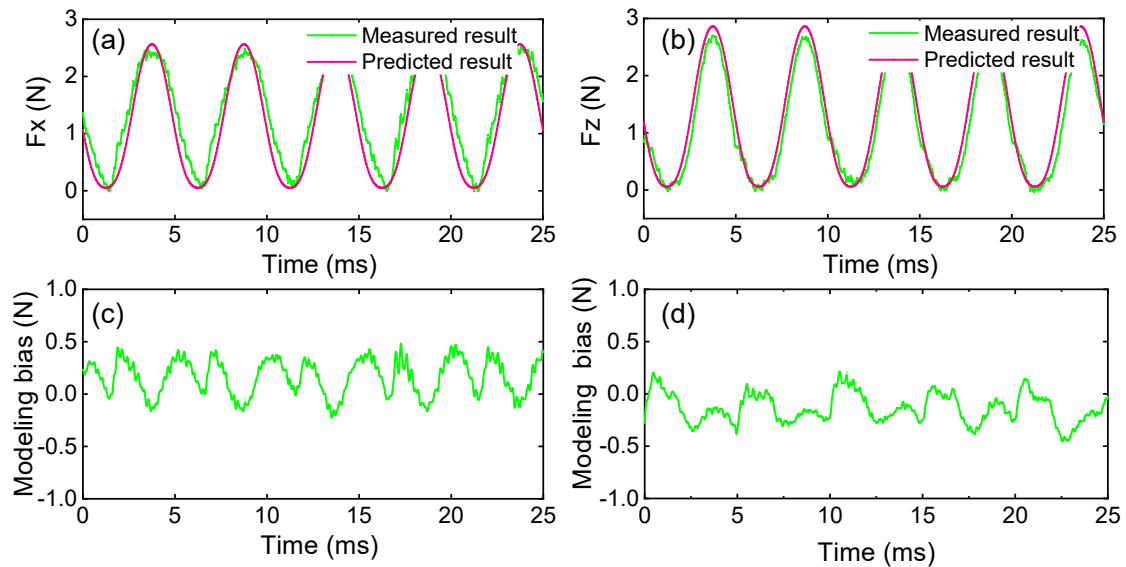


Figure 4.11 Comparison graphs of predicted and measured cutting forces of (a) F_x in Case 1 and (b) F_z in Case 1; modeling biases of (c) F_x in Case 1 and (d) F_z in Case 1.

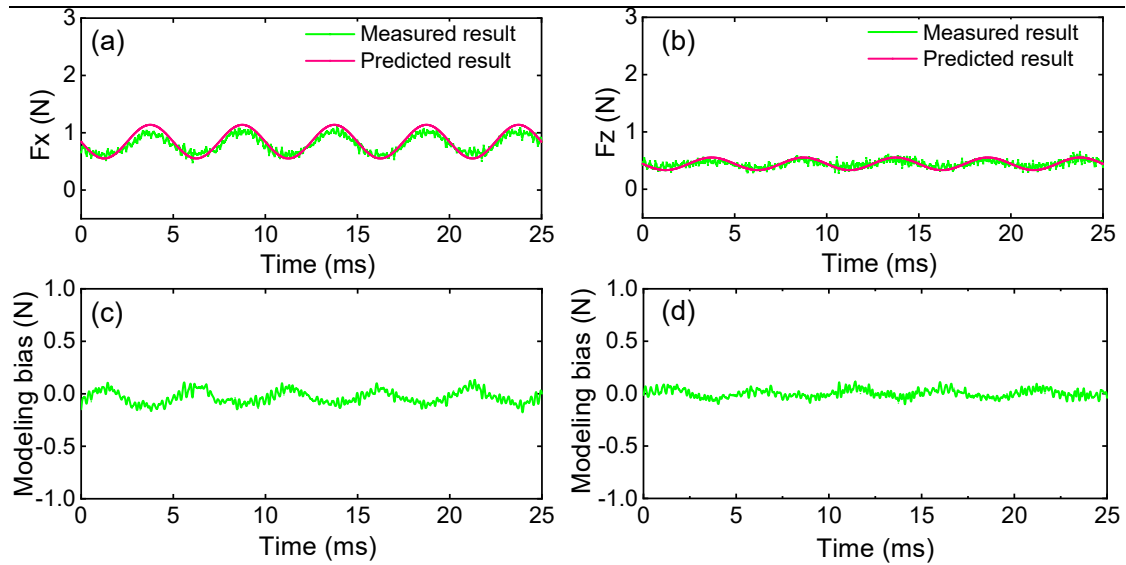


Figure 4.12 Comparison graphs of predicted and measured cutting forces of (a) F_x in Case 2 and (b) F_z in Case 2; modeling biases of (c) F_x in Case 2 and (d) F_z in Case 2.

4.5.3 Tool wear

The wear of the single-crystal diamond cutting tool associated with microstructure machining of pure titanium TA2 is preliminarily investigated in this study. The new cutting tool is examined to observe any existing damage on the rake face, flank face, and the cutting edge before experiments. Figure 4.13 shows SEM images of the rake face and flank face of the new cutting tool. These SEM images show that there is no tool wear and an extremely sharp and smooth cutting edge locates between the rake face and flank face. The single-crystal diamond cutting tool becomes worn after machining the shuttle-shaped microstructures and the bamboo-shaped microstructures with a short cutting distance (less than 1 m), as shown in Figure 4.14(a). A large quantity of material adhesion is observed on both the rake and flank faces of the cutting tool. The adherent materials are mainly located on the apex of the cutting tool and extend to the trailing edge between the rake face and the flank face. In order to investigate the

chemical composition of the adherent material, the EDX is performed on its surface. A clear signal of the presence of titanium in the adhesive material is observed by the EDX spectrum, as shown in Figure 4.14(b).

According to Zareena and Veldhuis's study (Zareena and Veldhuis, 2012), titanium chips have a strong inclination to bond to the cutting tool, especially after the cutting tool starts to wear. The adhesion of the titanium at the cutting tool influences the surface quality of the machined microstructures. Compared to copper or aluminum, the tool wear is much higher when machining titanium. This is because copper or aluminum has less solubility for carbon while titanium easily reacts with carbon (Zareena and Veldhuis, 2012). Besides, the high stress generated at the cutting edge may also accelerate the tool wear in micro/nanostructure machining (Dearnley and Grearson, 1986; Heidari and Yan, 2018; Yang and Liu, 1999). Therefore, more attention should be paid to minimizing the tool wear when machining microstructures on the TA2 surface.

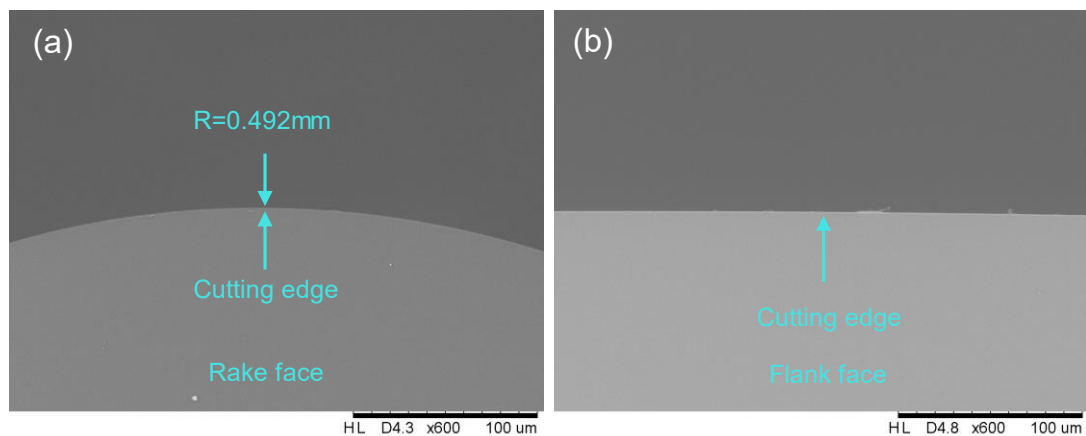


Figure 4.13 SEM images of the single-crystal diamond cutting tool before machining.

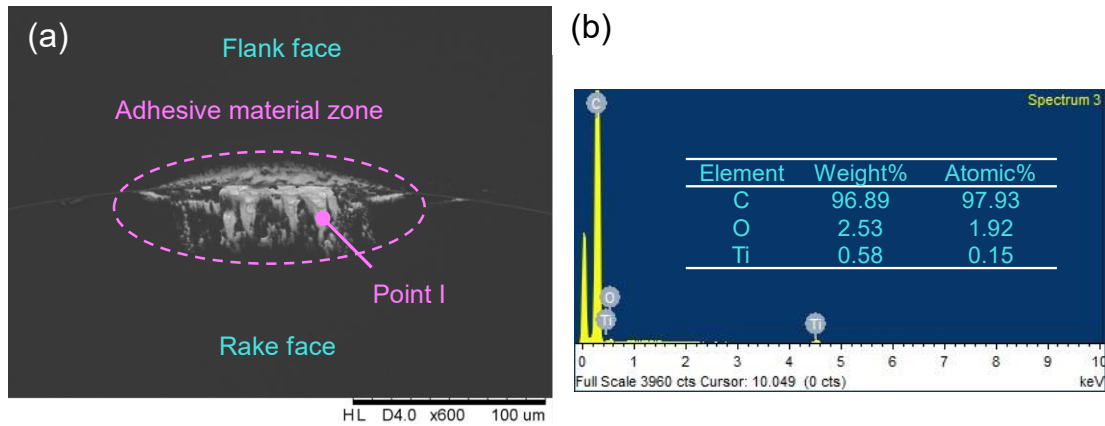


Figure 4.14 (a) SEM image of the single-crystal diamond cutting tool after machining and (b) the EDX spectrum of Point I.

4.6. Summary

In this chapter, a cutting force model is proposed for accurately predicting the instantaneous cutting force in the vibration-assisted ultraprecision machining considering the vibration motion-induced dynamic characteristics of material removal. The experimental results indicate that the proposed model agrees well with the measured results. The main conclusion can be summarized as follows:

(1) Compared with conventional machining and ultrasonic vibration-assisted machining, two typical characteristics of the vibration-assisted ultraprecision machining, i.e., time-vary material removal behavior and controllable vibration trajectory, are detailly illustrated according to the vibration trajectory of the cutting tool.

(2) A practical cutting force prediction model is developed to predict the instantaneous cutting force with the consideration of the process conditions, material property, and tool geometry. In this model, the instantaneous shear angle is analyzed by investigating the time-varying vibration motion. A non-equidistant shear zone is employed to evaluate the shear strain and shear strain rate inside the primary shear zone.

The instantaneous cutting area is modeled according to the geometrical relationship between the cutting tool dimensions and the maximum value of the instantaneous depth-of-cutting.

(3) Two kinds of microstructures, i.e., the shuttle-shaped and bamboo-shaped microstructures, are machined on the difficult-to-machine material TA2 surface. The experimental results of these two cases show that the cutting force prediction model corresponds well with the measured values and the average model error of the two cases is about 6%. It not only demonstrates the effectiveness and accuracy of the cutting force prediction model in the vibration-assisted ultraprecision machining, but also verifies the capability of the developed two-degree-of-freedom vibration-assisted ultraprecision machining on generating microstructures on the difficult-to-machine material.

Chapter 5 Micro/nanostructure machining on the magnesium alloy surface

5.1 Introduction

With the ever-increasing demand for lightweight in automotive, electronics, aerospace, biomedical, and other fields, magnesium alloys have received wide attention due to the characteristics of low density, high specific strength, high thermal conductivity, and so on (Cagan et al., 2020; Trang et al., 2018; Wang et al., 2021; Xu et al., 2015). However, to date, the exploration of micro/nanostructure generation on magnesium alloy surfaces remains a challenge due to the flammability and ignition of the magnesium alloy. Therefore, how to generate the micro/nanostructure on the magnesium alloy surface needs to be systematically studied.

This chapter applied the developed two-degree-of-freedom vibration-assisted ultraprecision machining system to generate the micro/nanostructures on the magnesium alloy surface. Then, the finite element model is established to simulate the machining process. The AZ31B, as a typical magnesium alloy, is selected as the workpiece material in this study. Experimental results show the various shape microstructures and sawtooth-shaped nanostructures are successfully machined on the magnesium alloy surface, demonstrating the effectiveness of this developed system. Furthermore, these sawtooth-shaped nanostructures have the function of inducing the optical effect and generating different colors on the workpiece surface. The colorful letter and colorful flower image are clearly viewed on the magnesium alloy surface. The corresponding cutting force, chip morphology, and tool wear are systematically

Chapter 5 Micro/nanostructure machining on the magnesium alloy surface
investigated to understand the machining of micro/nanostructures on the magnesium alloy surface.

5.2 Reliability evaluation of the 2DOF-VAUM system

Considering a long time and high frequency working in the machining, the lifetime of the piezoelectric actuator and the material fatigue of the mechanical structure in the 2DOF-VAUM system should be evaluated. For the piezoelectric actuator, the mean time to failure (MTTF), which denotes the expected time to failure, is employed to calculate its average lifetime. MTTF is a function of the applied voltage, the operational temperature, and the relative humidity.

$$\text{MTTF} = f_V \times f_T \times f_H \quad (5.1)$$

where f_V is the applied voltage factor, f_T is the operational temperature factor, and f_H is the relative humidity factor. The f_V is calculated by dividing the applied voltage by the maximum drive voltage.

Assuming that the piezoelectric actuator is operated with a voltage of 120V, at an operational temperature of 26°C, and in an environment with 75% relative humidity, the three factors ($f_V = 426.8$, $f_T = 138.8$, and $f_H = 2.8$) are obtained from the piezoelectric actuator manufacturers (Thorlabs, Inc.). Then the MTTF can be calculated as 165871.6hours, which is far larger than the usage time of the piezoelectric actuator.

For the material fatigue of the mechanical structure of the 2DOF-VAUM system, S-N curve is used to analyze the cyclic life of the material. S denotes the stress applied and N denotes the number of cycles before fracture. The maximum stress occurs when the maximal stroke (7μm) of the piezoelectric actuator is input into the mechanical structure. The maximum stress (176.22Mpa) can be obtained by the finite element

Chapter 5 Micro/nanostructure machining on the magnesium alloy surface simulation software, as shown in Figure 5.1. According to the S-N curve of the 304 stainless steel from the reference (Oshida and Deguchi, 1987), the number of cycles approaches infinity, demonstrating that there is no fatigue damage occurrence for the mechanical material when the 2DOF-VAUM system works.

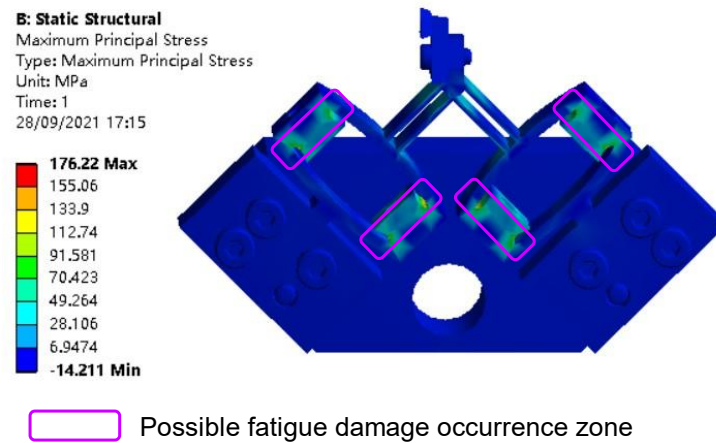


Figure 5.1 The maximum stress of the mechanical structure of the two-degree-of-freedom vibration-assisted ultraprecision machining.

5.3 Finite element model

To have a deeper understanding of the vibration-assisted ultraprecision machining process, a two-dimensional finite element model is established using the explicit module of the commercial software Abaqus 2021, as shown in Figure 5.2. The finite element model includes three parts: the cutting layer of the workpiece, the non-cutting layer of the workpiece, and the cutting tool. To improve the computational efficiency, the meshes in the cutting layer are refined and the meshes in the non-cutting layer are rough. The cutting tool is set as a rigid body and moves along the cutting trajectory. Its rake angle and clearance angle are set as 0° and 15° , respectively, as shown in Figure 5.2.

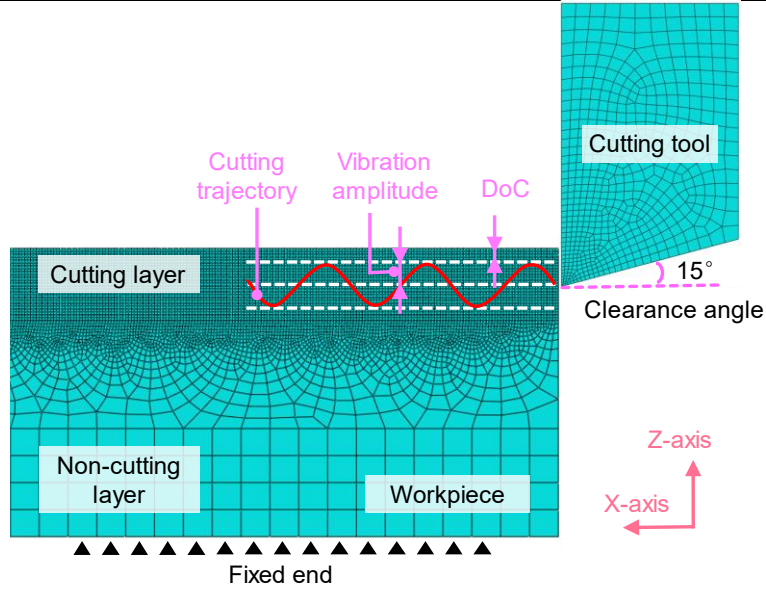


Figure 5.2 Finite element model of the vibration-assisted ultraprecision machining process.

The material flow stress model plays a crucial role in the finite element model (Z. Zhu et al., 2019a). In this study, the Johnson-Cook constitutive model is used to describe the elastoplastic deformation of the material, which considers the strain-strengthening effect, the relationship between flow stress and strain rate, and the relationship between flow stress and temperature (Aydın, 2021; JOHNSON and R., 1983; Z. Zhu et al., 2019a).

$$\sigma_s = (A + B \varepsilon_s^n) \left[1 + C \ln \left(\frac{\dot{\varepsilon}_s}{\dot{\varepsilon}_0} \right) \right] \left[1 - \left(\frac{T_s - T_0}{T_m - T_0} \right)^m \right] \quad (5.2)$$

where A , B , C , n , and m are the yield strength constant, hardening modulus constant, strain rate sensitivity coefficient constant, hardening coefficient constant, and thermal softening coefficient, respectively. $\dot{\varepsilon}_s$ is the deformation strain rate. $\dot{\varepsilon}_0$ is the reference shear strain rate that is set as 1.0 s^{-1} in this study. T_s , T_0 , and T_m are the absolute temperature, room temperature (293K), and melting temperature (873K) of the AZ31B magnesium alloy, respectively.

In addition, the Johnson-Cook damage model is employed to realize the workpiece material separation from the cutting layer (Johnson and Cook, 1985; Xu et al., 2021).

$$\varepsilon_f = \left[D_1 + D_2 \exp \left(D_3 \frac{\sigma_m}{\bar{\sigma}} \right) \right] \left[1 + D_4 \ln \left(\frac{\dot{\varepsilon}_s}{\dot{\varepsilon}_0} \right) \right] \left[1 + D_5 \left(\frac{T_s - T_0}{T_m - T_0} \right) \right] \quad (5.3)$$

where the D_1 - D_5 are the Johnson-Cook damage constants. σ_m and $\bar{\sigma}$ are the average normal stress and von Mises equivalent stress, respectively. When the equivalent plastic strain is larger than the damage strain ε_f , the material begins to fracture. The material properties and the parameters of the Johnson-Cook constitutive model and the Johnson-Cook damage model for AZ31B magnesium alloy are listed in Table 5.1 and Table 5.2.

The surface-to-surface contact condition is utilized and the two region zones, i.e., the sticking zone and the sliding zone, are applied to describe the contact between the cutting tool and the chips. The friction at the interface of the cutting tool and chips is controlled by the Coulomb law that is expressed as follows (Ruibin and Wu, 2016):

$$\tau_f = \begin{cases} \tau_s, & \mu\sigma_n \geq \tau_s \text{ (sticking zone)} \\ \mu\sigma_n, & \mu\sigma_n < \tau_s \text{ (sliding zone)} \end{cases} \quad (5.4)$$

where τ_f is the frictional stress. τ_s is the ultimate shear flow stress. μ is the friction coefficient between the cutting tool and workpiece, which is set as 0.2 in this study. σ_n is the normal stress on the contact surface.

The cutting trajectory of the cutting tool is given in Eqs. (4.4) and (4.5). In the software Abaqus, the periodic amplitude function is utilized to load the vibration trajectory of the 2DOF-VAUM system (Arefin et al., 2021).

$$a = \begin{cases} A_0 + \sum_{n=1}^N [A_n \cos n\omega(t - t_0) + B_n \sin n\omega(t - t_0)], & t \geq t_0 \\ A_0, & t < t_0 \end{cases} \quad (5.5)$$

where A_0 is the initial amplitude, ω is the circular frequency, t_0 is the starting time. A_n and B_n are the coefficients of the cosine and sine functions. N is the number of Fourier series terms. The ‘‘Dynamic, temp-disp, explicit’’ method is utilized to solve the finite

Chapter 5 Micro/nanostructure machining on the magnesium alloy surface element model. The detailed setting of the finite element model in software Abaqus is shown in Figure 5.3.

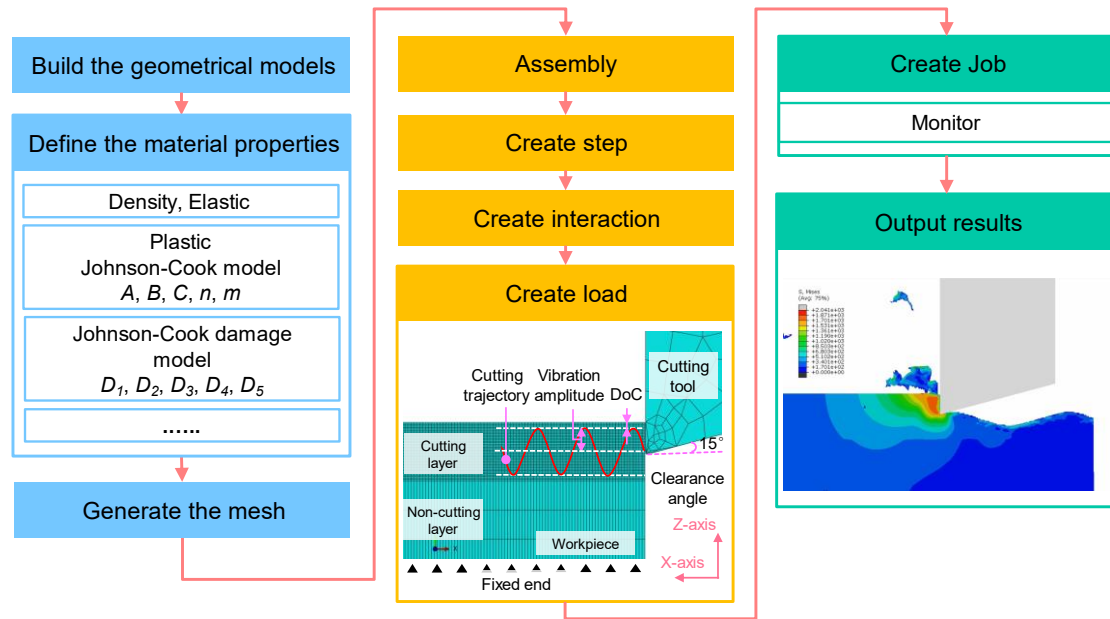


Figure 5.3 Simulation setting of the finite element model in software Abaqus.

Table 5.1 The properties of the AZ31B magnesium alloy.

Chemical composition (Weight, %)				Mechanical properties	
Mg	Balance	Si	0.16	Density (Kg/m ³)	1378
Al	2.96	Fe	0.003	Elastic modulus (Gpa)	44.8
Zn	0.52	Cu	0.006	Shear modulus (Gpa)	17
Mn	0.31	Ni	0.001	Poisson's ratio	0.35

Table 5.2 Johnson-Cook constants of the AZ31B magnesium alloy(Chen et al., 2019).

A (Mpa)	B (Mpa)	<i>n</i>	<i>m</i>	<i>C</i>	<i>D</i> ₁	<i>D</i> ₂	<i>D</i> ₃	<i>D</i> ₄	<i>D</i> ₅
153	291.8	0.1026	1.5	0.013	0.5	0.2895	3.719	0.013	1.5

5.4 Structural color generation principle

Nanostructures with specific facet spacing have an optical effect and can induce different color generations on the workpiece surface, which is an important function for micro/nanostructures. The color induced by the nanostructure is named structural color. In order to machine the optically functional nanostructures, the structural color

Chapter 5 Micro/nanostructure machining on the magnesium alloy surface
generation on the magnesium alloy surface is studied, which can extend the application range of the magnesium alloy to the optics field.

Figure 5.4 demonstrates how to generate structural color on the workpiece surface. Firstly, the size of the original image needs to be compressed to suit the workpiece size, as shown in Figure 5.4(a). In general, the smaller the single-pixel size, the higher the resolution of the structural color. However, the machining time dramatically increases with the increase of the resolution. In this study, the single-pixel size is set as $70\mu\text{m}$ to comprehensively balance the machining time and the resolution. Then, the RGB values of the compressed image are sorted into 16 different levels. The different level corresponds to the different facet spacing ($S_{i,j}$) of nanostructures. The facet spacing can be simultaneously controlled by the cutting velocity ($V_{i,j}$) that the ultraprecision lathe provides and the vibration frequency (f) that the 2DOF-VAUM system provides. So, there are two methods, i.e., adjusting the cutting velocity or adjusting the vibration frequency, to control the facet spacing according to Eq. (5.6). Since adjusting the cutting velocity is easier to realize through the velocity commands of the ultraprecision lathe, the cutting velocity is chosen to control the facet spacing according to the RGB value of each pixel in this study and the vibration frequency keeps constant.

$$S_{i,j} = V_{i,j}/f \quad (5.6)$$

After i -th line machining, the cutting tool feeds a single-pixel size along the Y-axis of the ultraprecision lathe, as shown in Figure 5.4(b). The cycle begins until finish the whole structural color machining on the workpiece surface.

In essence, the structural color can be viewed due to the physical interaction between the visible light and the sawtooth-shaped nanostructure, as shown in Figure 5.4(c). It can be described by the grating equation (Du et al., 2021a; Peng et al., 2018):

$$\sin\theta_i + \sin\theta_v = m\lambda_{i,j}/S_{i,j} \quad (m = 0, \pm 1, \pm 2, \pm 3, \dots) \quad (5.7)$$

where θ_i and θ_v are the incident angle and viewing angle. m is the reflection order. $\lambda_{i,j}$ is the wavelength of diffracted light.

The white light with different wavelengths is applied as the incident light and the sawtooth-shaped nanostructure plays a role as the reflection grating. Assuming that $\theta_i = 0$ and $m = 1$, the wavelength $\lambda_{i,j}$ of a certain color can be derived as:

$$\lambda_{i,j} = S_{i,j}\sin\theta_v \quad (5.8)$$

A certain color can be observed when the facet spacing is $S_{i,j}$. Therefore, the different colors can be flexibly generated by controlling the facet spacing of sawtooth-shaped nanostructures.

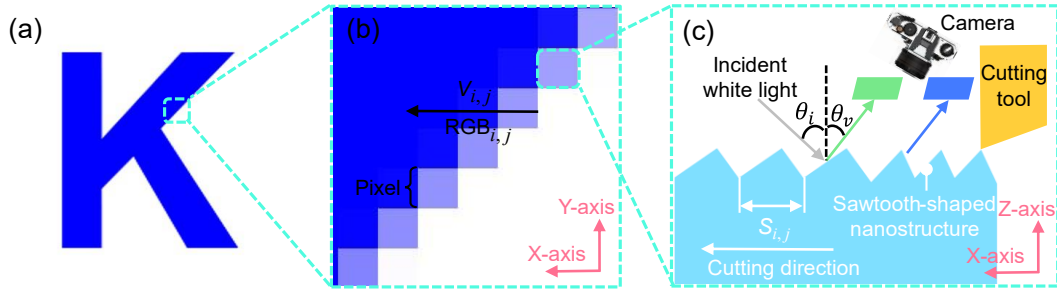


Figure 5.4 Generation principle of the structural color.

5.5 Experimental procedures

The experiments were performed on the hardware platform, as shown in Figure 5.5. The AZ31B magnesium alloy cube (Keple Technology Co., Ltd., China) with dimensions of $15 \times 15 \times 5 \text{ mm}^3$ was glued into a fixture, which was stationed on the spindle of the four-axis ultraprecision lathe (350FG, Moore Nanotechnology, America). For obtaining a proper planer surface with high surface quality, the workpiece was pre-machined with a spindle speed of 1400rpm using the ultraprecision turning process.

The depth-of-cutting and feed rate were set as $2\mu\text{m}$ and $2\text{mm}/\text{min}$ for the pre-machining. The nose radius of the used single-crystal diamond cutting tool (Apex Diamond Products Ltd.) is 0.509mm . In the micro/nanostructure machining, the developed 2DOF-VAUM system was mounted on the dynamometer via a screw. The computer provided command signals, which were converted into analog signals by the multifunction I/O device (USB-6341, National Instruments Corp.) and were magnified by the piezo amplifiers (E617.001, Physik Instrumente GmbH & Co.KG). The magnified analog signals were inputted into the piezoelectric actuator (PK4FA2H3P2, Thorlabs Inc.) to drive the 2DOF-VAUM system. In the vibration-assisted ultraprecision machining process, two single-crystal diamond cutting tools with different nose radius were applied. The cutting tool with a nose radius of 0.515mm (N0.50mLEi, Contour Fine Tooling Inc.) was used to machine microstructures on the magnesium alloy surface. The cutting tool with a nose radius of 0.223mm (N0.20mLEi, Contour Fine Tooling Inc.) was used to machine the sawtooth-shaped nanostructure to generate the structural colors. The detailed machining parameters are listed in Table 5.3. When finishing one cutting motion, the cutting tool would return to the origin point in the X-axis and feed a pitch (named as cross-feed) along Y-axis and the cycle starts again.

The cutting forces were measured through the Kistler force measurement system, which consists of this dynamometer (9256C1, Kistler Instrument Corp.), a charge amplifier (5080, Kistler Multichannel Charge amplifier), and PC software (Dyno ware), as shown in Figure 5.5(b). The sampling rate of capturing cutting force data was set as 50kHz for sufficiently collecting the cutting forces. As the force sensor may have electrical drift which means the zero point of the output signal may move to a positive

Chapter 5 Micro/nanostructure machining on the magnesium alloy surface

or negative value during experiments, the software Dyno ware was used to compensate for this electrical drift. After the experiments, the workpieces were cleaned in the ultrasonic cleaner using alcohol for 10minutes. A scanning electron microscope (SEM) (Hitachi Electron Microscope TM3000) was utilized to observe the chips and the tool wear. The Renishaw micro-Raman spectroscopy system was employed to analyze the tool wear mechanism. This laser beam can be tightly focused on the tool wear zone via the confocal microscope with three objectives (10×, 50×, and 100×). The Raman scattering spectrum range was set at from 600 to 2300 cm^{-1} with a spectral resolution of 0.3 cm^{-1} . The laser source (532nm) was used as an excitation source. All the data analysis has applied the software Wire 5.1, including cosmic ray removal, baseline subtraction, and peak pick.

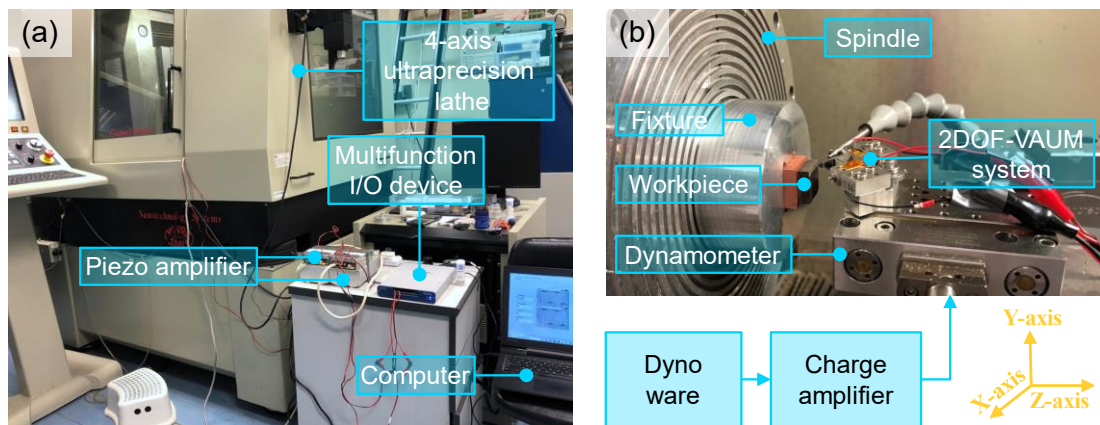


Figure 5.5 The experiment setup of the micro/nanostructure machining. (a) Full-view and (b) close-up view.

Table 5.3 The machining parameters.

	Case1	Case2	Case3	Structural color machining
Cutting speed (mm/min)	500	500	500	Varying
Depth-of-cutting (mm)	0.004	0.004	0.004	0.003
Cross-feed (mm)	0.160	0.160	0.160	0.07
Voltage amplitude (V)	40	40	40	30
Vibration frequency (Hz)	300	300	300	1000
Phase difference	0°	90°	180°	0°

5.6 Results and discussion

5.6.1 Microstructure topography characterization

Figure 5.6 shows the microstructures with different shapes on the magnesium alloy surface. The insets in Figure 5.6 (top right) show the magnification images of these microstructures. For Case 1 and Case 2, the main features (shapes and layout) look similar, but the edges of the microstructures display complete differences. Case 1 shows the sharp and linear edges while Case 2 shows the smooth and curved edges, as marked using the pink line in Figure 5.6. The microstructures in Case 3 show the bamboo shape, which is different from both Case 1 and Case 2. Different vibration trajectories caused by the phase difference lead to these results. The vibration trajectory in Case 1 is the straight-line motion along the Z-axis direction (depth-of-cutting direction), while the two-dimensional elliptical trajectory in Case 2 is generated along the X-axis direction (cutting direction) and Z-axis direction. The elliptical trajectory creates smooth and curved edges. The vibration trajectory in Case 3 is also a straight-line motion but its direction is along the X-axis direction, so the bamboo-shaped microstructures distributing in the X-axis direction can be generated.

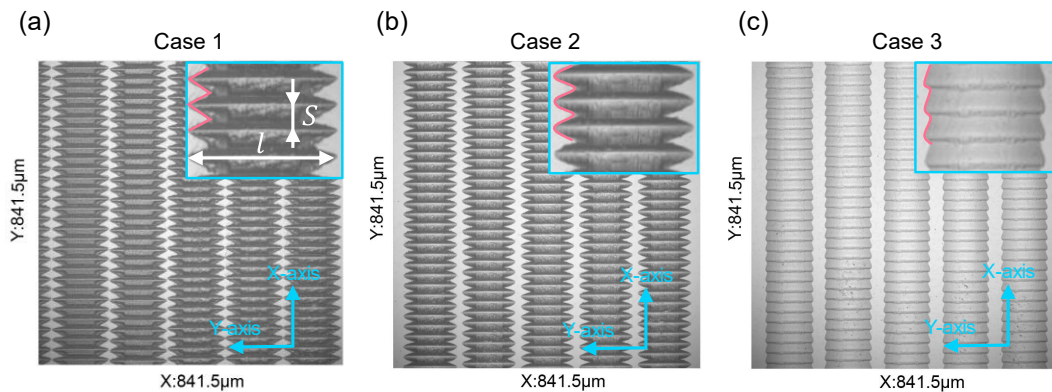


Figure 5.6 Optical micrographs of microstructures of (a) Case 1, (b) Case 2, and (c) Case 3.

The theoretical value of the facet spacing can be calculated ($S = 27.7\mu\text{m}$) according to Eq. (5.6). The corresponding measured results are $27.6\mu\text{m}$ in Case1, $28.1\mu\text{m}$ in Case2, and $27.9\mu\text{m}$ in Case3, respectively. Therefore, the relative errors with respect to the theoretical value are 0.36%, 1.44%, and 0.72%, indicating a close agreement with the theoretical value. In addition, the length (l) of each microstructure along the Y-axis direction can be calculated by:

$$l = 2\sqrt{R^2 - [R - (DoC + A_v)]^2} \quad (5.9)$$

where R is the radius of the cutting tool, DoC is the depth-of-cutting, and A_v is the vibration amplitude of the 2DOF-VAUM system.

The theoretical lengths for three cases are obtained ($165.6\mu\text{m}$, $154.1\mu\text{m}$, and $132.8\mu\text{m}$) according to the machining parameters. The corresponding measured results are $152.8\mu\text{m}$ in Case1, $145.2\mu\text{m}$ in Case2, and $131.9\mu\text{m}$ in Case3, respectively. The relative errors with respect to the theoretical results are 7.73%, 5.78%, and 0.68%, which may be caused by the cutting tool positioning before the experimental machining.

5.6.2 Cutting force analysis in microstructure generation

Cutting force is a significant indication to monitor the machining process during generating microstructure on the magnesium alloy surface. Figure 5.7 shows the measured and simulated cutting forces of the above three cases. F_x and F_z represent the cutting forces along the X-axis direction and Z-axis direction, respectively. The simulated cutting forces are obtained by inputting the identical machining parameters into the finite element model. It is observed that the cutting forces periodically increase and decrease, and the cycle time (3.33ms) of cutting forces is in accordance with the vibration period (3.33ms) of the 2DOF-VAUM system. The removal of material begins

as soon the cutting tool touches the magnesium alloy surface. The cutting forces increase when the cutting tool advances into the workpiece as more amount of workpiece materials are removed. The cutting forces decrease with the reduction of the material removal volume. When the phase difference changes (0° in Case1, 90° in Case2, and 180° in Case3), the effects on the cutting force are also obvious in the value size and shape trend, as shown in Figure 5.7(a), (b), and (c).

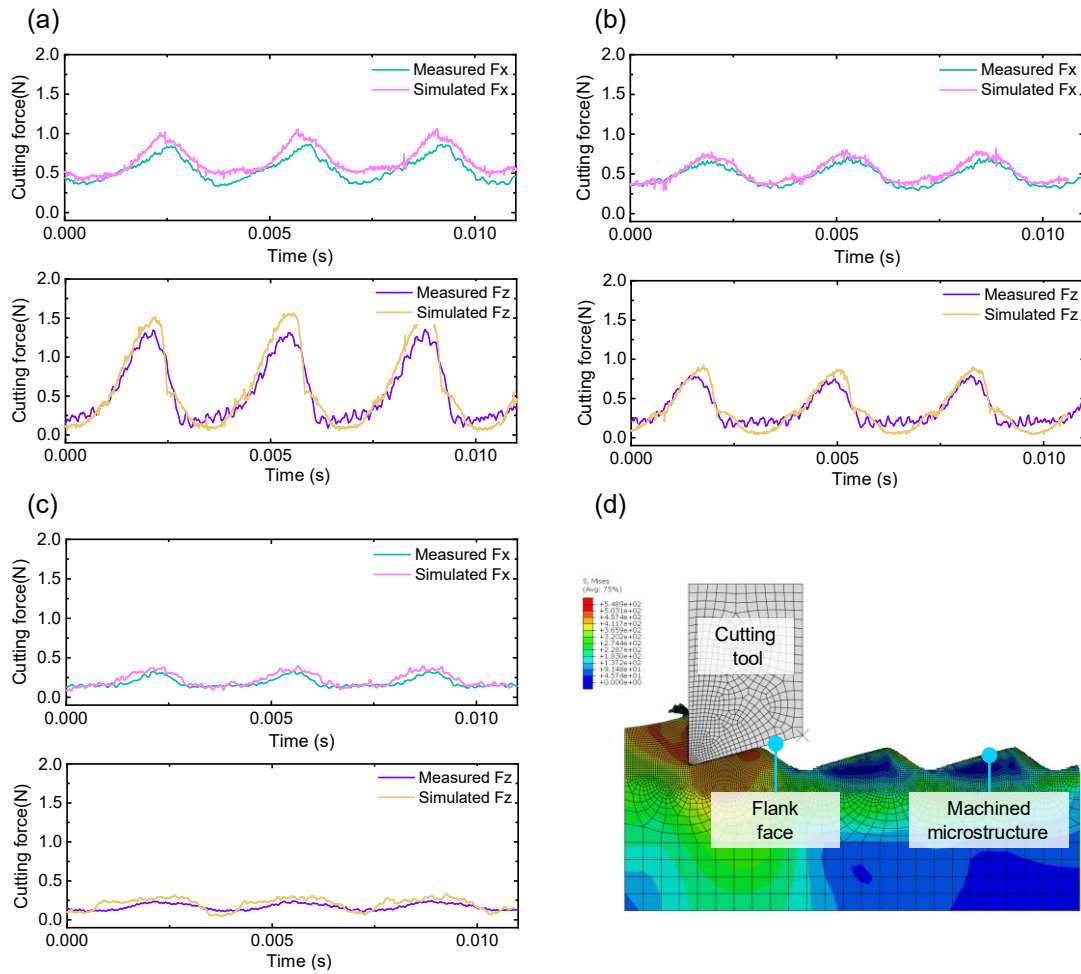


Figure 5.7 The measured and simulated cutting forces. (a) Case1, (b) Case 2, (c) Case 3, and (d) snapshot of the simulated machining process in Case1.

Both F_x and F_z reduce with the increase of the phase difference from 0° to 180° . It is because the increase of the phase difference leads to the decrease of the depth-of-cutting, which causes the reduction of the material removal volume. Figure 5.7(d)

Chapter 5 Micro/nanostructure machining on the magnesium alloy surface

shows the simulated machining process of the vibration-assisted ultraprecision machining in Case1.

Besides, the simulated cutting forces using the finite element model show good agreement with the measured cutting force. The average peak-to-valley values of the simulated and measured F_x in Case 1 are 0.56N and 0.52N, and that of the simulated and measured F_z in Case 1 are 1.53N and 1.34N. The model errors of F_x and F_z in Case 1 can be quantitatively calculated to be 7.69% and 14.18%, respectively. Similarly, the model errors of F_x and F_z in Case 2 and Case 3 are 11.33%, 10.55%, 18.62%, and 18.27%, respectively, which demonstrates the effectiveness of the finite element model on the cutting force simulation during the microstructure machining.

5.6.3 Chip morphology investigation

Chip investigation is another indication to reflect the machining process during the microstructure machining. The chips in the pre-machining (ultraprecision turning) process and the vibration-assisted ultraprecision machining process are collected. Their morphologies are shown in Figure 5.8. As can be seen from the SEM images, fracture features at the side of chips are formed in both machining processes as evidenced by the plastic shearing. The ultraprecision turning process produces very long and continuous chips, and their shape looks like the folded long ribbon. The vibration-assisted ultraprecision machining process produces shorter and discontinuous chips. Since the depth-of-cutting dynamically changes with the vibration trajectory in the ultraprecision diamond surface texturing process, the thickness of chips changes with time. The uneven thickness leads to the uneven stiffness of chips. Chips will break at the place with small stiffness. The magnification image in Figure 5.8(b) shows the

Chapter 5 Micro/nanostructure machining on the magnesium alloy surface

lamellar structure along the chip flow direction and each lamellar structure contains many segments, which demonstrates that the vibration-assisted ultraprecision machining process is different from the ultraprecision turning process. Ultraprecision diamond surface machining process possesses the time-varying depth-of-cutting. Furthermore, there are no burn marks of chips for all experiments, which indicates that the vibration-assisted ultraprecision machining process is safe, and no fire hazard exists.

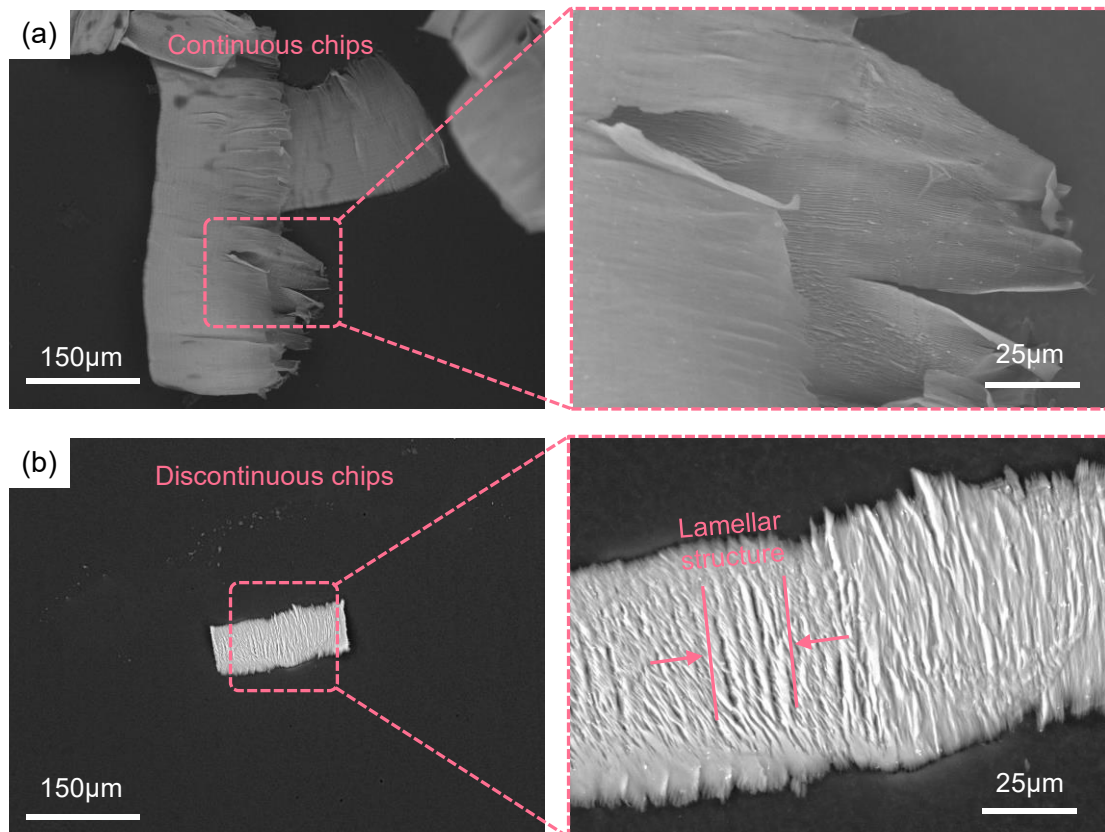


Figure 5.8 SEM images of the chip morphology. (a) The ultraprecision turning process and (b) the vibration-assisted ultraprecision machining process.

5.6.4 Structural color observation

Before the sawtooth-shaped nanostructure machining, an optical mirror surface with the surface roughness of $0.003\mu\text{m}$ was firstly obtained using the ultraprecision turning process to guarantee surface finish, as shown in Figure 5.9(a). For obtaining the

Chapter 5 Micro/nanostructure machining on the magnesium alloy surface

cutting velocity that each pixel corresponds, as described in Section 5.4, the viewing angle θ_v was assumed to be 45° , and the longest visible wavelength (deep red) and shortest visible wavelength (deep violet) were set as 700nm and 400nm, respectively. The 16 levels of the RGB values are evenly distributed between 400nm and 700nm. According to Eqs. (5.6) and (5.8), the cutting velocity $V_{i,j}$ with respect to the RGB value of each pixel can be calculated. Then the position and velocity commands can be generated accordingly. Besides, the machined regions display vivid colors while the non-machined regions remain the original color of the magnesium alloy, which can be controlled by adjusting the depth-of-cut.

Figure 5.9(b) shows the letters “SKL”, “HKPU”, and “Mg alloy” in different colors, which are captured by a digital camera. Figure 5.9(c) shows the colorful flower on the magnesium alloy surface without using any coating material and pigment. The machining times for these two structural colors are 41mins and 39mins, respectively, which demonstrates that the developed machining system is a very highly efficient machining way to generate the structural color.

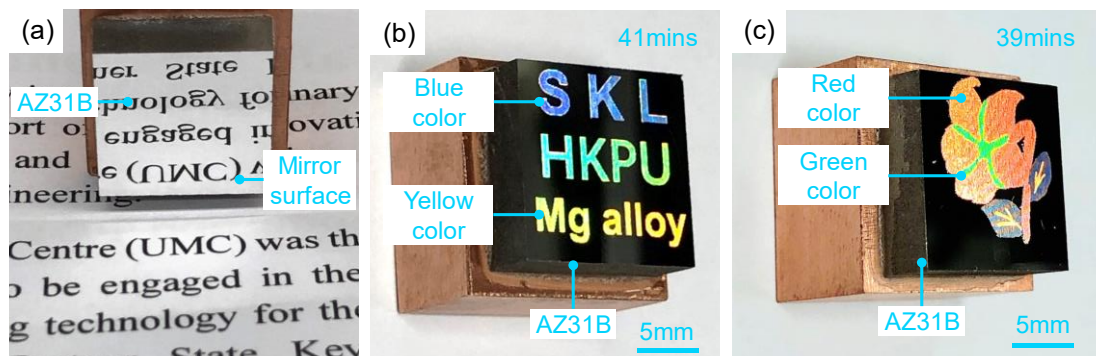


Figure 5.9 Photographs of (a) mirror surface, (b) colorful letters “SKL”, “HKPU”, and “Mg alloy”, and (c) colorful flower.

To investigate the three-dimensional morphologies of nanostructures that induce the different color generation, an atomic force microscope (AFM) (Park XE-70, Park

Systems, Inc.) was employed. Figure 5.10 shows the three-dimensional morphology of nanostructures on the letter “S” and “M” in Figure 5.9. It can be clearly found that these nanostructures have periodic sawtooth-like profiles. The average facet spacings of the nanostructures in the letter “S” and “M” are 625nm and 737nm, which agree well with the theoretical results (612nm and 744nm). These sawtooth-shaped nanostructures further demonstrate the developed vibration-assisted ultraprecision machining system has the capability of flexibly generating micro/nanostructures on the magnesium alloy surface.

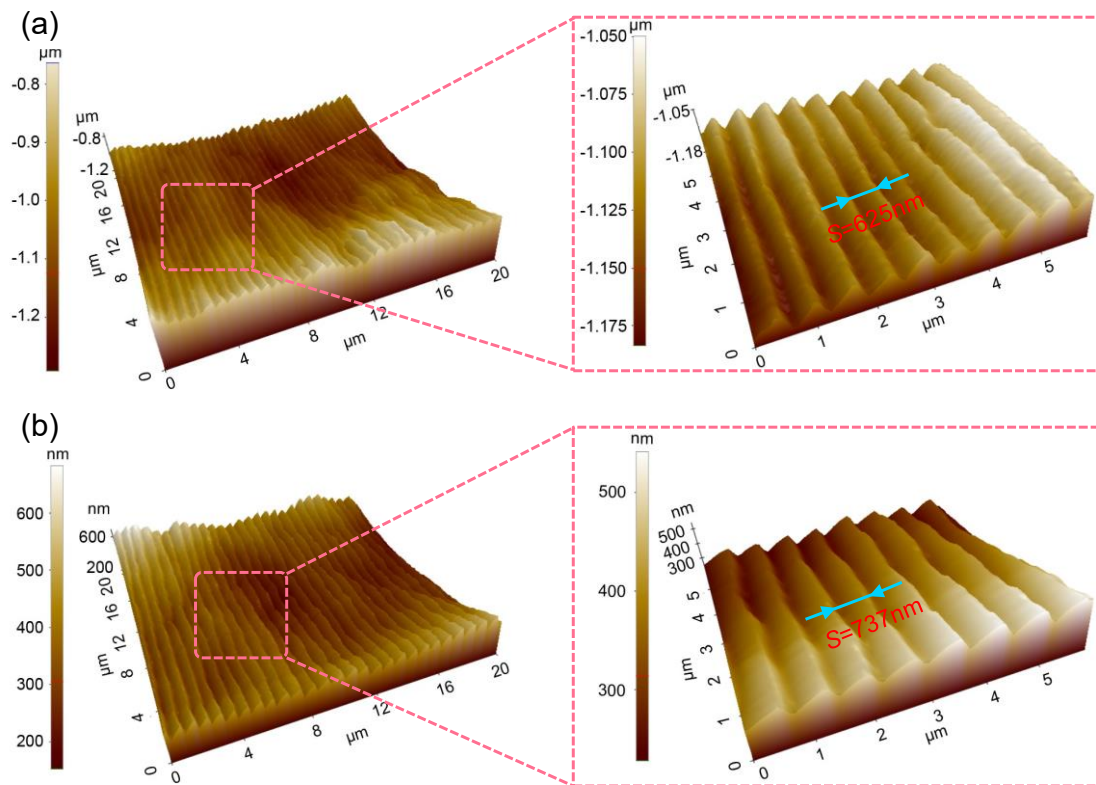


Figure 5.10 AFM images of nanostructures of (a) letter “S” in Figure 5.9 and (b) letter “M” in Figure 5.9.

5.6.5 Tool wear mechanism exploration

Figure 5.11 (a) and (b) show SEM images of the new cutting tool from the two viewing angles. A very sharp cutting edge between the rake face and flank face can be observed. After the microstructure machining experiments, the micro-chipping and flank wear are clearly found, as shown in Figure 5.11(c) and (d). The worst wear occurs on the apex of the cutting tool and then spreads along the cutting edge. The damage volume of the rake face is larger than that of the flank face since the rake face plays the main role in removing the material during micro/nanostructure machining, as described in Figure 3.6.

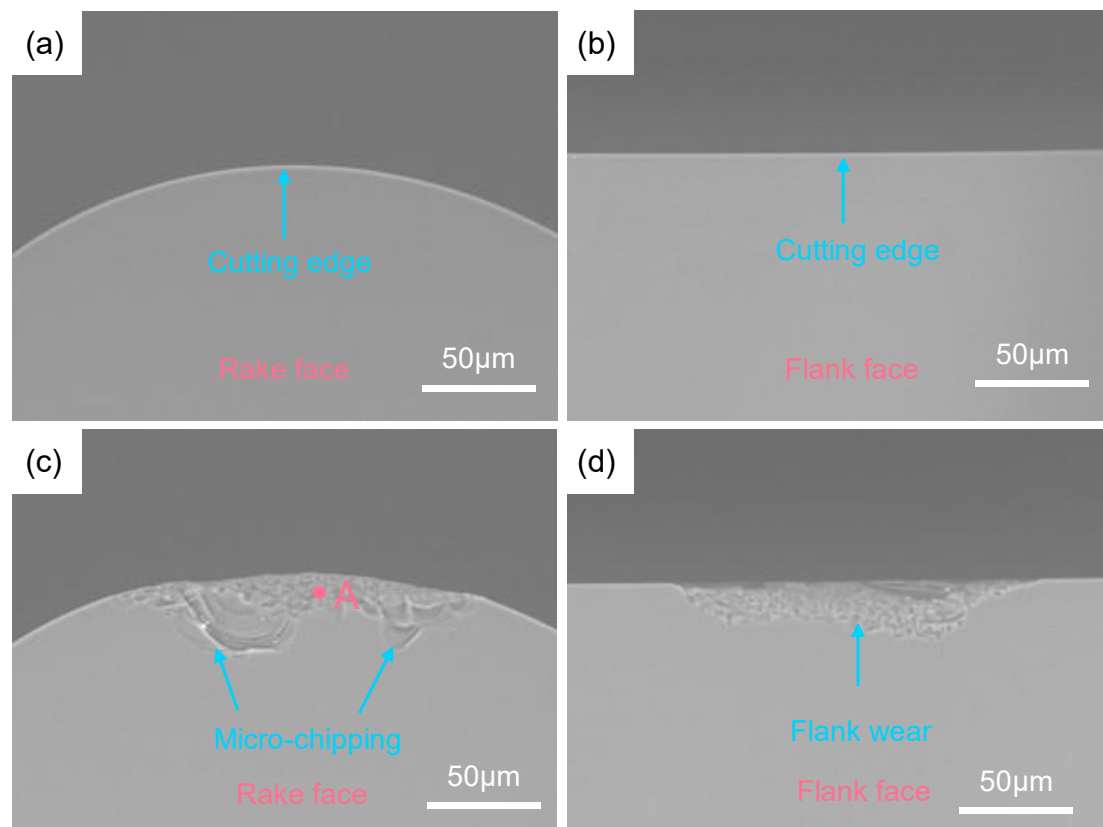


Figure 5.11 SEM images of the single-crystal diamond cutting tool. (a) Rake face of the new cutting tool, (b) flank face of the new cutting tool, (c) rake face of the worn cutting tool, and (d) flank face of the worn cutting tool.

To further explore the tool wear mechanism associated with micro/nanostructure machining of the magnesium alloy, Raman spectroscopy was employed to find possible microstructural changes of the diamond (Marton et al., 2013). The Raman spectrum on the rake face of the new cutting tool exhibits a very sharp and single peak at 1332cm^{-1} , as shown in Figure 5.12(a). When the laser of the Renishaw micro spectrometer was focused on the point A of the tool wear zone in Figure 5.11(c), it is seen from Figure 5.12(b) that the single peak becomes two peaks, called D-band and G-band. They are located at around 1354cm^{-1} and 1583cm^{-1} , respectively. The D-band and G-band provide direct evidence for the diamond-graphite transformation of the cutting tool. Therefore, it is concluded that the tool wear in the micro/nanostructure machining of the AZ31B magnesium alloy is related to the diamond graphitization. There are two factors to cause diamond graphitization: high temperature and high pressure. The surface temperature of the workpiece is almost kept at around 21°C , which is measured by an infrared thermometer. The cutting tool-workpiece interface area is extremely small in the micro/nanostructure machining of the magnesium alloy. So, the high pressure may lead to the graphitization of the partial diamond crystal (Gogotsi et al., 1999)(Zhang et al., 2011).

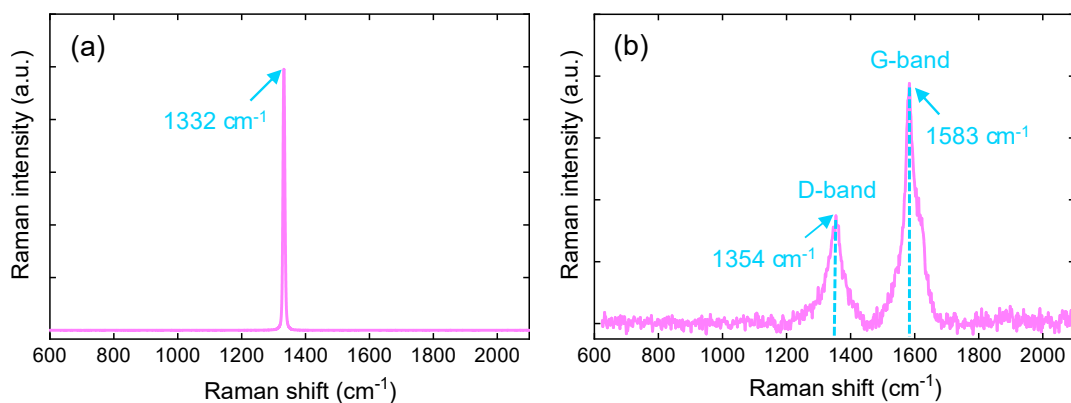


Figure 5.12 Raman spectrum of (a) the new single-crystal diamond cutting tool and (b) the worn single-crystal diamond cutting tool.

5.7 Summary

In this work, the developed two-degree-of-freedom vibration-assisted ultraprecision machining system was applied to machine the various micro/nanostructures on the magnesium alloy surface. The systematic study on micro/nanostructure generation, cutting force analysis, chip morphology, and tool wear was carried out. The main conclusions of this chapter have been drawn:

(1) The reliability of the 2DOF-VAUM system is evaluated. As a reliability index, the mean time to failure of this system was analyzed (more than 160000h), which was far larger than its normal usage time.

(2) A finite element model was established to simulate the micro/nanostructure machining and the corresponding cutting forces. The experimental results showed the simulated cutting forces were in good agreement with the measured results. The maximal value of cutting forces in all cases was less than 2N, demonstrating that the magnesium alloy possesses better machinability.

(3) Different shape microstructures (dimple-shaped microstructures and bamboo-shaped microstructures) were successfully machined on magnesium alloy surfaces, showing the effectiveness of the developed 2DOF-VAUM system.

(4) Sawtooth-shaped nanostructures were also machined, which induced the different color generation by manipulating the facet spacing of nanostructures. The colorful letters “SKL”, “HKPU”, and “Mg alloy” as well as colorful flower were observed with high saturation on the workpiece surface, which could expand the application range of the magnesium alloy to the field of optics. And the corresponding generation principle of these colors was also in-detail illustrated.

(5) The graphitization of the single-crystal diamond cutting tool in the machining of micro/nanostructures was found, which is the reason for the tool wear. This study provides an effective and flexible machining method for generating micro/nanostructures on the easy-to-flame material magnesium alloy surfaces, which are potentially applied to optics, functional decoration, biomedicines, etc.

Chapter 6 Generation, hiding, and replication of nanostructure-induced optical information

6.1 Introduction

Optical information is an indispensable part of human society and has various potential applications, such as information displays, anti-counterfeiting, and healthcare monitoring (Isapour and Lattuada, 2018; Kulce et al., 2021). It is well known that optical information more easily grabs the attention of the public due to the rapid growth of the internet, such as 4G or 5G. So far, the main methods to generate the optical information are to use dyes or pigments. But these ways can lead to pollution problems (Li et al., 2021). Optical information generated by the light interaction with the micro/nanostructures is an environment-friendly alternative (Fu et al., 2018).

The concept of optical information generation and hiding using developed the two-degree-of-freedom vibration-assisted ultraprecision machining system is proposed for the first time in this chapter. The nanostructures on the workpiece surface act as the reflection grating, which can induce optical information generation. Inspired by the 7-segment digital tubes, a skillful method of optical information hiding is proposed by controlling the facet spacings of nanostructures in different segments. Fast replication can be used in massive production. This chapter uses a cellulose acetate replication sheet to realize optical information replication. Experimental results show the effectiveness of the proposed method on optical information generation, hiding, and fast replication. The optical information “Let’s Beat COVID-19 Together” can be

machined on the workpiece via QR code. The optical information “LOVE” is only observed at a certain viewing angular. The corresponding principles are also illustrated in this chapter.

6.2 Optical information generation and hiding

Figure 6.1 demonstrates the generation and hiding principles of the optical information induced by nanostructures. In order to machine the nanostructures, the periodic vibration trajectory is a straight-line reciprocating motion along the depth-of-cutting direction, which is provided by the developed two-degree-of-freedom vibration-assisted ultraprecision machining system. The display principle of the optical information is demonstrated in Figure 6.1(a). Different facet spacings ($S_{i,j}$) of nanostructures induce different color generation. Fundamentally, the optical information can be generated due to the physical interaction between the visible light and the periodic nanostructures, which is similar to the generation of structure color, as depicted in Section 5.4. In this study, the optical information is stored and expressed in the QR code due to its remarkable advantages, such as high error-correction capability and large storage capacity (Garateguy et al., 2014; Lin et al., 2015; Tkachenko et al., 2016; Y. Zhu et al., 2019). The QR code image is firstly recognized and compressed according to the length and width of the workpiece. Then the single-pixel size is set by considering the machining time and the resolution of an image. Next, the cutting velocity ($V_{i,j}$) of each pixel is calculated based on the RGB value of each pixel. In this chapter, the optical information “Let’s Beat COVID-19 Together” can be taken as an example to show the optical information generation on the workpiece surface, as shown

in Figure 6.1(b), which can be read by smartphones. Due to the high popularity of the smartphone, it is convenient to obtain this optical information.

The method of the optical information hiding is inspired by the 7-segment digital tubes, as shown in Figure 6.1(c). A letter can be composed of seven bright segments (a, b, c, d, e, f, and g). If the letter “L” is hoped to be displayed, the facet spacings in segments d, e, and f remain identical and simultaneously distinguish from the facet spacing in segments a, b, c, and g. Similarly, other letters can be also displayed in accordance with the aforementioned principle. If the letter “L” is to be hidden, the difference in the facet spacing between two groups of segments only needs to control. In this case, the number ‘8’ (disturbance information) is visible and the letter “L” (useful information) is hidden. Only useful information can be observed when the viewing angle reaches the certain angle.

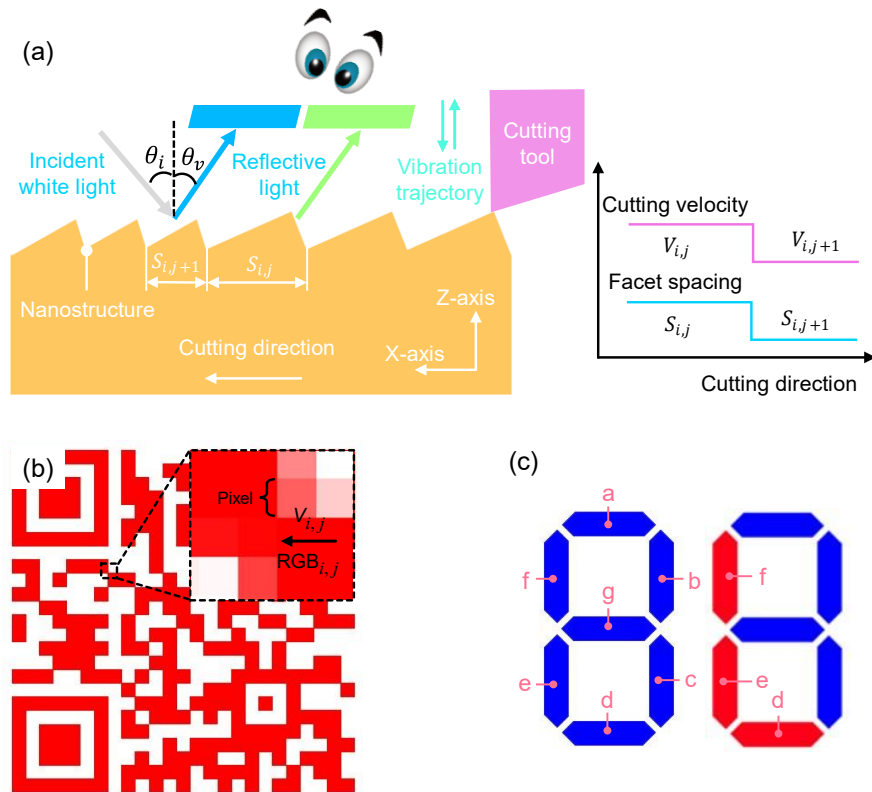


Figure 6.1 Schematic illustration of the optical information generation and hiding.

The display region of the optical information can be selected by actively controlling the nominal depth-of-cut. The regions without information remain the original color of the workpiece while the machined regions display optical information. According to this method, the toolpaths of the QR code and hidden information “LOVE” is shown in Figure 6.2(a) and (b). The Z-axis value of the workpiece surface is set as $0\mu\text{m}$. The nominal depth-of-cut is set as $6\mu\text{m}$. When a region needs to be machined, the cutting tool will enter into the workpiece at a distance of $4\mu\text{m}$. If the region does not need to be machined, the cutting tool will leave the workpiece with a distance of $30\mu\text{m}$ along the Z-axis direction. The distance between two toolpaths (along the Y-axis direction) equals the single-pixel size, $70\mu\text{m}$, in this study. After the i -th toolpath, the cutting tool will move to $(i+1)$ -th toolpath until finish all toolpaths.

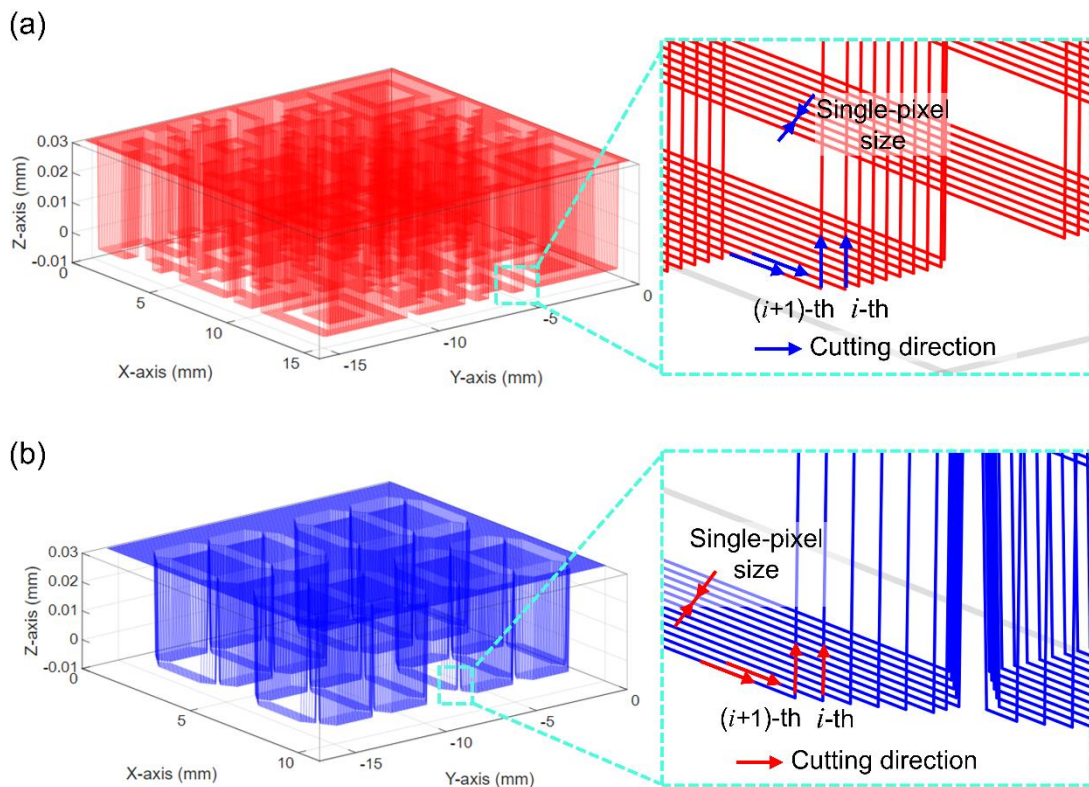


Figure 6.2 Toolpaths of (a) QR code and (b) hidden information “LOVE”.

6.3 Optical information replication

Optical information replication is a recognized technology for mass production, which copies the optical information to other carriers by casting or impressing surface topography into the surface of the carrier. Cellulose acetate replication sheet, as a kind of replication material, provides a convenient method of replicating optical information. In this chapter, it is employed to replicate original optical information for realizing mass production.

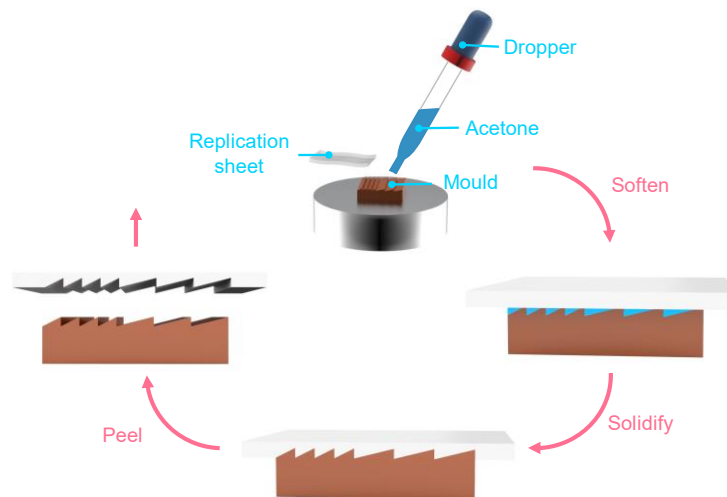


Figure 6.3 Schematic illustration of the replication steps of optical information.

Figure 6.3 depicts the whole steps of the fast replication of the optical information. The regular nanostructures that contain the optical information are taken as a mold. Firstly, the mold surface is covered with acetone using a dropper. A piece of the replication sheet of a size suitable to cover the mold surface is cut from the large area sheet (Replicating Material AGG255, Cellulose Acetate, Agar Scientific, EM Japan) and are immediately placed over the mold surface with gentle pressure. Make sure there are no air bubbles trapped during this process otherwise the fast replication result will

not be ideal. Then, the replication sheet is solidified for about 5mins for flowing inside the nanostructures of the mold surface. Acetone can evaporate for 10 mins at room temperature. The replication sheet is next peeled very easily from the dry sample surface. Finally, a polymer replica with the optical information can be obtained.

6.4 Experimental procedures

The optical information generation and hiding experiments are to apply the developed two-degree-of-freedom vibration-assisted ultraprecision machining system, as shown in Figure 6.4(a). Pure copper with a purity of 99.9% (Keple Technology Co., Ltd., China) was selected as the workpiece and the optical information was generated and hidden on their surfaces. The natural single-crystal diamond cutting tool with a radius of 0.228mm (Contour Fine Tooling Inc., UK) is selected as the cutting tool. The workpiece was firstly flatted to guarantee the surface quality before experiments. These machining parameters are the same as Section 3.5.2. In the optical information generation and hiding stage, the experimental settings are the same as Section 5.5. Figure 6.4(b) shows the photograph of the fast replication process.

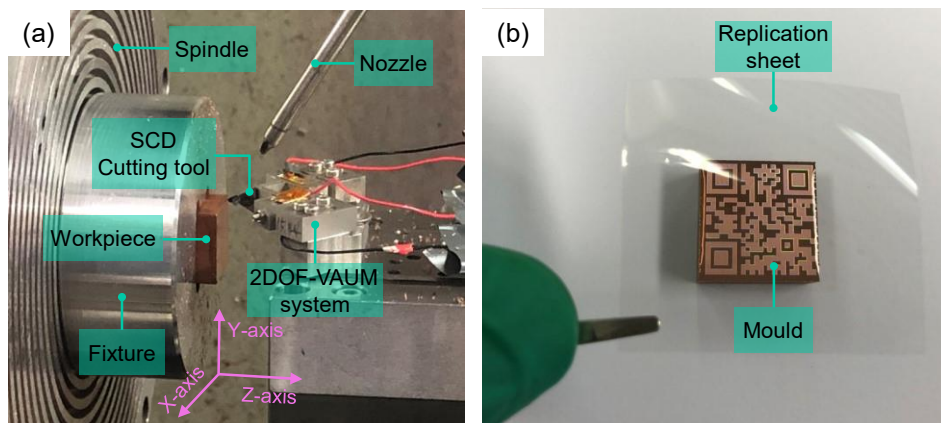


Figure 6.4 The experiment setup of the optical information generation, hiding, and replication.

6.5 Results and discussion

6.5.1 Optical information readout

Before the machining of the optical information generation and hiding, an optical mirror surface with a surface roughness of $0.002\mu\text{m}$ was firstly obtained to ensure a surface finish. In optical information generation, the viewing angle θ_v was set as 45° , and the longest visible wavelength and shortest visible wavelength were set as 700nm and 400nm , respectively. The 32 levels of the RGB values of the original information are evenly distributed between 400nm and 700nm . According to Eqs. (5.6) and (5.8), the nominal cutting velocity $V_{i,j}$ of each pixel can be calculated, and then the position and velocity commands can be generated accordingly.

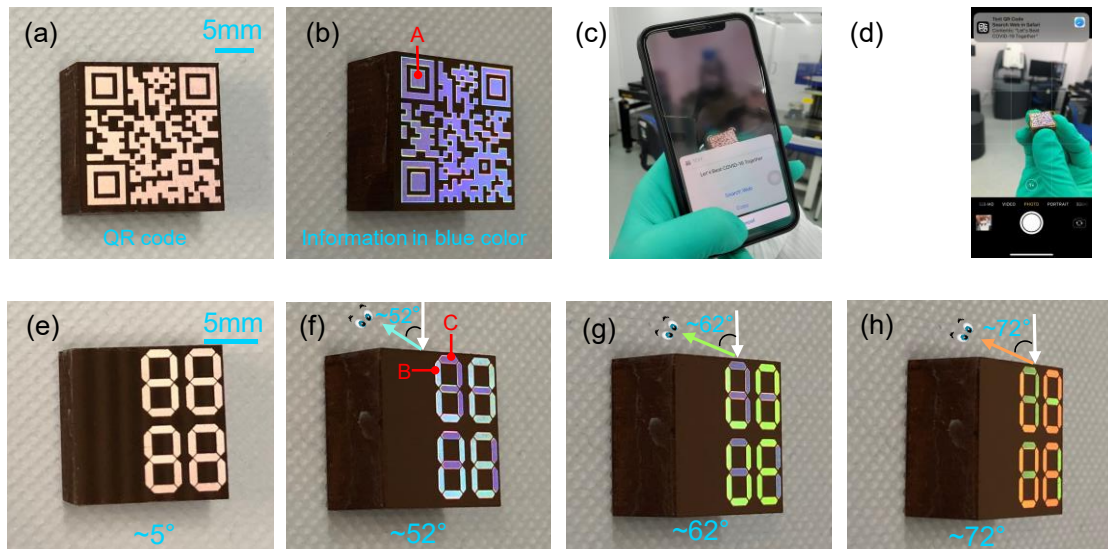


Figure 6.5 Generation and hiding results of optical information.

The QR code of the optical information “Let’s Beat COVID-19 Together” is viewed, as shown in Figure 6.5(a) and (b). It can be also read via a smartphone with a QR code scanning function, as shown in Figure 6.5(c) and (d).

Figure 6.5(e)-(h) show the hiding and display results of the word “LOVE”. When the view angle θ_v is in the range of 0° - 52° , the valuable optical information is hidden and the disturbance information “8888” is observed, as shown in Figure 6.5(e). In this study, the useful information, i.e., the word “LOVE”, can be read when the viewing angle θ_v locates in 52° - 72° , as shown in Figure 6.6(f)-(h). As seen from the observation results, any pigment or coating materials that may cause environmental pollution in the optical information generation and hiding are not used. Hence, controlling spacing to generate and hide the optical information is an environmentally friendly method, and it is realized by the developed two-degree-of-freedom vibration-assisted ultraprecision machining system.

According to the rapid replication method that is stated in Section 6.3, the optical information “Let’s Beat COVID-19 Together” was replicated, as shown in Figure 6.6(a) and (b). The replicated optical information can be easily read by a smartphone, demonstrating the effectiveness of the proposed replication method.

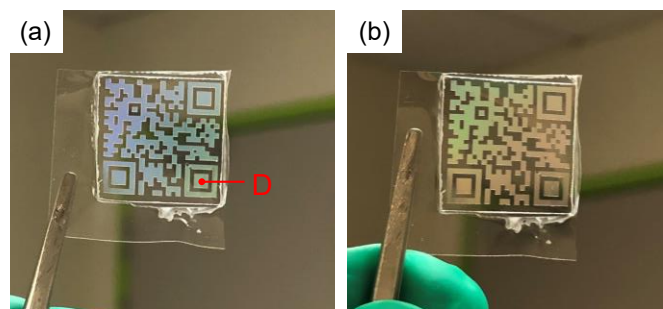


Figure 6.6 Replication results of optical information “Let’s Beat COVID-19 Together”.

6.5.2 Nanostructure topography characterization

Figure 6.7 shows the three-dimensional topographies of nanostructures using the AFM technique. It can be found that these nanostructures have the periodic saw-tooth-like profile.

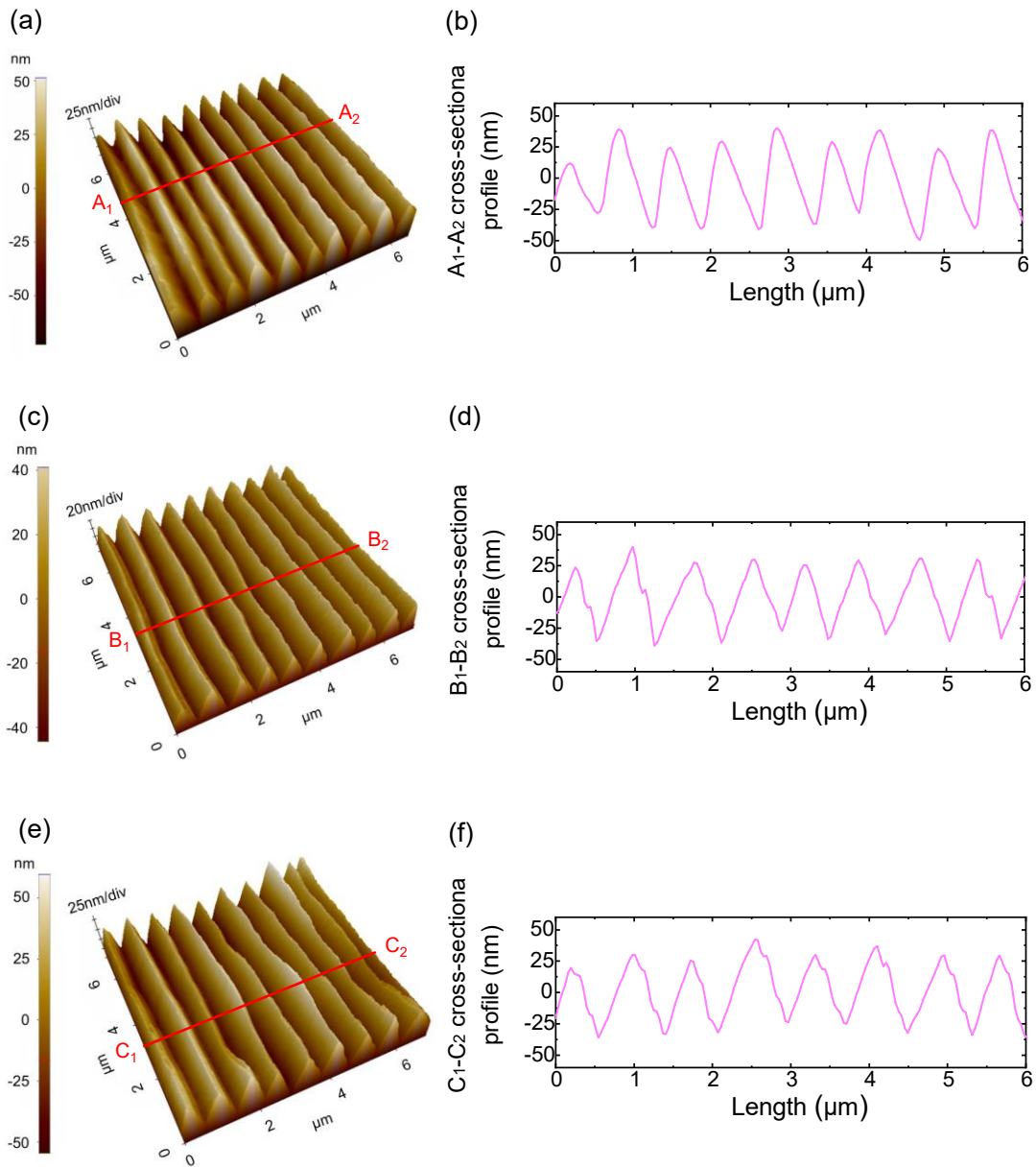


Figure 6.7 Three-dimensional topographies and profiles of the nanostructures. (a) AFM image of point A in Figure 6.5(b), (b) A₁-A₂ cross-sectional profile, (c) AFM image of point B in Figure 6.5(f), (d) B₁-B₂ cross-sectional profile, (e) AFM image of point C in Figure 6.5(f), and (f) C₁-C₂ cross-sectional profile.

The theoretical value of each facet spacing can be calculated by Eq. (5.8). The average value of experimental results can be obtained according to the cross-sectional profile in Figure 6.7. The comparison results of them are listed in Table 6.1. Taking the theoretical result as “true”, the difference between the theoretical value and

Chapter 6 Generation, hiding, and replication of nanostructure-induced optical information

experimental value is less than 3%, demonstrating the high machining accuracy of the developed two-degree-of-freedom vibration-assisted ultraprecision machining system.

Table 6.1 Comparison results of the theoretical value and experimental value of the facet spacing.

	Point A	Point B	Point C
Theoretical value (nm)	690.9	739.4	761.1
Experimental value (nm)	681.4	736.6	781.3
Difference	1.38%	0.38%	2.65%

The replicated optical information of the three-dimensional topography was also characterized, as shown in Figure 6.8(a). The corresponding D_1 - D_2 cross-sectional profile was plotted in Figure 6.8(b). Although the replicated optical information in Figure 6.6 can be easily recognized by the smartphone and the replication time is short, the replicated topography is not very regular. The irregular facet spacing is also found in the cross-section profile in Figure 6.8(b). Therefore, a new replication method with high accuracy needs to be explored in the future.

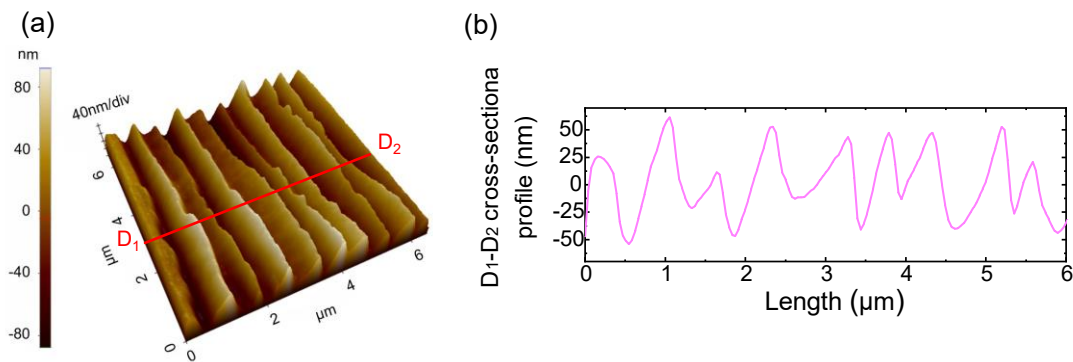


Figure 6.8 Three-dimensional topography of the replicated nanostructures. (a) AFM image of point D in Figure 6.6 and (b) D_1 - D_2 cross-sectional profile.

6.6 Summary

In this chapter, the concept of the generation and hiding of nanostructure-induced optical information on the metallic surface is proposed for the first time using developed

two-degree-of-freedom vibration-assisted ultraprecision machining system. The main conclusions of this chapter have been drawn:

(1) The vivid optical information “Let’s Beat COVID-19 Together” was machined on the workpiece surface in the form of the QR code, which can be easily read via the scan function of the smartphone. The word “LOVE” can be hidden by adjusting the facet spacing of nanostructures. The useful information only is obtained when the view angle locates at 52° - 72° . The difference between the theoretical value and experimental value about the facet spacing is less than 3%, which shows the high machining accuracy of the developed two-degree-of-freedom vibration-assisted ultraprecision machining system on the optical information generation and hiding.

(2) A rapid replication method of the optical information is proposed based on the cellulose acetate replication sheet. The optical information “Let’s Beat COVID-19 Together” is rapidly replicated on its surface, which can be easily recognized by the smartphone.

This environmentally friendly method of optical information generation, hiding, and replication in this chapter could be used for optical information security applications such as anti-counterfeiting in paper currency and brand tags.

Chapter 7 Conclusions and suggestions for future work

7.1 Conclusions

Micro/nanostructures are widely applied in various industries, such as optics, tribology, biology, and so on. The current machining methods, such as beam-assisted process, chemical etching process, lithography process, and ultraprecision fly cutting, face the problems of low machining efficiency, low surface quality, and high cost. To draw these issues, this thesis developed a novel two-degree-of-freedom vibration-assisted ultraprecision machining system and carried out research from three aspects (the design of the machining system, the modeling of the cutting force, and the applications of the micro/nanostructures). The main contributions and findings are summarized as follows:

(1) Design a novel two-degree-of-freedom vibration-assisted ultraprecision machining system.

To improve the machining efficiency and machining accuracy of micro/nanostructures, a novel two-degree-of-freedom vibration-assisted ultraprecision machining (2DOF-VAUM) system is developed based on the improved quasi-ellipse amplification mechanism. A performance test platform is established to evaluate the bandwidth and coupling ratio of the 2DOF-VAUM system, which are two significant quantitative indices of the working performances. Test results show that the bandwidth of the designed 2DOF-VAUM system can be up to 3000Hz, and the coupling ratios are 2.32% in the cutting direction and 4.86% in the depth-of-cutting direction, which solves

the drawbacks of the existing vibration-assisted machining system: low degree-of-freedom or low bandwidth.

Besides, a multi-physics finite element model is built to simulate the working performances of the 2DOF-VAUM system. The simulation results of these two indices agree well with the measurement results, verifying the effectiveness of this simulation model, which is a useful simulation approach not only in the area of ultraprecision machining but also in the area of micro/nano-positioning platform when simulating the working performances of the piezo-actuated system.

Considering the influences of the three-dimensional geometric shape of the cutting tool and the elastic recovery of workpiece material, a numerical simulation algorithm of micro/nanostructure generation on the metal surface is developed. The average geometrical error of this algorithm is less than $0.1\mu\text{m}$, demonstrating the accuracy of this algorithm. It also enables to provide guidance in the machining parameter selection before machining micro/nanostructures.

(2) Establish a practical cutting force model.

This model can predict the instantaneous cutting force in machining micro/nanostructures with the consideration of the machining parameters, the material property of the workpiece, and the geometrical shape of the cutting tool. Firstly, two typical features of the vibration-assisted ultraprecision machining, i.e., time-varying material removal behavior and controllable vibration trajectory, are investigated to deeply understand this process. Then, the mathematical expression of the instantaneous shear angle is established according to the time-varying vibration motion. A non-equidistant shear zone is utilized to evaluate the shear strain and shear strain rate inside the primary shear zone. According to the geometrical relationship between the radius

size of the cutting tool and the maximum value of the instantaneous depth-of-cutting, the instantaneous cutting area is modeled. Two kinds of microstructures, i.e., the shuttle-shaped and bamboo-shaped microstructures, on the difficult-to-machine pure titanium TA2 surface are machined. The experimental results of these two cases show that the established cutting force prediction model corresponds well with the experimental values. The average model error of the two cases is about 6%, demonstrating the effectiveness and accuracy of this cutting force model during micro/nanostructure machining.

(3) Explore the machinability of micro/nanostructures on the easy-to-flame material magnesium alloy surfaces.

The developed 2DOF-VAUM system is applied to machine micro/nanostructures on the magnesium alloy for solving the flammability and ignition of the magnesium alloy when using other machining processes. Various micro/nanostructures are successfully generated on the AZ31B magnesium alloy surface, demonstrating the effectiveness of the 2DOF-VAUM system on machining micro/nanostructures. There are no burn marks for all experiments, indicating the safety of the vibration-assisted ultraprecision machining process.

The sawtooth-shaped nanostructures have the function of inducing different color generations. The colorful letters “SKL”, “HKPU”, and “Mg alloy” as well as the colorful flower are observed with high saturation on the workpiece surface, which can extend the application of the magnesium alloy to the field of optics. The corresponding generation principle of these structural colors was also in detail illustrated. Besides, after machining micro/nanostructures on the magnesium alloy surface, the graphitization of the single-crystal diamond cutting tool is found, which leads to the

tool wear. The reason for graphitization is the high pressure of the cutting tool-workpiece interface area during micro/nanostructure machining, which provides the theoretical basis for solving the tool wear phenomenon in the future.

(4) Generate, hide, and replicate the optical information

Combining with information science, the developed 2DOF-VAUM system is employed to generate and hide optical information. The optical information “Let’s Beat COVID-19 Together” is machined on the workpiece surface in the form of a QR code. The word “LOVE” is hidden by controlling the facet spacing of the nanostructures, demonstrating the effectiveness of the developed 2DOF-VAUM system on optical information generation and hiding. This environmentally friendly method could be widely applied in the information display, information communication, and information protection in the future.

7.2 Suggestions for future work

Although systematic research on the vibration-assisted ultraprecision machining system, including the system design, cutting force modeling, and functional micro/nanostructure machining, have been conducted in this thesis, there remains some significant work to be done. Outlined below are several suggestions for future work.

(1) The nonlinearities of the vibration-assisted ultraprecision machining should be considered due to the hysteresis effect caused by the piezoelectric actuator. The hysteresis is a nonlinear relationship between the input voltage and output displacement of the piezoelectric actuator. In general, the hysteresis effect can be suppressed by suitable control strategies, such as the Preisach model, Bouc-Wen model, H_∞ robust control, and sliding mode control. However, the stability and reliability of these models in micro/nanostructure machining remain unclear, especially when the two-degree-of-

freedom vibration-assisted ultraprecision machining system works on a high frequency. Hence, a controller that can suppress the hysteresis effect needs to be designed in the vibration-assisted ultraprecision machining system.

(2) Although various micro/nanostructured surfaces have been machined on the copper alloy, pure copper, pure titanium, and magnesium alloy in this study, the investigation of micro/nanostructure machining on the brittle materials, such as silicon, germanium, ceramics, and glass, is not carried out. There are great challenges in obtaining micro/nanostructured surfaces with ultra-smooth because the brittle fractures and micro-crack would propagate into the finished surface. The machining mechanism of the brittle material is also different from the ductile material. All brittle materials undergo a transition from brittle to ductile machining region and the maximum depth-of-cut must be strictly no larger than the critical depth-of-cutting (Z. Zhu et al., 2019b). Therefore, the brittle material removal mechanism, determination of the critical depth-of-cutting, and determination of the maximum feed rate need to be explored for getting crack-free micro/nanostructured surfaces with high machining efficiency.

(3) Although the structural colors have been machined on the metallic surface using the developed vibration-assisted ultraprecision machining system, the resolution is not very high. It is caused by the dimension and shape of the cutting tool and the image recognition algorithm. In this study, the cutting tool with a radius of at least 200 μm was used. The large radius limits the size of the single-pixel along the Y-axis direction of the machining system. The size of the single pixel cannot be decreased to less than 10 μm . If designing a novel vibration-assisted ultraprecision machining system with a new type of cutting tool, this challenge can be efficiently solved, as shown in Figure 7.1(a) and (b). The new type of cutting tool has a straight-line-shaped cutting edge, and

its width is about $7\mu\text{m}$, which can make the size of a single-pixel with less than $10\mu\text{m}$ a reality.

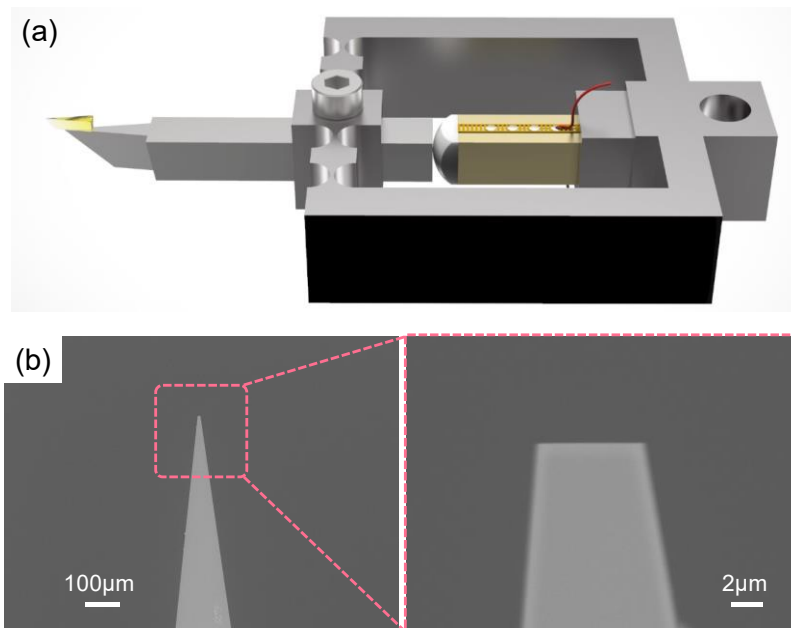


Figure 7.1 (a) The mechanical structure of the novel vibration-assisted ultraprecision machining system and (b) SEM images of the new type of single-crystal diamond cutting tool.

(4) In terms of the applications of the micro/nanostructure, the self-propelled motion of water droplets is of considerable importance in various heat transfer and microfluidic technologies. In 2006, Linke et al. found that the water droplets perform self-propelled motion when they are placed on a hot surface. The surface has a sawtooth-shaped structure and the temperature of the hot surface have to be heated to the Leidenfrost regime (the film-boiling regime) (Linke et al., 2006). This discovery offers interesting new possibilities for manipulating droplets and has been recognized as a key breakthrough in the directed motion of liquid droplets. However, most of them focus on the millimeter scale sawtooth-shaped structure. Hence, more attention needs be put into micro/nanoscale sawtooth-shaped structure. The experimental setup of water droplet self-transport is shown in Figure 7.2. The sample is placed on the heating

platform. A thermometer is used to monitor the sample temperature. The water droplet motion is captured using a high-speed camera.

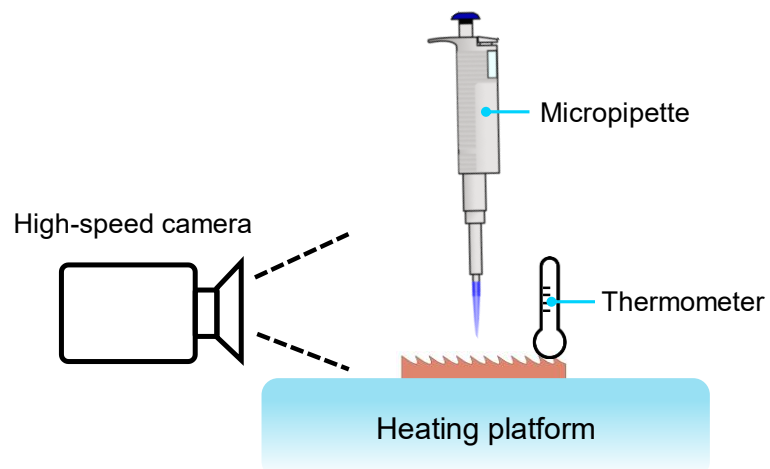


Figure 7.2 The schematic of the experimental setup of water droplet self-transport.

Appendices

Appendix I Multifunction I/O device (USB-6341, National Instruments Corp.)

The multifunction I/O device provides a mix of I/O with multichannel, output rate, and sample rates to meet experimental requirements. The USB-6341 provides digital I/O, analog I/O, and four 32-bit counters/timers for pulse width modulation. The main specifications are listed in Table A.1 and Table A.2.

Table A.1 Analog input specifications of the multifunction I/O device.

Analog input specification	Value
Number of channels	16 single ended or 8 differential
Analog-to-digital converter resolution	16 bits
Timing resolution	10 ns
Timing accuracy	50 ppm of sample rate
Input range	$\pm 0.2V, \pm 1V, \pm 5V, \pm 10V$
Input coupling	DC
Small signal bandwidth (-3 dB)	1.2 MHz
Maximum working voltage for analog inputs (signal + common mode)	$\pm 11V$ of AI GND

Table A.2 Analog output specifications of the multifunction I/O device.

Analog output specification	Value
Number of channels	2
Digital-to-analog converter resolution	16 bits
Maximum update rate (simultaneous):	
1 channel	900 kSample/s
2 channels	840 kSample/s per channel
Timing accuracy	50 ppm of sample rate
Timing resolution	10 ns
Output range	$\pm 10 V$
Output impedance	0.2 Ω

Appendix II High-performance piezo amplifier (E-617, Physik Instrumente)

The high-performance piezo amplifier is a linear amplifier of the analog signal for driving the piezoelectric actuator. The main specifications of the E-617 amplifier are listed in Table A.3.

Table A.3 Specifications of the E-617 amplifier.

Specification	Value
Input voltage range	-2 to 12 V
Output voltage	-30 to 130 V
Peak power (<5 ms)	280 W
Peak current (<5 ms)	2000 mA
Average output current (>5 ms)	1000 mA
Voltage gain	10 \pm 0.1
Amplifier bandwidth, small signal	3.5 kHz
Suggested capacitive load	>3 μ F
Output impedance	0.5 Ω

Appendix III 4-axis ultra-precision machine (350FG, Moore Nanotechnology)

Moore nanotechnology 350FG is four axis CNC machining system for on-axis machining of freeform surfaces and micro/nanostructures with the workpiece capacity of 500mm diameter × 300mm long as well as the programming resolution of 1 nanometer linear and 0.00001° rotary. The main specifications of the moore nanotechnology 350FG are listed in Table A.4.

Table A.4 Specifications of the moore nanotechnology 350FG.

Specification	Value
Axial Stiffness	140 N/μm
Radial Stiffness	87 N/μm
Travel of X-axis	350mm
Travel of Y-axis	150mm
Travel of Z-axis	300mm
Feedback resolution of the linear axis	0.034nm
Feed rate of X-axis (maximum)	1500mm/min
Feed rate of Y-axis (maximum)	1500mm/min
Feed rate of Z-axis (maximum)	1500mm/min
Positioning accuracy of C-axis	≤ ±2.0 arc seconds
Feedback resolution of C-axis	0.07 arc seconds
Maximum speed (Positioning mode) of C-axis	1,500 rpm

Appendix IV Multicomponent dynamometer (9256C1, Kistler Instrument Corp.)

The multicomponent dynamometer can measure the three orthogonal components of the cutting force along the X-, Y-, and Z-axis with high sensitivity. Besides, this dynamometer is protected against cutting fluid or splashing water. The main specifications of the multicomponent dynamometer 9256C1 are listed in Table A.5.

Table A.5 Specifications of the multicomponent dynamometer 9256C1.

Specification	Value
Operating temperature range	0-70°C
Natural frequency	
$F_n(x)$	≈5.1kHz
$F_n(y)$	≈5.5kHz
$F_n(z)$	≈5.6kHz
Rigidity	
C_x	>250N/μm
C_y	>250N/μm
C_z	>300N/μm
Sensitivity	
F_x	≈-26pC/N
F_y	≈-26pC/N
F_z	≈-13pC/N
Threshold	<0.002N
Measuring range	-250N...250N
Overload	-300N/300N

Appendix V Capacitive displacement sensor (Elite, Lion Precision)

The capacitive displacement sensor consists of the sensor driver (CPL290) and sensor probe (C8-3.2-2.0). It is an ultraprecision and noncontact displacement measurement device, which is generally applied to measure conductive targets. The output voltage is proportional to the changes in the gap between the probe and the target. As the target approaches the probe, the output voltage will become positive. The main specifications of the CPL290 and C8-3.2-2.0 are listed in Table A.6 and Table A.7.

Table A.6 Specifications of the CPL290.

Specification	Value
Linearity Error	$\pm 0.2\%$ F. S. or better, dependent on calibration
Error Band	$\pm 0.3\%$ F. S. or better, dependent on calibration
Standard Bandwidth (-3 db)	15kHz -10%+30%
Coarse Zero Adjustment Range	± 10 VDC
Fine Zero Adjustment Range	± 1 VDC
Operating Temperature	4°-50°C
Output Impedance	0 Ω
Output Max Voltage	± 13.5 VDC
Output Max Current	10mA

Table A.7 Specifications of the C8-3.2-2.0.

Specification	Value
Near gap	125 μ m
Measurement range	50 μ m
Sensitivity	0.400V/ μ m
Bandwidth	15kHz
Peak-to-peak resolution	7.30nm
RMS resolution	0.84nm
Linearity error	0.06%
Error band	0.07%

Reference

- Ahn, J., Lim, H., Son, S., 1999. Improvement of micro-machining accuracy by 2-dimensional vibration cutting. *Proc ASPE* 2–5.
- An, Q.L., Fu, Y.C., Xu, J.H., 2011. Experimental study on turning of TC9 titanium alloy with cold water mist jet cooling. *Int. J. Mach. Tools Manuf.* 51, 549–555. <https://doi.org/10.1016/j.ijmachtools.2011.03.005>
- Arefin, S., Zhang, X., Neo, D.W.K., Kumar, A.S., 2021. Effects of cutting edge radius in vibration assisted micro machining. *Int. J. Mech. Sci.* 208, 106673. <https://doi.org/10.1016/J.IJMECSCI.2021.106673>
- Astakhov, V.P., Osman, M.O.M., 1996. An analytical evaluation of the cutting forces in self-piloting drilling using the model of shear zone with parallel boundaries. Part 1: Theory. *Int. J. Mach. Tools Manuf.* 36, 1187–1200. [https://doi.org/10.1016/0890-6955\(96\)00024-7](https://doi.org/10.1016/0890-6955(96)00024-7)
- Astakhov, V.P., Osman, M.O.M., Hayajneh, M.T., 2001. Re-evaluation of the basic mechanics of orthogonal metal cutting: velocity diagram, virtual work equation and upper-bound theorem. *Int. J. Mach. Tools Manuf.* 41, 393–418. [https://doi.org/10.1016/S0890-6955\(00\)00084-5](https://doi.org/10.1016/S0890-6955(00)00084-5)
- Aydın, M., 2021. Numerical study of chip formation and cutting force in high-speed machining of Ti-6Al-4V bases on finite element modeling with ductile fracture criterion. *Int. J. Mater. Form.* 14, 1005–1018. <https://doi.org/10.1007/s12289-021-01617-9>

Reference

- Bai, W., Sun, R., Gao, Y., Leopold, J., 2016. Analysis and modeling of force in orthogonal elliptical vibration cutting. *Int. J. Adv. Manuf. Technol.* 83, 1025–1036. <https://doi.org/10.1007/s00170-015-7645-6>
- Bai, W., Sun, R., Roy, A., Silberschmidt, V. V., 2017. Improved analytical prediction of chip formation in orthogonal cutting of titanium alloy Ti6Al4V. *Int. J. Mech. Sci.* 133, 357–367. <https://doi.org/10.1016/J.IJMECSCI.2017.08.054>
- Balmert, S.C., Donahue Carey, C., Falo, G.D., Sethi, S.K., Erdos, G., Korkmaz, E., Falo, L.D., 2021. Dissolving Undercut Microneedle Arrays for Multicomponent Cutaneous Vaccination HHS Public Access. <https://doi.org/10.1016/j.jconrel.2019.11.023>
- Bechert, D.W., Bruse, M., Hage, W., 2000. Experiments with three-dimensional riblets as an idealized model of shark skin. *Exp. Fluids* 28, 403–412. <https://doi.org/10.1007/s003480050400>
- Bhushan, B., Jung, Y.C., Koch, K., 2009. Micro-, nano- And hierarchical structures for superhydrophobicity, self-cleaning and low adhesion. *Philos. Trans. R. Soc. A Math. Phys. Eng. Sci.* 367, 1631–1672. <https://doi.org/10.1098/rsta.2009.0014>
- Biswas, A., Bayer, I.S., Biris, A.S., Wang, T., Dervishi, E., Faupel, F., 2012. Advances in top–down and bottom–up surface nanofabrication: Techniques, applications & future prospects. *Adv. Colloid Interface Sci.* 170, 2–27. <https://doi.org/10.1016/J.CIS.2011.11.001>
- Brandner, J.J., Anurjew, E., Bohn, L., Hansjosten, E., Henning, T., Schygulla, U., Wenka, A., Schubert, K., 2006. Concepts and realization of microstructure heat exchangers for enhanced heat transfer. *Exp. Therm. Fluid Sci.* 30, 801–809. <https://doi.org/10.1016/j.expthermflusci.2006.03.009>

Reference

- Brinksmeier, E., Karpuschewski, B., Yan, J., Schönemann, L., 2020. Manufacturing of multiscale structured surfaces. *CIRP Ann.* 69, 717–739. <https://doi.org/10.1016/J.CIRP.2020.06.001>
- Bruzzone, A.A.G., Costa, H.L., Lonardo, P.M., Lucca, D.A., 2008. Advances in engineered surfaces for functional performance. *CIRP Ann. - Manuf. Technol.* <https://doi.org/10.1016/j.cirp.2008.09.003>
- Cademartiri, L., Bishop, K.J.M., 2015. Programmable self-assembly. *Nat. Mater.* 14, 2–9. <https://doi.org/10.1038/nmat4184>
- Cagan, S.C., Pruncu, C.I., Buldum, B.B., 2020. An investigation into ball burnishing process of magnesium alloy on CNC lathe using different environments. *J. Magnes. Alloy.* 8, 1061–1070. <https://doi.org/10.1016/J.JMA.2020.06.008>
- Cao, J., Shen, X., Yu, Z., Zheng, J., 2020. Engineering the crystalline silicon surface by femtosecond laser processing in liquid: Hierarchical micro/nanostructure and amorphization. *Mater. Chem. Phys.* 248, 122909. <https://doi.org/10.1016/j.matchemphys.2020.122909>
- Chen, C., Li, J., Zhan, S., Yu, Z., Xu, W., 2016. Study of Micro Groove Machining by Micro ECM. *Procedia CIRP* 42, 418–422. <https://doi.org/10.1016/j.procir.2016.02.224>
- Chen, H., Zhang, L., Zhang, P., Zhang, D., Han, Z., Jiang, L., 2017. A Novel Bioinspired Continuous Unidirectional Liquid Spreading Surface Structure from the Peristome Surface of *Nepenthes alata*. *Small* 13, 1–6. <https://doi.org/10.1002/sml.201601676>
- Chen, J.N., Xu, R.N., Zhang, Z., Chen, X., Ouyang, X.L., Wang, G.Y., Jiang, P.X., 2018. Phenomenon and Mechanism of Spray Cooling on Nanowire Arrayed and

Reference

- Hybrid Micro/ Nanostructured Surfaces. *J. Heat Transfer* 140, 1–16.
<https://doi.org/10.1115/1.4039903>
- Chen, W., Zheng, L., Teng, X., Yang, K., Huo, D., 2019. Finite element simulation and experimental investigation on cutting mechanism in vibration-assisted micro-milling. *Int. J. Adv. Manuf. Technol.* 105, 4539–4549.
<https://doi.org/10.1007/s00170-019-03402-0>
- Chen, Y., Wang, J., An, Q., 2021. Mechanisms and predictive force models for machining with rake face textured cutting tools under orthogonal cutting conditions. *Int. J. Mech. Sci.* 195, 106246.
<https://doi.org/10.1016/J.IJMECSCI.2020.106246>
- Chen, Y.L., Cai, Y., Tohyama, K., Shimizu, Y., Ito, S., Gao, W., 2017. Auto-tracking single point diamond cutting on non-planar brittle material substrates by a high-rigidity force controlled fast tool servo. *Precis. Eng.* 49, 253–261.
<https://doi.org/10.1016/j.precisioneng.2017.02.014>
- Cheung, C.F., Kong, L.B., Lee, W.B., To, S., 2006. Modelling and simulation of freeform surface generation in ultra-precision raster milling. *Proc. Inst. Mech. Eng. Part B J. Eng. Manuf.* 220, 1787–1801.
<https://doi.org/10.1243/09544054JEM548>
- Chun, D.M., Ngo, C.V., Lee, K.M., 2016. Fast fabrication of superhydrophobic metallic surface using nanosecond laser texturing and low-temperature annealing. *CIRP Ann. - Manuf. Technol.* 65, 519–522. <https://doi.org/10.1016/j.cirp.2016.04.019>
- Clement, R., Huang, J.L., Sun, Z.H., Wang, J.Z., Zhang, W.J., 2013. Motion and stress analysis of direct-driven compliant mechanisms with general-purpose finite

Reference

- element software. *Int. J. Adv. Manuf. Technol.* 65, 1409–1421.
<https://doi.org/10.1007/s00170-012-4266-1>
- Cuttino, J.F., Miller, A.C., Schinstock, D.E., 1999. Performance optimization of a fast tool servo for single-point diamond turning machines. *IEEE/ASME Trans. Mechatronics* 4, 169–179. <https://doi.org/10.1109/3516.769543>
- Dahmardeh, M., Nojeh, A., Takahata, K., 2011. Possible mechanism in dry micro-electro-discharge machining of carbon-nanotube forests: A study of the effect of oxygen. *J. Appl. Phys.* 109. <https://doi.org/10.1063/1.3587158>
- Dearnley, P.A., Grearson, A.N., 1986. Evaluation of principal wear mechanisms of cemented carbides and ceramics used for machining titanium alloy IMI 318. *Mater. Sci. Technol.* 2, 47–58.
- Deiab, I., Raza, S.W., Pervaiz, S., 2014. Analysis of Lubrication Strategies for Sustainable Machining during Turning of Titanium Ti-6Al-4V Alloy. *Procedia CIRP* 17, 766–771. <https://doi.org/10.1016/J.PROCIR.2014.01.112>
- Devaraj, A., Joshi, V. V., Srivastava, A., Manandhar, S., Moxson, V., Duz, V.A., Lavender, C., 2016. A low-cost hierarchical nanostructured beta-titanium alloy with high strength. *Nat. Commun.* 7, 1–8. <https://doi.org/10.1038/ncomms11176>
- Ding, H., Zhang, Q., Gu, H., Liu, X., Sun, L., Gu, M., Gu, Z., 2020. Controlled Microstructural Architectures Based on Smart Fabrication Strategies. *Adv. Funct. Mater.* 30, 1–14. <https://doi.org/10.1002/adfm.201901760>
- Doraiswamy, A., Jin, C., Narayan, R.J., Mageswaran, P., Mente, P., Modi, R., Auyeung, R., Chrisey, D.B., Ovsianikov, A., Chichkov, B., 2006. Two photon induced polymerization of organic–inorganic hybrid biomaterials for microstructured

Reference

-
- medical devices. *Acta Biomater.* 2, 267–275.
<https://doi.org/10.1016/J.ACTBIO.2006.01.004>
- Dornfeld, D., Min, S., Takeuchi, Y., 2006. Recent advances in mechanical micromachining. *CIRP Ann. - Manuf. Technol.* 55, 745–768.
<https://doi.org/10.1016/j.cirp.2006.10.006>
- Du, H., Yin, T., Yip, W.S., Zhu, Z., To, S., 2021a. Generation of structural colors on pure magnesium surface using the vibration-assisted diamond cutting. *Mater. Lett.* 299, 130041. <https://doi.org/10.1016/j.matlet.2021.130041>
- Du, H., Yip, W., Zhu, Z., To, S., 2021b. Development of a two-degree-of-freedom vibration generator for fabricating optical microstructure arrays. *Opt. Express* 29, 25903–25921.
- Du, H.H., Yip, W.S., Zhu, Z.W., To, S., 2022. Ultra-Precision Diamond Machined Freeform Optical Parts and Structures. *Encycl. Mater. Met. Alloy.* 462–477.
<https://doi.org/10.1016/B978-0-12-819726-4.00141-1>
- Dubey, A.K., Yadava, V., 2008. Laser beam machining-A review. *Int. J. Mach. Tools Manuf.* 48, 609–628. <https://doi.org/10.1016/j.ijmachtools.2007.10.017>
- Elka, E., Elata, D., Abramovich, H., 2004. The electromechanical response of multilayered piezoelectric structures. *J. Microelectromechanical Syst.* 13, 332–341. <https://doi.org/10.1109/JMEMS.2004.825307>
- Engel, U., Eckstein, R., 2002. Microforming—from basic research to its realization. *J. Mater. Process. Technol.* 125–126, 35–44. [https://doi.org/10.1016/S0924-0136\(02\)00415-6](https://doi.org/10.1016/S0924-0136(02)00415-6)

Reference

- Enlund, J., Isberg, J., Karlsson, M., Nikolajeff, F., Olsson, J., Twitchen, D.J., 2005. Anisotropic dry etching of boron doped single crystal CVD diamond. *Carbon N. Y.* 43, 1839–1842. <https://doi.org/10.1016/j.carbon.2005.02.022>
- Faraji Rad, Z., Prewett, P.D., Davies, G.J., 2021. High-resolution two-photon polymerization: the most versatile technique for the fabrication of microneedle arrays. *Microsystems Nanoeng.* 7. <https://doi.org/10.1038/s41378-021-00298-3>
- Fawcett, S.C., 1990. Small amplitude vibration compensation for precision diamond turning. *Precis. Eng.* 12, 91–96. [https://doi.org/10.1016/0141-6359\(90\)90033-U](https://doi.org/10.1016/0141-6359(90)90033-U)
- Fernandez-Zelaia, P., Melkote, S.N., 2019. Statistical calibration and uncertainty quantification of complex machining computer models. *Int. J. Mach. Tools Manuf.* 136, 45–61. <https://doi.org/10.1016/J.IJMACHTOOLS.2018.09.004>
- Ferraris, E., Reynaerts, D., Lauwers, B., 2011. Micro-EDM process investigation and comparison performance of Al₃O₂ and ZrO₂ based ceramic composites. *CIRP Ann. - Manuf. Technol.* 60, 235–238. <https://doi.org/10.1016/j.cirp.2011.03.131>
- Fu, F., Shang, L., Chen, Z., Yu, Y., Zhao, Y., 2018. Bioinspired living structural color hydrogels. *Sci. Robot.* 3. <https://doi.org/10.1126/SCIROBOTICS.AAR8580>
- Fu, M.W., Chan, W.L., 2013. A review on the state-of-the-art microforming technologies. *Int. J. Adv. Manuf. Technol.* 67, 2411–2437. <https://doi.org/10.1007/s00170-012-4661-7>
- Fu, Y., Bryan, N.K.A., 2004. Influence of astigmatism on the fabrication of diffractive structures by use of focused ion-beam milling. *Opt. Express* 12, 3954. <https://doi.org/10.1364/opex.12.003954>

Reference

- Fu, Z., Zhang, X., Wang, X., Yang, W., 2014. Analytical modeling of chatter vibration in orthogonal cutting using a predictive force model. *Int. J. Mech. Sci.* 88, 145–153. <https://doi.org/10.1016/J.IJMECSCI.2014.08.005>
- Gao, T., Xu, Z., Fang, F., Gao, W., Zhang, Q., Xu, X., 2012. High performance surface-enhanced Raman scattering substrates of Si-based Au film developed by focused ion beam nanofabrication. *Nanoscale Res. Lett.* 7, 1–8. <https://doi.org/10.1186/1556-276X-7-399>
- Gao, W., Araki, T., Kiyono, S., Okazaki, Y., Yamanaka, M., 2003. Precision nanofabrication and evaluation of a large area sinusoidal grid surface for a surface encoder. *Precis. Eng.* 27, 289–298. [https://doi.org/10.1016/S0141-6359\(03\)00028-X](https://doi.org/10.1016/S0141-6359(03)00028-X)
- Gao, Y., Sun, R., Leopold, J., 2018. An analytical force model for modulation-assisted turning. *J. Manuf. Process.* 31, 712–730. <https://doi.org/10.1016/j.jmapro.2017.12.024>
- Gao, Y., Sun, R.L., Chen, Y.N., Leopold, J., 2016. Mechanical and thermal modeling of modulation-assisted machining. *Int. J. Adv. Manuf. Technol.* 86, 2945–2959. <https://doi.org/10.1007/s00170-016-8421-y>
- Garateguy, G.J., Arce, G.R., Lau, D.L., Villarreal, O.P., 2014. QR images: Optimized image embedding in QR codes. *IEEE Trans. Image Process.* 23, 2842–2853. <https://doi.org/10.1109/TIP.2014.2321501>
- Ge, S., Liu, W., Zhou, S., Li, S., Sun, X., Huang, Y., Yang, P., Zhang, J., Lin, D., 2018. Design and preparation of a micro-pyramid structured thin film for broadband infrared antireflection. *Coatings* 8. <https://doi.org/10.3390/coatings8050192>

Reference

- Geiger, M., Kleiner, M., Eckstein, R., Tiesler, N., Engel, U., 2001. Microforming. *CIRP Ann.* 50, 445–462. [https://doi.org/10.1016/S0007-8506\(07\)62991-6](https://doi.org/10.1016/S0007-8506(07)62991-6)
- Geng, Q., Wang, D., Chen, P., Chen, S.C., 2019. Ultrafast multi-focus 3-D nano-fabrication based on two-photon polymerization. *Nat. Commun.* 10, 1–7. <https://doi.org/10.1038/s41467-019-10249-2>
- Gittard, S.D., Ovsianikov, A., Chichkov, B.N., Doraiswamy, A., Narayan, R.J., 2010. Two-photon polymerization of microneedles for transdermal drug delivery. *Expert Opin. Drug Deliv.* 7, 513–533. <https://doi.org/10.1517/17425241003628171>
- Gogotsi, Y.G., Kailer, A., Nickel, K.G., 1999. Transformation of diamond to graphite. *Nature* 401, 663–664. <https://doi.org/10.1038/44323>
- Grzelczak, M., Vermant, J., Furst, E.M., Liz-marza, L.M., 2010. Directed Self-Assembly of Nanoparticles 4, 3591–3605.
- Guo, P., Ehmann, K.F., 2013a. Development of a tertiary motion generator for elliptical vibration texturing. *Precis. Eng.* 37, 364–371. <https://doi.org/10.1016/j.precisioneng.2012.10.005>
- Guo, P., Ehmann, K.F., 2013b. An analysis of the surface generation mechanics of the elliptical vibration texturing process. *Int. J. Mach. Tools Manuf.* 64, 85–95. <https://doi.org/10.1016/j.ijmachtools.2012.08.003>
- Guo, P., Lu, Y., Ehmann, K.F., Cao, J., 2014. Generation of hierarchical microstructures for anisotropic wetting by elliptical vibration cutting. *CIRP Ann.* 63, 553–556. <https://doi.org/10.1016/J.CIRP.2014.03.048>

Reference

- Guo, P., Yang, Y., 2019. A novel realization of diffractive optically variable devices using ultrasonic modulation cutting. *CIRP Ann.* 68, 575–578. <https://doi.org/10.1016/J.CIRP.2019.04.014>
- Hahn, C., Hajebifard, A., Berini, P., 2020. Helium focused ion beam direct milling of plasmonic heptamer-arranged nanohole arrays. *Nanophotonics* 9, 393–399. <https://doi.org/10.1515/nanoph-2019-0385>
- Hatefi, S., Abou-El-Hossein, K., 2020. Review of single-point diamond turning process in terms of ultra-precision optical surface roughness. *Int. J. Adv. Manuf. Technol.* 106, 2167–2187. <https://doi.org/10.1007/s00170-019-04700-3>
- He, Y., Zhou, T., Dong, X., Liu, P., Zhao, W., Wang, X., Hu, Y., Yan, J., 2020. Generation of high-saturation two-level iridescent structures by vibration-assisted fly cutting. *Mater. Des.* 193, 108839. <https://doi.org/10.1016/j.matdes.2020.108839>
- Heidari, M., Yan, J., 2018. Nanometer-scale chip formation and surface integrity of pure titanium in diamond turning. *Int. J. Adv. Manuf. Technol.* 95, 479–492. <https://doi.org/10.1007/s00170-017-1185-1>
- Hnilova, M., Karaca, B.T., Park, J., Jia, C., Wilson, B.R., Sarikaya, M., Tamerler, C., 2012. Fabrication of hierarchical hybrid structures using bio-enabled layer-by-layer self-assembly. *Biotechnol. Bioeng.* 109, 1120–1130. <https://doi.org/10.1002/bit.24405>
- Hösel, T., Müller, C., Reinecke, H., 2011. Spark erosive structuring of electrically nonconductive zirconia with an assisting electrode. *CIRP J. Manuf. Sci. Technol.* 4, 357–361. <https://doi.org/10.1016/j.cirpj.2011.05.005>

Reference

- Hsieh, Y.-T., Lee, Y.-C., 2013. Metal contact printing photolithography for fabrication of submicrometer patterned sapphire substrates for light-emitting diodes. *J. Vac. Sci. Technol. B, Nanotechnol. Microelectron. Mater. Process. Meas. Phenom.* 31, 011604. <https://doi.org/10.1116/1.4774061>
- Isapour, G., Lattuada, M., 2018. Bioinspired Stimuli-Responsive Color-Changing Systems. *Adv. Mater.* 30, 1–36. <https://doi.org/10.1002/adma.201707069>
- Jahan, M.P., Wong, Y.S., Rahman, M., 2009. A study on the quality micro-hole machining of tungsten carbide by micro-EDM process using transistor and RC-type pulse generator. *J. Mater. Process. Technol.* 209, 1706–1716. <https://doi.org/10.1016/j.jmatprotec.2008.04.029>
- Jerald, J., Kumanan, S., Leo Kumar, S.P., Chandrakar, H. V., 2013. Experimental investigation and optimisation of process parameters in micro-electrical discharge machining. *Int. J. Manuf. Technol. Manag.* 27, 88–100. <https://doi.org/10.1504/IJMTM.2013.058617>
- Jieqiong, L., Jinguo, H., Mingming, L., Yan, G., Wenhui, Z., 2017. Development of nonresonant elliptical vibration cutting device based on parallel piezoelectric actuator. *AIP Adv.* 7. <https://doi.org/10.1063/1.4978262>
- Jieqiong, L., Jinguo, H., Xiaoqin, Z., Zhaopeng, H., Mingming, L., 2016. Study on predictive model of cutting force and geometry parameters for oblique elliptical vibration cutting. *Int. J. Mech. Sci.* 117, 43–52. <https://doi.org/10.1016/J.IJMECSCI.2016.08.004>
- Johnson, G.R., Cook, W.H., 1985. Fracture characteristics of three metals subjected to various strains, strain rates, temperatures and pressures. *Eng. Fract. Mech.* 21, 31–48. [https://doi.org/10.1016/0013-7944\(85\)90052-9](https://doi.org/10.1016/0013-7944(85)90052-9)

Reference

- JOHNSON, R., G., 1983. A constitutive model and data for materials subjected to large strains, high strain rates, and high temperatures. *Proc. 7th Int. Sympo. Ballist.* 541–547.
- Jung, Y.C., Bhushan, B., 2009. Wetting behavior of water and oil droplets in three-phase interfaces for hydrophobicity/philicity and oleophobicity/philicity. *Langmuir* 25, 14165–14173. <https://doi.org/10.1021/la901906h>
- Karg, M., König, T.A.F., Retsch, M., Stelling, C., Reichstein, P.M., Honold, T., Thelakkat, M., Fery, A., 2015. Colloidal self-assembly concepts for light management in photovoltaics. *Mater. Today* 18, 185–205. <https://doi.org/10.1016/J.MATTOD.2014.10.036>
- Kim, B.H., Na, C.W., Lee, Y.S., Choi, D.K., Chi, C.N., 2005. Micro electrochemical machining of 3D micro structure using dilute sulfuric acid. *CIRP Ann. - Manuf. Technol.* 54, 191–194. [https://doi.org/10.1016/S0007-8506\(07\)60081-X](https://doi.org/10.1016/S0007-8506(07)60081-X)
- Kim, H.S., Lee, K. Il, Lee, K.M., Bang, Y.B., 2009. Fabrication of free-form surfaces using a long-stroke fast tool servo and corrective figuring with on-machine measurement. *Int. J. Mach. Tools Manuf.* 49, 991–997. <https://doi.org/10.1016/j.ijmachtools.2009.06.011>
- Kinoshita, S., Yoshioka, S., Miyazaki, J., 2008. Physics of structural colors. *Reports Prog. Phys.* 71. <https://doi.org/10.1088/0034-4885/71/7/076401>
- Kulce, O., Mengu, D., Rivenson, Y., Ozcan, A., 2021. All-optical information-processing capacity of diffractive surfaces. *Light Sci. Appl.* 10. <https://doi.org/10.1038/s41377-020-00439-9>

Reference

- Lawson, R.A., Robinson, A.P.G., 2016. Overview of materials and processes for lithography, *Frontiers of Nanoscience*. Elsevier. <https://doi.org/10.1016/B978-0-08-100354-1.00001-6>
- Lee, X.-H., Moreno, I., Sun, C.-C., 2013. High-performance LED street lighting using microlens arrays. *Opt. Express* 21, 10612. <https://doi.org/10.1364/oe.21.010612>
- Li, B., Wang, X., Hu, Y., Li, C., 2011. Analytical prediction of cutting forces in orthogonal cutting using unequal division shear-zone model. *Int. J. Adv. Manuf. Technol.* 54, 431–443. <https://doi.org/10.1007/s00170-010-2940-8>
- Li, J., Liu, Z., 2018. Focused-ion-beam-based nano-kirigami: From art to photonics. *Nanophotonics* 7, 1637–1650. <https://doi.org/10.1515/nanoph-2018-0117>
- Li, K., Li, T., Zhang, T., Li, H., Li, A., Li, Z., Lai, X., Hou, X., Wang, Y., Shi, L., Li, M., Song, Y., 2021. Facile full-color printing with a single transparent ink. *Sci. Adv.* 7, 1–9. <https://doi.org/10.1126/sciadv.abh1992>
- Lin, H., Cheung, H.Y., Xiu, F., Wang, F., Yip, S., Han, N., Hung, T., Zhou, J., Ho, J.C., Wong, C.Y., 2013. Developing controllable anisotropic wet etching to achieve silicon nanorods, nanopencils and nanocones for efficient photon trapping. *J. Mater. Chem. A* 1, 9942–9946. <https://doi.org/10.1039/c3ta11889d>
- Lin, S.S., Hu, M.C., Lee, C.H., Lee, T.Y., 2015. Efficient QR Code Beautification With High Quality Visual Content. *IEEE Trans. Multimed.* 17, 1515–1524. <https://doi.org/10.1109/TMM.2015.2437711>
- Lin, Y., Xu, J., 2018. Microstructures Fabricated by Two-Photon Polymerization and Their Remote Manipulation Techniques: Toward 3D Printing of Micromachines. *Adv. Opt. Mater.* 6, 1–11. <https://doi.org/10.1002/adom.201701359>

Reference

- Ling, M., Cao, J., Zeng, M., Lin, J., Inman, D.J., 2016. Enhanced mathematical modeling of the displacement amplification ratio for piezoelectric compliant mechanisms. *Smart Mater. Struct.* 25. <https://doi.org/10.1088/0964-1726/25/7/075022>
- Linke, H., Alemán, B.J., Melling, L.D., Taormina, M.J., Francis, M.J., Dow-Hygelund, C.C., Narayanan, V., Taylor, R.P., Stout, A., 2006. Self-propelled leidenfrost droplets. *Phys. Rev. Lett.* 96, 2–5. <https://doi.org/10.1103/PhysRevLett.96.154502>
- Liu, M., Du, H., Cheng, Y., Zheng, H., Jin, Y., To, S., Wang, S., Wang, Z., 2021. Explosive Pancake Bouncing on Hot Superhydrophilic Surfaces. *ACS Appl. Mater. Interfaces* 13, 24321–24328. <https://doi.org/10.1021/acsami.1c05867>
- Liu, Q., Zhou, X., Liu, Z., Lin, C., Ma, L., 2014. Long-stroke fast tool servo and a tool setting method for freeform optics fabrication. *Opt. Eng.* 53, 092005. <https://doi.org/10.1117/1.oe.53.9.092005>
- Liu, S., Zhang, X., Seeger, S., 2019. Solvent-Free Fabrication of Flexible and Robust Superhydrophobic Composite Films with Hierarchical Micro/Nanostructures and Durable Self-Cleaning Functionality. *ACS Appl. Mater. Interfaces* 11, 47. <https://doi.org/10.1021/acsami.9b15318>
- Liu, X., Wu, D., Zhang, J., Hu, X., Cui, P., 2019. Analysis of surface texturing in radial ultrasonic vibration-assisted turning. *J. Mater. Process. Technol.* 267, 186–195. <https://doi.org/10.1016/j.jmatprotec.2018.12.021>
- Liu, Y., Zheng, Y., Gu, Y., Lin, J., Lu, M., Xu, Z., Fu, B., 2019. Development of piezo-actuated two-degree-of-freedom fast tool servo system. *Micromachines* 10, 337. <https://doi.org/10.3390/mi10050337>

Reference

- Liu, Y., Zhu, D., Zhu, L., 2012. Micro electrochemical milling of complex structures by using in situ fabricated cylindrical electrode. *Int. J. Adv. Manuf. Technol.* 60, 977–984. <https://doi.org/10.1007/s00170-011-3682-y>
- Lu, H., Lee, D., Kim, J., Kim, S., 2014. Modeling and machining evaluation of microstructure fabrication by fast tool servo-based diamond machining. *Precis. Eng.* 38, 212–216. <https://doi.org/10.1016/j.precisioneng.2013.06.004>
- Lu, L., Hu, S., Liu, L., Yin, Z., 2016. High speed cutting of AZ31 magnesium alloy. *J. Magnes. Alloy.* 4, 128–134. <https://doi.org/10.1016/J.JMA.2016.04.004>
- Lutey, A.H.A., Gemini, L., Romoli, L., Lazzini, G., Fuso, F., Faucon, M., Kling, R., 2018. Towards laser-textured antibacterial surfaces. *Sci. Rep.* 8, 1–10. <https://doi.org/10.1038/s41598-018-28454-2>
- Ma, C., Shamoto, E., Moriwaki, T., Zhang, Y., Wang, L., 2005. Suppression of burrs in turning with ultrasonic elliptical vibration cutting. *Int. J. Mach. Tools Manuf.* 45, 1295–1300. <https://doi.org/10.1016/J.IJMACHTOOLS.2005.01.011>
- Ma, Y., Jiang, L., Hu, J., Liu, H., Wang, S., Zuo, P., Ji, P., Qu, L., Cui, T., 2020. Multifunctional 3D Micro-Nanostructures Fabricated through Temporally Shaped Femtosecond Laser Processing for Preventing Thrombosis and Bacterial Infection. *ACS Appl. Mater. & Interfaces* 12, 17155–17166. <https://doi.org/10.1021/acsami.9b20766>
- Maekawa, K., Shirakashi, T., Usui, E., 1983. Flow Stress of Low Carbon Steel At High Temperature and Strain Rate (Part 2) - Flow Stress Under Variable Temperature and Variable Strain Rate. *Bull. Japan Soc. Precis. Eng.* 17, 167–172.

Reference

- Malshe, A., Rajurkar, K., Samant, A., Hansen, H.N., Bapat, S., Jiang, W., 2013. Bio-inspired functional surfaces for advanced applications. *CIRP Ann. - Manuf. Technol.* 62, 607–628. <https://doi.org/10.1016/j.cirp.2013.05.008>
- Mao, Z., Cao, W., Hu, J., Jiang, L., Wang, A., Li, X., Cao, J., Lu, Y., 2017. A dual-functional surface with hierarchical micro/ nanostructure arrays for self-cleaning and antireflection. <https://doi.org/10.1039/c7ra11186j>
- Marton, M., Vojs, M., Zdravecká, E., Himmerlich, M., Haensel, T., Krischok, S., Kotlár, M., Michniak, P., Veselý, M., Redhammer, R., 2013. Raman spectroscopy of amorphous carbon prepared by pulsed arc discharge in various gas mixtures. *J. Spectrosc.* 1. <https://doi.org/10.1155/2013/467079>
- Mayer, Martin, Schnepf, Max J, F König, Tobias A, Fery, Andreas, Mayer, M, Schnepf, M J, F König, T A, Fery, A, 2018. Colloidal Self-Assembly Concepts for Plasmonic Metasurfaces. <https://doi.org/10.1002/adom.201800564>
- Merchant, M.E., 1945. Mechanics of the metal cutting process. I. Orthogonal cutting and a type 2 chip. *J. Appl. Phys.* 16, 267–275.
- Molnar, T.G., Berezvai, S., Kiss, A.K., Bachrathy, D., Stepan, G., 2019. Experimental investigation of dynamic chip formation in orthogonal cutting. *Int. J. Mach. Tools Manuf.* 145, 103429. <https://doi.org/10.1016/J.IJMACHTOOLS.2019.103429>
- Moufki, A., Devillez, A., Segreti, M., Dudzinski, D., 2006. A semi-analytical model of non-linear vibrations in orthogonal cutting and experimental validation. *Int. J. Mach. Tools Manuf.* 46, 436–449. <https://doi.org/10.1016/J.IJMACHTOOLS.2005.04.017>
- Muanchan, P., Ito, H., 2018. Replication of Micro- / Nanostructures. Springer Singapore. https://doi.org/10.1007/978-981-10-6588-0_19-1

Reference

- Mukaida, M., Yan, J., 2017. Fabrication of hexagonal microlens arrays on single-crystal silicon using the tool-servo driven segment turning method. *Micromachines* 8. <https://doi.org/10.3390/mi8110323>
- Oshida, Y., Deguchi, A., 1987. Martensite Formation and the Related Toughness in 304 Stainless Steel During Low Temperature Fatigue. *Fatigue Fract. Eng. Mater. Struct.* 10, 363–372. <https://doi.org/10.1111/j.1460-2695.1987.tb00486.x>
- Oxley, P.L.B., Shaw, M.C., 1990. Mechanics of machining: an analytical approach to assessing machinability. *J. Appl. Mech.* 57, 253–253.
- Patterson, S.R., M.E.B., 1985. Design and testing of a long-range, precision fast tool servo system for diamond turning. *Precis. Eng.* 7, 123–128. [https://doi.org/10.1016/0141-6359\(85\)90030-3](https://doi.org/10.1016/0141-6359(85)90030-3)
- Peng, C.Y., Hsu, C.W., Li, C.W., Wang, P.L., Jeng, C.C., Chang, C.C., Wang, G.J., 2018. Flexible Photonic Crystal Material for Multiple Anticounterfeiting Applications. *ACS Appl. Mater. Interfaces* 10, 9858–9864. <https://doi.org/10.1021/acsami.8b00292>
- Radha, B., Lim, S.H., Saifullah, M.S.M., Kulkarni, G.U., 2013. Metal hierarchical patterning by direct nanoimprint lithography. *Sci. Rep.* 3, 1–8. <https://doi.org/10.1038/srep01078>
- Ramesh, A., Akram, W., Mishra, S.P., Cannon, A.H., Polycarpou, A.A., King, W.P., 2013. Friction characteristics of microtextured surfaces under mixed and hydrodynamic lubrication. *Tribol. Int.* 57, 170–176. <https://doi.org/10.1016/j.triboint.2012.07.020>
- Raut, H.K., Dinachali, S.S., Loke, Y.C., Ganesan, R., Ansah-Antwi, K.K., Góra, A., Khoo, E.H., Ganesh, V.A., Saifullah, M.S.M., Ramakrishna, S., 2015. Multiscale

Reference

- ommatidial arrays with broadband and omnidirectional antireflection and antifogging properties by sacrificial layer mediated nanoimprinting. *ACS Nano* 9, 1305–1314. <https://doi.org/10.1021/nn5051272>
- Ren, L., Xu, X., Liu, H., Yang, K., Qi, X., 2021. Biocompatibility and Cu ions release kinetics of copper-bearing titanium alloys. *J. Mater. Sci. Technol.* 95, 237–248. <https://doi.org/10.1016/J.JMST.2021.03.074>
- Rotella, G., Orazi, L., Alfano, M., Candamano, S., Gnilitskyi, I., 2017. Innovative high-speed femtosecond laser nano-patterning for improved adhesive bonding of Ti6Al4V titanium alloy. *CIRP J. Manuf. Sci. Technol.* 18, 101–106. <https://doi.org/10.1016/J.CIRPJ.2016.10.003>
- Ruibin, X., Wu, H., 2016. Study on cutting mechanism of Ti6Al4V in ultra-precision machining. *Int. J. Adv. Manuf. Technol.* 86, 1311–1317. <https://doi.org/10.1007/s00170-015-8304-7>
- Sato, O., Kubo, S., Zhong-Ze, G.U., 2009. Structural color films with lotus effects, superhydrophilicity, and tunable stop-bands. *Acc. Chem. Res.* 42, 1–10. <https://doi.org/10.1021/ar700197v>
- Saxena, K.K., Qian, J., Reynaerts, D., 2018. A review on process capabilities of electrochemical micromachining and its hybrid variants. *Int. J. Mach. Tools Manuf.* 127, 28–56. <https://doi.org/10.1016/j.ijmachtools.2018.01.004>
- Sezen, M., 2016. Focused Ion Beams (FIB) — Novel Methodologies and Recent Applications for Multidisciplinary Sciences. *Mod. Electron Microsc. Phys. Life Sci.* <https://doi.org/10.5772/61634>

Reference

- Shamoto, E., Moriwaki, T., 1999. Ultraprecision diamond cutting of hardened steel by applying elliptical vibration cutting. *CIRP Ann. - Manuf. Technol.* 48, 441–444. [https://doi.org/10.1016/S0007-8506\(07\)63222-3](https://doi.org/10.1016/S0007-8506(07)63222-3)
- Shamoto, E., Suzuki, N., Hino, R., 2008. Analysis of 3D elliptical vibration cutting with thin shear plane model. *CIRP Ann.* 57, 57–60. <https://doi.org/10.1016/J.CIRP.2008.03.073>
- Sharif, S., Rahim, E.A., 2007. Performance of coated- and uncoated-carbide tools when drilling titanium alloy—Ti-6Al4V. *J. Mater. Process. Technol.* 185, 72–76. <https://doi.org/10.1016/J.JMATPROTEC.2006.03.142>
- Srinivasa, Y. V., Shunmugam, M.S., 2013. Mechanistic model for prediction of cutting forces in micro end-milling and experimental comparison. *Int. J. Mach. Tools Manuf.* 67, 18–27. <https://doi.org/10.1016/J.IJMACHTOOLS.2012.12.004>
- Su, Y.W., Wu, C.S., Chen, C.C., Chen, C.D., 2003. Fabrication of two-dimensional arrays of CdSe pillars using E-beam lithography and electrochemical deposition. *Adv. Mater.* 15, 49–51. <https://doi.org/10.1002/adma.200390008>
- Sui, H., Zhang, X., Zhang, D., Jiang, X., Wu, R., 2017. Feasibility study of high-speed ultrasonic vibration cutting titanium alloy. *J. Mater. Process. Technol.* 247, 111–120. <https://doi.org/10.1016/J.JMATPROTEC.2017.03.017>
- Sun, S., Brandt, M., Dargusch, M.S., 2009. Characteristics of cutting forces and chip formation in machining of titanium alloys. *Int. J. Mach. Tools Manuf.* 49, 561–568. <https://doi.org/10.1016/j.ijmachtools.2009.02.008>
- Suzuki, N., Haritani, M., Yang, J., Hino, R., Shamoto, E., 2007. Elliptical vibration cutting of tungsten alloy molds for optical glass parts. *CIRP Ann. - Manuf. Technol.* <https://doi.org/10.1016/j.cirp.2007.05.032>

Reference

- Suzuki, N., Yokoi, H., Shamoto, E., 2011. Micro/nano sculpturing of hardened steel by controlling vibration amplitude in elliptical vibration cutting. *Precis. Eng.* 35, 44–50. <https://doi.org/10.1016/j.precisioneng.2010.09.006>
- Ta, D. V., Dunn, A., Wasley, T.J., Kay, R.W., Stringer, J., Smith, P.J., Connaughton, C., Shephard, J.D., 2015. Nanosecond laser textured superhydrophobic metallic surfaces and their chemical sensing applications. *Appl. Surf. Sci.* 357, 248–254. <https://doi.org/10.1016/j.apsusc.2015.09.027>
- Tan, S.J., Zhang, L., Zhu, D., Goh, X.M., Wang, Y.M., Kumar, K., Qiu, C.W., Yang, J.K.W., 2014. Plasmonic color palettes for photorealistic printing with aluminum nanostructures. *Nano Lett.* 14, 4023–4029. <https://doi.org/10.1021/nl501460x>
- Tan, X., Xie, B., 2015. Simulation Analysis of Laser Shock Forming for TA2 Titanium Sheet Based on ABAQUS, in: *Proceedings of the 2015 International Conference on Advanced Engineering Materials and Technology*. Atlantis Press, pp. 446–450. <https://doi.org/10.2991/icaemt-15.2015.87>
- Tang, H., Li, Y., 2014. Development and Active Disturbance Rejection Control of a Compliant Micro-/Nanopositioning Piezostage with Dual Mode. *IEEE Trans. Ind. Electron.* 61, 1475–1492. <https://doi.org/10.1109/TIE.2013.2258305>
- Tanvir Ahmmed, K.M., Grambow, C., Kietzig, A.M., 2014. Fabrication of micro/nano structures on metals by femtosecond laser micromachining. *Micromachines* 5, 1219–1253. <https://doi.org/10.3390/mi5041219>
- Tekumalla, S., Gupta, N., Gupta, M., 2020. Influence of turning speed on the microstructure and properties of magnesium ZK60 alloy pre-processed via turning-induced-deformation. *J. Alloys Compd.* 831. <https://doi.org/10.1016/j.jallcom.2020.154840>

Reference

- Tkachenko, I., Puech, W., Destruel, C., Strauss, O., Gaudin, J.M., Guichard, C., 2016. Two-Level QR code for private message sharing and document authentication. *IEEE Trans. Inf. Forensics Secur.* 11, 571–583. <https://doi.org/10.1109/TIFS.2015.2506546>
- To, S., Zhu, Z., Wang, H., 2016. Virtual spindle based tool servo diamond turning of discontinuously structured microoptics arrays. *CIRP Ann. - Manuf. Technol.* 65, 475–478. <https://doi.org/10.1016/j.cirp.2016.04.047>
- Torgersen, J., Qin, X.H., Li, Z., Ovsianikov, A., Liska, R., Stampfl, J., 2013. Hydrogels for two-photon polymerization: A toolbox for mimicking the extracellular matrix. *Adv. Funct. Mater.* 23, 4542–4554. <https://doi.org/10.1002/adfm.201203880>
- Tounsi, N., Vincenti, J., Otho, A., Elbestawi, M.A., 2002. From the basic mechanics of orthogonal metal cutting toward the identification of the constitutive equation. *Int. J. Mach. Tools Manuf.* 42, 1373–1383. [https://doi.org/10.1016/S0890-6955\(02\)00046-9](https://doi.org/10.1016/S0890-6955(02)00046-9)
- Trang, T.T.T., Zhang, J.H., Kim, J.H., Zargarán, A., Hwang, J.H., Suh, B.C., Kim, N.J., 2018. Designing a magnesium alloy with high strength and high formability. *Nat. Commun.* 9. <https://doi.org/10.1038/s41467-018-04981-4>
- Ushiba, S., Shoji, S., Masui, K., Kuray, P., Kono, J., Kawata, S., 2013. 3D microfabrication of single-wall carbon nanotube/polymer composites by two-photon polymerization lithography. *Carbon N. Y.* 59, 283–288. <https://doi.org/10.1016/j.carbon.2013.03.020>
- Varatharajulu, M., Duraiselvam, M., Kumar, M.B., Jayaprakash, G., Baskar, N., 2021. Multi criteria decision making through TOPSIS and COPRAS on drilling

Reference

-
- parameters of magnesium AZ91. *J. Magnes. Alloy.*
<https://doi.org/10.1016/J.JMA.2021.05.006>
- Viswanathan, R., Ramesh, S., Subburam, V., 2018. Measurement and optimization of performance characteristics in turning of Mg alloy under dry and MQL conditions. *Measurement* 120, 107–113.
<https://doi.org/10.1016/J.MEASUREMENT.2018.02.018>
- Wang, F., Huo, Z., Liang, C., Shi, B., Tian, Y., Zhao, X., Zhang, D., 2019. A Novel Actuator-Internal Micro/Nano Positioning Stage with an Arch-Shape Bridge-Type Amplifier. *IEEE Trans. Ind. Electron.* 66, 9161–9172.
<https://doi.org/10.1109/TIE.2018.2885716>
- Wang, J., Du, H., Gao, S., Yang, Y., Zhu, Z., Guo, P., 2019. An ultrafast 2-D non-resonant cutting tool for texturing micro-structured surfaces. *J. Manuf. Process.* 48, 86–97. <https://doi.org/10.1016/j.jmapro.2019.10.023>
- Wang, X., Sun, T., 2009. Fast tool servo system for online compensation of error motion on an ultraprecision lathe. *4th Int. Symp. Adv. Opt. Manuf. Test. Technol. Adv. Opt. Manuf. Technol.* 7282, 728211. <https://doi.org/10.1117/12.830820>
- Wang, Y., Li, F., Bian, N., Du, H.Q., Da Huo, P., 2021. Mechanism of plasticity enhancement of AZ31B magnesium alloy sheet by accumulative alternating back extrusion. *J. Magnes. Alloy.* <https://doi.org/10.1016/J.JMA.2021.08.035>
- Whitesides, G.M., 2006. The origins and the future of microfluidics. *Nature* 442, 368–373. <https://doi.org/10.1038/nature05058>
- Wilhelmi, O., Reyntjens, S., Van Leer, B., Anzalone, P.A., Giannuzzi, L.A., 2010. *Focused Ion and Electron Beam Techniques, Handbook of Silicon Based MEMS*

Reference

- Materials and Technologies. Elsevier Inc. <https://doi.org/10.1016/B978-0-8155-1594-4.00020-6>
- Wu, B., Zhou, M., Li, J., Ye, X., Li, G., Cai, L., 2009. Superhydrophobic surfaces fabricated by microstructuring of stainless steel using a femtosecond laser. *Appl. Surf. Sci.* 256, 61–66. <https://doi.org/10.1016/j.apsusc.2009.07.061>
- Wu, D.W., Liu, C.R., 1985. An Analytical Model of Cutting Dynamics. Part 2: Verification. *J. Eng. Ind.* 107, 112–118. <https://doi.org/10.1115/1.3185973>
- Wu, H., Jiao, Y., Zhang, C., Chen, C., Yang, L., Li, J., Ni, J., Zhang, Yachao, Li, C., Zhang, Yiyuan, Jiang, S., Zhu, S., Hu, Y., Wu, D., Chu, J., 2019. Large area metal micro-/nano-groove arrays with both structural color and anisotropic wetting fabricated by one-step focused laser interference lithography. *Nanoscale* 11, 4803–4810. <https://doi.org/10.1039/c8nr09747j>
- Xiong, W., Zhou, Y.S., He, X.N., Gao, Y., Mahjouri-Samani, M., Jiang, L., Baldacchini, T., Lu, Y.F., 2012. Simultaneous additive and subtractive three-dimensional nanofabrication using integrated two-photon polymerization and multiphoton ablation. *Light Sci. Appl.* 1, 1–4. <https://doi.org/10.1038/lsa.2012.6>
- Xu, C.L., Wang, Y.Z., 2018. Self-assembly of stearic acid into nano flowers induces the tunable surface wettability of polyimide film. *Mater. Des.* 138, 30–38. <https://doi.org/10.1016/J.MATDES.2017.10.057>
- Xu, H., Zhang, Y., Peng, R., Zhu, L., Lu, Y., 2021. Simulation and experimental study on the strength of Al7075-T6 clinched joint. *Eng. Fail. Anal.* 129, 105735. <https://doi.org/10.1016/J.ENGFAILANAL.2021.105735>

Reference

- Xu, W., Birbilis, N., Sha, G., Wang, Y., Daniels, J.E., Xiao, Y., Ferry, M., 2015. A high-specific-strength and corrosion-resistant magnesium alloy. *Nat. Mater.* 14, 1229–1235. <https://doi.org/10.1038/nmat4435>
- Xu, Z., Fang, F., Gao, H., Zhu, Y., Wu, W., Weckenmann, A., 2012. Nano fabrication of star structure for precision metrology developed by focused ion beam direct writing. *CIRP Ann. - Manuf. Technol.* 61, 511–514. <https://doi.org/10.1016/j.cirp.2012.03.118>
- Xu, Z.W., Fang, F.Z., Fu, Y.Q., Zhang, S.J., Han, T., Li, J.M., 2009. Fabrication of micro/nano-structures using focused ion beam implantation and XeF₂ gas-assisted etching. *J. Micromechanics Microengineering* 19. <https://doi.org/10.1088/0960-1317/19/5/054003>
- Yan, G., Fang, F., 2019. Fabrication of optical freeform molds using slow tool servo with wheel normal grinding. *CIRP Ann.* 68, 341–344. <https://doi.org/10.1016/J.CIRP.2019.04.083>
- Yan, X.T., Jin, Y.K., Chen, X.M., Zhang, C., Hao, C.L., Wang, Z.K., 2020. Nature-inspired surface topography: design and function. *Sci. China Physics, Mech. Astron.* 63, 0–15. <https://doi.org/10.1007/s11433-019-9643-0>
- Yang, H., Li, H., Ma, J., Li, G., Huang, D., 2021. Breaking bending limit of difficult-to-form titanium tubes by differential heating-based reconstruction of neutral layer shifting. *Int. J. Mach. Tools Manuf.* 166, 103742. <https://doi.org/10.1016/J.IJMACHTOOLS.2021.103742>
- Yang, S., Aizenberg, J., 2005. Microlens arrays with integrated pores. *Mater. Today* 8, 40–46. [https://doi.org/10.1016/S1369-7021\(05\)71288-8](https://doi.org/10.1016/S1369-7021(05)71288-8)

Reference

- Yang, X., Liu, C.R., 1999. Machining titanium and its alloys, *Machining Science and Technology*. <https://doi.org/10.1080/10940349908945686>
- Yang, Y., Guo, P., 2019. Global tool path optimization of high-resolution image reproduction in ultrasonic modulation cutting for structural coloration. *Int. J. Mach. Tools Manuf.* 138, 14–26. <https://doi.org/10.1016/J.IJMACHTOOLS.2018.11.002>
- Yang, Y., Pan, Y., Guo, P., 2017. Structural coloration of metallic surfaces with micro/nano-structures induced by elliptical vibration texturing. *Appl. Surf. Sci.* 402, 400–409. <https://doi.org/10.1016/j.apsusc.2017.01.026>
- Yang, Zhongze, Xu, W., Wu, H., Wan, X., Chen, Y., Shan, D., Guo, B., 2020. Enhancing hoop strength of titanium alloy tube by cross spinning. *Int. J. Mach. Tools Manuf.* 152, 103530. <https://doi.org/10.1016/J.IJMACHTOOLS.2020.103530>
- Yang, Zhichao, Zhu, L., Zhang, G., Ni, C., Lin, B., 2020. Review of ultrasonic vibration-assisted machining in advanced materials. *Int. J. Mach. Tools Manuf.* 156, 103594. <https://doi.org/10.1016/J.IJMACHTOOLS.2020.103594>
- Yao, N., Epstein, A.K., 2010. Surface nanofabrication using focused ion beam. *Microsc. Sci. Technol. Appl. Educ.* 2190–2199.
- Yao, X., Song, Y., Jiang, L., 2011. Applications of bio-inspired special wettable surfaces. *Adv. Mater.* 23, 719–734. <https://doi.org/10.1002/adma.201002689>
- Yip, W. S., To, S., 2019. Control of the ductile and brittle behavior of titanium alloys in diamond cutting by applying a magnetic field. *Sci. Rep.* 9, 1–9. <https://doi.org/10.1038/s41598-019-40702-7>

Reference

- Yip, Wai Sze, To, S., 2019. Reduction of Minimum Cutting Thickness of Titanium Alloys in Micro Cutting by a Magnetic Field Assistance. *IEEE Access* 7, 152034–152041. <https://doi.org/10.1109/ACCESS.2019.2945526>
- Yip, W.S., To, S., 2017. Tool life enhancement in dry diamond turning of titanium alloys using an eddy current damping and a magnetic field for sustainable manufacturing. *J. Clean. Prod.* 168, 929–939. <https://doi.org/10.1016/J.JCLEPRO.2017.09.100>
- Yong, L., Ruiqin, H., 2013. Micro electrochemical machining for tapered holes of fuel jet nozzles. *Procedia CIRP* 6, 395–400. <https://doi.org/10.1016/j.procir.2013.03.085>
- Yuan, Y., Zhang, D., Jing, X., Ehmann, K.F., 2020. Freeform surface fabrication on hardened steel by double frequency vibration cutting. *J. Mater. Process. Technol.* 275. <https://doi.org/10.1016/j.jmatprotec.2019.116369>
- Yuan, Z., Bin, J., Wang, X., Peng, C., Wang, M., Xing, S., Xiao, J., Zeng, J., Xiao, X., Fu, X., Chen, H., 2014. Fabrication of superhydrophobic surface with hierarchical multi-scale structure on copper foil. *Surf. Coatings Technol.* 254, 151–156. <https://doi.org/10.1016/J.SURFCOAT.2014.06.004>
- Zareena, A.R., Veldhuis, S.C., 2012. Tool wear mechanisms and tool life enhancement in ultra-precision machining of titanium. *J. Mater. Process. Technol.* 212, 560–570. <https://doi.org/10.1016/J.JMATPROTEC.2011.10.014>
- Zerilli, F.J., Armstrong, R.W., 1987. Dislocation-mechanics-based constitutive relations for material dynamics calculations. *J. Appl. Phys.* 61, 1816–1825. <https://doi.org/10.1063/1.338024>

Reference

- Zhang, D., Gao, B., Zhao, C., Liu, H., 2018. Visualized Quantitation of Trace Nucleic Acids Based on the Coffee-Ring Effect on Colloid-Crystal Substrates. *Langmuir* 35, 248–253. <https://doi.org/10.1021/acs.langmuir.8b03609>
- Zhang, H., Zhao, P., Ge, Y., Tang, H., Shi, Y., 2018. Chip morphology and combustion phenomenon of magnesium alloys at high-speed milling. *Int. J. Adv. Manuf. Technol.* 95, 3943–3952. <https://doi.org/10.1007/s00170-017-1511-7>
- Zhang, J., Cui, T., Ge, C., Sui, Y., Yang, H., 2016. Review of micro/nano machining by utilizing elliptical vibration cutting. *Int. J. Mach. Tools Manuf.* <https://doi.org/10.1016/j.ijmachtools.2016.04.008>
- Zhang, J., Suzuki, N., Shamoto, E., 2013. Investigation on machining performance of amplitude control sculpturing method in elliptical vibration cutting. *Procedia CIRP* 8, 328–333. <https://doi.org/10.1016/j.procir.2013.06.111>
- Zhang, L., Naples, N.J., Zhou, W., Yi, A.Y., 2019. Fabrication of infrared hexagonal microlens array by novel diamond turning method and precision glass molding. *J. Micromechanics Microengineering* 29. <https://doi.org/10.1088/1361-6439/ab10ff>
- Zhang, S.J., To, S., Zhu, Z.W., Zhang, G.Q., 2016. A review of fly cutting applied to surface generation in ultra-precision machining. *Int. J. Mach. Tools Manuf.* <https://doi.org/10.1016/j.ijmachtools.2016.01.001>
- Zhang, X., Jiang, L., Zeng, Z., Fang, F., Liu, X., 2015. High angular accuracy manufacture method of micro v-grooves based on tool alignment by on-machine measurement. *Opt. Express* 23, 27819. <https://doi.org/10.1364/oe.23.027819>

Reference

- Zhang, Y., Li, S., Zhu, K., 2020. Generic instantaneous force modeling and comprehensive real engagement identification in micro-milling. *Int. J. Mech. Sci.* 176, 105504. <https://doi.org/10.1016/J.IJMECSCI.2020.105504>
- Zhang, Z., Yan, J., Kuriyagawa, T., 2011. Study on tool wear characteristics in diamond turning of reaction-bonded silicon carbide. *Int. J. Adv. Manuf. Technol.* 57, 117–125. <https://doi.org/10.1007/s00170-011-3289-3>
- Zhao, Z., To, S., Zhu, Z., Yin, T., 2020. A theoretical and experimental investigation of cutting forces and spring back behaviour of Ti6Al4V alloy in ultraprecision machining of microgrooves. *Int. J. Mech. Sci.* 169, 105315.
- Zheng, Y., Gao, X., Jiang, L., 2006. Directional adhesion of superhydrophobic butterfly wings. *Soft Matter* 3, 178–182. <https://doi.org/10.1039/b612667g>
- Zhou, M., Ngoi, B.K.A., Yusoff, M.N., Wang, X.J., 2006. Tool wear and surface finish in diamond cutting of optical glass. *J. Mater. Process. Technol.* 174, 29–33. <https://doi.org/10.1016/J.JMATPROTEC.2005.02.248>
- Zhou, M., Zhang, H.J., Chen, S.J., 2010. Study on diamond cutting of nonrationally symmetric microstructured surfaces with fast tool servo. *Mater. Manuf. Process.* 25, 488–494. <https://doi.org/10.1080/10426910903365836>
- Zhu, W. Le, Duan, F., Zhang, X., Zhu, Z., Ju, B.F., 2018. A new diamond machining approach for extendable fabrication of micro-freeform lens array. *Int. J. Mach. Tools Manuf.* 124, 134–148. <https://doi.org/10.1016/j.ijmachtools.2017.10.007>
- Zhu, W. Le, Yang, X., Duan, F., Zhu, Z., Ju, B.F., 2019. Design and Adaptive Terminal Sliding Mode Control of a Fast Tool Servo System for Diamond Machining of Freeform Surfaces. *IEEE Trans. Ind. Electron.* 66, 4912–4922. <https://doi.org/10.1109/TIE.2017.2786281>

Reference

- Zhu, W. Le, Zhu, Z., He, Y., Ehmman, K.F., Ju, B.F., Li, S., 2017. Development of a Novel 2-D Vibration-Assisted Compliant Cutting System for Surface Texturing. *IEEE/ASME Trans. Mechatronics* 22, 1796–1806. <https://doi.org/10.1109/TMECH.2017.2693996>
- Zhu, X., Yan, W., Levy, U., Mortensen, N.A., Kristensen, A., 2017. Resonant laser printing of structural colors on high-index dielectric metasurfaces. *Sci. Adv.* 3, 1–9. <https://doi.org/10.1126/sciadv.1602487>
- Zhu, Y., Xu, W., Shi, Y., 2019. High-capacity encryption system based on single-shot-ptychography encoding and QR code. *Opt. Commun.* 435, 426–432. <https://doi.org/10.1016/J.OPTCOM.2018.11.040>
- Zhu, Z., Du, H., Zhou, R., Huang, P., Zhu, W. Le, Guo, P., 2020. Design and trajectory tracking of a nanometric ultra-fast tool servo. *IEEE Trans. Ind. Electron.* 67, 432–441. <https://doi.org/10.1109/TIE.2019.2896103>
- Zhu, Z., To, S., Zhang, S., 2015a. Theoretical and experimental investigation on the novel end-fly-cutting-servo diamond machining of hierarchical micro-nanostructures. *Int. J. Mach. Tools Manuf.* 94, 15–25. <https://doi.org/10.1016/j.ijmachtools.2015.04.002>
- Zhu, Z., To, S., Zhang, S., 2015b. Large-scale fabrication of micro-lens array by novel end-fly-cutting-servo diamond machining. *Opt. Express* 23, 20593. <https://doi.org/10.1364/OE.23.020593>
- Zhu, Z., To, S., Zhang, S., 2015c. Active control of residual tool marks for freeform optics functionalization by novel biaxial servo assisted fly cutting. *Appl. Opt.* 54, 7656. <https://doi.org/10.1364/ao.54.007656>

Reference

- Zhu, Z., To, S., Zhu, W. Le, Huang, P., Zhou, X., 2019a. Cutting forces in fast-/slow tool servo diamond turning of micro-structured surfaces. *Int. J. Mach. Tools Manuf.* 136, 62–75. <https://doi.org/10.1016/j.ijmachtools.2018.09.003>
- Zhu, Z., Tong, Z., To, S., Jiang, X., 2019b. Tuned diamond turning of micro-structured surfaces on brittle materials for the improvement of machining efficiency. *CIRP Ann.* 68, 559–562. <https://doi.org/10.1016/j.cirp.2019.04.092>
- Zhu, Z., Zhou, X., 2012. A novel fractional order model for the dynamic hysteresis of piezoelectrically actuated fast tool servo. *Materials (Basel)*. 5, 2465–2485. <https://doi.org/10.3390/ma5122465>
- Zhu, Z., Zhou, X., Liu, Z., Wang, R., Zhu, L., 2014. Development of a piezoelectrically actuated two-degree-of-freedom fast tool servo with decoupled motions for micro-/nanomachining. *Precis. Eng.* 38, 809–820. <https://doi.org/10.1016/j.precisioneng.2014.04.009>
- Zuo, Yinxiu, Zheng, Liuzheng, Zhao, Chao, Liu, Hong, Zuo, Y, Zheng, L, Zhao, C, Liu, H, 2019. 903849 (1 of 29) Micro-/Nanostructured Interface for Liquid Manipulation and Its Applications. <https://doi.org/10.1002/sml.201903849>